

# 13<sup>th</sup> Interventional MRI Symposium 2022

October 14 - 15, 2022

Leipzig, Germany

[www.imri2020.org](http://www.imri2020.org)

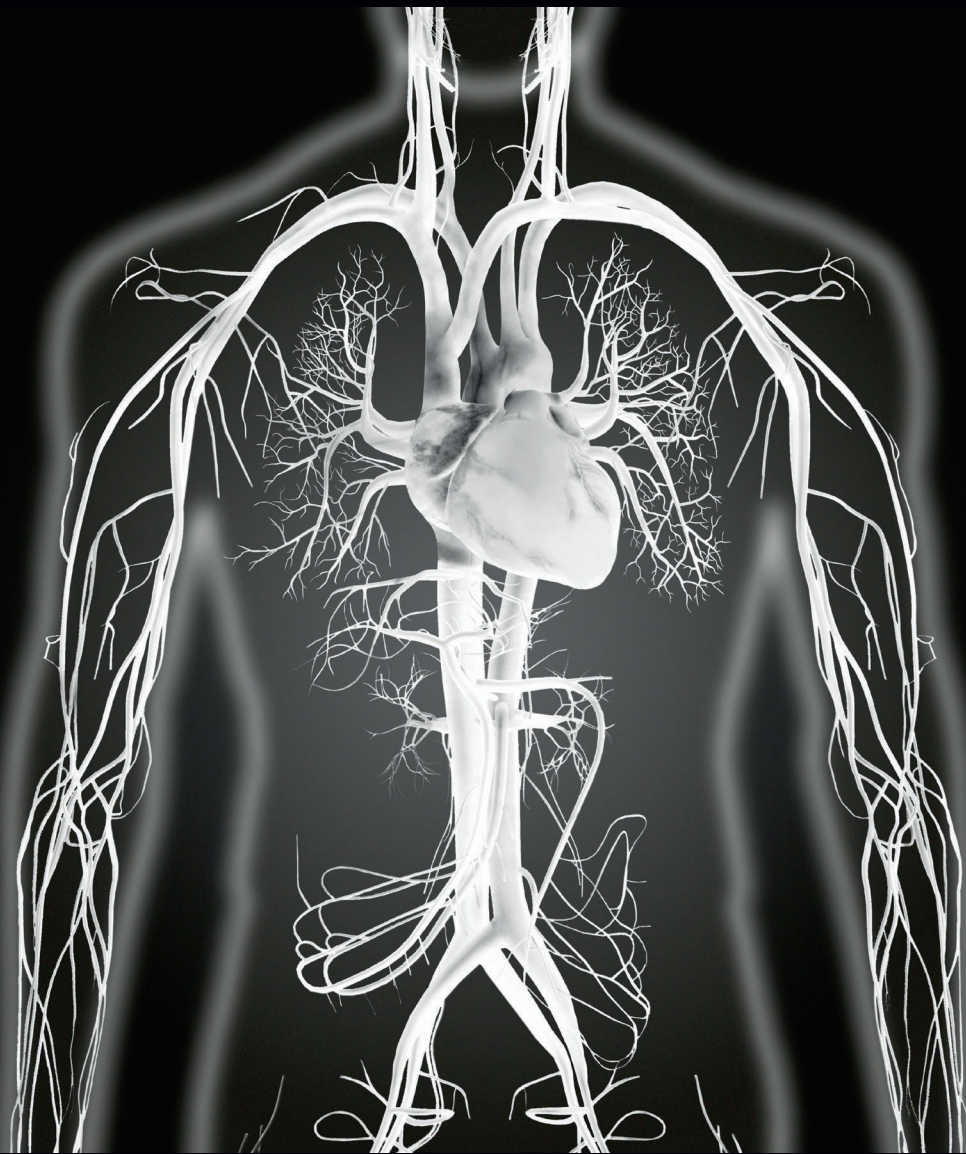


endorsed by



ESMRMB  
European Society for Magnetic Resonance in Medicine and Biology





## MR Safe and Visible Guidewires

[www.marvistech.com](http://www.marvistech.com)  
[info@marvistech.com](mailto:info@marvistech.com)

*The MarVis MR guidewires are not yet cleared for sale or use in humans in the U.S.*

## Preface

Dear colleagues and friends,

After two postponements due to the Covid-19 pandemic, we are eagerly looking forward to the October 2022 on-site iMRI Symposium in Leipzig. After the last gathering in 2018 in Boston, this will mark the reunion of the interventional MRI community with opportunities to interact with opinion leaders and innovators in the field, meet old friends or find new ones. This event is jointly organized by the University of Leipzig, the Department of Radiology at Brigham and Women's Hospital, Harvard Medical School in Boston, and the Department of Radiology and Radiological Science at Johns Hopkins University in Baltimore – in close cooperation with Hannover Medical School, University of Magdeburg and Emory Healthcare, Atlanta.

The iMRI Symposium provides an ideal platform for researchers, clinicians and healthcare professionals alike to present their latest results. Sessions with both technical and clinical topics are composed of lectures by invited speakers and proffered scientific papers. The meeting is endorsed by the ISMRM (International Society for Magnetic Resonance in Medicine) and the ESMRMB (European Society for Magnetic Resonance in Medicine and Biology) and supported by the Ferenc Jolesz National Center for Advanced Technologies Image Guided Therapy (NCIGT) at Harvard Medical School and the Innovation Center for Computer Assisted Surgery (ICCAS) at University of Leipzig.

We are hoping to see you soon in Leipzig!

August 14, 2022  
Leipzig

Clare Tempany  
Thomas Kahn  
Jonathan S. Lewin

## Table of Contents

---

### Ferenc Jolesz Memorial Lecture

---

The Impact of Artificial Intelligence on iMRI .....	1
<i>Ron Kikinis</i>	

---

### Session I: General Issues - Neuro

---

MR-guided neurosurgery – current status and future perspectives.....	2
<i>Arya Nabavi</i>	
Passive motor fMRI for intraoperative 3T MRI: First results .....	3
<i>Gilbert Hangel, Jonathan Wais, Matthias Tomschik, Philipp Pruckner, Christian Dorfer, Gregor Kasprian and Karl Rössler</i>	
Transcranial MR-guided focused ultrasound surgery .....	4
<i>Nathan McDannold</i>	
MRI and MPI of intra-arterial stem cell administration.....	5
<i>Ali Shakeri-Zadeh, Shreyas Kuddannaya, Adnan Bibic, Piotr Walczak and Jeff Bulte</i>	
MR-Guided Vagal Cryoablation for the Treatment of Obesity in a Canine Animal Model .	6
<i>Dara Kraitchman, Tina Ehtiati, Cheri Rice, Adham Khalil, Yingli Fu and Clifford R. Weiss</i>	

---

### Session II: Prostate

---

MRI-guided prostate biopsies .....	7
<i>Alexander Schaudinn, Nicolas Linder, Constantin Ehrengut, Toni Franz, Lars-Christian Horn, Holger Gößmann, Harald Busse and Timm Denecke</i>	
Comparison of Prostatic Lesion Conspicuity Using a Fast Balanced SSFP Sequence to Shorten in-Bore Robotic Transrectal MRI-Guided Biopsy: a Feasibility Study .....	8
<i>Joan C Vilanova, Josep Puig, Anna Pérez de Tudela, Montse Planas, Sònia Sala, Santi Thió-Henestroza and Juanjo Artazkoz</i>	
MR-guided prostate interventions - update on focal therapy with MRgFUS .....	9
<i>Clare Tempny</i>	
MR guided Focused Ultrasound ablation for intermediate risk prostate cancer .....	10
<i>Sangeet Ghai, Nathan Perlis, Kateri Corr, Rosanna Chan, Stuart McCluskey, Theodorus van der Kwast and Antonio Finelli</i>	
MR-guided prostate interventions - the Mayo experience .....	12
<i>David Woodrum, Scott Thompson, Daniel Adamo, Derek Lomas, Christopher Favazza, Aiming Lu, Lance Mynderse and Eugene Kwon</i>	
Interventional MRI in prostate cancer.....	13
<i>Jurgen Fütterer</i>	
MR guided cryoablation of oligo-metastatic prostate cancer to the obturator lymph nodes	14
<i>David Woodrum, Scott Thompson, Daniel Adamo, Derek Lomas, Christopher Favazza, Aiming Lu, Lance Mynderse and Eugene Kwon</i>	

AI-Based prediction of iceball boundaries in focal cryoablation of prostate cancer.....	15
<i>Pedro Moreira, Kemal Tuncali, Clare Tempany and Junichi Tokuda</i>	
MRI guided focal laser ablation (MRgFLA) for localized intermediate-risk prostate cancer – results of a phase II trial.....	16
<i>Sangeet Ghai, Nathan Perlis, Kateri Corr, Alex Zisman, Mark Gertner, Rosanna Chan, Stuart McCluskey, Theodorus van der Kwast and Antonio Finelli</i>	
Use of salvage MRI-guided focal or integrated boost high dose rate brachytherapy for recurrent prostate cancer.....	19
<i>Inmaculada Navarro-Domenech, Cynthia Ménard, Zhihuiamy Liu, Lisa Joseph, Maroie Barkati, Alejandro Berlin, Guila Delouya, Daniel Taussky, Marie-Claude Beauchemin, Benedicte Nicolas, Samuel Kadoury, Alexandra Rink, Srinivas Raman, Aravindhan Sundaramurthy, Robert Weersink, Dominic Beliveau-Nadeau, Joelle Helou and Peter Chung</i>	
<hr/> <b>Session IV: MR-Thermometry - Technology</b> <hr/>	
How accurate and reliable is MR thermometry?.....	20
<i>Kagayaki Kuroda</i>	
Prospective Phase Correction – A Novel Approach to Phase Drift Correction in Proton Resonance Frequency Shift Thermometry with Non-Cartesian Sequences .....	21
<i>Othmar Belker, Karen Meyer zu Hartlage, Marcel Gutberlet, J. Joaquin Löning Caballero, Daniel Reimert, Frank Wacker and Bennet Hensen</i>	
Accuracy of MRI real-time 3D temperature mapping during microwave heating - in-vitro results in gel phantoms.....	22
<i>Olaf Dietrich, Sergio Lentini, Osman Öcal, Pierre Bour, Thibaut Faller, Jens Ricke and Max Seidensticker</i>	
Susceptibility-corrected Proton Resonance Frequency Shift-based Magnetic Resonance thermometry for monitoring microwave ablation in the porcine liver .....	23
<i>Marcel Gutberlet, Bennet Hensen, Susanne Hellms, Christopher Werlein, Danny Jonigk, Inga Bruesch, Regina Rumpel, Eva-Maria Wittauer, Phillip Alexander Gronski, Florian W. R. Vondran, Dennis Parker and Frank Wacker</i>	
Using Magnetic Resonance Fingerprinting for Proton Resonance Frequency Shift based Temperature Monitoring of Microwave Ablation.....	24
<i>Moritz Gutt, J. Joaquin Löning Caballero, Dominik Horstmann, Frank Wacker, Bennet Hensen and Marcel Gutberlet</i>	
A robust motion compensation algorithm for volumetric MR-temperature monitoring during micro-wave ablation of liver tumor in patients.....	25
<i>Valéry Ozenne, Bruno Quesson, Pierre Bour, Thibaut Faller, Osman Öcal, Sergio Lentini, Max Seidensticker and Olaf Dietrich</i>	
Clinical Experience of 3D MR Thermometry for Liver Microwave Ablation.....	26
<i>Junichi Tokuda, Vincent M Levesque, Mariana C. Bernardes, Ravi Seethamraju and Kemal Tuncali</i>	

Performance of advanced DWI and MR thermometry near interventional needle-like devices.....	27
<i>James Holmes, Collin Buelo, Ruiqi Geng, Matt Tarasek, Desmond Yeo, Chris Brace, Diego Hernando, Aaron Faacks and Shane Wells</i>	
Real-time automatic temperature regulation during in-vivo MRI-guided Laser-induced Thermotherapy (MR-LITT).....	28
<i>Manon Desclides, Valéry Ozenne, Pierre Bour, Guillaume Machinet, Christophe Pierre, Stéphane Chemouny and Bruno Quesson</i>	
Feasibility of PRF thermometry at 0.55T .....	29
<i>Waqas Majeed, Axel Joachim Krafft, Henrik Odéen, Dennis Parker, Jianing Pang and Himanshu Bhat</i>	
Implementation of a real-time 3D-thermometry pipeline in Gadgetron for hepatic thermal ablation.....	30
<i>Dominik Horstmann, Karen Meyer zu Hartlage, Daniel Reimert, J. Joaquin Löning Caballero, Othmar Belker, Frank Wacker, Bennet Hensen and Marcel Gutberlet</i>	
A new versatile MR-guided high-intensity Focused Ultrasound (MRgHIFU) device: system performance assessment and clinical feasibility .....	31
<i>Paolo Cabras, Pierre Auloge, Erik Dumont, Benoit Wach, Elodie Breton, Afshin Gangi and Jonathan Vappou</i>	
<hr/> <b>Session V: Neuro - Ablation - Robotics</b> <hr/>	
Interventional MR Neurography - Applied Precision Medicine.....	32
<i>Jan Fritz</i>	
Retroperitoneal Lateral Femoral Cutaneous Nerve Blocks in the Work-Up of Thigh Pain: Performance Analysis of a New Technique .....	33
<i>Danoob Dalili, Shivani Ahlawat, Delaram Shakoor, Ali Rashidi, Amanda Isaac and Jan Fritz</i>	
Accurate targeting in lumbar and sacral nerve root infiltrations using MRI guidance, with 5-month follow-up.....	34
<i>Pauline C. Guillemain, Rares Salomir, Orane Lorton, Enrique Maturana, Alex Stöckli, Pierre-Alexandre Poletti, Nicolas Lauper, Dennis Dominguez, Sana Boudabbous and Max Scheffler</i>	
3 Tesla MR Neurography Guided Nerve Blocks for The Treatment of Pudendal Neuralgia.	35
<i>Danoob Dalili, Shivani Ahlawat, Amanda Isaac, Ali Rashidi, Arya Haj-Mirzaian and Jan Fritz</i>	
Percutaneous Ablations Using High Field Strength MRI: 12 Year Experience .....	36
<i>Kemal Tuncali</i>	
MRI-guided radiofrequency ablation of small HCC nodules (d ≈ 12 mm) in pretreated livers - use of the gadoxetic-acid plateau phase.....	37
<i>Sebastian Ebel, Hans Jonas Meyer, Gordian Prasse, Daniel Seehofer, Thomas Berg, Harald Busse, Andrea Hofmann, Holger Gößmann and Timm Denecke</i>	
MR-guided robotic interventions - pathway to autonomous and AI-assisted approach .....	38
<i>Nobuhiko Hata</i>	

Demonstration of versatile anatomically designed instrument alignment units for the remote operated ÅµRIGS instrument micropositioning system .....	39
<i>Robert Odenbach, Ivan Fomin, Niklas Thoma, Bennet Hensen, Frank Wacker and Georg Rose</i>	
MRI-Compatible Low Profile Robots for In-Bore Interventions .....	40
<i>Kevin Cleary, Karun Sharma, Elizabeth Fischer, Charles Dumoulin, Gang Li, Jan Fritz, Anthony Gunderman, Yue Chen, Reza Monfaredi, Dan Stoianovici and Iulian Iordachita</i>	
A piezo-driven MR-compatible Assistance System for Image-guided Interventions (eGantryMate).....	41
<i>Andreas Reichert, Ali Caglar Özen, Simon Reiss, Thomas Lottner, Niklas Verloh, Srdjan Milosavljevic, Michael Vogele and Michael Bock</i>	
<hr/> <b>Session VI: Cardiovascular</b> <hr/>	
MRI guided cardiac catheterisation in congenital heart disease.....	42
<i>Kuberan Pushparajah, Sebastien Roujol, Reza Razavi, Mari Nieves, Shaihan Malik, Grzegorz Kowalik and Alexander Neofytou</i>	
Tissue characterization of the acute ablation lesion directly after CMR-guided atrial flutter ablation .....	43
<i>G.P. Bijvoet, H.M.J.M. Nies, R.J. Holtackers, V.M. Smit-Fun, J. Smink, D. Linz, K. Vernooy, J.E. Wildberger, R. Nijveldt, S.M. Chaldoupi and C. Muhl</i>	
Towards MRI-guided cardiovascular interventions and focused ultrasound neuromodulation.....	44
<i>C. Martin Reich, Denis Gholami Bajestani, Christina Mulik, Gregor Schaeffers, Vincent Hammersen, Senta Schauer, Michael Schmid, Alexander Hegel, Kim Hoeger, Eva Pruy, Michael Steinmetz, Lisa Landgraf, Thies Jochimsen, Osama Sabri and Andreas Melzer</i>	
Deep artifact suppression for in-line real-time reconstruction of accelerated complex MR-Data: Application to interventional cardiac MR-thermometry .....	45
<i>Olivier Jaubert, Valéry Ozenne, Maxime Yon, Javier Montalt-Tordera, Jennifer Steeden, Vivek Muthurangu and Bruno Quesson</i>	
MR-Guided Coronary Catheterization in a Porcine Model at 3T: Success Rate and Learning Curve.....	46
<i>Simon Reiss, Thomas Lottner, Timo Heidt, Ali Özen, Constantin von Zur Mühlen and Michael Bock</i>	
MR-guided Treatment of Vascular Malformations .....	47
<i>Clifford R. Weiss</i>	
Combined 3D printed and silicone moulded vascular phantoms to develop and train catheter-based MRI-guided interventions.....	48
<i>Denis Gholami Bajestani, C. Martin Reich, Christina Mulik and Andreas Melzer</i>	

Artifact exploration of metallic and non-metallic guidewires at 0.55T, 1.5T, and 3T MR systems.....	49
<i>Waltraud Buchenberg, Klaus Düring, Martin Rube and Axel Joachim Krafft</i>	
<hr/> <b>Session VII: Technology - Management</b> <hr/>	
Techniques and devices for interventional MRI guidance .....	50
<i>Harald Busse, Sebastian Ebel, Gordian Prasse, Hans-Jonas Meyer, Holger Gößmann and Timm Denecke</i>	
Intensity-Based Tracking Technique to Register Devices in MRI-Guided Procedures .....	51
<i>Ivan Fomin, Robert Kowal, Marcel Gutberlet, Bennet Hensen, Frank Wacker, Oliver Speck and Georg Rose</i>	
Testing of a Transperineal Guide Grid for MR guided prostate procedures using Optical and Fiducial Fusion.....	52
<i>David Woodrum, Scott Thompson, Daniel Adamo, Christopher Favazza, Aiming Lu, Pezhman Foroughi, Alican Demir, Kenny Harlan and Lance Mynderse</i>	
Development of a Clinical Interventional MRI Service at Mayo Clinic Rochester: 2009-2021 .....	53
<i>Scott Thompson, Daniel Adamo, Erica Knavel Koepsel, Brian Welch, Derek Lomas, Devin Barker, David Ekrem, Patrick Hanson, Wayne Stenzel, Katie Gehling, Michelle Eggert, Lori Cranston, Desirae Howe-Clayton, Deb Berg, Paige Callahan, E. Matthew Hoffman, Timothy Curry, Christopher Favazza, Aiming Lu, Krzysztof Gorny, Joel Felmlee, Lance Mynderse and David Woodrum</i>	
<hr/> <b>Session VIII: Ablation</b> <hr/>	
MR-guided abdominal interventions.....	56
<i>Frank Wacker</i>	
Ablation and immunotherapy - a GI oncologists view.....	57
<i>Arndt Vogel</i>	
Extreme MR Ablation Cases: The Power of MRI Guidance.....	59
<i>David Woodrum, Scott Thompson, Daniel Adamo, Derek Lomas, Christopher Favazza, Aiming Lu and Lance Mynderse</i>	
<hr/> <b>Session IX: Focused Ultrasound - Joint Session with the European Focused Ultrasound Charitable Society (EUFUS)</b> <hr/>	
MR-guided focused ultrasound in Musculoskeletal Diseases.....	60
<i>Roberto Blanco Sequeiros</i>	
Retrospective analysis of MR-guided high intensity focused ultrasound (MRgFUS) in 65 patients with symptomatic lumbosacral facet joint arthritis.....	61
<i>Daniel Markus Düx, Markus Düx, Christian Stroszczyński and Lukas Beyer</i>	
Assessment of intercostal sonication capabilities of a dedicated transducer by MR-ARFI/thermometry .....	66
<i>Fanny Dabrin, Mathieu Guyot, Valéry Ozenne, Stéphane Chemouny, Pierre Bour and Bruno Quesson</i>	



MR-HIFU therapy of uterine fibroids – experience within an interdisciplinary fibroid center .....	67
<i>Jakob Leonhardi, Hans Surup, Nikolaos Bailis, Christiane Weisgerber, Romy Handzel, Sylvia Stark, Bahriye Aktas, Mireille Martin, Andreas Melzer, Harald Busse, Sebastian Ebel and Timm Denecke</i>	
Combination of MRI-guided focused ultrasound and radiation therapy - experimental rodent study .....	68
<i>Xinrui Zhang, Sebastian Greiser, Franziska Lange, Robbert van Gorkum, Marc Fournelle, Daniel Speicher, Steffen Tretbar, Andreas Melzer and Lisa Landgraf</i>	
Validation of the accuracy of a new transcostal phased-array HIFU transducer dedicated to hepatic ablation.....	69
<i>Orane Lorton, Pauline C. Guillemain, Yacine M’Rad, Andrea Peloso, Sana Boudabbous, Ryan Holman, Pierre-Alexandre Poletti, Alexis Ricoeur and Rares Salomir</i>	
<hr/> <b>Poster Session:</b> <hr/>	
Towards a Specialized Software for Interventional Radiology.....	70
<i>Julian Alpers, Sathish Balakrishnan, Mathews Jabaraj Soloman, Laureen Polenz, Juan Sebastián Sánchez López, Mathias Becker, Maciej Pech, Frank Wacker and Bennet Hensen</i>	
Lateral Femoral Cutaneous Nerve Cryoablation for the Treatment of Meralgia Paresthetica: First Results of a Pilot Study .....	71
<i>Sven Walter, Danoob Dalili and Jan Fritz</i>	
3 Tesla Selective MR neurography-guided anterior femoral cutaneous nerve blocks for diagnosing anterior thigh neuralgia .....	72
<i>Danoob Dalili, Shivani Ahlawat, Amanda Isaac, Ali Rashidi and Jan Fritz</i>	
One-Stop-Shop 3-Tesla MRI and MR-Guided MR Arthrography of The Shoulder: A Clinical Practice Evaluation with MSK Fellows .....	73
<i>Danoob Dalili, Amanda Isaac and Jan Fritz</i>	
Focal MR-guided High-Dose-Rate Brachytherapy for Localized Prostate Cancer: A Prospective Clinical Trial.....	74
<i>Enrique Gutierrez, Matthew Ramotar, Joelle Helou, Srinivas Raman, Rachel Glicksman, Alexandra Rink, Robert Weersink, Peter Chung and Alejandro Berlin</i>	
Comparison of preprocedural and intraprocedural distances of the urethra to the prostatic capsule when performing prostate ablation with the TULSA-PRO device .....	75
<i>David Sella, Greg Frey, Chandler Dora, Jordan Legout and Ali Montazeri</i>	
Estimating Uncertainty of 3D Ablation Zones using MR-Thermometry.....	76
<i>Simon Schröer, Marcel Gutberlet, Karen Meyer zu Hartlage, J. Joaquin Löning Caballero, Frank Wacker and Bennet Hensen</i>	
Higher resolution T1-weighted imaging of a liver lesion: a step to correlate thermal dose and lesion extent.....	77
<i>Thibaut Faller, Dounia El Hamrani, Pierre Bour, Clément Marcelin, Mathieu Guyot, Valéry Ozenne and Bruno Quesson</i>	

Rapid 3D post-ablation assessment of thermal ablation using accelerated Wave-Encoding MRI.....	78
<i>Quentin Lebret, Pierre Bour, Valéry Ozenne and Bruno Quesson</i>	
Real time volumetric MR-temperature monitoring during microwave ablation of a patient with hepatocellular carcinoma .....	79
<i>Osman Öcal, Sergio Lentini, Pierre Bour, Thibaut Faller, Jens Ricke, Olaf Dietrich and Max Seidensticker</i>	
Echo time selection in PRFS MR-thermometry to minimize errors in adipose tissues .....	80
<i>Anne Josset, Jonathan Vappou, Karine Choquet, Ounay Ishak and Elodie Breton</i>	
Assessment of MR compatibility of focused ultrasound systems.....	81
<i>Christakis Damianou, Nikolas Evripidou and Marinos Giannakou</i>	
Design of a new MR-compatible HIFU device for intercostal sonication into the heart .....	82
<i>Mathieu Guyot, Erik Dumont and Bruno Quesson</i>	
Combination of MRI-guided HIFU, bioluminescence imaging and transgenic mouse model to assess efficiency of noninvasive thermal therapies for solid tumors and their microenvironments .....	83
<i>Dounia El Hamrani, Pauline Jeanjean, Coralie Genevois, Franck Couillaud and Bruno Quesson</i>	
MR-guided high intensity focused ultrasound therapy monitoring using transient supersonic shearwave MR-elastography.....	84
<i>Ounay Ishak, Elodie Breton, Karine Choquet, Anne Josset, Paolo Cabras and Jonathan Vappou</i>	
MR-HIFU as treatment option for desmoid tumors of the abdominal wall: clinical setup and first results .....	85
<i>Hans Surup, Jakob Leonhardi, Julian Donig, Nikolaos Bailis, Albrecht Hoffmeister, Till Schönherr, Stefan Niebisch, Ines Gockel, Andreas Melzer, Mireille Martin, Sebastian Ebel, Holger Gößmann, Harald Busse and Timm Denecke</i>	
A simple MRI-guided robotic system for breast biopsy.....	86
<i>Anastasia Antoniou, Marinos Giannakou and Christakis Damianou</i>	
Prospective Observational Study of Pain Severity and Pain Interference Outcomes Following Percutaneous MRI-guided Laser Ablation or Cryoablation for Focal Painful Peripheral, Soft Tissue Vascular Malformations: 12-month Outcomes.....	87
<i>Scott Thompson, Erica Knavel Koepsel, Garret Powell, Emily Bendel, Haraldur Bjarnason, Stephanie Polites, Daniel Adamo, Desirae Howe-Clayton, Christopher Favazza, Aiming Lu, Katelyn Anderson, Megha Tollefson and David Woodrum</i>	
MRI-guided Conventional Catheter Ablation of Isthmus-dependent Atrial Flutter Using Active Catheter Imaging .....	91
<i>Stefan Ulbrich, Yan Huo, Jakub Tomala, Michael Wagner, Utz Richter, Liying Pu, Julia Mayer, Angela Zedda, Axel Joachim Krafft, Katherine Lindborg, Christopher Piorkowski and Thomas Gaspar</i>	
MRI-Driven Endovascular Thrombectomy .....	92
<i>Martin Phelan and Metin Sitti</i>	

Peripheral MR Lymphangiography: Integration into Clinical Workflow in a Hybrid MR-US Interventional Suite .....	93
<i>Scott Thompson, Erica Knavel Koepsel, Emily Bendel, Christopher Favazza, Aiming Lu, Jeremy Collins and David Woodrum</i>	
Hybrid Deformable Registration for Motion Compensation - A Feasibility Study with Realtime 3D MRI-US. ....	95
<i>Jhimli Mitra, Chitresh Bhushan, Soumya Ghose, David Mills, Aqsa Patel, Matthew Tarasek, Thomas Foo, Shane Wells, Sydney Jupitz, Bryan Bednarz, Chris Brace, James Holmes and Desmond Yeo</i>	
Convection triggers MRI amplitude and phase signal changes during proton beam irradiation of liquid water phantoms .....	96
<i>Juliane Peter, Sebastian Gantz, Leonhard Karsch, Jörg Pawelke and Aswin Hoffmann</i>	
Improving Accuracy of White Marker Contrast-Based Rapid 3D Passive MR Biopsy Needle Localization by Utilizing a Total Variation-Regularized Image Reconstruction.....	97
<i>Jonas F. Faust, Daniel Polak, Mark E. Ladd and Florian Maier</i>	
Transfer Function Measurement Setup for TRACRwire at 0.55T .....	98
<i>Ozgur Kocaturk, D. Korel Yildirim, Dogangun Uzun, Nasser Rafiee and Robert Lederman</i>	
MRI-Visible Pen for Marking the Entry Point of an MRI-Guided Needle Intervention.....	101
<i>Alexander Brockmann, Joachim Albrecht and Florian Maier</i>	
CNN-based Segmentation of Multiple Needles for Magnetic Resonance-guided Interventions .....	102
<i>Amanda Aleong, Peter Chung, Alejandro Berlin and Robert Weersink</i>	
Interactive Real-Time MRI-Guided Needle Tracking using Scanner Remote Control.....	103
<i>Amanda Aleong, Junichi Tokuda, Pedro Moreira, Ravi Seethamraju, Gerald Moran and Robert Weersink</i>	
Acousto-optics based active MRI markers for real-time device tracking.....	104
<i>Yusuf S. Yaras, Lee W. Bradley, D. Korel Yildirim, John Oshinski, Robert Lederman, Ozgur Kocaturk and F. Levent Degertekin</i>	
Effects of device trajectory variations on RF-induced heating at low field MRI systems .....	105
<i>Ali Özen, Maximilian Russe, Thomas Lottner, Simon Reiss, Isil Unal, Sebastian Littin, Maxim Zaitsev and Michael Bock</i>	
Metamaterial Inspired Surface Resonators as Wireless Coil .....	106
<i>Robert Kowal, Lucas Knoll, Enrico Pannicke, Max Joris Hubmann, Ivan Fomin, Daniel Gareis, Selina Scherbel, Bennet Hensen, Georg Rose, Frank Wacker and Oliver Speck</i>	
Multi-Channel Receive Coil for MRI-Guided Interventions .....	107
<i>Robert Kowal, Enrico Pannicke, Daniel Gareis, Selina Scherbel, Lucas Knoll, Ivan Fomin, Max Joris Hubmann, Bennet Hensen, Georg Rose, Frank Wacker and Oliver Speck</i>	

Assessing MR compatible biopsy grids for interventional procedures .....	108
<i>Elizabeth Fischer, Kevin Cleary, Karun Sharma, Nicholas Mouzakis, Mikias Gebremeskel, Pavel Yarmolenko and Reza Monfaredi</i>	
Sensorless and Cost-Efficient Force Feedback Signal Acquisition for Bowden Cable Driven Manipulators and Robotics during Image-Guided Procedures .....	109
<i>Marcel Eisenmann, Ivan Fomin, Robert Odenbach, Bennet Hensen, Frank Wacker and Georg Rose</i>	
Multifunctional, elastic and non-metallic Bowden-cable coupling mechanism for the modularization and remote control of the $\mu$ RIGS instrument micropositioning system.....	110
<i>Niklas Thoma, Robert Odenbach, Ivan Fomin, Bennet Hensen, Frank Wacker and Georg Rose</i>	
Local MRI Wireless RF Coils to Boost Calibration Reference Signal Prior to MRI Guided Interventional Treatments .....	111
<i>Joel Felmlee, Aiming Lu, Christopher Favazza, Lance Mynderse and David Woodrum</i>	
Radiofrequency Safety of External Defibrillation Electrodes at 1.5T.....	112
<i>Wyger Brink, Ralph Oosterveld and Ruud Verdaasdonk</i>	
Disposable & intuitive needle guide for needle-based interventions.....	113
<i>Juan Sebastián Sánchez López, Julian Alpers, Sathish Balakrishnan, Frank Wacker, Bennet Hensen, Maciej Pech and Mathias Becker</i>	
Coaxial needles: Optimizing visibility and operator confidence for MRI/US-guided intervention .....	114
<i>Aaron Faacks, James Holmes, Jhimli Mitra, Chitresh Bhushan, David Mills, Matthew Tarasek, Desmond Yeo, Christopher Brace and Shane Wells</i>	
Simultaneous T2-weighted MRI of 2 Orthogonal Slices for Real-time Lesion Tracking.....	115
<i>Samantha Hickey, Andreas Reichert, Wolfgang Ptacek, Thomas Bortfeld and Michael Bock</i>	
InGrid - Finding Incision Points the Easy Way.....	116
<i>Sathish Balakrishnan, Julian Alpers, Juan Sebastián Sánchez López, Mathias Becker, Maciej Pech, Frank Wacker and Bennet Hensen</i>	
Modularizable, MRI-Compatible and Elastic Abdominal Phantom to Perform Dynamic Interventional Experiments under Simulated Respiratory Cycles .....	117
<i>Katja Engel, Ivan Fomin, Thomas Gerlach, Bennet Hensen, Marcel Gutberlet, Frank Wacker and Georg Rose</i>	
A new multi-source MR-LITT device for creating conformal ablations .....	118
<i>Manon Desclides, Guillaume Machinet, Christophe Pierre, Valéry Ozenne, Stéphane Chemouny and Bruno Quesson</i>	
Investigation of Microwave ablation using dual applicators with real-time MR thermometry .....	119
<i>Aiming Lu, Liqiang Ren, Krzysztof Gorny, Joel Felmlee, Christopher Favazza, Daniel Adamo, Scott Thompson and David Woodrum</i>	

Feasibility of Quantitative MR-Based Hypoxia Measurements during MR-guided Gynecological Brachytherapy .....	121
<i>Junichi Tokuda, Gregory J. Ekchian, Robert A. Cormack, Michael Dyer, Evangelia Kaza and Michael J. Cima</i>	
Investigation of thermal injury risks from high-pressure gas supply line (HPGSL) during MR guided cryoablation .....	122
<i>Aiming Lu, Liqiang Ren, Christopher Favazza, Joel Felmlee, Daniel Adamo, Scott Thompson, Lance Mynderse and David Woodrum</i>	
Free-breathing T1-weighted 3D sequence in MR-guided liver interventions: Evaluation of workflow and diagnostic quality .....	124
<i>Julian Glandorf, Dominik Horstmann, Marcel Gutberlet, Daniel Düx, Frank Wacker and Bennet Hensen</i>	
Reduction of Electromagnetic Interferences of a commercially available MR approved microwave generator .....	125
<i>J. Joaquín Lönig Caballero, Karen Meyer zu Hartlage, Thomas Gerlach, Oliver Speck, Frank Wacker, Bennet Hensen and Marcel Gutberlet</i>	
Technical evaluation of motor evoked potential monitoring during MR-guided cryoablation of the shoulder .....	126
<i>Christopher Favazza, Scott Thompson, E. Matthew Hoffman, Joel Felmlee, Brian Welch, Daniel Adamo, David Woodrum and Aiming Lu</i>	
MR Guided Cryoablation of Renal Masses .....	128
<i>Daniel Adamo, Scott Thompson, Aiming Lu, Christopher Favazza, Erica Knavel Koepsel, Lance Mynderse and David Woodrum</i>	
Shaft heating risk mitigation during MRI-guided microwave ablation using non-actively-cooled applicators .....	129
<i>Aiming Lu, Liqiang Ren, Joel Felmlee, Christopher Favazza, Daniel Adamo, Scott Thompson and David Woodrum</i>	
Evaluation of Cryoablation Probe Artifacts at 0.55 T .....	131
<i>Florian Maier and Jurgen Fütterer</i>	
Investigation of cryoneedle induced RF heating risk during MRI-guided cryoablation at 1.5T .....	132
<i>Aiming Lu, Christopher Favazza, Joel Felmlee, Scott Thompson, Lance Mynderse, David Woodrum and Krzysztof Gorny</i>	
Intraoperative Neurophysiological Monitoring with Motor Evoked Potentials during MRI-guided Cryoablation: Initial Feasibility, Safety and Clinical Experience.....	133
<i>Scott Thompson, E. Matthew Hoffman, Garret Powell, Tatsuya Oishi, Laura Schmidt, Teresa Velez, Daniel Adamo, Christopher Favazza, Aiming Lu and David Woodrum</i>	
MRI-guided high-dose-rate interstitial brachytherapy of small hepatic malignancies (d <sub>max</sub> 12 mm) - use of the gadoteric-acid plateau phase .....	137
<i>Sebastian Ebel, Hans Jonas Meyer, Gordian Prasse, Daniel Seehofer, Thomas Berg, Kathrin Hering, Thomas Kuhnt, Harald Busse, Andrea Hofmann, Holger Gößmann and Timm Denecke</i>	

MR-based Volumetric Assessment of Thyroid Nodule Radiofrequency Ablation in  
Anthropomorphic Phantoms.....138  
*Tim Boers, Germen Wennemars, Sicco Braak, Michel Versluis, Srirang Manohar and  
Wyger Brink*

**Title: The Impact of Artificial Intelligence on iMRI**  
**Presenter: Ron Kikinis, M.D.**

**Abstract:** Artificial Intelligence (AI) is a powerful concept that has recently resulted in impactful technologies. Deep learning is one of those technologies which has become practical due to availability of powerful and affordable computational hardware and new software concepts. Deep learning has impacted many software applications such as natural language processing, voice recognition and computer vision. Large, annotated databases are a prerequisite for progress in this field. Unfortunately, creating well annotated and searchable databases with hundreds of thousands of subjects is not feasible today. Accordingly, AI research has focused on technical topics such as improved image registration and needle tracking. To enable research in this field, we will need to create annotated, accessible and searchable databases containing iMRI relevant data. The presentation will discuss these issues.

## MR-guided neurosurgery – current status and future perspectives

Arya Nabavi, MD, PhD, MaHM, IFAANS  
Director, Dept. of Neurosurgery  
Nordstadt Hospital, KRH  
Hanover, FRG

This overview will discuss the evolution of the concept of intra-operative MRI for Neurosurgery, a categorization of suit-designs, its impact and the potential role of the microscope, as one example in advancing surgical decision making.

Computer-assisted Navigation systems were introduced widely to guide neurosurgical operations. However, intraoperative deformation affects the accuracy of these systems at the most crucial surgical stages. The most logical and potentially furthest-reaching approach to address this problem, was to bring the imaging into the OR. Of the two potential concepts the most surgical, “near-online imaging” with integration of surgical and imaging space did not prevail. The current alternative designs, with scanners situated in adjacent rooms, incorporate many features, but result in “interdissection” MR-guided Neurosurgery.

However, maybe the most significant impact intraoperative MRI had, is the pressure on the development of new, non-MRI based methods to gather intraoperative information while preserving the surgical work-flow. The main focus in neurosurgery pertains to the ubiquitous surgical microscope. There have been significant improvements to enhance the information to be obtained microscopically.

Intraoperative MRI for Neurosurgery has invigorated the field of image guided neurosurgery, resulting in its own refinement and stimulating research even beyond imaging.



# Passive motor fMRI for intraoperative 3T MRI: First results

Gilbert Hangel<sup>1,2\*</sup>, Jonathan Wais<sup>1</sup>, Matthias Tomschick<sup>1</sup>, Philip Pruckner<sup>3</sup>, Christian Dorfer<sup>1</sup>, Gregor Kasprian<sup>3</sup>, Karl Rössler<sup>1</sup>

<sup>1</sup>Department of Neurosurgery, Medical University of Vienna; <sup>2</sup>High Field MR Centre, Department of Biomedical Imaging and Image-guided Therapy, Medical University of Vienna; <sup>3</sup>Division of Neuroradiology and Musculoskeletal Radiology, Department of Biomedical Imaging and Image-guided Therapy, Medical University of Vienna

**Purpose:** Using a recently installed 3T intraoperative MRI (ioMRI) with an 8-channel coil, we explored the methodological possibilities of a passive sensorimotor intraoperative fMRI (pifMRI) protocol under general anaesthesia. Previously, pifMRI was only demonstrated at 1.5T ioMRI systems<sup>1,2</sup>, while increased contrast and SNR at 3T<sup>3</sup> should allow higher resolutions, faster scans and greater reproducibility.

**Methods:** We used a 3T Skyra (Siemens) MRI with an 8-channel coil and head holder (NORAS) in a dual-room setup. *First*, we optimised the EPI acquisition using parallel imaging and multiband excitation to arrive at an optimal protocol. *Second*, we applied pifMRI to four patients (36f, 23f, 56m, 42f) undergoing tumour resection in proximity to the primary sensorimotor cortex. Clued by the stimulus system, an operator moved the subject's corresponding wrist or ankle. Data was compared to preoperative awake fMRI.

**Results:** We arrived at EPI scans with the following parameters: Multiband factor 2 and slice acceleration factor 2 with 24 reference lines for a final TR of 2 s, 3 mm isotropic resolution, at least 24 image slices, a TE of 30 ms, a block design with 135 volumes (15 alternating volumes on/off), and 4:30 min scan time.

The application to the intraoperative patient scans was successful without complications during pifMRI. The results showed activation consistent to preoperative fMRI in the primary sensorimotor areas before and after resection as demonstrated in Fig.1.

**Discussion:** We achieved both a feasible 3T fMRI protocol for intraoperative use and intraoperative mapping of the sensorimotor cortices in a small cohort of patients. To our knowledge, this is the first reported implementation of 3T pifMRI and features a shorter TR than previous studies. Yet, an extended evaluation with a larger sample size will be required to judge the possible benefits of this method.

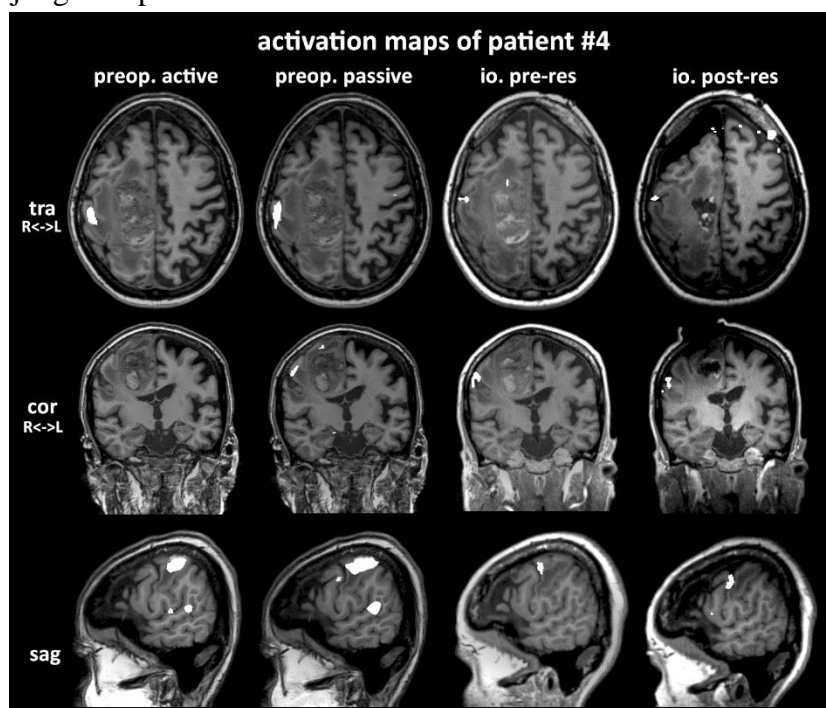


**Figure 1:** Activation maps of fMRI before surgery, and pifMRI before and after resection. pifMRI activation is smaller, but well aligned with awake fMRI. Post-resection activation is noticeably affected by brain shift.

## References

- 1: Gasser et al. 2005
- 2: Yamamoto et al. 2019
- 3: Triantafyllou et al. 2011

## **Transcranial MR-guided focused ultrasound surgery**

Nathan McDannold

Brigham and Women's Hospital, Harvard Medical School

Three of the mainstays of medicine – drugs, surgery, and radiation – all have significant limitations when it comes to the brain. With the wide spectrum of things that can go wrong in the central nervous system (CNS), the unique biology of the brain, and the distinct requirement to preserve and protect neural function, the need for different approaches and strategies to target CNS disorders is clear. New tools that are flexible, noninvasive, targeted, and that can safely be applied repeatedly are needed to overcome the barriers that have hindered the development of breakthrough therapies for CNS disorders. The only technology that we are aware of that has the potential to meet these needs is ultrasound. Acoustic energy can be focused to small volumes deep into tissue, sparing the surrounding tissues of any effects. The mechanical energy deposited in the focal region can be utilized in a surprisingly large number of ways and has fascinated neuroscientists for more than 60 years. After all these years of progress, the use of FUS in the brain is finally reaching patients in substantial numbers. Thermal ablation with transcranial MRI-guided FUS (TcMRgFUS) is now approved and reimbursed for treatment of essential tremor (ET) and Parkinson's-dominant tremor in the US and other countries, and several other functional neurosurgery applications are being investigated in clinical trials. BBB disruption with microbubble-enhanced FUS is now in clinical trials with devices from several companies and research sites. The use of FUS for neuromodulation is also now being explored in clinical trials and in healthy volunteers as a neuroscience tool. This talk will provide an overview of our clinical experience with FUS for thermal ablation, blood-brain barrier disruption, and neuromodulation.

## MRI and MPI of intra-arterial stem cell administration

A. Shakeri-Zadeh<sup>1</sup>, S. Kuddannaya<sup>1</sup>, A. Bibic<sup>1</sup>, P. Walczak<sup>2</sup>, J.W.M. Bulte<sup>1</sup>.

<sup>1</sup>The Russell H. Morgan Department of Radiology and Radiological Science, Johns Hopkins University School of Medicine, Baltimore, MD, USA; <sup>2</sup>Department of Diagnostic Radiology and Nuclear Medicine, University of Maryland School of Medicine, Baltimore, MD, USA.

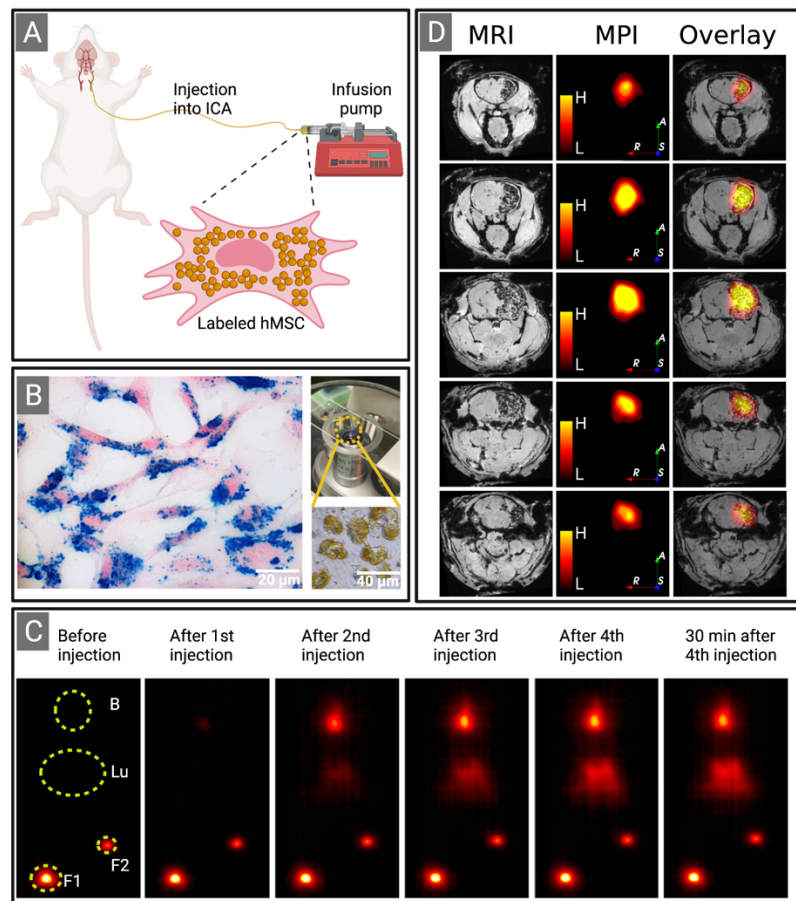
**Purpose:** For stem cell therapy of the CNS, intra-arterial (IA) injection into the carotid artery is an appealing delivery route because it avoids initial uptake by systemic organs, allowing large numbers of cells to be delivered directly to the brain. We used magnetic particle imaging (MPI) combined with magnetic resonance imaging (MRI) to track SPIO-labeled human mesenchymal stem cells (hMSCs) *in vivo*.

**Material and Methods:** SPIO-labeled cells were collected and prepared for IA injection into immunodeficient male Rag2 mice (n=6). Prussian blue staining and a Ferrozine-based spectrophotometric assay were used to assess intracellular iron uptake. Cells were delivered into brain using 4 separate injections (30,000 cells each) with a time interval of 6 min between each injection. Whole body standard *in vivo* 2D MPI was performed before and after each injection using a Magnetic Insight Momentum scanner. A final 2D MPI scan was obtained 30 min after the last injection. Animals were sacrificed and the heads were imaged *ex vivo* with MRI using a 17.4T vertical bore Bruker Biospec scanner and then again with MPI. For MPI and MRI we used the same FOV with 55 projections. Two fiducials containing 10,000 and 20,000 labeled hMSCs were placed within the MPI/MRI FOVs and used to register the MPI dataset with MRI using 3D slicer software.

**Results:** Figure 1 shows *in vivo* MP images of a mouse before and after IA injection, where hot spots in brain and lung as well as signal intensity alterations over time are present, and representative overlay images of *ex vivo* MRI and MPI datasets, where a unilateral distribution of labeled hMSCs at the side of IA injection can be seen. Aside from having quantitative and structural information together, the chief advantage of MPI/MRI hybrid imaging is the utilization of cold tracers (without radioactivity), allowing easy-to-interpret whole-body distribution studies, similar to PET/CT, SPECT/CT or PET/MRI hybrid imaging.

**Conclusion:** This successful example MPI application of *in vivo* tracking of hMSCs may encourage further use of this technique to probe the fate of therapeutic cells in various transplantation paradigms.

**Figure 1.** (A) Schematic outline of IA injection of Resovist-labeled hMSCs into the internal carotid artery (ICA). (B) Prussian blue staining of labeled hMSCs along with a microscopic image of live labeled cells before injection. (C) Serial MP images of a mouse before and after IA injection. In this panel, B, Lu, F1, and F2 stand for brain, lung, first fiducial (20,000 labeled hMSCs) and second fiducial (10,000 labeled hMSCs), respectively. (D) Five MPI/MRI slices from forebrain to midbrain (top to bottom) of a mouse injected with 120,000 labeled hMSCs.



## MR-Guided Vagal Cryoablation for the Treatment of Obesity in a Canine Animal Model

Dara L Kraitchman, VMD, PhD<sup>1</sup>; Tina Ehtiati, PhD<sup>2</sup>, Cheri Rice<sup>1</sup>, Adham Khalil, MD<sup>1</sup>, Yingli Fu, PhD<sup>1</sup>, Clifford R. Weiss, MD<sup>1</sup> <sup>1</sup>Russell H Morgan Department of Radiology and Radiological Science, John Hopkins University, Baltimore, MD; <sup>2</sup>Siemens Medical Solutions USA, Inc., Malvern, PA

**Purpose:** Cryoneurolysis has been used predominantly for the attenuation of nerve signals related to pain.<sup>1,2</sup> Recently, the technique of targeting nerves with MRI for cryoablation has expanded the indications based on safe percutaneous access and monitoring of the ablation zone.<sup>3-5</sup> It has long been known that interruption of the vagus nerve results in weight loss and decreased appetite.<sup>6,7</sup> Recently a pilot trial was designed to evaluate the feasibility of percutaneous, computed tomography (CT)-guided cryovagotomy in human subjects with class I or class II obesity.<sup>8</sup> The purpose of the current study was to assess the feasibility of MR-guided cryovagotomy in a canine model of obesity.

**Materials and Methods:** All animal studies were approved by the institutional animal care and use committee. Beagles (n=3; 2 males, ~10 kg) were fed in excess of their normal caloric intake to induce moderate obesity (>10% increase body mass). All studies were performed under isoflurane general anesthesia on a 1.5T MRI (Espree, Siemens) using an MR-compatible cryoablation system (Seednet, Galil/Boston Scientific). A pilot study was performed without cryoablation for image sequence planning in one dog with needle insertion without cryoablation. Subsequently, vagocryotomy was performed in each dog followed by weekly weights and monitoring of blood counts and chemistries. Serum was also obtained to measure gastric hormones.

Cone-beam CTs (6s Dyna Body preset CBCT, Artis Zee, Siemens) were obtained prior to and/or after vagocryotomy for comparison to MRI results. Scout MRIs were obtained followed by higher resolution 2D axial, coronal, and sagittal PD and axial 3D T1-weighted sequences (PD TSE:2s TR; 19 ms TE; 260 cm<sup>2</sup> FOV; 3.5 cm slice thickness; breath-hold T1 VIBE: fat saturation, 6.4 ms TR; 2.4 ms TE; 8° FA; 0.9 mm<sup>3</sup> pixel size) for planning the skin entry point and needle path. The dog's back was shaved and sterilely prepared. Lidocaine (2% 1-2 ml) was injected along the planned cryoprobe tract. A cryoprobe (Iceseed) was advanced to the region of the dorsal vagal trunk for cryoablation. Post-gadolinium (Gadovist) images were acquired. The dog was recovered after the procedure and continued on *ad libitum* feeding of normal dog chow with food enrichments. The dogs were monitored for at least 1 month after cryoablation with MRI and for changes in weight, blood parameters, and adverse events.

**Results:** Identification of critical structures to avoid as well as the posterior vagal trunk was possible with MRI but not CBCT (Fig). The cryoprobe was advanced above the diaphragm to the posterior vagus as it transitions along the posterolateral esophagus on the right side using a low resolution, axial PD scan consisting of ~5 slices. With the probe in position, double 2-minute freeze-1-minute-thaw (2/1/2) cycles were performed with monitoring of the ice ball formation during simultaneous scanning to induce vagal nerve injury. The probe was removed, post-gadolinium images were acquired to document probe location/injury, and the dogs recovered uneventfully. No adverse events were noted acutely or post-cryoablation. Persistent injury was noted at the 1-month MRI of the cryoablated zone. All dogs show a 50-90% acute excess weight loss. Two dogs maintain reduced weight loss; one dog has shown increased weight gain on a corticosteroid regime as part of another study. Histopathology is planned on two dogs, and one dog will be followed long-term.

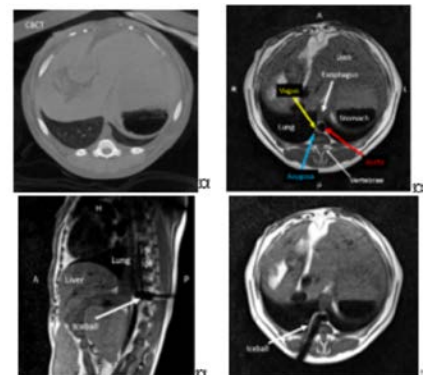
**Conclusions:** MR-guided cryovagotomy in obese dogs allows direct targeting of the vagus nerve with no adverse events and promise as a supplemental treatment for weight loss.

**Acknowledgments:** Siemens Medical Solutions, USA grant support

### References:

1. Trescot AM. *Pain Physician*. 2003;6:345-60
2. Lloyd JW, Barnard JDW and Glynn CJ. *The Lancet*. 1976;932-934
3. Joshi DH et al. *Skeletal Radiol*. 2017;46:983-987
4. Fritz J et al. *Skeletal Radiology*. 2013;42:579-86
5. Fritz J et al. *AJR*. 2009;192:W161-7
6. Kral JG et al. *World J Surg*. 1993;17:75-8.
7. Sarr MG et al. *Obes Surg*. 2012;22:1771-82.
8. Prologo JD et al. *Obesity (Silver Spring)*. 2019;27:1255-1265

Fig: Top: CBCT (left) demonstrating the poor soft tissue detail vs. axial PD MRI (right). Bottom: Intra-procedural images from an MR-guided percutaneous cryovagotomy in the same dog demonstrating the iceball as signal void (arrow).



## **MRI-guided prostate biopsies**

Alexander Schaudinn

Department of Diagnostic and Interventional Radiology, Leipzig University Hospital, Leipzig, Germany

### **Purpose**

The diagnostic workup of prostate cancer has evolved substantially over the last decade, with prebiopsy multiparametric MRI (mpMRI) now widely endorsed in international guidelines. The current recommendation in patients with a clinical suspicion for prostate cancer and positive mpMRI (PI-RADS  $\geq 3$ ) is to combine MRI-guided biopsy with systematic sampling. The objective of this talk is to provide a review and update on MRI-guided biopsies.

### **Methods and Discussion**

MRI targeting can be accomplished in three different ways: cognitive registration, MRI/ultrasound-fusion biopsy and in-bore biopsy. MRI/ultrasound fusion is the current standard approach for validating MRI-positive lesions. In-bore biopsy is the only method that allows for a proper documentation of the exact sampling location within the target lesion. The gland is typically accessed by a transperineal or transrectal (most common) route, a transgluteal approach is an option for patients without rectal access. These biopsies can be performed with navigational or robotic assistance but also manually.

Factors that favor an in-bore over an MRI/ultrasound-fusion approach include lesion size and location, size of the gland and cases with prior negative biopsy (after MRI/ultrasound fusion or cognitive biopsy) where the clinical suspicion for prostate cancer persists (backup option). Selected literature findings will be combined with our institutional experience (simple/assisted in-bore procedures) to discuss the advantages and disadvantages of different MRI biopsy methods with regard to cancer detection rates and procedure times. Procedural imaging and workflow aspects will also be included.

### **Conclusion**

Prebiopsy MRI has revolutionized the diagnostic pathway for prostate cancer, establishing MRI-guided biopsy as a clinical tool. The selection of a particular MRI-guided biopsy option (method, access route, advanced assistance) often depends on factors like the availability of equipment, procedural experience, individual patient characteristics or institutional cost-benefit considerations.

## Comparison of Prostatic Lesion Conspicuity Using a Fast Balanced SSFP Sequence to Shorten in-Bore Robotic Transrectal MRI-Guided Biopsy: a Feasibility Study.

**Objectives:** To determine whether a fast balanced steady-state free precession (bSSFP) sequence is feasible to visualize prostatic lesions compared to T2WI and DWI within the protocol of in-bore robotic transrectal MRI-guided biopsy.

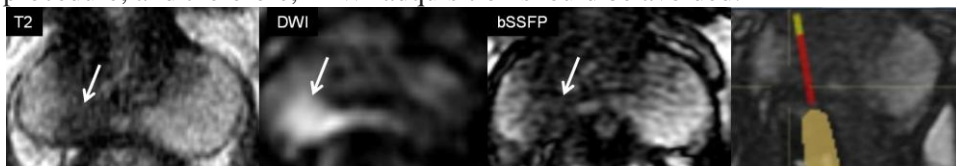
**Methods :** This retrospective study included 95 patients with a single cancer suspicious lesion interpreted on MRI using PI-RADS 2.1 category  $\geq 3$ , who underwent in-bore robotic transrectal MRI-guided biopsy without anesthesia. Two urologists independently rated lesion conspicuity on a 3-point scale (1 non-visible, 2 slightly visible, 3 clearly visible) for each sequence, such as axial FSE T2 (acquisition time, 4:30 min), axial DWI (b:1400 s/mm<sup>2</sup>; 4 min), axial bSSFP (20 s). Lesion conspicuity from the 3 sequences and for inter-reader reliability were evaluated.

### Results:

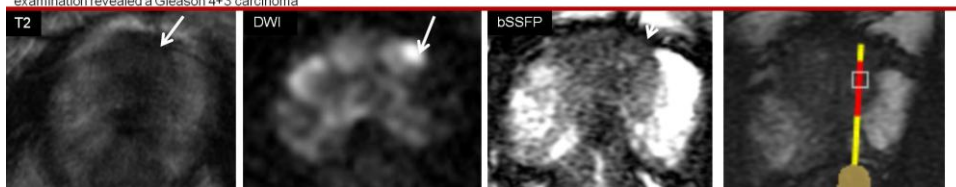
Prostate cancer was detected in 73% of the lesions. Overall; on T2WI, lesions were non-visible in 18% of cases, slightly visible in 54%, and clearly visible in 28%. On DWI, lesions were clearly visible in 86% of cases. For bSSFP, lesions were non-visible in 8%, slightly visible in 41% and clearly visible in 51%. Prostate cancer was slightly-clearly visible in 86% of cases on T2WI, 100% on DWI and 94% on bSSFP. Lesion was visible on PI-RADS 3 in 62% on T2WI, 83% on DWI, 83% on bSSFP; and for PI-RADS  $\geq 4$ , in 85% on T2WI, 100% on DWI and 93% on bSSFP. Lesion  $\leq 10$ mm was visible in 70% on T2WI, 96% on DWI and 87% on bSSFP. Lesion in the peripheral zone was visible in 86% on T2, 97% on DWI, 94% on bSSFP and; for transition zone, 67% on T2, 95% on DWI and 84% on bSSFP. Gleason 3+3 lesions were visible in 80% on T2WI, 100% on DWI, 78% on bSSFP; and Gleason  $\geq 3+4$  lesion was visible in 86% on T2, 100% on DWI and 97% in bSSFP. Inter-reader agreement correlation coefficient was excellent for T2WI (0.97) and bSSFP (0.94), and good for DWI (0.75).

### Conclusion

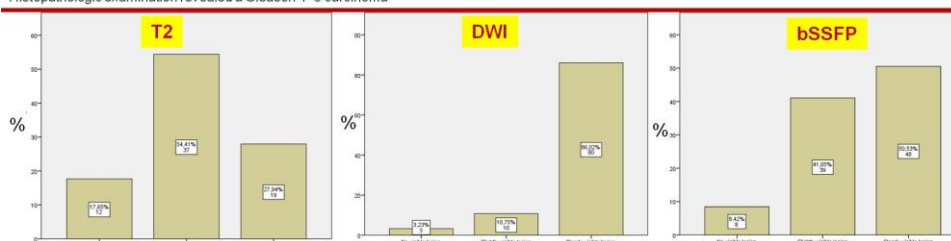
Fast bSSFP acquisition may be optimal to visualize prostatic lesions and to significantly reduce time of in-bore robotic transrectal MRI-guided biopsy. Fast bSSFP in combination with DWI acquisition provides clear visualization of prostatic lesions to target accurately during the procedure, and therefore, T2WI acquisition should be avoided.



51 yo, PSA 13 ng/ml, mpMRI category was PI-RADS 4. The focal lesion in right side of the PZ is clearly visible on the 3 sequences: T2, DWI and bSSFP. Target biopsy shows the needle track overlay with the optimal path and represented the sample core (red line) on the bSSFP image. Histopathologic examination revealed a Gleason 4+3 carcinoma



63 yo, PSA 12.4 ng/ml, mpMRI category was PI-RADS 3. The focal 7 mm lesion in left side of the anterior TZ is clearly visible on DWI, slightly visible on bSSFP and non visible on T2. Target biopsy shows the needle track overlay with the optimal path and represented the sample core (red line) on the bSSFP image. Histopathologic examination revealed a Gleason 4+3 carcinoma



Bar graph shows lesion visualization for the three sequences T2WI, DWI and bSSFP respectively

## MR-guided prostate interventions - update on focal therapy with MRgFUS

Clare M.C. Tempany-Afdhal MB BAO BCh Ferenc A. Jolesz MD Professor of Radiology, Harvard Medical School, Director of the Ferenc Jolesz National Center for Image-Guided Therapy  
Vice-Chair Research Department of Radiology Brigham & Women's Hospital 75 Francis St, L1 room 050  
Boston MA 02115

[ctempany@bwh.harvard.edu](mailto:ctempany@bwh.harvard.edu)

<http://www.ncigt.org>

This talk will focus the status of MRI guided prostate interventions and an update on focal therapy using MRI guided focused ultrasound. In the mid 2000s diffusion weighted MRI was introduced as a significant MR Pulse sequence for the detection and characterization prostate lesions. This sequence, along with T2W and Dynamic IV contrast enhance MR are the standard acquisitions in all prostate MR examinations. The American College of radiology and others established PI-RADS version 2 in 2016 and updated this in 2019 to PI-RADS version 2.1 which is in current use today. Multiple studies have demonstrated with level 1 evidence, the role of MRI for detection of clinically significant prostate cancer prior to prostate biopsy. Several of these studies will be reviewed during this talk including the *PRECISION* trial (NEJM 2018). For localized prostate cancer clinically significant cold gland therapies such as radical prostatectomy and radiation therapy are considered the standards of care but both treatment modalities are associated with considerable morbidity urinary incontinence erectile dysfunction and bowel dysfunction contributing to decreased quality of life as prostate cancer rarely causes a cancer specific mortality many men are now seeking less morbid therapies. Focal therapy is one such approach to a less morbid cancer treatment. Focal therapy is the localized ablation of an index lesion reduction of therapy to the critical normal structures such as the neurovascular bundles and external urethral sphincter. Along with the establishment of mpMRI examinations in the detection and characterization of prostate cancer, there has been a significant uptick in interest in the delivery of focal therapy to the MR defined target. There are multiple ablative methods in trials and some in clinical practice. These include MRgFUS, HiFU, Laser, Cryotherapy, and others. Most of these ablative techniques can be used either with or without MR with Ultrasound guidance being the alternative. There are several commercial MR guided FUS systems available- Profound and InSightec being two which will be introduced, and clinical trial data presented during this talk. One important study was the first multi-center clinical trial of focal therapy in the US- now published in *Lancet Oncology* is entitled *MRI guided focused ultrasound focal therapy for intermediate risk prostate cancer a phase 2B multicenter study* will be reviewed during this talk. This study (Ehdaie et al 2022 see footnote)) reports the results of treatment of 101 men using the InSightec device with a transrectal approach for mr guided focused ultrasound the 24 month biopsy outcomes in this study demonstrated that MRI guided focused ultrasound is safe and effective for treating GG 2 or 3 prostate cancer these results support focal therapy for select patients and its use in comparative trials if a tissue preserving approach is effective in delaying or eliminating the need for radical whole gland treatment in the long term.

*Ehdaie B, Tempany CM, Holland F, Sjoberg DD, Kibel AS, Trinh QD, Durack JC, Akin O, Vickers AJ, Scardino PT, Sperling D, Wong JYC, Yuh B, Woodrum DA, Mynderse LA, Raman SS, Pantuck AJ, Schiffman MH, McClure TD, Sonn GA, Ghanouni P. MRI-guided focused ultrasound focal therapy for patients with intermediate-risk prostate cancer: a phase 2b, multicentre study. Lancet Oncol. 2022 Jul;23(7):910-918. doi: 10.1016/S1470-2045(22)00251-0. Epub 2022 Jun 14. PMID: 35714666.*

## Abstract

Purpose: To explore oncologic and functional outcomes at 2 years following targeted focal therapy performed under MRI guided focused ultrasound (MRgFUS) for intermediate-risk csPCa.

Material and Methods: In this prospective phase II trial, between February 2016 and July 2019, men with MRI visible unifocal csPCa were treated by transrectal MRgFUS. Real time ablation monitoring was performed by MR thermography. Non-perfused volume was measured at treatment completion. Periprocedural complications were recorded. Follow-up included International Prostate Symptom Score (IPSS) and International Index of Erectile Function (IIEF-15) at 24 months, and mpMRI and biopsy at 6 and 24 months. LQMM models were used to model median change from baseline.

Results: Treatment was successfully completed in all 44 men, 36 with Grade Group (GG) 2 and 8 with GG3 disease (median age [IQR]: 67 years [62-70]). Median (IQR) prostate volume and tumor length 40cc (31.5-50.8) and 9mm (7-12.5) respectively. 17 PCa sites were in peripheral zone and 6 in transition zone. Median (IQR) non perfused volumes were 6.1cc (3.5-8.0). No major treatment-related adverse events occurred. 40 of 44 (91%) sites of PCa ( $\geq 6$ mm GG1 disease or any volume  $\geq$ GG2 disease) were free of disease at treatment site at study conclusion (24 months). Additional 3 of 44 participants (7%) had out of field new site of csPCa at 2 years. 37 men (84%) remained free of disease ( $\geq 6$ mm GG1 or any volume GG2) at 2 years. Median (IQR) IPSS and IIEF-15 were similar at baseline and 24 months (3.5 [IQR: 2.0-7.0] vs. 4.5 [IQR: 1.0-8.0],  $p=0.84$ ; 59.5 [25.2-65.0] vs. 31.5 [IQR: 16.2-61.0],  $p=0.34$ , respectively). 3 of 7 men with recurrent disease underwent salvage treatment (2 underwent salvage focal treatment by MRI laser



therapy and 1 participant underwent radical prostatectomy with negative margins). The remaining 41 of 44 (93%) men including 4 with small volume MR invisible csPCa remain on active surveillance.

Conclusions: Targeted focal therapy of intermediate-risk prostate cancer performed under MRgFUS is safe with very encouraging 2 year oncological and functional outcomes.

**Clinical Relevance:**

MRI guided targeted focal therapy is a feasible treatment option in men with localized clinically significant prostate cancer (csPCa).

**TITLE:** MR-guided prostate interventions - the Mayo experience

**AUTHORS:** <sup>1</sup>David A. Woodrum M.D., Ph.D., <sup>1</sup> Scott M. Thompson M.D, Ph.D., <sup>1</sup> Daniel A. Adamo M.D., <sup>2</sup> Derek Lomas M.D., <sup>1</sup> Christopher P. Favazza Ph.D., <sup>1</sup> Aiming Lu Ph.D., Ph.D., <sup>2</sup> Lance A. Mynderse M.D., <sup>2</sup>Eugene Kwon, M.D.

**AFFILIATIONS:**

1 Department of Radiology, Mayo Clinic, Rochester, MN, USA

2 Department of Urology, Mayo Clinic, Rochester, MN, USA

**PURPOSE:** To demonstrate the depth of prostate interventions for primary prostate cancer and recurrent prostate cancer at Mayo Clinic.

**MATERIALS AND METHODS:** Discuss the evolution of MR guided ablation for primary and recurrent prostate cancer since the first case performed in 2009. Will briefly discuss current criteria for primary prostate cancer ablation for us. Will provide an overview of the technologies which can be utilized. Will demonstrate the capability on monitoring precision provided by MRI. Will review what can be offered for recurrent MRI ablation treatments.

**RESULTS:** Since starting the MR guided ablation practice in 2009, we have done over 1500 procedures (ie ablations and biopsies) and have done over 750 prostate ablations. We will demonstrate the types of prostate ablations being performed and types of patients being treated. We will discuss the recurrent prostate ablation patients and how MR guided ablation can provide a new treatment option where the options are becoming severely limited.

**CONCLUSION:** MR guided ablation for prostate cancer can provide a very good alternative to standard treatment options for primary prostate patients and provide a new treatment option for recurrent prostate cancer patients when standard therapies have failed.

Interventional MRI in prostate cancer  
Jürgen Futterer  
Department of Medical Imaging  
Radboud University Nijmegen Medical Center  
The Netherlands

Minimal invasive Image-guided Interventions (MII) is emerging as a discipline in medicine. These interventions are medical procedures which can be combined with integrated sophisticated robotic and imaging technologies, primarily to perform minimally invasive surgery. This integrated technology approach offers distinct advantages for both patients and physicians. In image-guided procedures, the interventionalist is guided by images from various techniques, including X-ray, computed tomography (CT), MR and ultrasound. MII exploits recent advances in mpMRI that is able to both detect and locate prostate cancer and verify its nature without necessary recourse to biopsy. Having located and characterised the disease process this information can be used to inform the selective treatment of the diseased tissue with associated preservation of surrounding healthy tissue. MII can therefore be characterised by the following key steps: target generation, target verification, target destruction and treatment verification. As an emerging discipline, no single specialist area has the necessary competencies/expertise to deliver MII.

Most interventional procedures require medical imaging to guide the instrument to the target organ in the human body, to assess the outcome of the intervention, and to provide additional information about the functional improvement achieved with the intervention. At present, X-ray and ultrasound imaging are the most commonly used modalities in interventional procedures, but these current imaging modalities have major disadvantages: the ionizing X-rays are potentially dangerous for both patient and physician, and their contrast is limited to bone or iodine-containing contrast agents. Ultrasound on the other hand hardly penetrates bone, is reflected at tissue-air interfaces and is operator dependent. Due to these limitations, MR imaging has been proposed for image guidance in those interventional procedures that could be performed and preferably should be performed in the MR scanner. MR imaging provides an excellent soft tissue contrast, it can acquire images in arbitrary directions and with variable contrasts, and it offers a plethora of functional imaging technologies ranging from perfusion and flow measurements to the assessment of temperature changes or the quantification of a local drug release in molecular imaging. Numerous minimal invasive technologies such as cryosurgery, high intensity focused ultrasound, irreversible electroporation, photodynamic therapy and laser ablation have been used to perform focal therapy. For example MR image-guided laser ablation (MRgLA), in contrast to other ablative techniques, is fast and creates a sharply defined ablation zone and can be performed under local anesthesia in an outpatient setting. Therefore, the anticipated treatment related co-morbidities are expected to be considerably lower than those for the radical treatment options or other focal therapy strategies. MR guided ablation techniques will be discussed.

**TITLE:** MR guided cryoablation of oligo-metastatic prostate cancer to the obturator lymph nodes.

**AUTHORS:** <sup>1</sup>David A. Woodrum M.D., Ph.D., <sup>1</sup> Scott M. Thompson M.D, Ph.D., <sup>1</sup> Daniel A. Adamo M.D., <sup>2</sup> Derek Lomas M.D., <sup>1</sup> Christopher P. Favazza Ph.D., <sup>1</sup> Aiming Lu Ph.D., Ph.D., <sup>2</sup> Lance A. Mynderse M.D., <sup>2</sup>Eugene Kwon, M.D.

**AFFILIATIONS:**

1 Department of Radiology, Mayo Clinic, Rochester, MN, USA

2 Department of Urology, Mayo Clinic, Rochester, MN, USA

**PURPOSE:** To demonstrate feasibility and short-term followup of using MR guided cryoablation for treatment of oligo-metastatic prostate cancer to the obturator lymph nodes.

**MATERIALS AND METHODS:** Retrospective review from October 2020 to December 2021 for patient's treated with MR guided cryoablation for solitary prostate cancer metastasis to the obturator lymph node as identified by PET choline and/or PET PSMA imaging. Patient's underwent MR guided cryoablation using a transperineal needle placement under general anesthesia. Cryoablation was performed with continuous MR imaging monitoring so that the Iceball was grown to encompass the lesion with margins as permitted based on adjacent structures (ie ureter, obturator nerve. Sciatic nerve). Patients were discharged same day. PET imaging and PSA were performed every 3 months post-ablation with MRI of the pelvis as needed.

**RESULTS:** Review demonstrated 8 patients with 9 procedures during this time frame. All 9 procedures had negative 3 month post-ablation PET imaging based on local response to treatment. Figure 1 demonstrates an enlarged obturator lymph node of T2 weighted images corresponding to PET choline avid lesion. Figure 2 demonstrates intense post-Gadolinium enhancement. Figure 3 utilizes a proton density image to demonstrate the iceball with the ureter located medially and a cryoneedle between the ureter and iceball set to Thaw mode to limit the extent of the iceball medially. Figure 4 demonstrates a lack of enhancement after the procedure. PSA response was mixed depending on whether other metastases developed.

**CONCLUSION:** MR guided cryoablation can be utilized for treatment of oligo-metastatic prostate cancer to the obturator lymph nodes with good short-term results.

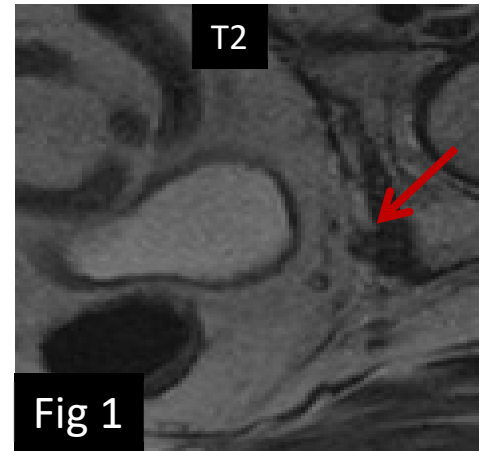


Fig 1

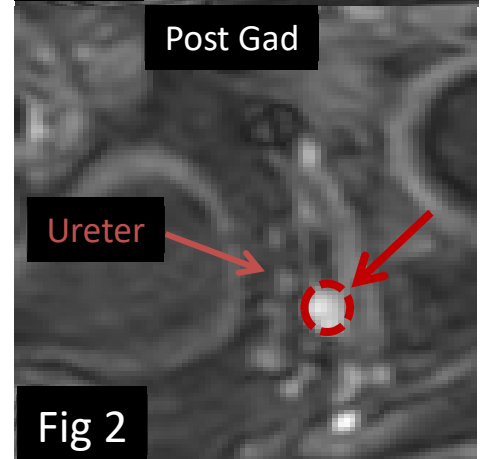


Fig 2

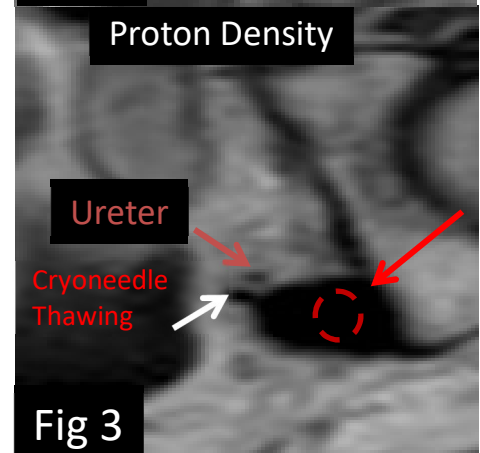


Fig 3

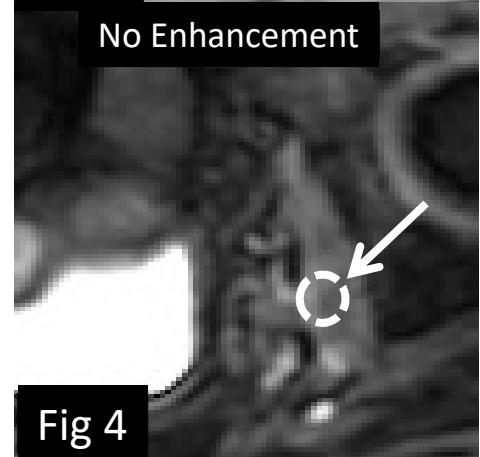


Fig 4

## AI-Based prediction of iceball boundaries in focal cryoablation of prostate cancer

Pedro Moreira, Kemal Tuncali, Clare Tempany, Junichi Tokuda  
Department of Radiology, Brigham and Women's Hospital, Boston, USA  
Harvard Medical School, Boston, USA

**Purpose.** Focal cryoablation (FC) has been investigated as a minimally invasive option for the management of low-risk organ-confined prostate cancer (PCa) and a salvage treatment option for post-radiation recurrence. Unlike radical treatments, FC aims to freeze and destroy only the lesion and the surrounding area using thin cryo-needles. Safe and effective cryoablation requires the deployment of the cryo-needles at optimal locations so that the ablation zone fully encompasses the tumor with a certain ablation margin while preserving surrounding healthy tissues. However, predicting the final shape of the iceball boundaries and monitoring the ablation margin in 3D are challenging tasks as it depends on patient-specific factors and proximity to heat sources. This study presents preliminary results using a deep learning approach to predict the final iceball boundaries in FC of PCa.

**Material and methods.** We trained a Convolutional Neural Network (CNN) based on the 3D U-Net using retrospective data of 40 FC procedures performed with an MRI-compatible cryoablation system (SeedNet MRI, Boston Scientific Natick, MA), and utilizing two to five 17-gauge cryoablation probes (Ice Seed, Boston Scientific Natick, MA) per patient. MR images of the needle placement were acquired before the freezing cycles to confirm the needle placement, and iceball images were performed at 12 to 15min of the first cycle ( $T_2$ -weighted TSE sequence, TR/TE = 2430/104ms, matrix = 192×134, slice thickness = 3mm, FOV = 180×157mm<sup>2</sup>). The needle placement was manually marked on each confirmation image by setting the pixel value to 1024 (Fig. 1). For training purposes, the ground truth is considered the manually segmented iceball. We trained our network using the negative Dice Similarity Coefficient (DSC) loss function, a batch size of 2, 200 epochs, and the Adam optimizer with a learning rate of 1e-03.

**Results.** We performed a Leave-One-Out Cross-Validation with the data split into 33 cases for training, 7 for validation and 1 for the cross-validation test. We repeated the cross-validation in 15 randomly selected cases and trained one network for each case. The average DSC between the predicted and segmented iceball was 0.71±0.10 (mean±SD). The average computational time to predict the iceball boundaries was 0.69±0.04 sec. An axial view of a representative case is presented in Fig. 1. Computational time is a crucial parameter to implement prediction models in a preoperative planning software. Previously published bioheat models takes several seconds to a few minutes to provide an accurate prediction or used pre-simulated iceballs [1][2].

**Conclusion.** We presented a deep learning model able to predict the iceball boundaries given a needle placement. Our model does not need any patient-specific biothermal parameters and it is able to predict the iceball in less than a second. We are currently working on including other features to the input image, such as varying the needle pixel value based on the distance to the tip and including the segmented urethral catheter. Nevertheless, these preliminary results suggest that using artificial intelligence techniques to predict isotherms in focal cryoablation is feasible.

**Acknowledgement.** The study was funded in part by the NIH (P41EB028741, 1R43EB032676)

### References

- [1] E. Golkar et al., "GPU-based 3D iceball modeling for fast cryoablation simulation and planning," *Int. J. Comput. Assist. Radiol. Surg.*, vol. 14, no. 9, pp. 1577–1588, 2019
- [2] F. E. Boas et al., "Development of a Searchable Database of Cryoablation Simulations for Use in Treatment Planning," *Cardiovasc. Intervent. Radiol.*, vol. 40, no. 5, pp. 761–768, 2017

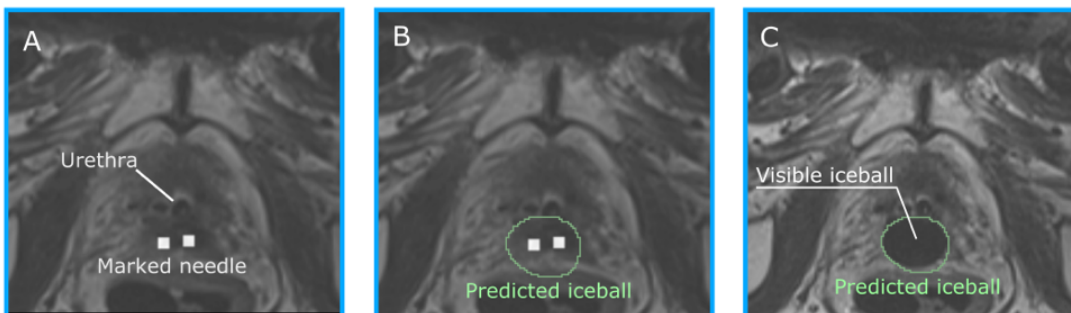


**Fig. 1** Predicted isotherm using deep learning approach. A) Axial view of the input image with the marked needle location, B) Iceball boundaries predicted by the trained model, and C) A comparison between the visible iceball achieved with the needle location and the predicted boundary.

**Title** MRI guided focal laser ablation (MRgFLA) for localized intermediate-risk prostate cancer – results of a phase II trial

## Abstract

**Purpose:** To explore oncologic and functional outcomes of targeted focal therapy performed under MRI guided focal laser ablation (MRgFLA) for low-intermediate risk clinically significant prostate cancer (csPCa).

**Material and Methods:** In this prospective phase II trial, between April 2018 and Jan 2020, men with MRI visible PCa were treated by transperineal MRgFLA. Real time ablation monitoring was performed by MR thermography. Non-perfused volume was measured at treatment completion. Periprocedural complications were recorded. Follow-up included International Prostate Symptom Score (IPSS) and International Index of Erectile Function (IIEF-15), at 6 weeks, and 6, 12, 18 and 24 months, and mpMRI and biopsy at 6 and 24 months. GEE model was used for statistical analysis and Holm method to adjust p-value.

**Results:** Treatment was successfully completed in all 25 men (26 sites of disease), 4 with Grade Group (GG) 1  $\geq 6$ mm, 15 with GG2 and 4 GG3 disease [median age(IQR): 64 years (61, 68)]. All sites were MRI visible. Median (IQR) prostate volume and tumor length 40cc (29.8, 51.9) and 9mm (7, 11.5) respectively. 19 PCa sites were in peripheral zone and 7 in transition zone. Median (IQR) non perfused volumes was 4.9cc (3.4, 7.4). No major treatment-related adverse events occurred. 23 of 26 (88%, 95%CI: 71%- 96%) sites of PCa were free of disease at treatment site ( $\geq 6$ mm GG1 disease or any volume  $\geq$ GG2 disease) on 6 month biopsy (median 6 cores) and 19 of 26 sites at 24 months (73%, 95%CI-54%- 86%) in the 25 participants. Additional 4 of 25 participants (16%) had new site of csPCa at 2 year biopsy. Median IIEF-15 and IPSS were similar at baseline and 24 months (baseline:63,IQR:44-65; 24 months:47,IQR:31-60; p=0.051 and baseline:6,IQR:3-12; 24 months:4,IQR:2-11; p=0.38 respectively). Six participants with recurrent or new disease underwent salvage treatment (external beam radiation in 4

and radical prostatectomy in 2). The remaining 19 of 25 (76%; 95%CI:57%-89%) men remained on active surveillance at 2 years.

Conclusions: Targeted focal therapy of intermediate-risk prostate cancer performed under MRgFLA is safe with encouraging 2 year oncological and functional outcomes.

**Clinical Relevance:**

MRI guided targeted focal laser therapy is a feasible treatment option in men with localized clinically significant prostate cancer (csPCa).



## Use of salvage MRI-guided focal or integrated boost high dose rate brachytherapy for recurrent prostate cancer

Inmaculada Navarro-Domenech<sup>1\*</sup>, Cynthia Ménard<sup>2\*</sup>, Zhihui (Amy) Liu<sup>1</sup>, Lisa Joseph<sup>1</sup>, Maroie Barkati<sup>2</sup>, Alejandro Berlin<sup>1</sup>, Guila Delouya<sup>2</sup>, Daniel Taussky<sup>2</sup>, Marie-Claude Beauchemin<sup>2</sup>, Benedicte Nicolas<sup>2</sup>, Samuel Kadoury<sup>3</sup>, Alexandra Rink<sup>1</sup>, Srinivas Raman<sup>1</sup>, Aravindhan Sundaramurthy<sup>1</sup>, Robert Weersink<sup>1</sup>, Dominic Beliveau-Nadeau<sup>2</sup>, Joelle Helou<sup>1</sup>, and Peter Chung<sup>1</sup>

<sup>1</sup>Princess Margaret Cancer Centre, University of Toronto, Toronto, Canada; <sup>2</sup>Centre Hospitaliser de l'Université de Montréal (CHUM), Montreal, Canada; <sup>3</sup>Polytechnique Montreal, Montreal, Canada. \*These authors have contributed equally to this work and share first authorship

**Keywords:** Prostate Cancer, Brachytherapy, Salvage, Radiotherapy, Magnetic Resonance Imaging.

### **Purpose:**

To report cancer control outcomes and toxicity in a combined cohort of patients with locally recurrent prostate cancer treated with salvage MRI-guided focal or integrated boost high dose rate (HDR) brachytherapy (BT).

### **Material and methods:**

A prospective cohort of 88 patients with visible local recurrence after prior radiotherapy (RT) treated across two institutions with MRI-guided salvage HDR-BT, delivered in 2 fractions over a median 7 days. Tumor target dose ranged from 22-26 Gy, using either an integrated boost (ibBT) or focal technique (fBT), delivered in two implants over a median of 7 days. Outcome metrics included cancer control and toxicity (CTCAE). Quality of life (QoL-EPIC) was analyzed in a one of the institutions.

### **Results:**

The median follow-up was 35 months (6 -134). The failure-free survival (FFS) at 3 and 5-year were 67% and 49%, respectively. Patients in the fBT cohort, had an earlier local recurrence. The cumulative incidence of local failure (LF) at 3-year in this group was 21%, however, at 5-year there was not a difference between fBT and ibBT cohorts (30% vs. 23% respectively,  $p=0.16$ ). LC outside the GTV was 17% in fBT vs. 7.8% ibBT ( $p=0.14$ ), while LF within the GTV occurred in 13% vs. 16%, respectively ( $p=0.81$ ). Predictors of LF outside fBT volumes included pre-salvage PSA $>7$  ng/mL ( $p=0.03$ ) and an interval time between prior RT and the diagnosis of local recurrence less than 5 years ( $p=0.039$ ). There was no grade 3 toxicity reported, and ibBT was associated with a higher rate of grade 2 toxicity ( $p<0.001$ ). ibBT cohort was associated with poorer QoL in the sexual domain score ( $p=0.069$ ), compared to fBT.

### **Conclusion:**

MRI-guided HDR-BT salvage approach achieved favorable cancer control outcomes. While an fBT was associated with less toxicity and better outcomes in QoL, earlier local failure rate was reported in this group. Better selection of patients and tumor targeted dose escalation may be warranted.

## How accurate and reliable is MR thermometry?

Kagayaki Kuroda  
Department of Human and Information Science,  
School of Information Science and Technology, Tokai University

MR thermometry using a proton resonance frequency (PRF) shift of water that is measured with phase mapping (1) is widely accepted in the monitoring of thermal therapies (2). The PRF technique gives a relative change of temperature with the gradient echo-based sequences that are commonly equipped on clinical scanners. Various factors affect the quantitative features of this technique, and thus, the inaccuracies in the temperature readings may cause excessive damage to the tissues. As warned by FDA (3), attention should be paid to accuracy and reliability issues of MR thermometry when used for MR-guided thermal therapies.

When the PRF technique is used, the fat signal must be suppressed or separated by using appropriate means, such as CHESS, Dixon, or IDEAL techniques. If the intensity of the incompletely suppressed fat signal is 10% of that of water, then approximately 1°C of the temperature error may be induced (4). Field drift should be compensated for because the induced phase shift can reach as large as 25 °C in 30 minutes (5). Tissue motion and deformation induced by respiration, cardiac pulsation, peristalsis, and patient body movement are some of the most significant sources of error. Tissue motion and deformation during a scan (intrascan motion) and between scans (interscan motion) should be treated differently. For intrascan motion, rapid imaging is the best approach. Such rapid imaging is also effective to reduce the error stemmed from the temperature change during scanning. The strategies for interscan motion depend on its application. For periodic motion induced by respiration, for instance, multiple baseline image libraries used in conjunction with navigated scans are acceptable. If the target region is relatively smaller compared with the entire organ, referenceless techniques may work (6-7).

Although the effect of thermally induced bulk susceptibility change in aqueous tissues is generally small, that in adipose tissues is in the range of 0.0039–0.0094 ppm/°C. MRS techniques (6) may be useful in reducing the error caused by the susceptibility effect, as well as tissue swelling and patient bulk motion, if an appropriate internal reference signal is found and a sufficient acquisition time is afforded. The susceptibility effect from the treatment devices will hide the temperature information and, thus, is problematic. Moreover, temperature coefficient variations because of electrolytes, pH, and macromolecules are also some of the sources of errors. Thermometry for adipose tissue needs a different approach than PRF. Previous studies have shown that T1 or T2 may be a good indicator (7).

The above-mentioned factors may not be completely avoided, and thus accuracy and reliability of MR thermometry strongly depend on the situations, but there should be practical criteria for maintaining accuracy and reliability. For example, when a temperature coefficient differs from -0.01 ppm/°C to -0.009 ppm/°C, the apparent peak temperature will increase by 11%, while the diameter of the heated area will increase by 5%, here assuming that the temperature elevation profile is a Gaussian function, as in the case of focused ultrasound or laser treatment of neuro diseases.

### References

1. Ishihara Y et al. *Magn Reson Med* 1995;34:814-23.
2. Odeen H et al. *Prog Nucl Magn Reson Spectrosc* 2019;110:34-61.
3. FDA. Letter to Health Care Providers. April 24, 2018.
4. Kuroda K et al. *Magn Reson Med* 1997;38:845 - 51.
5. Ferrer CJ et al. *Magn Reson Med* 2020;83(3):962-73.
6. Hofstetter LW et al. *J Magn Reson Imag* 2012;36(3):722-32.
7. Kuroda et al. *J Magn Reson Imag* 2018; 47:316-331.

## Prospective Phase Correction – A Novel Approach to Phase Drift Correction in Proton Resonance Frequency Shift Thermometry with Non-Cartesian Sequences

Belker, O.<sup>1,2</sup>, Meyer zu Hartlage, K.<sup>1,2</sup>, Gutberlet, M.<sup>1,2</sup>, Löning C., J.J.,<sup>1,2</sup>, Reimert, D.,<sup>1,2</sup>, Wacker, F.<sup>1,2</sup>, Hensen, B.<sup>1,2</sup>

<sup>1</sup>Hannover Medical School (MHH) <sup>2</sup>STIMULATE-Solution Centre for Image Guided Local Therapies

**Purpose:** Proton Resonance Frequency Shift (PRFS) - Thermometry is performed by calculating the difference in phase of hydrogen nuclei at a given time point to a reference phase, either baseline data acquired before a temperature change or a mathematical approximation, e.g., a polynomial suggested by [1]. A static main magnetic field ( $B_0$ ) is essential as slight distortions yield erroneous temperature calculations by altering the resonance frequency. Non-cartesian acquisition sequences are adopted in PRFS Thermometry to reduce scan time and improve motion robustness [2]. A drift of  $B_0$ , e.g., due to intense gradient utilization, leads to a systematically incorrect presumed temperature change. Further, clinical use demands real-time temperature data with high-temperature accuracy. Therefore, we have adopted a novel approach: Prospective Phase Correction (PPC). PPC assumes the k-Space center's phase change to be linear in time [3,4] and to characterize the global phase change, exploiting the ceaseless acquisition of the k-Space center in most non-cartesian sampling schemes. The suitability for a potential clinical implementation is evaluated based on a microwave ablation of a bioprotein phantom [5].

**Materials&Methods:** PPC assumes the phase drift to be homogeneous, linear in time, and TE. Therefore, the phase drift can be determined from baseline data and then extrapolated to all subsequent acquisitions. The phase drift was estimated for each coil individually (to account for potential minor spatial variations of  $B_0$ ) by solving a least-squares problem. The data was sampled on a 1.5T MR Scanner (MAGNETOM Avanto, Siemens Healthineers, Erlangen, Germany) with a multi gradient-echo 3D Stack of Stars sequence with eight echoes during a 3-minute baseline acquisition followed by a 10-minute microwave ablation of a bioprotein phantom with a modified ECO-100E (Eco Microwave System Co., Ltd., Nanjing, China), and two optical thermometers (FOTEMPtrafo, Weidmann Technologies Deutschland GmbH, Dresden, Deutschland) with a distance of approximately 1 cm (S1) and 2 cm (S2) from the applicator as a temperature reference. The 3-minute baseline was deliberately chosen after some pre-testing without ablation to ensure a sufficient sample size to estimate the phase drift. Noise-, gradient delay [6], and phase error correction [7] was applied prior to evaluating PPC and uncorrected data with TE-weighted thermometry [8]. The necrosis zones were calculated by the CEM43 model [9] and compared to the manually segmented ablation zone in a post-ablative T2-weighted Turbo-Spin-Echo sequence) via the DICE coefficient. The standard deviation of the temperature was calculated in a manually selected non-heated area for each voxel over a range of ten images.

**Results:** With a DICE coefficient of 0.832, a sensitivity of 0.743, and a false positive rate of 0.042, the PPC corrected CEM43 estimation of the ablation zone shows greater accordance to the manually segmented ablation zone than the uncorrected CEM43 estimation with a DICE coefficient of 0.779, a sensitivity of 0.646 and a false positive rate of 0.03. Concerning temperature accuracy, the PPC-corrected thermometry data shows an error of  $(2.973 \pm 2.390)$  °C at S1 and an error of  $(0.799 \pm 0.547)$  °C at S2. In contrast, uncorrected Thermometry shows an error of  $(6.198 \pm 4.169)$  °C at S1 and an error of  $(5.386 \pm 3.233)$  °C at S2. Furthermore, in the unheated area, the PPC shows a mean standard deviation of 0.584 °C, while the uncorrected data yields a mean standard deviation of 3.122 °C.

**Conclusion:** Even though the ablation of a stationary phantom does not reflect an ordinary clinical situation, especially as the respiratory and bulk movement can be neglected, PPC appears to be a promising approach to phase drift correction. Temperature accuracy and DICE score both improved compared to the non-corrected thermometry. The implementation is straightforward as no mask is required, and computational effort is negligible as no intricate calculations are necessary after calibration. Future assessments should include the comparison of the DICE coefficients and temperature accuracy to other methods of  $B_0$ -correction. Additionally, the assumption of the phase drift's linearity in time should be evaluated for acquisitions longer than ten minutes. Instead of using the k-space center, FIDs could be implemented as navigator echoes for repeated phase measurement to extrapolate the phase drift [3,4].

**References:** [1]: RIEKE V. et al., Magn Reson Med 2004;51:1223–1231. ; [2]: SVEDIN, BT et al; Magn Reson Med 2018;79(3) 1407–1419; [3] FERRER, CJ et al., Magn Reson Med. 2020; 83(3): 962– 973.; [4] SVEDIN, BT. et al., Magn Reson Med 2016;76:206–213; [5]: BU-LIN, Z et al; International Journal of Hyperthermia 2008 24(7) 568–576; [6]: BLOCK, KT et al; In: Proceedings of the 19th Annual Meeting of ISMRM, Montreal, Canada (2011), S. 2816; [7]: MOUSSAVI, A et al., Magn Reson Med 2014;71:308–312; [8]: MADORE, B et al; Magn Reson Med 2011;66(3) 658–668; [9]: PEARCE, JA et al; International Journal of Hyperthermia 29 ,2013, Nr. 4, S. 262–280

# Accuracy of MRI real-time 3D temperature mapping during microwave heating – in-vitro results in gel phantoms

Olaf Dietrich<sup>1</sup>, Sergio Lentini<sup>1</sup>, Osman Öcal<sup>1</sup>, Pierre Bour<sup>2</sup>, Thibaut Faller<sup>2</sup>, Jens Ricke<sup>1</sup>, Max Seidensticker<sup>1</sup>

1 Department of Radiology, University Hospital, LMU Munich, Munich, Germany

2 Certis Therapeutics, Pessac, France

**Introduction:** In the context of microwave ablation of liver tumors, MRI has the ability to quantitatively monitor the energy delivery using temperature mapping [1,2], whose accuracy is relevant with regard to efficacy and safety of the procedure. The purpose of this study was to quantify the accuracy of MRI real-time 3D temperature mapping during microwave heating in vitro.

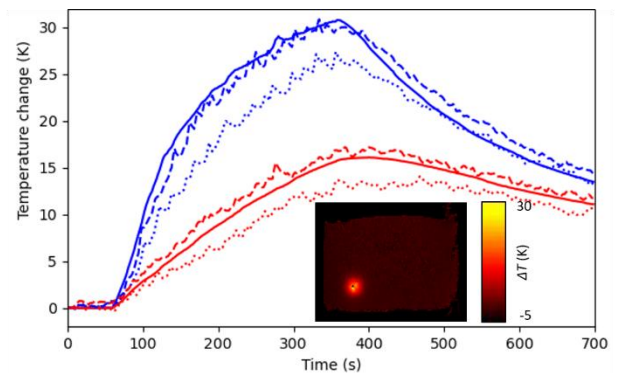
**Methods:** Agar-based gel phantoms were heated with an MR conditional microwave system (AveCure, MedWaves, San Diego, CA, USA) for 5 minutes. The temperature was monitored with two fiber-optical temperature sensors positioned approximately 5 and 10 mm distant from the probe. Proton-resonance-frequency-based MR thermometry was performed with a gradient-echo single-shot EPI sequence acquiring 25 slices (3 mm slice thickness) with in-plane resolution of 2.2×2.2 mm<sup>2</sup>. The temporal resolution was 2 s. The MRI measurement was performed for 700 s (60 s pre-heating, 300..450 s heating, 190..340 s post-heating) resulting in 350 individual 3D temperature measurements over time. In total, 10 phantom experiments were performed resulting in 7000 (temporally down-sampled) reference temperature-sensor values.

Single-pixel regions of interest (ROI) at the position corresponding to the tip of the fiber-optical temperature sensors were independently defined by two experienced radiologists based on the EPI magnitude images. The temperature curves of the two sensors were then compared to the MRI temperature data at the ROIs by calculating the root-mean-squared error (RMSE) over the complete 700-second time course. To account for the remaining uncertainty about the exact sensor tip location (and the volume over which the sensor integrates the gel temperature), 18 neighboring voxels around the original ROI (3×3×3 cube without the 8 corner voxels) were also evaluated and the voxel with the smallest RMSE value was additionally selected for further evaluation.

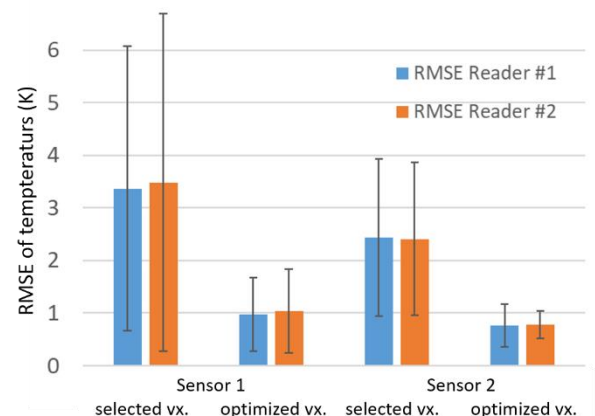
**Results:** Typical temperature-over-time curves are shown in the first figure (only reader #1); the data corresponding to the 2 sensors are shown in blue and red. The reference temperature measured by the sensors is displayed as solid line, the MRI temperatures are shown as dotted line (original voxels) and dashed line (neighboring voxels with smallest RMSE).

The maximum temperature changes measured by the fiber-optical sensors were between 8.0 K and 50.7 K (median: 20.6 K). The RMSE values (from both readers and 9 of 10 measurements) are summarized in the second figure; the mean RMSE values of the originally selected voxels were between 2.4 and 3.5 K. When evaluating the optimal voxels from the neighborhood, the RMSE values were between 0.8 and 1.0 K. In one excluded measurement, the reached temperature was too high and the gel was partly vaporized.

**Conclusion:** Accurate real-time MRI temperature mapping with typical averaged errors (RMSE) of about 1 K is feasible in gel phantoms during microwave heating. Further evaluation in in vivo environments is needed.



Temperature time curves of sensors (solid) and MRI (dotted, dashed); temperature map at time point 250 s.



RMSE temperature differences of both readers (blue, orange) and both sensors at selected voxels (vx.) and optimized neighbor voxels.

## Susceptibility-corrected Proton Resonance Frequency Shift (PRFS)-based Magnetic Resonance (MR) thermometry for monitoring microwave ablation (MWA) in the porcine liver

Bennet Hensen<sup>1</sup>, Susanne Hellms<sup>1</sup>, Christopher Werlein<sup>1</sup>, Danny Jonigk<sup>1</sup>, Phillip Alexander Gronski<sup>1</sup>, Inga Bruesch<sup>1</sup>, Regina Rumpel<sup>1</sup>, Eva-Maria Wittauer<sup>1</sup>, Florian W. R. Vondran<sup>1</sup>, Dennis L. Parker<sup>2</sup>, Frank Wacker<sup>1</sup>, Marcel Gutberlet;

<sup>1</sup>Hannover Medical School, Germany, <sup>2</sup>University of Utah, USA

**Purpose:** Due to low rates of complications and shortened hospitalization, MWA of hepatic tumors is of growing clinical importance<sup>1</sup>. MR guided thermal ablation allows intraprocedural treatment monitoring by MR thermometry<sup>2</sup>. Therefore, a better control of the ablation zone especially near heat sensitive tissue (e.g. bowel) and improved decision making during the procedure is given. PRFS allows accurate temperature mapping of thermal ablation because of its linear temperature dependency in the relevant range. However, increased heat transfer near the microwave applicator may lead to vaporization of tissue water, tissue carbonization and gas release and therefore may change magnetic susceptibility which impairs PRFS-based thermometry<sup>3</sup>. Aim of this study was to correct PRFS-based thermometry for changes of magnetic susceptibility to improve the prediction of ablation zones in hepatic MWA.

**Methods:** In a study of microwave ablation of the porcine liver (5 animals/12 procedures), PRFS based thermometry was performed using a respiratory-triggered 2D spoiled gradient echo sequence (TE: 9.6 ms, TR: 20 ms, flip angle: 12°, bandwidth: 260 Hz/pixel, matrix size: 256x256, spatial resolution: 2x2 mm<sup>2</sup>, slice thickness: 3 mm). At the tip of the microwave applicator, two slices perpendicular to the applicator were assessed with a distance of 10 mm. Heat induced susceptibility changes along the microwave applicator were modeled to correct thermometry. Ablation zones of uncorrected (raw) and susceptibility corrected (corr) thermometry were compared to histology and to post-ablative T1 weighted (T1w) contrast enhanced (CE) MR imaging (one minute after bolus of 0.025 mmol/kg Gd-EOB-DTPA).

**Results:** In Figure 1, exemplary ablation zones with the corresponding individual dice coefficient (Dice), sensitivity (Sen) and false positive rate (FPR) of T1w CE and uncorrected and susceptibility correct thermometry are provided with histology (first row) and T1w CE (second row) as reference. For all procedures, in comparison to histology, dice coefficient (76% vs. 79%, P<0.01) and sensitivity (72% vs. 74%, P<0.01) were significantly increased and FPR (12% vs. 5%) significantly decreased in susceptibility corrected compared to uncorrected thermometry using histology as reference. Correspondingly, dice coefficient (72% vs. 83%, P<0.001) and sensitivity (72% vs. 82%, P<0.001) were also significantly increased but FPR was not significantly lower (18% vs. 13%) after correction using T1w CE as ground truth.

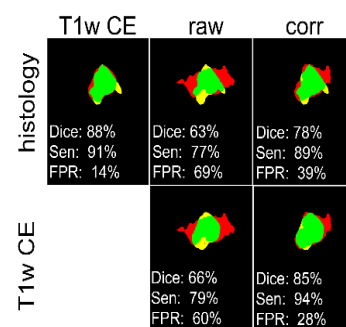


Figure 1: Ablation zones of T1w CE, uncorrected (raw) and susceptibility corrected (corr) PRFS-based thermometry in comparison to histology and T1w CE. Intersection, false negative and false positive area are shown as green, yellow and red area.

**Conclusion:** Susceptibility corrected thermometry significantly improved prediction of ablation zones in hepatic MWA. Further improvement will include 3D thermometry and more sophisticated methods to model susceptibility changes more accurately.

**References:** <sup>1</sup>Barkhausen J, et al. Rofo 2017;189(7):611-623. <sup>2</sup>Rieke V, et al. J Magn Reson Imaging 2008;27(2):376-390. <sup>3</sup>Malone DE, et al. Radiology 1994;193(1):233-237.

# Using Magnetic Resonance Fingerprinting for Proton Resonance Frequency Shift based Temperature Monitoring of Microwave Ablation

Moritz Gutt<sup>1</sup>, Josef Joaquin Löning Caballero<sup>2</sup>, Dominik Horstmann<sup>2</sup>, Prof. Dr. Frank Wacker<sup>2</sup>, Dr. Bennet Hensen<sup>2</sup>, Dr. Marcel Gutberlet<sup>2</sup>  
<sup>1</sup>Leibniz University Hannover (LUH) <sup>2</sup>Hannover Medical School (MHH)

**Introduction:** Magnetic Resonance Fingerprinting (MRF) is a framework which can be utilized to acquire multiple quantitative parameter maps at once whilst being relatively fast compared to other quantitative methods<sup>1</sup>. MRF assumes that, given the right pulse sequence, tissue generates a unique signal evolution based on its underlying parameters. The measured signal can therefore be matched with a pregenerated dictionary in order to acquire the quantitative parameter maps.

In clinical practice, MR guided temperature monitoring during minimally invasive tumor ablation is an important topic. However, a high accuracy in estimating the temperature as well as the resulting necrosis zone is needed to provide a real impact on the clinical routine. Due to the high error tolerance<sup>1</sup> of the matching process and the ability to quantize multiple parameters at once, MRF might be a promising framework to use here. In this proof-of-concept approach, the applicability of MRF in proton resonance frequency shift (PRFS) based temperature monitoring of microwave ablation (MWA) is shown by measuring the B0 off-resonance.

**Methods:** For data acquisition a 2D multi-echo radial FLASH sequence was used. In order to achieve additional sensitivity to the B0 off-resonance, the echo times were varied with every TR. Thus, the total range of TEs was between 2.57 ms and 29.114 ms with a step size of 0.336 ms, leading to 80 different echo times. The field of view was 320 x 320 mm<sup>2</sup> with a resolution of 256 x 256 and a slice thickness of 5 mm. The dictionary consisted of off resonance values between -200 Hz and 200 Hz with a step size of 0.1 Hz. For every echo time, 10 spokes were acquired such that the k-space was undersampled by a factor of 40. The temporal resolution was 2.9 s.

The toolbox BART<sup>2</sup> was used for reconstructing the data from each TE with parallel imaging and compressed sensing (PICS). After reconstruction, the dictionary matching process was performed by taking the highest inner product between the reconstructed signals and the dictionary entries. The temperature change was calculated afterwards by utilizing the linear dependency of the temperature and the proton resonance frequency of water between temperatures of -15 °C and 100 °C<sup>3</sup>. Additionally, a necrosis map was calculated by the CEM43<sup>4</sup> model. In order to verify this proof-of-concept, a microwave ablation (modified ECO-100E, Eco Microwave System Co., Ltd., Nanjing, China, 2.45 GHz, 150 W) on a static bioprotein phantom<sup>5</sup> was performed on a 1.5 T scanner and monitored by the fingerprinting sequence. A fiber optical temperature sensor was used for gaining reference temperatures. After the ablation, manual segmentation of the ablation zone in a post-ablative T2-weighted Turbo-Spin-Echo sequence (TE=156 ms, TR=10960 ms) was done and used as a ground truth for comparison with the calculated necrosis map.

**Results:** The fingerprinting method achieved a temperature accuracy of 1.9 °C ± 1.0 °C compared to the temperature sensor. The comparison of the ablation zone with the ground truth yielded a dice score of 89.48%.

**Discussion:** This proof-of-principle approach has shown that MRF is a valid tool for temperature monitoring, yet further research has to be done to discover its full potential. In future studies an MRF sequence which is additionally sensitive to T1 relaxation could be utilized to simultaneously quantize the B0 off-resonance and T1 and therefore be able to monitor the temperature of adipose tissue as well. Further improvements could probably also be achieved with a more efficient k-space sampling like a spiral readout and with correction algorithms for gradient delays and phase errors.

[1] POORMAN, ME et al; *JMRI* 2020;51:675–692 [2] UECKER, M et al; *Proc. Intl. Soc. Mag. Reson. Med.* 23 (2015), S. 2486 [3] RIEKE, V et al; *JMRI* 2008 27(2) 376–390 [4] PEARCE, JA et al; *International Journal of Hyperthermia* 29 (2013), Nr. 4, S. 262–280 [5] BU-LIN, Z et al; *International Journal of Hyperthermia* 2008 24(7) 568–576

# A robust motion compensation algorithm for volumetric MR-temperature monitoring during micro-wave ablation of liver tumor in patients.

Valery Ozenne<sup>1</sup>, Bruno Quesson<sup>1</sup>, Pierre Bour<sup>2</sup>, Thibaut Faller<sup>2</sup>, Osman Öcal<sup>3</sup>, Sergio Lentini<sup>3</sup>, Max Seidensticker<sup>3</sup>, Olaf Dietrich<sup>3</sup>.

<sup>1</sup>Univ. Bordeaux, CNRS, CRMSB, UMR 5536, IHU Liryc, F-33000 Bordeaux, France, <sup>2</sup>Certis Therapeutics, Pessac, France, <sup>3</sup>Department of Radiology, University Hospital, LMU Munich, Munich, Germany.

**Introduction:** Micro-wave tumor ablation (MWA) in the liver could benefit from magnetic resonance guidance that enable real-time temperature and lesion size monitoring during the energy delivery [1]. Nevertheless, motion of abdominal organs causes significant challenges [2] and can be addressed either by synchronizing the acquisition with the physiological motion or by acquiring continuously the acquisition and compensating for the effect of displacement on magnitude and phase images using additional image processing method [3]. In such context, local intensity changes during MWA ablation (due to changes in tissue properties with heating) may be interpreted as motion and lead to local erroneous displacement vector fields, which can compromise MR temperature mapping. We investigate the use of a novel motion compensation algorithm [4, 5] during liver tumor ablation. The performance of the method was retrospectively evaluated on experimental images under gated conditions.

**Methods:** Patient: The study was performed at the University Hospital of Munich and was approved by the local health authorities. The patient underwent MWA procedure to ablate a primitive liver tumor. During the procedure, the patient was under general anesthesia and was continuously cared by medical staff. Ablation device: An AveCure micro-wave system (MedWaves, San Diego, USA) was used to perform the ablation. A 14-gauge large antenna was used. Ablation duration was set to 10 minutes. A stack of 13 contiguous slices (no slice gap) was acquired dynamically (350 repetitions) on a 1.5T MRI scanner (Magnetom Aera, Siemens Healthineers, Erlangen, Germany) during the exhalation phase using a gradient-echo echo planar imaging (EPI) sequence (TR/TE=2070/18ms). The acquisition was performed under respiratory gating using a cushion positioned in the patient abdomen. Temperature, thermal dose monitoring and lesion size was computed retrospectively using 3 workflows: a) standard phase subtraction (gold standard), b) *conventional H&S* motion compensation [6], c) *PCA-based H&S* motion compensation [4]. The impact of flow field, temperature and lesion volume size error were compared using maximal endpoint error (EE) of the displacement in the heated area for a time frame, RMSE of the temperature elevation during the ablation and Bland Altman plot.

**Results and conclusion:** An intensity signal decrease of 50% was observed in the vicinity of the needle. The maximal EE was in the range of 1-3 mm with *conventional H&S* and of 0.1-1 mm with *PCA-based H&S*. The flow field distortion estimated using *conventional H&S* optical-flow resulted in temperature errors up to 30°C while *PCA-based* method result in temperature error lower than 5°C. The 95% uncertainty for lesion size evolution (every ten frames) was reduced using the *PCA-based H&S* (Fig. 1), but a more limited impact on the thermal dose and corresponding lesion estimation was found due to the ablation duration. Under gated conditions, the performances of the proposed algorithm in term of motion field, temperature and lesion size accuracy outmatch the *conventional H&S* algorithm. Acquisition under free breathing are being evaluated.

**Reference:** [1] Gorny K.R. et al. Phys Med. 2019. [2] Kägebein U. et al. Topics in Magnetic Resonance Imaging, 2018. [3] Roujol S. et al. MRM, 2010. [4] Denis de Senneville B., et al. IEEE Trans. Med. Imaging, 2015. [5] Toupin S. et al, Physics in Medicine & Biology, 2017. [6] Horn B.K. and Schunck B.G. Artif. Intell. 1981.

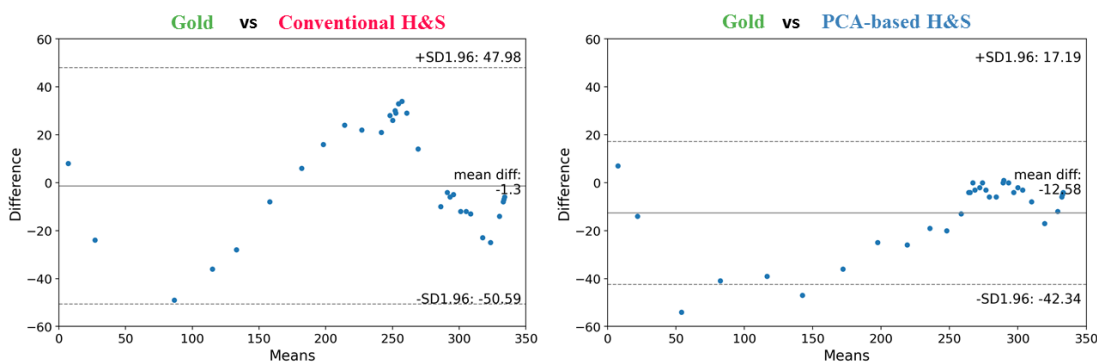


Figure 1 : Comparison of the lesion size evolution in voxel (every ten frames) between the gold standard with *conventional H&S* or with *PCA-based H&S*.

# Clinical Experience of 3D MR Thermometry for Liver Microwave Ablation

Junichi Tokuda<sup>1</sup>, Vincent M. Levesque<sup>1</sup>, Mariana C. Bernardes<sup>1</sup>, Ravi Seethamraju<sup>2</sup>, Kemal Tuncali<sup>1</sup>

<sup>1</sup> Department of Radiology, Brigham and Women's Hospital and Harvard Medical School

<sup>2</sup> Siemens Medical Solutions USA Inc., Boston, Massachusetts, United States

**Purpose.** Percutaneous liver ablation is a promising alternative to surgical resection for primary and metastatic hepatic malignancies, as the majority (80-90%) of the tumors are unresectable [1,2]. Microwave ablation (MWA) is emerging as a preferred ablation modality thanks to its larger ablation zones, shorter ablation times, and possibly better local tumor control compared to radiofrequency ablation (RFA) [3]. Intraprocedural MRI has the potential to improve the clinical outcome of MWA thanks to its superior soft-tissue contrast and ability to obtain temperature distribution [4]. We report our clinical experience of using 3D MR thermometry to monitor liver MWA at our institution.

**Materials and Methods.** MRI-guided microwave ablation was carried out percutaneously using a 14-gauge or 16-gauge MWA probe (AveCure, MedWaves Inc.) in a 3T MRI scanner (Verio DOT, Siemens). Once the probe position was confirmed on either a T1 or T2-weighted MRI, the MWA system was turned on for baseline imaging for MR thermometry. The MWA system was operated at 120°C for 5-15 minutes depending on the size of the lesion and the proximity to surrounding critical structures. During ablation, both MR thermometry images were acquired with a breath-hold every 2-3 minutes using one of the following sequences: a 2D multislice gradient echo (TR/TE: 65/10ms, flip angle: 30°, matrix: 256x116, pixel size: 1.016 mm<sup>2</sup>, slice thickness: 5 mm, slices: 5, total acquisition time 28s), 2D multislice EPI (TR/TE: 83/8.3ms, EPI factor: 7, flip angle: 25°, matrix: 128x125, pixel size: 3.91 mm<sup>2</sup>, slice thickness: 5 mm, slices: 5, acquisition time: 7s), or 3D gradient echo (TR/TE: 15/10ms, flip angle: 14°, matrix: 192x96, pixel size: 1.5625 mm<sup>2</sup>, slice thickness: 2 mm, slices: 16, acquisition time: 14s). The images were immediately processed using a 3D Slicer with a custom-made plug-in to visualize a temperature map based on the proton resonance frequency (PRF) method [5].

**Results.** Among 67 MRI-guided liver MWAs cases (HCC: 27, metastatic liver cancers: 40), 57 were monitored with MR thermometry. Representative temperature maps correlated with a post-procedural T1-weighted MR image shows the ablation zone was well correlated with the area greater than 55°C on the temperature map on the axial plane involving the probe (Fig 1). MR thermometry was also useful in monitoring the shaft heating, which leads to thermal damage to the subcutaneous tissues and the skin. However, our visual assessment noted that the radius of the heated area on the 3D temperature map along the craniocaudal axis tends to be shorter than the radius along the anteroposterior axis, likely due to the larger susceptibility needle artifact.

**Conclusion.** Our preliminary evaluation of MR thermometry for microwave ablation successfully visualized the temperature change around the probe tip.

**References.** [1] Roayaie S, et al. *Hepatology*. 2015 Aug;62(2):440–451. [2] Sotirchos VS, et al. *Radiology*. 2016 Sep;280(3):949–959. [3] Shady W, et al. *J Vasc Interv Radiol*. 2018 Feb;29(2):268-275. [4] Morikawa S, et al. *J Magn Reson Imaging*. 2002;16(5):576-83. [5] Rieke V, et al. *J Magn Reson Imaging*. 2008;27(2):376-90. [6] Qiu-Jie S, et al. *Int J Hyperthermia*. 2011;27(2):124-31.

**Acknowledgments.** The study was funded in part by the National Institutes of Health (R01EB020667, R01CA235134, P41EB028741). The EPI-based thermometry was provided as WIP by Siemens.

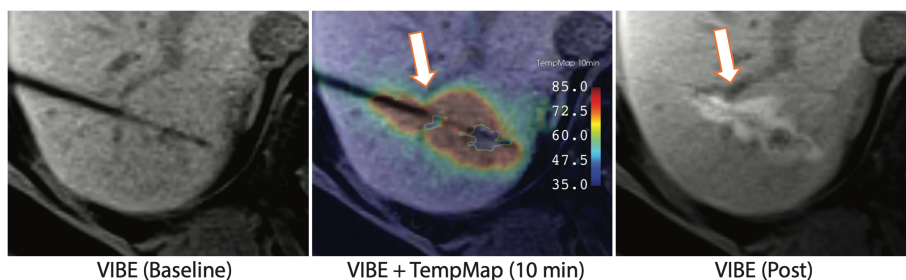


**Fig. 1:** Representative temperature maps obtained during MWA of metastatic tumor: (a) VIBE MRI before ablation; (b) temperature map after 10 minutes of ablation overlaid onto the VIBE image; and (c) post-ablation VIBE MRI. The heat sink effect is observed near the blood vessel on both temperature map and post-ablation MRI.



# Performance of advanced DWI and MR thermometry near interventional needle-like devices

JH Holmes, CJ Buelo, R Geng, M Tarasek, DT Yeo, CL Brace, D Hernando, A Faacks, SA Wells

University of Iowa, Iowa City, IA, USA, Departments of Radiology and Biomedical Engineering; University of Wisconsin-Madison, Madison, WI, USA, School of Medicine and Public Health, Departments of Radiology, Urology, Medical Physics, and Biomedical Engineering; GE Research, Niskayuna, NY, USA

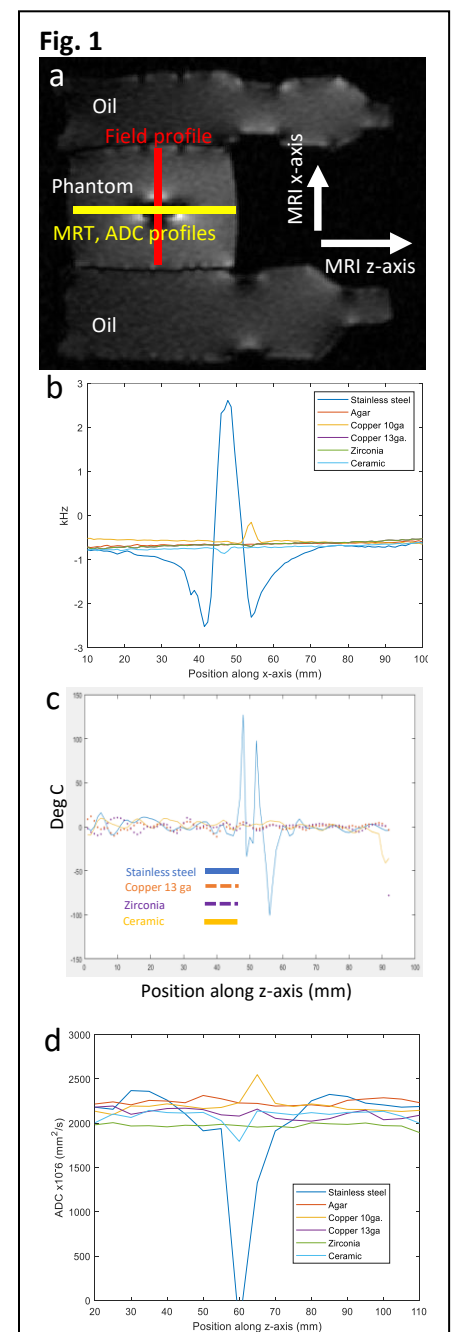
**Purpose:** MR guided interventions benefit significantly from the exquisite soft tissue contrast afforded by MRI. Aside from conventional anatomic imaging, advanced quantitative methods such as diffusion weighted imaging (DWI) and MR thermometry (MRT) provide invaluable intra- and post-procedure soft tissue information. However, percutaneous interventional devices including ablation applicators and biopsy needles present significant challenges in the MRI environment including magnetic susceptibility related artifacts. Conventional devices are typically made of stainless steel (SS), which has a high magnetic susceptibility that distorts the static magnetic field and introduces image artifacts. The accuracy of ADC from advanced motion robust DWI methods with multi-shot reconstruction as well as MRT proximal to high susceptibility devices are also typically degraded. In this work, we present first experiences evaluating the performance of DWI and MRT adjacent to four different coaxial device materials.

**Materials and Methods:** MRI was performed at 3T (Premier, GE Healthcare, Waukesha, WI) on six phantoms, including a control (no device) and five different coaxial needle-like devices. Each device was secured at a 60° angle on a 10 cm cubic mold. A total of 1L of degassed 1.4% agar/0.025% gadobenate dimeglumine solution was solidified around each device. Device gauge (ga) and materials were: 15-ga SS (reference standard), 10-gauge copper (Cu10), 13-ga copper (Cu13), 14-ga ceramic and 14-ga zirconia. Static magnetic field  $B_0$  maps were acquired using a 3D MAVRIC-SL acquisition (acquired resolution = 0.9x0.9x5mm) [1]. DWI was performed using 2D multi-shot EPI with MODI diffusion gradients [2] (acquired resolution = 2.5x2.5x5mm, TR/TE = 4s/65.9ms). 2D SPGR MRT was acquired with each phantom placed between bottles of vegetable oil (acquired resolution = 2x2x2mm, TR/TE = 2.1/120ms, flip angle = 10°). The setup and measurement profiles are shown in Fig. 1a.

**Results:** Profiles of the  $B_0$  field maps demonstrate significant off-resonance due to the SS device (Fig. 1b). However, the copper, ceramic, and zirconia devices introduced much less off-resonance. The MRT-derived temperature changes in the absence of applied heat are shown in Fig. 1c. A localized region of temperature artifact is noted adjacent to the devices with much greater artifact observed with the SS. The vegetable oil did not display a PRFS shift and thus serves as a null temperature change reference (not shown). Profiles of the ADC maps measured across the phantoms show localized bias with the SS device (Fig. 1d) that is reduced for the other devices.

**Conclusions:** Percutaneous interventional devices including ablation applicators and biopsy needles manufactured with SS produce large distortions to the  $B_0$  field and associated imaging artifacts. Alternative materials should be used to minimize imaging artifacts. Future work will include further MR sequence optimization to minimize sensitivity to local distortions to the static magnetic field.

**References:** [1] Koch et al. MRM. 2011;65:71-82. [2] Zhang et al. MRM. 2019;82:302-311.



# Real-time automatic temperature regulation during in-vivo MRI-guided Laser-induced Thermotherapy (MR-LITT)

**Author List:** Manon Desclides<sup>1,2</sup>, Valéry Ozenne<sup>1</sup>, Pierre Bour<sup>2</sup>, Guillaume Machinet<sup>3</sup>, Christophe Pierre<sup>3</sup>, Stéphane Chemouny<sup>2</sup>, Bruno Quesson<sup>1</sup>

<sup>1</sup>Univ. Bordeaux, CNRS, CRMSB, UMR 5536, IHU Liryc, F-33000 Bordeaux, France, <sup>2</sup>Certis Therapeutics, Pessac, France, <sup>3</sup>ALPhANOV, Talence, France

## Purpose

We present a technique that automatically regulates tissue temperature during LITT. Real-time rapid MR-thermometry data are processed on the fly and serve as input to a PID controller that dynamically controls the laser power. In vivo validation in swine muscle is presented.

## Material and Methods

A prototype (Alphanov, France) LITT device (976 nm wavelength, 200  $\mu$ m fiber core diameter) with a distal glass diffuser tip (1.8 mm diameter) of 1 cm length was inserted into a leg muscle of an anesthetized pig (N=2, ~35 kg body mass, protocol approved by ethic committee). MR-thermometry was performed at 1.5 T (Avanto, Siemens Healthcare): single shot EPI, 8 slices positioned perpendicular to the laser tip and acquired every second, TE=21 ms, FOV=158x158 mm<sup>2</sup>, 3 mm slice thickness, FA=70°, GRAPPA acceleration=2, bandwidth/pixel = 1370 Hz. The implemented controller is a proportional-integral-derivative (PID) algorithm incorporating the Bio-Heat Transfer Equation (R. Salomir *et al*, *Magn Reson Med*. 2000 Mar;43(3):342-7) that automatically adjusted the laser output to force tissue temperature evolution to follow a predefined profile.

## Results

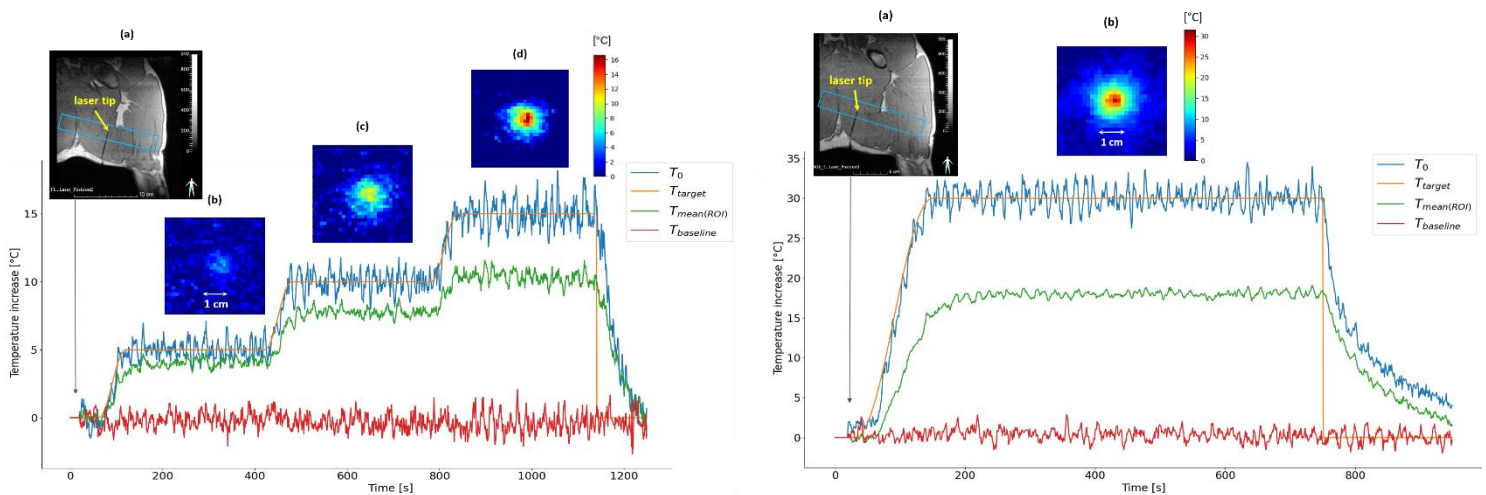


**Figure 1:** Examples of automatic temperature regulation during LITT in the left leg muscle of a 33 kg swine: temperature-time profile with (left) 3 successive plateaus (5°C, 10°C and 15°C temperature increase - 300 s duration each) and (right) one plateau of 30°C temperature increase. Target profile (orange), maximal (blue) and mean (green) temperature curves over the 3x3x3 pixels ROI centered on the maximal temperature are displayed. Red curve shows temperature evolution in a non-heated pixel. **Images: coronal slice from a 3D MPRAGE sequence (a) showing the position of the thermometry stack of slices (blue rectangle) and temperature maps (b, c and d, same color scale) obtained in the middle of each temperature plateau.**

For both experiments, we observe a good correspondence between target and maximal temperature values, with -0.052°C and -0.098°C mean values of differences and confidence interval (RMSE) of 0.82°C and 1.4 °C during heating, respectively.

## Conclusion

The proposed regulation algorithm provides a precise control of in-vivo tissue temperature in leg muscle over long heating durations (>15 minutes) for low/medium and high temperatures increases. Such method can be used for various therapeutic strategies such as coagulation necrosis, local drug delivery or in combination with immunotherapy, where different heating protocols are required.

**Purpose:** In this study, we evaluate the feasibility of PRF thermometry in the brain and prostate at 0.55T. MR-guided therapy at lower  $B_0$  offers key advantages over high-field alternatives, such as reduced cost, improved device safety profiles, and specific absorption rate. The addition of MR thermometry to the MRI toolset will further empower low field MRI for guiding interventional procedures.

**Methods:** We utilized segmented EPI for image acquisition since it is well suited to take advantage of longer  $T2^*$  and reduced  $B_0$  inhomogeneity associated with the lower  $B_0$  and enables fast SNR-efficient acquisitions with long TEs and TRs to compensate for reduced temperature sensitivity and SNR loss respectively.

All human imaging protocols conformed to institutional volunteer scanning policies. Healthy volunteers were imaged on a 0.55T MAGNETOM Free.Max (Siemens Shenzhen Magnetic Resonance Ltd., Shenzhen, China) using prototype 3D segmented EPI sequences. The following parameters were used to acquire dynamic series for assessment of temperature uncertainty in the absence of heating:

- Brain
  - 3D Segmented EPI: TR 76ms, TE 42ms, water-selective excitation,  $1.25 \times 2.5 \times 3 \text{mm}^3$  voxel,  $192 \times 96 \times 26$  matrix, echo train length (ETL) 25, BW 704Hz/pixel, temporal resolution 8s/volume, FA  $28^\circ$
  - 2D Segmented EPI: TR 75ms, TE 38ms, water-selective excitation,  $1.09 \times 2.18 \times 3.5 \text{mm}^3$  voxel,  $256 \times 128$  matrix, ETL 5, BW 130Hz/pixel, temporal resolution 1.95s/slice, FA  $40^\circ$
- Prostate: TR 100ms, TE 45ms, water-selective excitation,  $2 \times 3 \times 3 \text{mm}^3$  resolution,  $128 \times 128 \times 12$  matrix, ETL 23, BW 398 Hz/pixel, 7.2s/volume

A Principal Component Analysis (PCA) based algorithm was used to remove baseline phase changes. Phase difference images were scaled by  $-1/(\gamma B_0 TE \times 0.01 \text{ppm}/^\circ\text{C})$  to estimate temperature difference  $\Delta T$  relative to baseline. Since the expected temperature change in absence of external heating is 0, the temporal standard deviation ( $\sigma_T$ ) of the estimated  $\Delta T$  series was used to assess  $\Delta T$  stability.

**Results:** Figures 1 through 3 summarize estimated  $\Delta T$  uncertainty in the brain and prostate, respectively.

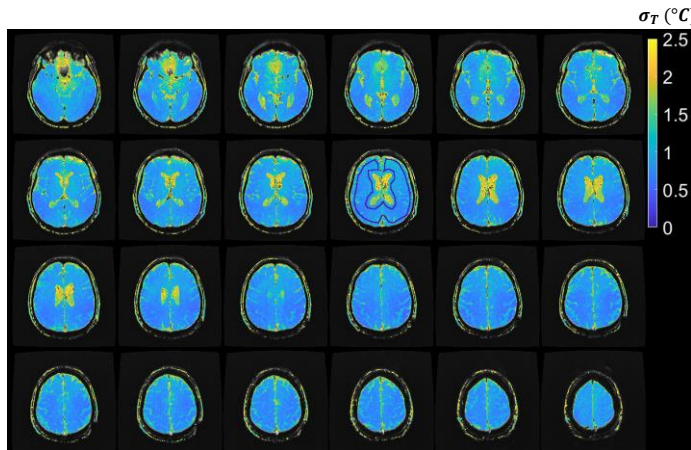


**Figure 1:**  $\sigma_T$  in the brain with 3D acquisition (ETL 25, TE 42ms).  $\sigma_T$  values of less than  $2.5^\circ\text{C}$  are overlaid on representative magnitude images.  $\sigma_T$  is less than  $1^\circ\text{C}$  in most of the brain, demonstrating excellent precision. Average  $\sigma_T$  of  $0.9 \pm 0.2^\circ\text{C}$  was observed in the ROI indicated

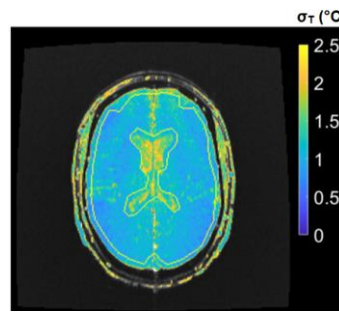


**Figure 2:**  $\sigma_T$  in the brain with 2D segmented acquisition.  $\sigma_T$  values of less than  $2.5^\circ\text{C}$  are overlaid on representative magnitude image. Average  $\sigma_T$  of  $1.1 \pm 0.2^\circ\text{C}$  was observed in the ROI indicated on the figure, demonstrating good precision.

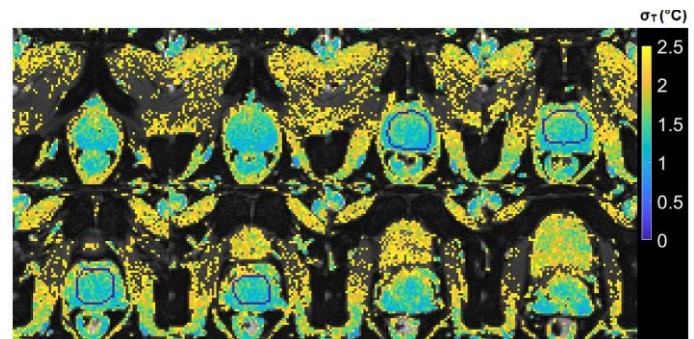


**Figure 3:**  $\sigma_T$  in the prostate.  $\sigma_T$  values of less than  $2.5^\circ\text{C}$  are overlaid on representative magnitude images (8 out of 12 axial slices; cropped to show details). Average  $\sigma_T$  of  $1.4 \pm 0.3^\circ\text{C}$  was observed in the indicated ROI.

**Discussion:** Our results obtained with the proposed 2D and 3D protocols suggest that it is feasible to perform PRF thermometry via segmented EPI sequences in the brain and prostate at 0.55T.

Observed  $\sigma_T$  values are within acceptable thresholds to monitor irreversible tissue damage. Frame rates achieved in this study are comparable with those used clinically at higher field strengths.

## Implementation of a real-time 3D-thermometry pipeline in Gadgetron for hepatic thermal ablation

Dominik Horstmann<sup>1,2</sup>, Karen Meyer zu Hartlage<sup>1,2</sup>, Daniel Reimert<sup>1,2</sup>, J. Joaquin Löning Caballero<sup>1,2</sup>, Othmar Belker<sup>1,2</sup>, Prof. Dr. Frank Wacker<sup>1,2</sup>, Dr. Bennet Hensen<sup>1,2</sup>, Dr. Marcel Gutherlet<sup>1,2</sup>.

<sup>1</sup>Hannover Medical School <sup>2</sup>STIMULATE-Solution Centre for Image Guided Local Therapies

**Introduction:** The clinical relevance of MR guided minimally invasive ablation for tumor treatment is steadily rising. Guidance via MR thermometry makes real-time imaging and arbitrary slice positioning possible while assuring precise knowledge of the size of the ablation zone. However, low temporal and spatial resolution as well as insufficient coverage of the ablation zone hamper the success of current clinical thermometry. Besides, for moving organs such as the liver, robust real-time 3D thermometry for clinical application is not yet available. Purpose of this work was to implement a real-time proton resonance frequency (PRF)-based 3D MR thermometry pipeline for monitoring thermal liver ablations.

**Methods:** Fast thermometry data acquisition was performed by a multigradient echo 3D stack-of-stars sequence<sup>1</sup> with temporal resolution of 12 s, spatial resolution of 2.5 mm isotropically, field of view of 320 x 320 x 60 mm<sup>3</sup>, TR of 14.5 ms, receiver bandwidth of 1090 Hz/pixel as well as eight TEs ranging from 1.2 ms to 10.5 ms. The thermometry pipeline, including image reconstruction as well as calculation of temperature and necrosis maps, was implemented in Gadgetron<sup>2</sup> running in a Docker<sup>3</sup> container on an external GPU-server. The toolbox BART<sup>4</sup> was used for parallel imaging and compressed sensing (PICS) as well as GPU accelerated reconstruction. For further acceleration of data sampling, random sampling in combination with acceleration of factor 3 in kz-direction were performed whereas acceleration of data processing was achieved by parallelization of the source code via the Python library multiprocessing<sup>5</sup>. Apart from that, the acquired data were corrected for noise, gradient delay<sup>6</sup>, phase drift<sup>7</sup> and phase errors<sup>8</sup>. For thermometry, all eight echoes were combined to temperature maps according to Madore<sup>9</sup> et al. The necrosis maps were optionally calculated by the CEM43<sup>10</sup> or the thresh52<sup>11</sup> model. To test the pipeline, microwave ablations (modified ECO-100E, Eco Microwave System Co., Ltd., Nanjing, China, 2.45 GHz, 150 W) on nine static bioprotein phantoms<sup>12</sup> were performed on a 1.5 T scanner (MAGNETOM Avanto, Siemens Healthcare) and monitored by the described stack-of-stars sequence. Fiber optical temperature sensors (FOTEMPtrafo, Weidmann Technologies Deutschland GmbH, Dresden, Deutschland) were used for gaining reference temperatures. Retrospectively, the calculated necrosis zones were compared to a ground truth determined by manual segmentation of the ablation zone in a post-ablative T2-weighted Turbo-Spin-Echo sequence (1 x 1 x 1 mm<sup>3</sup>, TE=156 ms, TR=10960 ms).

**Results:** The implemented real-time 3D thermometry pipeline yielded temperature accuracies of 1.15 °C ± 0.69 °C compared to the temperature sensors. In non-heated areas the standard deviation of the measured temperature was 0.71 °C ± 0.24 °C. The comparison of the ablation zone with the ground truth yielded dice scores of 84.02 % ± 2.36 %. For a 3D volume with 24 slices and 8 echoes the processing time was about 26 s.

**Discussion:** The experiments show that the thermometry pipeline is already close to real-time 3D thermometry. Further research will focus on acceleration of reconstruction time as well as on more efficient data sampling via for example stack-of-spirals data acquisition. Additionally, the pipeline will be optimized for moving phantoms as, in the future, it is planned to be used for clinical applications in moving organs such as the liver. The modular and opensource character of the pipeline makes future improvements and extensions easy to integrate.

[1] SVEDIN, BT et al; *Magn Reson Med* 2018;79(3) 1407–1419 [2] HANSEN, MS; et al *Magn Reson Med* 2013;69(6) 1768–1776 [3] MERKEL, D: Linux Journal,19. Mai 2014 <https://www.linuxjournal.com/content/docker-lightweight-linux-containers-consistent-development-and-deployment>– visited 12.04.2022. [4] UECKER, M et al; *Proc. Intl. Soc. Mag. Reson. Med.* 23 (2015), S. 2486 [5] <https://docs.python.org/3/library/multiprocessing.html>, visited 25.03.2022 [6] BLOCK, KT et al; In: *Proceedings of the 19th Annual Meeting of ISMRM, Montreal, Canada* (2011), S. 2816 [7] RIEKE, V et al; *JMRI* 2008 27(2) 376–390 [8] MOUSSAVI, A et al; *Magn Reson Med* 2017;71(1) 308–312 [9] MADORE, B et al; *Magn Reson Med* 2011;66(3) 658–668 [10] PEARCE, JA et al; *International Journal of Hyperthermia* 29 (2013), Nr. 4, S. 262–280 [11] KICKHEFEL, A et al; *JMRI* 2011 33(3) 704–712 [12] BU-LIN, Z et al; *International Journal of Hyperthermia* 2008 24(7) 568–57

# A NEW VERSATILE MR-GUIDED HIGH-INTENSITY FOCUSED ULTRASOUND (MRgHIFU) DEVICE: SYSTEM PERFORMANCE ASSESSMENT AND CLINICAL FEASIBILITY

Paolo Cabras<sup>1,2</sup>, Pierre Auloge<sup>3</sup>, Erik Dumont<sup>2</sup>, Benoit Wach<sup>1</sup>, Elodie Breton<sup>1</sup>, Afshin Gangi<sup>1,3</sup>, and Jonathan Vappou<sup>1</sup>

<sup>1</sup>Université de Strasbourg, CNRS, ICube, UMR7357, Strasbourg, France; <sup>2</sup>Image Guided Therapy, Pessac, France; <sup>3</sup>Department of Interventional Imaging, Strasbourg University Hospital, France

**Purpose:** Originally developed for the treatment of uterine fibroids, whole-body MRgHIFU systems are not optimal for treating musculoskeletal tumors because of the difficulty in patient positioning<sup>1</sup>, as well as the need for a dedicated, expensive water-filled MR-table. We have developed a new portable MRgHIFU device in which the transducer can be directly positioned on the patient.

**Methods:** The proposed device relies on: (1) An MR-safe flexible supporting device that allows free manipulation of the transducer. Up to 4 supporting legs with adaptable length can support the transducer holder. Once the transducer is in the desired position, the supporting device is rigidified using the granular jamming principle<sup>2</sup>. (2) A navigation software that guides the physician during the transducer positioning process outside the MRI bore, through a virtual environment, displaying the target, the planned configuration, and the actual position of the transducer in real time. Once the transducer has been positioned, the HIFU ablation is monitored in real time using Proton Resonance Frequency Shift (PRFS) Thermometry. Positioning accuracy was first evaluated in a phantom. First clinical results on a patient suffering from a bone metastasis in the forearm are also presented.

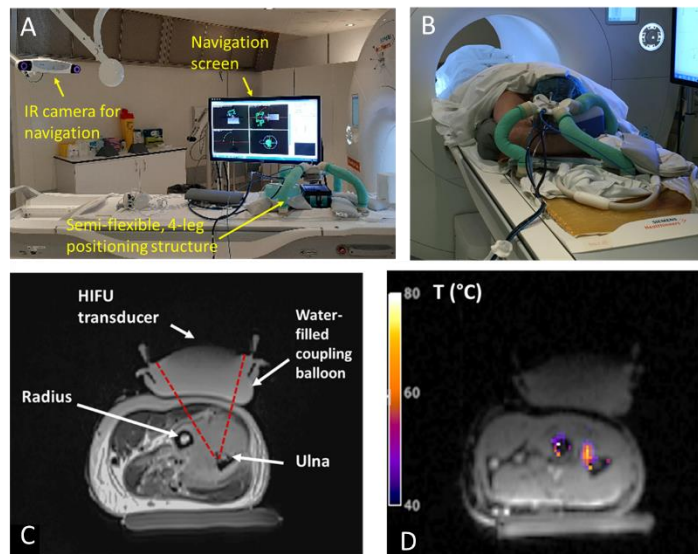


Fig. 1 : (A) General setup; (B) Experimental setup for the presented clinical case: the transducer is positioned over the forearm; (C) Transverse MR image showing the HIFU transducer, and the target on the ulna; (D) Real-time MR Thermometry during the ablation

**Results:** The average targeting error of the complete process was found to be equal to  $5 \pm 2$  mm in terms of focus position, and  $4 \pm 2$  degrees in terms of transducer orientation. In the clinical trial, the lesion to be treated in the first patient was an ellipsoid of  $81 \times 47 \times 34$  mm<sup>3</sup>. Five different transducer positions were necessary to cover the whole volume, in addition to using electronic steering (using a 128-element, 1MHz transducer) for each transducer pose. The patient was successfully treated: Pain score decreased from 8/10 to 3/10 four days after treatment, and 85% of the lesion was treated. Pain palliation was durable, and no adverse effects were reported.

**Conclusion:** The proposed MRgHIFU device allows easy and accurate positioning of the HIFU transducer directly on the patient. This system is intended to be modular and flexible: It can be easily adapted to a variety of clinical applications that may require different HIFU transducers in terms of central frequency, aperture, number of elements and geometry. We expect this device to increase the accessibility to MRgHIFU therapies thanks to its versatility and its intrinsic low-cost nature.

**References:** 1. Joo, B. *et al.* Pain Palliation in Patients with Bone Metastases Using Magnetic Resonance-Guided Focused Ultrasound with Conformal Bone System: A Preliminary Report. *Yonsei Med J* **56**, 503–509 (2015).  
2. Behringer, R. P. & Chakraborty, B. The physics of jamming for granular materials: a review. *Rep Prog Phys* **82**, 012601 (2019).

## **Interventional MR Neurography - Applied Precision Medicine**

Jan Fritz, M.D.

Associate Professor of Radiology

Chief, Division of Musculoskeletal Radiology

NYU Grossman School of Medicine

jan.fritz@nyulangone.org

Precision medicine aims to provide individualized patient care designed to optimize accuracy, efficiency and therapeutic benefit for particular groups and individual patients with specific conditions. Interventional pain management is a field where the application of precision medicine has an enormous impact through direct visualization of variant course and anatomy of submillimeter interventional targets, instrument placement under direct visualization of the target without the need to rely on anatomic landmarks, and direct process monitoring ranging from visualization of injectants to temperature during ablation processes in conjunction with targeted and non-targeted structures. Interventional MR Neurography represents a minimally invasive precision medicine technique that combines all the criteria above, including targeting small nerves in challenging human body areas for highly accurate nerve blocks, intramuscular injections, and ablations (1). This cross-sectional technique uniquely combines the highest tissue contrast and high spatial resolution anatomic detail, which enables the precise identification and selective targeting of peripheral nerves, accurate needle guidance and navigation of the tip of injection and cryoablation needles within the immediate vicinity of a nerve. Based on T2 and T1 properties, Interventional MR Imaging can directly visualize injected drugs to assess appropriate drug distribution without the need of an artificial contrast agent and documentation of the absence of spread to confounding nearby nerves (2). Similarly, Interventional MR Neurography provides the unique ability to visualize and monitor the ice ball during cryoablation. 3-Tesla field strength offers high spatial and temporal resolution for improved visualization of small targets and increased efficiency (3). MR Neurography guidance exclusively combines the absence of procedure-related exposure to ionizing radiation with the capability to resolve small nerves in deeply situated locations. This talk will discuss techniques and diagnostic and interventional procedures of high-field Interventional MR Neurography of various small peripheral nerves and complex pain syndromes.

### References

1. Fritz J, Dellon AL, Williams EH, Belzberg AJ, Carrino JA. 3 Tesla high-field MR neurography for guiding nerve blocks and its role in pain management. *Magnetic Resonance Imaging Clinics of North America*. Magn Reson Imaging Clin N Am. 2015; 23(4):533-45.
2. Fritz J, Dellon AL, William EH, Rosson G, Belzberg AJ, Eckhauser FE. Diagnostic Accuracy of Selective 3-Tesla MR Neurography-guided Retroperitoneal Genitofemoral Nerve Blocks for the Diagnosis of Genitofemoral Neuralgia. *Radiology*. 2017 Oct;285(1):176-185.
3. Fritz J, Chhabra A, Wang KC, Carrino JA. Magnetic resonance neurography-guided nerve blocks for the diagnosis and treatment of chronic pelvic pain syndrome. *Neuroimaging Clin N Am*. 2014;24(1):211-34.

# Retroperitoneal Lateral Femoral Cutaneous Nerve Blocks in the Work-Up of Thigh Pain: Performance Analysis of a New Technique

**Author Block:** D. Dalili<sup>1</sup>, S. Ahlawat<sup>2</sup>, D. Shakoor<sup>3</sup>, A. Rashidi<sup>2</sup>, A. Isaac<sup>4</sup>, J. Fritz<sup>5</sup>;

<sup>1</sup>South West London Elective Orthopaedic Centre, London, United Kingdom, <sup>2</sup>Johns Hopkins, Baltimore, MD, <sup>3</sup>Yale University School of Medicine, New Haven CT, <sup>4</sup>Kings College London, United Kingdom, <sup>5</sup>NYU Grossman School of Medicine, New York, NY.

**Purpose:** Lateral femoral cutaneous nerve (LFCN) blocks under the inguinal ligament are frequently performed in the work-up of thigh pain. However, the LFCN course is highly variable at the level of the inguinal ligament, which may interfere with successful blocks. Therefore, we developed a technique to block the LFCN in the retroperitoneum, proximal to the inguinal ligament. We describe the technique, efficacy in the work-up of anterior thigh pain, and patient-reported procedural experience.

## Materials and methods

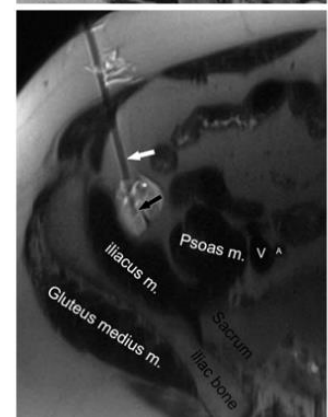
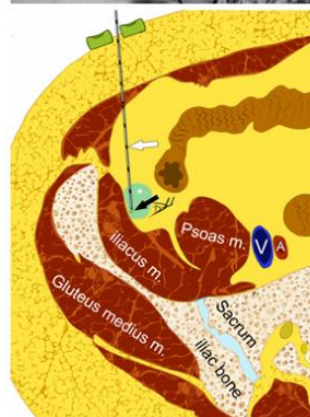
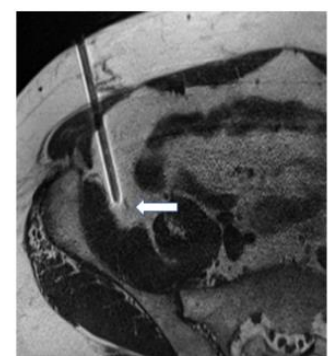
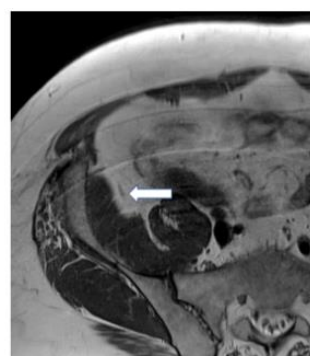
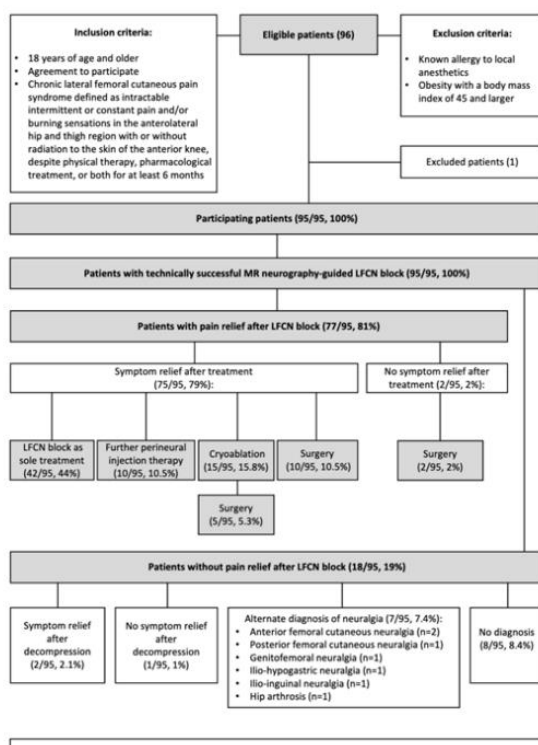
Following IRB approval and informed consent, patients referred for LFCN blocks in the setting of unclear anterior thigh pain were included. The retroperitoneal LFCN blocks were performed under MR neurography guidance to map and target the LFCN at the iliacus muscle level proximal to the inguinal ligament. An anterior approach in the lower abdomen was employed. Outcome variables included technical success, complications, learning curve, efficacy, and patient-reported experience. P-values  $\leq 0.05$  were considered statistically significant. Descriptive and binary logistic regression statistical analyses were performed.

## Results

Between 2016 and 2019, 123 LFCN blocks were performed in 95 participants (59 women; 54 (18-91) years-of-age; BMI, 30 (17-46) kg/m<sup>2</sup>). Successful drug delivery was achieved in all participants. No complications occurred. Total procedure time was 25 (6-53) min for unilateral blocks and 29 (23-42) min for bilateral blocks. LFCN blocks achieved > 50% pain relief in 77/95 (81%) participants, which was followed by > 50% symptom relief following subsequent treatments in 75/95 (79%). The majority of patients (>80%) reported overall satisfaction.

## Conclusion

Retroperitoneal LFCN Blocks under MRN guidance have a high technical success rate and effectively identify pain generators in anterior thigh pain. Patients tolerate the procedure well.



**Title:** Accurate targeting in lumbar and sacral nerve root infiltrations using MRI guidance, with 5-month follow-up

**Authors:** Pauline C. Guillemin<sup>1</sup>, Rares Salomir<sup>1</sup>, Orane Lorton<sup>1</sup>, Enrique Maturana<sup>1</sup>, Alex Stöckli<sup>1</sup>, Pierre-Alexandre Poletti<sup>1</sup>, Nicolas Lauper<sup>2</sup>, Dennis Dominguez<sup>2</sup>, Sana Boudabbous<sup>1</sup>, Max Scheffler<sup>1</sup>

**Affiliations:** <sup>1</sup>Division of Radiology, Geneva University Hospitals, Geneva, Switzerland; <sup>2</sup>Division of Orthopedic Surgery and Traumatology, Geneva University Hospitals, Geneva, Switzerland

**Purpose:** Diagnostic and therapeutic spinal nerve root infiltrations for radicular pain can be performed under magnetic resonance imaging (MRI) guidance with high soft tissue contrast and visualization of the expected drug spread area around the nerve root on fat-saturated T2 subtraction images. The aim of this study was to evaluate 5-month responses following MRI-guided infiltrations.

**Material & Methods:** Thirty-three 3T MRI-guided nerve root infiltrations were performed in 29 patients between January 2017 and January 2022, with a dedicated surface coil. In a first step, the optimal needle path was determined by a radiologist using an axial T2-weighted turbo spin echo sequence (time to echo, 103 ms; repetition time, 2,3 ms; slice thickness, 2.5 mm), repeated a second time for confirmation after placement of a small silicone marker on the chosen skin puncture point. A breathhold proton density-weighted sequence was used to control 20G or 22G needle (Cytocut MRI, MDL, Delebio, Italy) advancement until the needle came to lie behind the nerve root. A subtraction image was then obtained using a fat-saturated T2-weighted sequence acquired before and after injection of a small amount of sterile saline. Finally, dexamethasone and lidocaine/ropivacaine injections were performed. For the evaluation of pain relief, the primary end point was the patient's response 1 week after the infiltration and then every month up to 5 months, using a visual analog scale (VAS) or a numeric rating scale (NRS), with 0 = no pain, 1-3 = mild pain, 4-6 = moderate pain, and 7-10 = severe pain.

**Results:** Complete follow-up responses were obtained in 28 patients. Of these, 26 patients (93%) showed a significant reduction in pain one week after the infiltration, 23 patients (82%) one month thereafter, 21 patients (75%) two months thereafter, 20 patients (71%) three months thereafter, 18 patients (64%) four months thereafter, and 13 patients (46%) five months thereafter. Of the 28 patients, 2 patients (7%) underwent back surgery, denying any improvement felt 1 month after the procedure. No major or minor complication occurred. Mean MRI room occupation time was 42 min.

**Conclusion:** Twenty-eight MRI-guided nerve root infiltration for radicular pain were associated with an overall positive response rate of 64% after 4 months and 46% after five months.

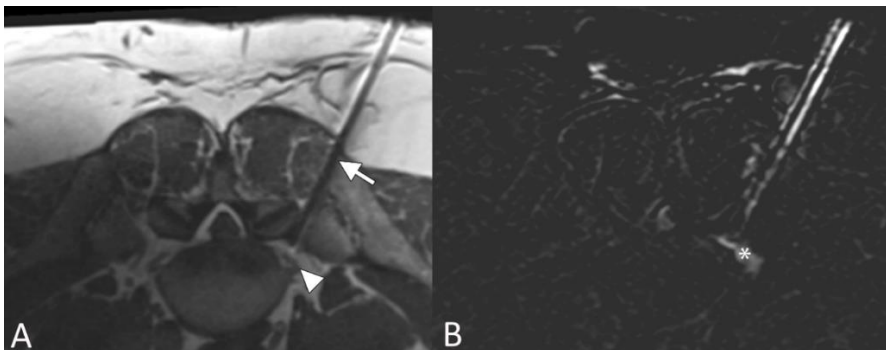


**Figure:** Foraminal left L5 nerve root infiltration in a 49-year-old man. **(A)** The MRI-safe 20G needle (arrow) passes between the left superior articular process of the sacrum and the superior tip of the left sacral ala. Its distal tip lies directly behind the exiting nerve root (arrowhead). **(B)** Subtraction image of T2-weighted fat-saturated sequence obtained after injection of a small amount of sterile saline, surrounding the nerve root posteriorly (asterisk).



### 3 Tesla MR Neurography Guided Nerve Blocks for The Treatment of Pudendal Neuralgia

**Author Block:** D. Dalili<sup>1</sup>, S. Ahlawat<sup>2</sup>, D. A. Isaac<sup>3</sup>, A. Rashidi<sup>2</sup>, A. Haj-Mirzaian<sup>2</sup>, J. Fritz<sup>4</sup>;

<sup>1</sup>South West London Elective Orthopaedic Centre, London, United Kingdom, <sup>2</sup>Johns Hopkins, Baltimore, MD, <sup>3</sup>Kings College London, United Kingdom, <sup>4</sup>NYU Grossman School of Medicine, New York, NY.

**Purpose:** To evaluate prospectively the safety and efficacy of 3-Tesla magnetic resonance (MR) neurography-guided pudendal blocks for the diagnosis and treatment of pudendal neuralgia (PN).

#### Materials and methods

Following institutional review board approval and informed written consent, 77 patients with pudendal neuralgia were included. MR neurography-guided pudendal nerve blocks were performed using commercially available, MR-compatible needles for drug delivery via a posterolateral approach utilizing a clinical wide-bore 3 Tesla MRI system. Outcome variables included technical success, complications, procedure time, learning curve, pre- and post-procedural numerical visual analogue scale (VAS) score (0= no discomfort to 10= worst discomfort), efficacy and patient experience. P-values  $\leq 0.05$  were considered statistically significant. Descriptive and regression statistical analyses were performed.

#### Results

148 PNBs were performed in 77 subjects (49 men, 28 women; mean age, 50 years; age range, 18-79 years; mean body mass index (BMI), 25.5 kg/m<sup>2</sup>, BMI range 18-47 kg/m<sup>2</sup>), 48 bilateral and 52 unilateral (L = 25, R = 18). Successful drug delivery was achieved in all patients. No complications occurred. Total procedure time was 22:13 minutes (range 8:13 to 44:27) in unilateral blocks and 33:05 minutes (range 13:43 to 66:38) in bilateral blocks. The mean pre-procedure VAS score was 5.87 (range 1-10). The mean post-procedure VAS score was 1.83 (range 0-7). PNBs achieved appropriate anaesthesia in 57/77 (73%) subjects. The majority of patients (>86%) reported immediate pain relief, comfort and acceptable examination time and positioning.

#### Conclusion

Selective MR neurography-guided PNBs are safe and effective procedures with high technical success and patient satisfaction in patients with PN. 3T MR-neurography guided PNBs achieve good to excellent results and can be repeated with therapeutic benefits in a subgroup of patients, alleviating the need for more invasive procedures.

Table 5. MR neurography interobserver reader agreement

Laterality	Imaging feature	Inter-reader agreement
Left	STL Thickness <sup>a</sup>	0.913
	NVB Thickness <sup>b</sup>	0.839
	Obturator internus <sup>c</sup>	0.956
	PN abnormality <sup>d</sup>	0.921
	Contact with STL <sup>e</sup>	0.753
	Scarring <sup>f</sup>	0.88
	Falciform process of STL <sup>g</sup>	1.00
Right	Mass lesion <sup>h</sup>	1.00
	STL Thickness <sup>a</sup>	0.968
	NVB Thickness <sup>b</sup>	0.871
	Obturator internus <sup>c</sup>	0.978
	PN abnormality <sup>d</sup>	0.962
	Contact with STL <sup>e</sup>	0.961
	Scarring <sup>f</sup>	1.00
Falciform process of STL <sup>g</sup>	1.00	
Mass lesion <sup>h</sup>	1.00	

<sup>a</sup>Thickness (mm\*) in AP dimensions of the Sacrotuberous ligament at entrance of Alcock's canal (PDWI)  
<sup>b</sup>Maximal thickness of the neurovascular bundle (NVB) within Alcock's canal on T2WI  
<sup>c</sup>Maximal thickness of the Obturator Internus muscle on Axial T1 or PDWI (mm\*)  
<sup>d</sup>PN abnormal (visualized, thick and hyperintense) or Normal (not visualized)  
<sup>e</sup>Contact of the Sacrotuberous ligament to the NVB at the entrance of Alcock's canal  
<sup>f</sup>Scarring in the region of Alcock's canal  
<sup>g</sup>Falciform process of STL (visualized discretely = normal) or scarred/thickened (abnormal)  
<sup>h</sup>Presence of mass lesion  
 \* measured to the nearest millimeter

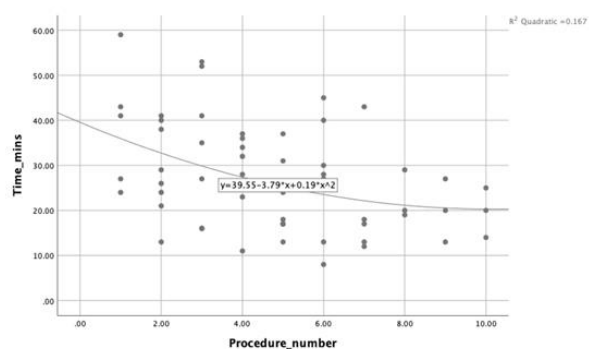
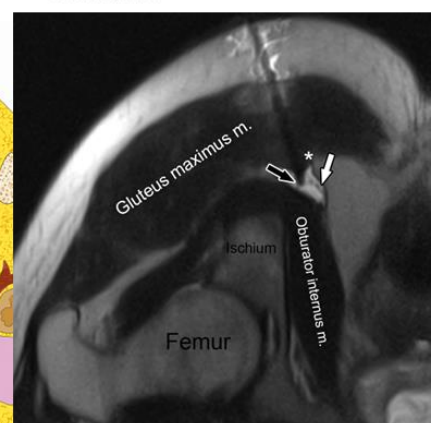
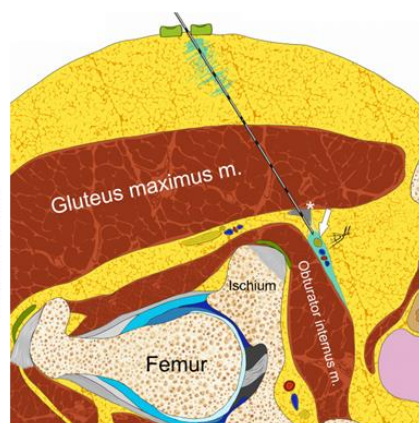


Table 7: Association between the MRN findings and successful diagnostic injection

MRN finding	Beta-coefficient (95% confidence interval)	P value
PN abnormality	6.170 (1.342-28.366)	0.019**
Contact with STL	1.567 (0.587-5.037)	0.368
STL thickness <sup>a</sup>	1.156 (0.820-1.453)	0.213
NVB thickness <sup>b</sup>	1.090 (0.738-1.607)	0.664
scarring	2.471 (0.292-20.908)	0.407
Falciform process of STL	1.479 (0.164-13.387)	0.728
Mass lesion	Not converged***	Not converged***
Obturator internus thickness <sup>c</sup>	0.994 (0.885-1.122)	0.918

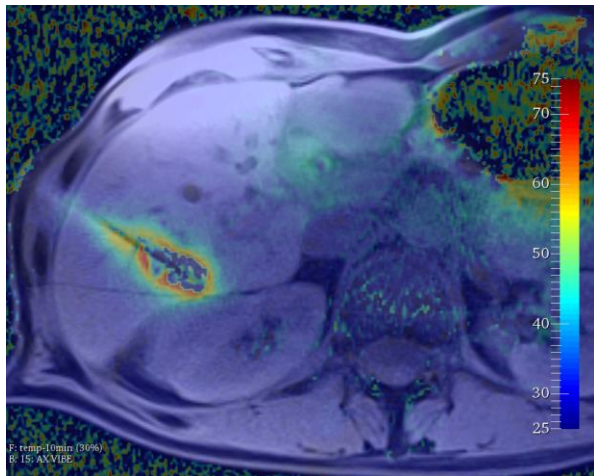


## Percutaneous Ablations Using High Field Strength MRI: 12 Year Experience

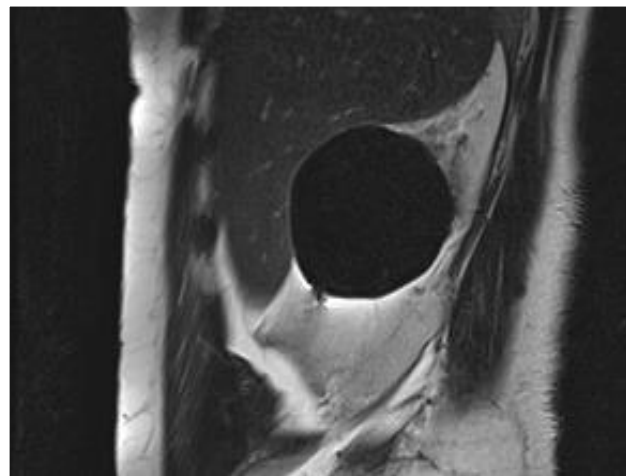
Kemal Tuncali, M.D.  
Assistant Professor of Radiology  
Harvard Medical School  
Clinical Director, Interventional MRI  
Department of Radiology  
Brigham and Women's Hospital  
75 Francis St  
Boston, Massachusetts 02115  
Email: ktuncali@bwh.harvard.edu

The primary purpose of MR imaging to guide percutaneous procedures is to take advantage of superior tissue definition, imaging speed, and ablation monitoring/control. This is best achieved with higher field strength magnets and has become possible with the introduction of “wide-bore” scanners.

Since 2010, we have performed 771 percutaneous tumor ablation procedures in a 3T wide-bore MRI (Siemens Verio, Erlangen, Germany) including 693 cryoablations and 78 microwave ablations in the kidney (n=422), liver (n=143), prostate (n=51), adrenal (n=19), and other sites including bone/soft tissue (n=136). Most used MRI coils were spine coil elements combined with body matrix coil or loop coil. Most used pulse sequences were half-Fourier T2WI (HASTE), spoiled gradient echo T1WI (VIBE) and less commonly T1 or T2WI (TSE). High-quality cutting-edge MR imaging during percutaneous ablations has led to research activities in computerized monitoring methods [1], MRI compatible needle guidance devices [2], and MR thermometry for cryoablation [3] and microwave ablation.



MRI-monitored microwave ablation of liver tumor.



MRI-monitored cryoablation of kidney tumor.

### References:

1. Scalera J, Liu X, Zientara GP, Tuncali K. From Subjective to Objective: Quantitative Computerized Monitoring Tool for MRI-guided Cryoablation. CLIP 2015, LNCS 9401, pp 88-95, Springer International Publishing 2016
2. Hata N, Ninni B, King F, Kato T, Tokuda J, Tuncali K. Early clinical feasibility study of body mounted and motorized needle guidance tool in abdominal MRI-guided cryoablation. ISMRM, Paris, 2018.
3. Tokuda J, Tuncali K, Seethamraju RT, Tempny CM, Schmidt EJ. Monitoring Cryoablation using Short Inversion Recovery Ultrashort Echo Time (STIR-UTE) MRI. ISMRM, Honolulu, 2017

## MRI-guided radiofrequency ablation of small HCC nodules ( $d \leq 12$ mm) in pretreated livers – use of the gadoxetic-acid plateau phase

Ebel S<sup>1</sup>, Meyer HJ<sup>1</sup>, Prasse G<sup>1</sup>, Seehofer D<sup>2</sup>, Berg T<sup>3</sup>, Busse H<sup>1</sup>, Hofmann A<sup>1</sup>, Gößmann H<sup>1</sup>, Denecke T<sup>1</sup>

<sup>1</sup> Department of Diagnostic and Interventional Radiology, University Hospital Leipzig, Germany

<sup>2</sup> Department of Hepatobiliary Surgery and Visceral Transplantation, University Hospital Leipzig, Germany

<sup>3</sup> Department of Gastroenterology, Hepatology, Infectiology and Pneumology, University Hospital Leipzig, Germany

**Background** MRI enables an outstanding tissue characterization and is therefore commonly used for percutaneous radiofrequency ablation (RFA). In cirrhotic livers, with numerous defects from prior surgery or ablation, however, reliable visualization and exact localization of small (lesion diameter  $d \leq 12$  mm) hepatocellular carcinoma (HCC) can be challenging without adequate contrast enhancement.

**Purpose** To investigate the feasibility, technical success and safety of using the gadoxetic acid plateau for tumor visualization during percutaneous MRI-guided RFA of small ( $d \leq 12$  mm) HCC nodules.

**Methods** This is a retrospective case study of 52 patients (17 female),  $64.2 \pm 16.9$  years old (mean  $\pm$  SD), with small HCC ( $d \leq 12$  mm) nodules that were not visible in non-contrast MR images. The decision for an RFA treatment of the patients had been made by an interdisciplinary tumor board. RF ablation was carried out in a 1.5-T MRI (Magnetom Aera, Siemens Healthcare, Erlangen, Germany).

Feasibility was assessed by analyzing proper identification of the target tumor, tumor delineation during MRI-guided needle positioning and number of needle adjustments required for accurate placement. Technical success was defined as complete ablation with a safety margin of 5 mm. Safety was assessed from reports of procedure-related complications.

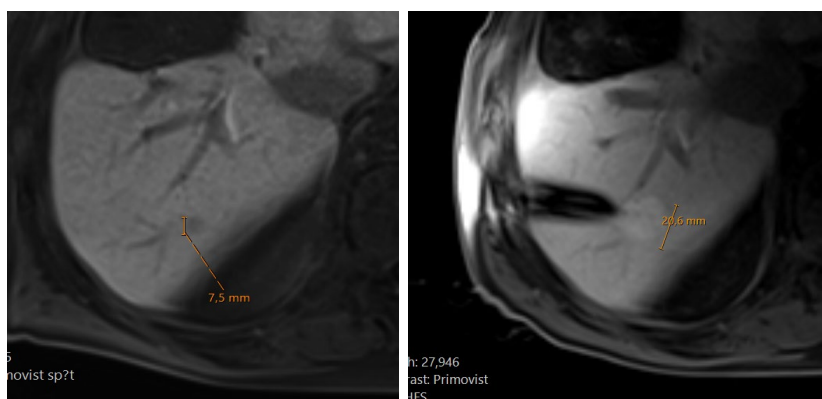


**Fig. 1.** Sample case with contrast-enhanced (gadoxetic acid) transverse T1-weighted MR images before (left) and after (right) RF ablation. Original diameter of this small (round) HCC nodule was 7.5 mm. Post-ablation image confirms successful ablation with a safety margin of 5 mm (resulting diameter here: 20.6 mm).

**Results** In all 52 cases, target tumors were not visible in non-contrast MR images but in the late post-contrast phase (gadoxetic acid). In 5 cases, planning imaging showed new lesions, which were either treated in the same session ( $n=4$ ) or altered the therapeutic approach ( $n=1$ ) because of an extrahepatic tumor seeding. Mean ( $\pm$  SD) tumor diameter was  $9.3 (\pm 1.8)$  mm and the number of needle adjustments was  $4 (\pm 3)$ . Post-ablation imaging showed a technical success rate of 100% (51 cases, 56 tumors), a sample case is shown in Figure 1.

No major complications occurred. Follow-up imaging (after  $12.4 \pm 9.3$  months) showed no local tumor progression or recurrence. In 14 patients (27.5%), new HCC nodules were identified distant to the respective ablation areas.

**Conclusions** Use of the gadoxetic-acid plateau phase for MRI-guided ablation of otherwise MR-occult lesions is a feasible approach for an effective and safe treatment of small HCC nodules.

# MR-guided robotic interventions - pathway to autonomous and AI-assisted approach

Nobuhiko Hata, PhD

*National Center for Image Guided Therapy, Brigham and Women's Hospital and Harvard Medical School,  
Boston, MA, USA*

*hata@bwh.harvard.edu*

---

*Keywords:* Robotics, Autonomy, AI, Physician Assistance Technology

---

The MRI-guided intervention has evolved to embrace robot as an enabling tool for percutaneous therapies. Researchers have proposed motorized needle alignment tools for pelvic, abdominal, and neuro intervention and presented their benefits in precision needle alignments in clinical MRI-guided interventions. The role of robots in MRI-guided intervention has been limited to needle alignment; interventionists still conduct the needle placements (insertion). In bench-top studies, however, researchers have shown proofs-of-concept to partially automate the needle insertion to assist physicians in addressing needle deflections. Therefore, this presentation aims to review the automation of robotic needle insertion in MRI-guided interventions, accelerated partly by the increasing use of Artificial Intelligence (AI). We will review how AI replaces explicit biomechanical modeling to predict and cancel needle deflections. Then, we will review the AI-driven online real-time identification of tissues, lesions, and tools in intra-operative MRI, which are quickly replacing traditional segmentation-based approaches. An ultimate goal of the talk is to propose an integrated system that collectively uses an AI-based needle deflection-compensation modeler, AI-based object recognition tools, and a motorized needle pushing and steering. For the first time, such an integrated system will enable a cooperatively controlled, hands-on robotic needle placement manipulator to achieve high-precision needle placement - a much-discussed concept in the recent editorial article in Science Robotics as Level 1 automation (Yang et al., 2018).

## Demonstration of versatile anatomically designed instrument alignment units for the remote operated $\mu$ RIGS instrument micropositioning system

Robert Odenbach<sup>1</sup>, Ivan Fomin<sup>1</sup>, Niklas Thoma<sup>1</sup>, Bennet Hensen<sup>2</sup>, Frank Wacker<sup>2</sup>, Georg Rose<sup>1</sup>  
<sup>1</sup>Otto-von-Guericke University Magdeburg, Germany, <sup>2</sup>Hannover Medical School, Germany

**Purpose:** Arranging an optimal placement and fixation of instrument support- and alignment-tools on patients is often not trivial. Depending on the required precision, criticality and anatomic location for the intended procedure, different mechanical techniques are used in commercially available products and research demonstrators. These are ranging from small footprint devices that can be stucked at the patient's skin, up to highly complex stereotactic frames that are screwed directly onto the patient's skull.

In terms of iMRI, instrument fixation on the interventional location can be even more challenging due to spatial limitations inside the narrow tunnel and the additional need for the placement of RF-coils in close vicinity to the interventional area. Therefore, most MR-guided interventions are performed free hand and under significant physical and mental handicaps for the interventionists [1]. Our  $\mu$ RIGS-instrument-micropositioning-demonstrator has proven great potential for remotely operated and universally realizable iMRI-procedures [2]. To provide an optimal instrument fixation on differently shaped anatomic contours of the patient, we demonstrate three differently designed instrument alignment base modules (IABM) to be equipped with the specific instrument positioning unit (IPU) of the  $\mu$ RIGS-system.

**Material and Methods:** The three IABMs for the  $\mu$ RIGS-instrument-positioning-unit (IPU) were designed as planar, cylindrical and spherical two degree of freedom and remotely controllable manipulation modules. The IABM-demonstrators were fully fabricated out of non-metallic material and controlled with the  $\mu$ RIGS' motor unit [2]. For realistic testing, the IABMs were placed on several anatomic locations of a proband (male, 29 yrs.) inside the tunnel of our 3T MRI-system (Magnetom Skyra, Siemens Healthineers), see Fig. 1.



**Fig. 1:** Comparison of the differently configured IPUs installed on a planar- (left), spherical- (center) and cylindrical-IABM (right) in the according test scenario inside the MRI-tunnel: Left: Simulation of spine intervention; Center: Sim. of a shoulder-joint intervention; Right: Sim. of an elbow-joint intervention.

**Results:** The differently shaped demonstrators of the IABMs could be attached on the proband's anatomy relatively fast, reliably and precisely using hook-and-loop tapes. The test has proven full technical remote operation of the IABMs kinematics through the motor unit placed in far distance to the tunnel. Every IABM offered a minimum of a 20 mm long lateral or radial displacement of the IPU relative to the coordinate origin.

**Conclusion:** In this work, we have proven the feasibility for placement of the  $\mu$ RIGS-system even on highly challenging anatomical regions, such as joints and extremities. The three basic designs of the IABMs (planar, cylindrical and spherical) satisfy most of the iMRI-instrument-placement-needs as the instrument can be laterally adjusted always remaining in close distance to the puncture point. The installation of the IABMs was short in time and sturdy. In future research, we will test the versatile  $\mu$ RIGS-IABMs in clinical iMRI trials.

**Funding:** The work of this paper is funded by the Federal Ministry of Education and Research within the Research Campus *STIMULATE* under the numbers '13GW0473A' and '13GW0473B'

**References:** [1] Sánchez López, J S; Odenbach, R: Flexible and low-cost instrument holding concept for interventional MRI [2] Fomin, I; Odenbach, R; Pannicke, E; Hensen, B.; Wacker, F.; Rose, G.:  $\mu$ RIGS - ultra-light micropositioning robotics for universal MRI guided interventions; in Current directions in biomedical engineering - Berlin: De Gruyter, Vol. 7 (2021)

## MRI-Compatible Low Profile Robots for In-Bore Interventions

K Cleary<sup>1</sup>, K Sharma<sup>1</sup>, E Fischer<sup>1</sup>, C Dumoulin<sup>2</sup>, G Li<sup>1</sup>, J Fritz<sup>3</sup>, A Gunderman<sup>4</sup>, Y Chen<sup>4</sup>, R Monfaredi<sup>1</sup>, D Stoianovici<sup>5</sup>, I Iordachita<sup>5</sup>

<sup>1</sup>Children's National Health System, Washington, DC, USA

<sup>2</sup>Cincinnati Children's Hospital Medical Center, Cincinnati, OH, USA

<sup>3</sup>NYU Langone, NYC, USA

<sup>4</sup>Georgia Institute of Technology, Atlanta, GA, USA

<sup>5</sup>Johns Hopkins University, Baltimore, MD, USA

**Abstract.** Our research team is developing several low profile MRI-compatible robots for minimally invasive interventions. The first robot is a four degree of freedom (DOF) system called ArthroBot for shoulder arthrography in pediatric patients. The second robot is a six-degree of freedom system called PainReliefBot for perineural injections used to treat pain in adult and pediatric patients. The third robot is a two DOF system intended to be used with an MRI compatible drill for long bone biopsy. The fourth robot is a concentric tube system for intracerebral hemorrhage evacuation under MRI. In this abstract we focus on the PainReliefBot system, but in the talk, we will discuss all four systems.

**Purpose.** Chronic pain management is an important clinical problem in both adult and pediatric patients. MRI-guided interventions for pain management have benefits such as exquisite image quality and visualization of peripheral nerves and surrounding tissue as well as elimination of radiation exposure for both the patient and clinical staff, which is particularly important in the pediatric environment.

**Materials and Methods.** The proposed workflow consists of several steps including patient positioning, securing the robot, MRI imaging, registration of robot and MRI coordinate systems, path planning, and robotic guidance to the target.

**Results.** A cadaver study was completed as shown in Figure 1. We were able to successfully target both facet (Figure 2) and epidural joints.

**Conclusions.** We have developed a modular robotic system for precise injection of nerve roots under MRI imaging. We have submitted an investigational device exemption (IDE) application to the FDA for a clinical trial at our pediatric hospital using the robotic system.

**Acknowledgements.** This work was partially supported by the National Institutes of Health (NIH) under Grants R01EB025179, R01CA172244, R01NS116148, and R01 EB020003.

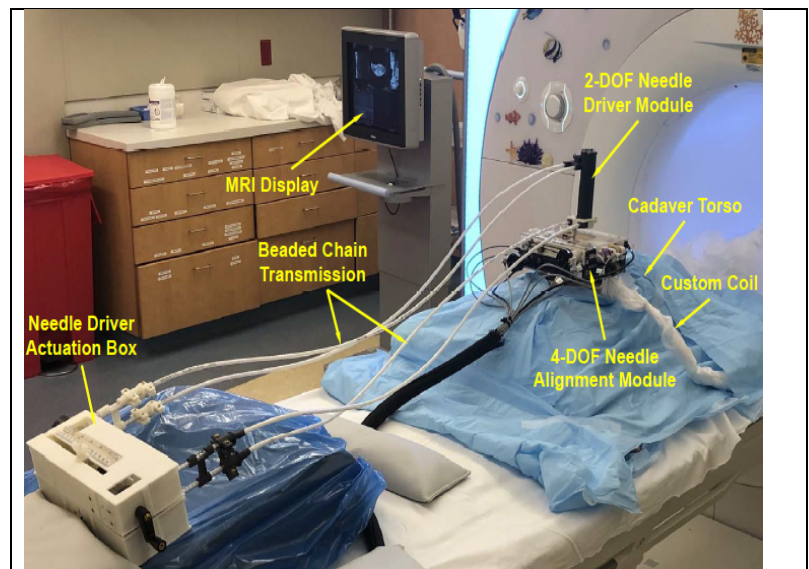


Figure 1: cadaver study with PainReliefBot for back pain

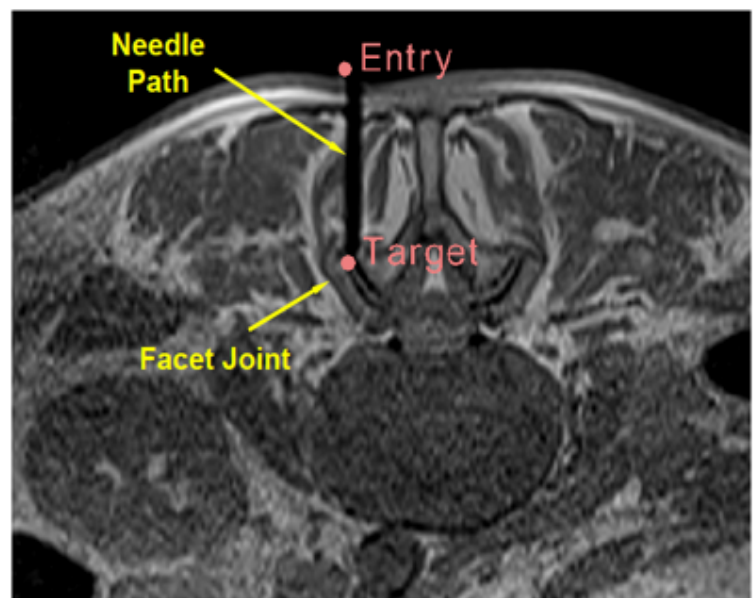


Figure 2: needle placed in facet joint

# A piezo-driven MR-compatible Assistance System for Image-guided Interventions (eGantryMate)

Andreas Reichert<sup>1</sup>, Ali Caglar Özen<sup>1</sup>, Simon Reiss<sup>1</sup>, Thomas Lottner<sup>1</sup>, Niklas Verloh<sup>2</sup>, Srdjan Milosavljevic<sup>3</sup>, Michael Voegelé<sup>3</sup>, Michael Bock<sup>1</sup>

<sup>1</sup>Dept. of Radiology – Medical Physics, & <sup>2</sup>Dept. of Radiology, University Medical Center Freiburg, Freiburg, Germany

<sup>3</sup>Interventional Systems GmbH, Kitzbühel, Austria

**Purpose:** MR-guided interventions benefit from assistance during instrument positioning. The closed bore magnet design, however, limits the available space for devices and the magnetic field impedes the usage of conventional actuators. Here, we present the extension of a small patient-mounted assistance system with piezo motors for in-bore instrument manipulation. The system is combined with a sequence for real-time instrument tracking and the accuracy of needle insertions is evaluated in a phantom.

**Material and Methods:** The assistance system (prototype, Interventional Systems GmbH, Kitzbühel, Austria) is based on a previously described design [1]. It comprises a base plate and two movable plates with a distal instrument holder (Fig. 1, left). In the extended design, each plate can be individually moved in two translational degrees of freedom (forward-backward – FB, left-right – LR) with linear piezo motors (Piezo LEGS, PiezoMotor, Sweden) via a battery-driven controller. Movements of the upper plate in FB/LR direction relative to the lower plate translate to rotations of the distal instrument holder with approx.  $\pm 30^\circ$ . The entire device is shielded and the 5m-long cable between the controller and the motor unit is equipped with floating resonant RF traps (BALUNs) at every 80cm and a low pass suppression filter. For device detection, a contrast agent filled end-effector is used which can be automatically tracked and followed with a phase-only cross correlation (POCC) sequence (Fig. 2) [2–6]. All experiments were performed in a 1.5T whole body system (Aera, Siemens Healthineers) using the system’s bottom part of a head coil for signal reception. First, GRE images without and with the moving device were acquired to check for possible signal interferences.

Then the assistance system was fixed to a flexible holding arm and needle insertion experiments were performed in a gelatin phantom with embedded fiducial targets (target number: 11, mean diameter: 7.6 mm). For each target, real-time navigation was used with the POCC sequence (TR/TE = 3.4/1.5 ms, BW = 898 Hz/px,  $SL_{bSSFP} = 4.5$  mm,  $SL_{FLASH} = 10$  mm, FOV = 243×300 mm, matrix = 192×156,  $TA_{Cycle} = 1.4$  s) until the projected needle pathway was aligned with the target center. Afterwards, the needle (16G, Somatex GmbH, Teltow) was inserted through a dedicated needle channel under online monitoring with the POCC sequence. The lateral distance of the needle pathway to the geometric center of each target was evaluated in a 3D GRE data set (0.5mm<sup>3</sup>).

**Results & Discussion:** No signal interferences could be observed during device operation. In the targeting experiments, all targets were successfully punctured in a mean total procedure time (duration for instrument positioning and needle insertion) of 4.2 minutes. A mean lateral distance of the insertion point to the target centers of  $1.3 \pm 0.8$  mm was found which is comparable to previous studies with the unmotorized version of the assistance system [1]. Handling of the device was very intuitive and no special training was required. Future work will focus on the application in more realistic clinical scenarios. With its flexible design, the device is not limited to percutaneous interventions but could be equipped, e.g. with an ultrasound applicator. Based on this preliminary work, the system demonstrates its potential as an accurate and versatile tool for MR-guided interventions.

## References:

[1] Reichert A, et al. Tomography 2019;5:266–73. [2] Reichert A, et al. Proc Intl Soc Mag Reson Med, 2022. [3] Reichert A, et al. Magn Reson Med 2021;85:1039–46. [4] Reichert A et al. Magn Reson Mater Phys Biol Med 2018;31:781–8. [5] Krafft AJ, et al. Phys Med 2013;29:607–14. [6] de Oliveira A, et al. Magn Reson Med 2008;59:1043–50.

## Acknowledgements:

Parts of this work were supported by a grant from the German Federal Ministry for Economic Affairs and Energy (BMWi) under the grant program “Zentrales Innovationsprogramm Mittelstand (ZIM),” grant number ZF4535603BA9, as part of the IraSME funding “E-GantryMate.”



**Fig. 1:** (Left) Assistance System & Controller (Right) Experimental Setup

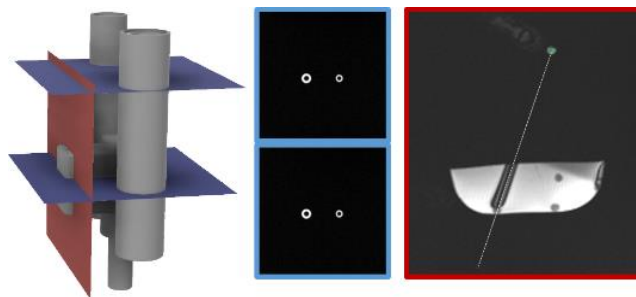


**Fig. 2:** POCC sequence: (Left) Position of FLASH tracking (blue) and bSSFP targeting images (red). (Center) Targeting images. (Right) Targeting image with overlay.

## MRI for Guided Right and Left Heart Cardiac Catheterization: A Prospective Study in Congenital Heart Disease

Mari Nieves Velasco Forte, MRCPH,<sup>1,2,3\*</sup> Sébastien Roujol, PhD,<sup>1</sup> Bram Ruijsink, PhD,<sup>1,2</sup> Israel Valverde, MD,<sup>1,2,3</sup> Phuoc Duong, MRCPH,<sup>1,2</sup> Nick Byrne, MSc,<sup>1,4</sup> Sascha Krueger, PhD,<sup>5</sup> Steffen Weiss, PhD,<sup>5</sup> Yousef Arar, MD,<sup>6</sup> Surendranath R. Veeram Reddy, MD,<sup>6</sup> Tobias Schaeffter, PhD,<sup>1</sup> Tarique Hussain, PhD,<sup>1,6</sup> Reza Razavi, MD,<sup>1,2</sup> and Kuberan Pushparajah, MD<sup>1,2</sup>

From the <sup>1</sup>School of Biomedical Engineering and Imaging Sciences, King's College London, London, UK; <sup>2</sup> Department of Congenital Heart Disease, Evelina London Children's Hospital, Guy's and St Thomas' NHS Foundation Trust, London, UK; <sup>3</sup> Cardiovascular Pathology Unit, Institute of Biomedicine of Seville, IBIS, Virgen del Rocio University Hospital/CSIC/University of Seville, Seville, Spain; <sup>4</sup> Department of Medical Physics, Guy's and St. Thomas' NHS Foundation Trust, London, UK; <sup>5</sup>Philips Research Europe, Hamburg, Germany; and <sup>6</sup>Department of Pediatrics, UT Southwestern Medical Center, Dallas, Texas, USA

**Background:** Improvements in outcomes for patients with congenital heart disease (CHD) have increased the need for diagnostic and interventional procedures. Cumulative radiation risk is a growing concern. MRI-guided interventions are a promising ionizing radiation-free, alternative approach.

**Purpose:** To assess the feasibility of MRI-guided catheterization in young patients with CHD using advanced visualization passive tracking techniques. Study Type: Prospective.

**Population:** A total of 30 patients with CHD referred for MRI-guided catheterization and pulmonary vascular resistance analysis (median age/weight: 4 years / 15 kg).

**Field Strength/Sequence:** 1.5T; partially saturated (pSAT) real-time single-shot balanced steady-state free-precession (bSSFP) sequence.

**Assessment:** Images were visualized by a single viewer on the scanner console (interactive mode) or using a commercially available advanced visualization platform (iSuite, Philips). Image quality for anatomy and catheter visualization was evaluated by three cardiologists with >5 years' experience in MRI-catheterization using a 1–5 scale (1, poor, 5, excellent). Catheter balloon signal-to-noise ratio (SNR), blood and myocardium SNR, catheter balloon/blood contrast-to-noise ratio (CNR), balloon/myocardium CNR, and blood/myocardium CNR were measured. Procedure findings, feasibility, and adverse events were recorded. A fraction of time in which the catheter was visible was compared between iSuite and the interactive mode.

**Statistical Tests:** T-test for numerical variables. Wilcoxon signed rank test for categorical variables.

**Results:** Nine patients had right heart catheterization, 11 had both left and right heart catheterization, and 10 had single ventricle circulation. Nine patients underwent solely MRI-guided catheterization. The mean score for anatomical visualization and contrast between balloon tip and soft tissue was 3.9 ± 0.9 and 4.5 ± 0.7, respectively. iSuite provided a significant improvement in the time during which the balloon was visible in relation to interactive imaging mode (66 ± 17% vs. 46 ± 14%, P < 0.05).



## Tissue characterization of the acute ablation lesion directly after CMR-guided atrial flutter ablation.

**Authors:** G.P. Bijvoet<sup>1,2</sup>, H.M.J.M. Nies<sup>1,2</sup>, R.J. Holtackers<sup>1,2</sup>, V.M. Smit-Fun<sup>1</sup>, J. Smink<sup>3</sup>, D. Linz<sup>1,2</sup>, K. Vernooy<sup>1,2</sup>, J.E. Wildberger<sup>1,2</sup>, R. Nijvelde<sup>4</sup>, S.M. Chaldoupi<sup>1,2</sup> and C. Mihal<sup>1,2</sup>.

**Affiliations:** <sup>1</sup> Maastricht University Medical Center, Maastricht, the Netherlands. <sup>2</sup> Cardiovascular Research Institute Maastricht (CARIM), Maastricht University, Maastricht, the Netherlands. <sup>3</sup> Philips Healthcare, Best, the Netherlands. <sup>4</sup> Radboud University Medical Center, Nijmegen, the Netherlands.

**PURPOSE:** To investigate tissue characteristics of acute ablation lesions directly after cardiac magnetic resonance (CMR)-guided atrial flutter ablation.

**BACKGROUND:** CMR-guided ablation is a novel technique for atrial flutter treatment. Besides a safe and feasible method for ablation, CMR is potentially able to investigate tissue changes caused by the ablation procedure.

**MATERIAL AND METHODS:** Eight patients with a typical isthmus-dependent atrial flutter were prospectively enrolled, and treated with CMR-guided ablation. All patients underwent a successful cavo-tricuspid isthmus ablation with bidirectional block. Pre-ablation and postablation imaging was performed with T2-weighted imaging (T2W, edema, n=8), first-pass perfusion imaging (atrial perfusion, n=5) and late gadolinium enhancement (LGE, n=5).

**RESULTS:** Acute post-ablation imaging showed edema, perfusion defect and necrosis in the ablation region in all patients (table 1). T2W imaging also suggested increased wall thickness. The LGE images demonstrated ablation necrosis with a central area of sparse contrast uptake, consistent with previously reported areas of microvascular damage and hemorrhage (Figure 1). Perfusion defects were present in all assessed patients and appeared larger than the region of LGE, suggesting a border zone of tissue alteration beyond the necrotic area.

**CONCLUSION:** CMR guided ablation offers the unique opportunity of therapy guidance and direct therapy evaluation. Imaging characteristics of acute ablation lesions directly after CMR-guided atrial flutter ablation suggest edema and perfusion defects, as well as necrosis and a core of microvascular damage of ablation areas.

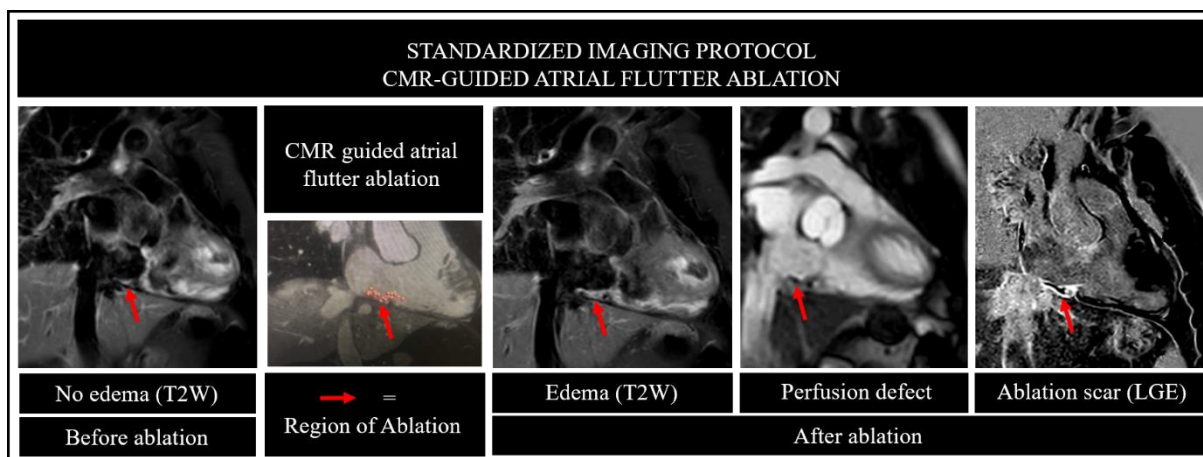


**Figure 1:** Imaging performed before, during and directly after CMR-guided atrial flutter ablation.

Imaging characteristics of acute ablation lesion	
Visual presence of edema (T2W)	8/8
Pre-ablation ratio T2W signal intensity CTI vs ref. muscle	1.7 ± 0.3 [1.3 - 2.0]*
Postablation ratio T2W signal intensity CTI vs ref. muscle	3.4 ± 0.5 [2.9 - 4.4]*
Increase ratio T2W signal intensity (%)	206 ± 11% [186-222]
Increase wall thickness (%)	205 ± 44% [140-300]
Perfusion defect (first-pass perfusion)	5/5
Ablation necrosis (LGE)	5/5
Central sparsity of contrast uptake (LGE)	5/5
CTI = cavo-tricuspid isthmus, n = number of subjects, T2W = T2 weighted image, LGE = late gadolinium enhancement, * ratio >2.0 indicates edema	

**Table 1:** Imaging characteristics of acute ablation lesion

C. M. Reich<sup>1</sup>, D. Gholami Bajestani<sup>1</sup>, C. Mulik<sup>1</sup>, G. Schäfers<sup>2</sup>, V. Hammersen<sup>2</sup>, S. Schauer<sup>3</sup>, M. Schmid<sup>3</sup>, K. Höger<sup>4</sup>, A. Hegel<sup>4</sup>, E. Pruy<sup>5</sup>, M. Steinmetz<sup>6,7</sup>, L. Landgraf<sup>1</sup>, T. Jochimsen<sup>8</sup>, O. Sabri<sup>8</sup>, A. Melzer<sup>1</sup>;

## **Towards MRI-guided cardiovascular interventions and focused ultrasound neuromodulation**

1 Innovation Center Computer Assisted Surgery (ICCAS), Leipzig University, Leipzig, Germany

2 MRI-STaR GmbH, Gelsenkirchen, Germany

3 EPflex Feinwerktechnik GmbH, Dettingen an der Erms, Germany

4 Admedes GmbH, Pforzheim, Germany

5 Bavaria Medizin Technologie GmbH (BMT), Weßling, Germany

6 Universitätsmedizin Göttingen (UMG), Göttingen, Germany

7 DZHK (German Center for Cardiovascular Research), partner site Göttingen

8 Department of Nuclear Medicine, Leipzig University Hospital (UKL), Germany

### **Background**

The substantive advantages of MR imaging such as the presentation of soft tissue structures and vascular functions, reduced radiation exposure and temperature mapping made it attractive for cardiac interventions, biopsies and cancer treatment in the last decade. Nevertheless, MRI-guidance yet still has not reached the limits of its beneficial possibilities due to a “standoff” between clinicians and manufacturers. Our consortium of researchers, clinicians and OEMs work together in joint R&D projects with the goal to realize MRI-guided interventions. This work aims to describe the necessary steps to accomplish iMRI for endomyocardial biopsy (EMB), vena cava filter (VCF) placement and retrieval, thrombectomy, stenting, angioplasty, and focused ultrasound (FUS) neuromodulation.

### **Discussion**

First and foremost, established devices and workflows have to be adapted to the MR environment. For the instruments, this means reducing electrically conductive, metallic, and magnetic materials to the absolute necessary, often resulting in an overall design adaption. Composite materials with iron oxide MRI markers and selfexpanding nitinol structures are the protagonists to develop MRI compatible medical catheter-delivered devices (EPflex, BMT, Admedes). To ensure MR Safety in the iterative development process, the behaviour of digital models are simulated (MRI-STaR) and samples are tested constantly in the MRI (UKL). In a further state, the applicability is tested with clinicians on specific patient models under MRI-guidance (UMG). Concurrently, a technical setup to convert a diagnostic MRI unit temporarily into an interventional real-time MRI suite (UKL) with easy-to-use devices is tested thoroughly. To ensure a smooth operation in the MR environment adapted workflows of the procedures with emphasis on patient safety are elaborated. Preclinical verification of the functionality of the devices and procedures will be provided in animal trials (UMG, UKL, Heart Center Leipzig).

### **Conclusion**

MRI-visibility of prototypes of catheter-based interventional devices was successfully proven. The applicability of the devices in combination with a technical iMRI setup and clinical workflow could be demonstrated in several in-vitro experiments. The overall feasibility to conduct catheter-based interventions on standard MRI systems opens the way to broaden the spectrum of the utilisation of a conventional MRI system for interventional purposes. The upcoming project 3MP-FUS addresses development and testing of a multi-modal multi-parameter platform-independent focused ultrasound system for neuromodulation (Fraunhofer IBMT, Max Planck Institute CBS, MRI-STaR, and Localite). The goal is a flexible and cost-efficient system integration to enable MRI-guided neuromodulation with FUS.

### **Funding for this study**

German Federal Ministry of Education and Research: „KMU-innovativ: Medizintechnik“, contract numbers 13GW0242B, 13GW0288D; "Bildgeführte Diagnostik und Therapie – Neue Wege in der Intervention" 13GW0365C; initiative project 13GW0619

# Deep artifact suppression for in-line real-time reconstruction of accelerated complex MR-Data: Application to interventional cardiac MR-thermometry

Olivier Jaubert<sup>1</sup>, Valéry Ozenne<sup>2</sup>, Maxime Yon<sup>2</sup>, Javier Montalt-Tordera<sup>3</sup>, Jennifer Steeden<sup>3</sup>, Vivek Muthurangu<sup>3</sup> and Bruno Quesson<sup>2</sup>.

<sup>1</sup> Department of Computer Science, University College London, London WC1E 6BT, United Kingdom; Centre for Cardiovascular Imaging, Institute of Cardiovascular Science, University College London, London WC1N 1EH, United Kingdom. <sup>2</sup>Univ. Bordeaux, CNRS, CRMSB, UMR 5536, IHU Liryc, F-33000 Bordeaux, France. <sup>3</sup>Centre for Cardiovascular Imaging, Institute of Cardiovascular Science, University College London, London WC1N 1EH, United Kingdom.

**Introduction:** Cardiac MR temperature imaging allows non-invasive monitoring in-vivo, of the cardiac muscle temperature and lesion formation during arrhythmia thermal ablative treatment [1]. Continuous radial golden angle gradient echo (GRE) acquisition combined with intra-scan motion correction [2] could overcome the limitations of Cartesian or EPI sampling acquisition [3,4]. Radial GRE offers high spatial ( $0.86 \times 0.86 \text{mm}^2$ ) resolutions, and is robust to motion and susceptibility artefact. It is also independent of external ECG-gating. However it requires high acceleration rates ( $\times 10$ – $\times 20$ ). Here we propose a low-latency deep artifact suppression algorithm [5] to enable reconstruction of artefact free, high SNR complex images with an acceleration factor of 10. Proposed MR thermometry was compared to the state of art direct temperature estimation algorithm [6] and validated in-line using the Gadgetron framework [7] to achieve a rate of 1 frame per second.

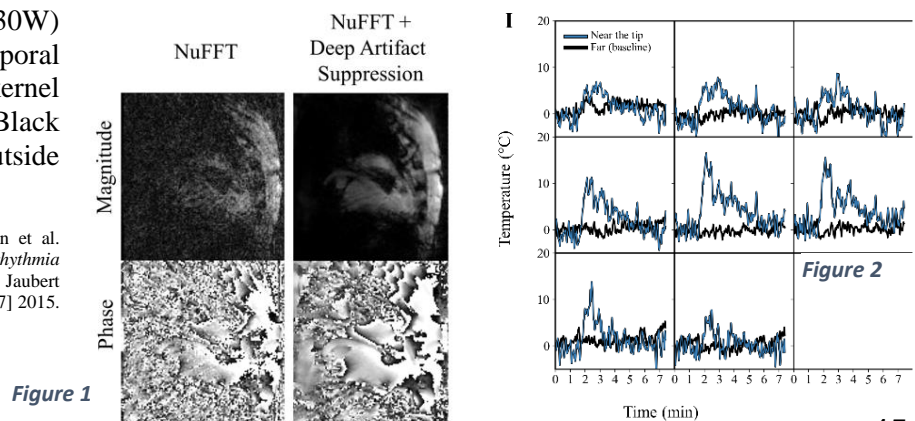
**Methods:** Continuous GRE radial golden angle acquisitions were used to monitor RF ablations in agar-gel phantom and in vivo in a sheep heart (approved by the ethics committee of Bordeaux University). An MR compatible RFA catheter (Vision-MR Ablation Catheter, Imricor, Burnsville) with two embedded micro-coils (proximal and distal) was used to perform the ablation. Catheter navigation was performed through the left ventricle under MRI guidance using active tracking via the prototype Monte Carlo platform (Siemens Healthcare). Acquisition parameters were performed on a 1.5T (Aera, Siemens, Germany): FOV/resolution/slice thickness=  $220 \times 220 \text{mm}^2 / 0.86 \times 0.86 \text{mm}^2 / 3 \text{mm}$ , TR/TE/FA=  $24.14 \text{ms} / 20 \text{ms} / 15^\circ$ . Temperature maps were reconstructed using two methods: (1, gold standard) direct estimation from the undersampled k-space data combined with a hybrid multi-baseline reference-less treatment [6] of the image model correcting for susceptibility induced phase variation due to organ motion. (2, proposed method) NUFFFT followed by fast deep artifact suppression (aka prediction by the trained U-Net on *unseen thermometry data*) and a model based phase subtraction [4]. The temporal resolution was set to 0.97s by using 40 spokes. The U-Net was trained for deep artifact suppression using 320 aortic flow complex datasets [5]. Background phase, noise and simulated sampling were applied to the images to emulate the thermometry data. Training was performed using an average SSIM loss [5], ADAM optimizer, 50 epochs and learning rate of  $5 \text{E}-4$ . A sliding window reconstruction is performed with a step size of 1 and window of 24 frames.

**Results and conclusion:** NUFFFT followed by deep artifact suppression successfully reconstructed thermometry images both in vivo (Fig. 1) and on a phantom from radial GRE data accelerated by a factor of 10. The U-Net learn from aortic flow datasets showing the excellent generalizability of the method to unseen data and prohibiting “fake heating” artefacts which could happen with a network trained with thermometry dataset. *Ex vivo experiment:* an increase of  $\sigma(T)$  (spatial mean  $\pm$  standard deviation over the ROIs) values were observed for the deep artifact suppression reconstruction with a mean value of  $0.9 \pm 0.5$  versus  $0.6 \pm 0.1$  for the Direct Estim method. The resulting temperature evolution curves exhibit a higher SNR for the proposed method compared to the one obtained with Direct Estim and succeed to better depict the temperature evolution is several spatial locations. *In vivo experiment:* the proposed method showed consistent evolution of the tissue temperature near the catheter, with a  $\sigma(T)$  before heating close to  $1^\circ\text{C}$  at the vicinity of the catheter tip. A maximal temperature increase of  $17^\circ\text{C}$  at the contact with the catheter can be observed (Fig. 2). Additionally, the proposed reconstruction is extremely fast (on average 42 ms per frame: 20 ms for NUFFFT and 170 ms for deep artifact suppression) paving the way for real-time application, with low-latency reconstructions in pre-clinical or clinical studies.

**Figure 1** (left panel) GRE-radial golden angle magnitude and phase images reconstructed using NUFFFT (left) and NUFFFT followed by deep artifact suppression (right).

**Figure 2** (right panel) RF POWER (30W) were send at 1min30 for 60s. Temporal evolution of the temperature in a  $3 \times 3$  kernel of voxels near the tip of the catheter. Black line depicts baseline temperature outside heating zone.

**Reference:** [1] Toupin, S. *et al. JCMR* 2017. [2] Yon et al. Scientific Report, 2022. [3] Kolandaivelu, A. *et al. Circ. Arrhythmia Electrophysiol.* 2010. [4] Ozenne, V. *et al. MRM*, 2017. [5] Jaubert O, et al. *MRM*, 2021. [6] Gaur, P. & Grissom, W. *MRM*, [7] 2015. Hansen et al. *MRM*, 2013.



# MR-Guided Coronary Catheterization in a Porcine Model at 3T: Success Rate and Learning Curve

Simon Reiss<sup>1</sup>, Thomas Lottner<sup>1</sup>, Timo Heidt<sup>2</sup>, Ali Özen<sup>1</sup>, Constantin von zur Mühlen<sup>2</sup>, Michael Bock<sup>1</sup>

<sup>1</sup>Dept. Radiology, Medical Physics & <sup>2</sup>Dept. Cardiology and Angiology I, Medical Center Univ. of Freiburg, Faculty of Medicine, Univ. of Freiburg, Germany;

**Introduction:** Due to the small size of the coronary arteries, MR-guided coronary catheterization remains challenging and has so far been limited to animal studies with small numbers of subjects. Here, we describe a procedure for reliable intubation of the left coronary artery (LCA) and assess the success rate and procedure duration based on a study with 24 pigs.

**Methods:** Catheterization of the LCA was performed at a 3 T system (MAGNETOM Prisma, Siemens Healthcare). Each procedure started with the acquisition of conventional localizer sequences followed by a 3D compressed-sensing accelerated whole heart navigator- and ECG-gated prototype FLASH sequence (provided by the system vendor). The 3D dataset was used to specify three planes covering the ostium of the LCA. These planes were used as the reference for real-time guidance of the catheter (Fig. 1). In 22 pigs real-time imaging was done with a interactively controllable FLASH sequence (4.5 frames/second) and the images were displayed by mirroring the host display to an in-room monitor (BOLDScreen 24, Cambridge Research Systems Ltd). In the last two pigs, a prototype interventional navigation software (provided by the system vendor) installed on a separate computer was used to control the imaging acquisition and display the imaging results. The software allowed the interventional cardiologist to interactively start/stop the image acquisition and toggle between the pre-defined imaging planes via a prototype in-room foot switch without the need to communicate to the personnel operating the MRI at the host console. The LCA was intubated with a commercial 6F coronary guiding catheter (Terumo, Terumo Europe E.V.) equipped with a single loop coil for active tip visualization [1-4]. The success of the intubation was verified in real-time by injection of a small dose of diluted gadolinium contrast agent (1:20) which was imaged with an ECG-gated saturation recovery FLASH sequence in short-axis view (Fig. 2).

**Results:** Intubation of the LCA was successful in all 24 pigs (95%-CI of the success rate = [0.86, 1.00]). The average acquisition time of the 3D prototype whole-heart localizer was ( $8.4 \pm 1.8$ ) min. The mean elapsed time of the real-time imaging part of the procedure was ( $3.5 \pm 2.6$ ) min. The mean duration of actual catheter navigation during that time was ( $1.4 \pm 0.5$ ) min, excluding communication, changing of imaging planes, etc. A learning curve is observed over the 24 trials (Fig. 3): using a linear model, the elapsed time decreased by ( $0.16 \pm 0.07$ ) min per trial ( $p = 0.03$ ) and the navigation time decreased by ( $0.03 \pm 0.01$ ) min per trial ( $p = 0.02$ ). The ratio of the navigation time to the elapsed time was ( $55 \pm 23$ ) % and increased by ( $1.1 \pm 0.6$ ) % per trial, however, the increase was non-significant ( $p = 0.1$ ). Using the prototype interventional navigation software, a 100 % time efficiency of the real-time guidance was achieved in one trial.

**Conclusion:** MR-guided catheterization of the LCA at 3T is reliable and fast and may become important for cardiac MRI research and clinical applications. Active device visualization plays a key role for the precise catheter navigation. Dedicated interventional software can help to further reduce the procedure duration by providing direct control over the real-time imaging to the interventionalist.

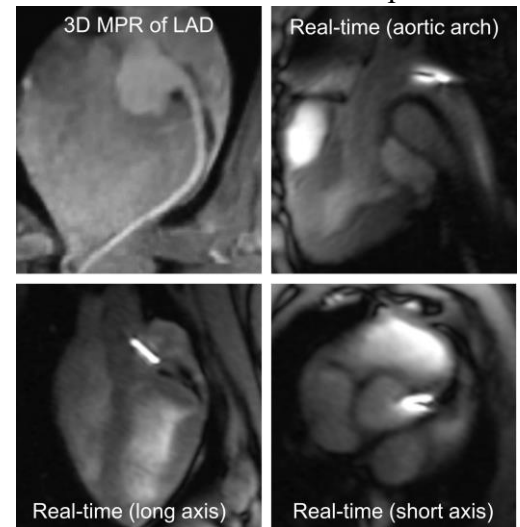


Figure 1: MPR of the LCA from the 3D whole-heart dataset and three real-time images acquired during navigation of the catheter to the LCA

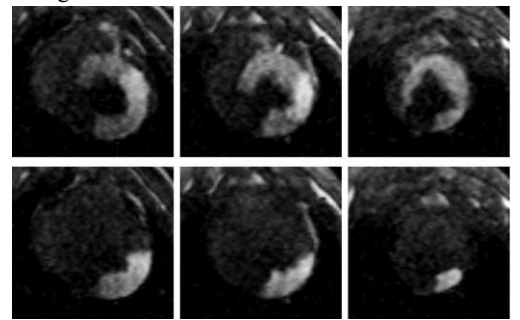


Figure 2: Selective perfusion measurement of the LCA after successful intubation (upper row). By further advancing the catheter the LAD or LCX can be intubated (here, LCX) which is verified by another perfusion measurement (lower row).

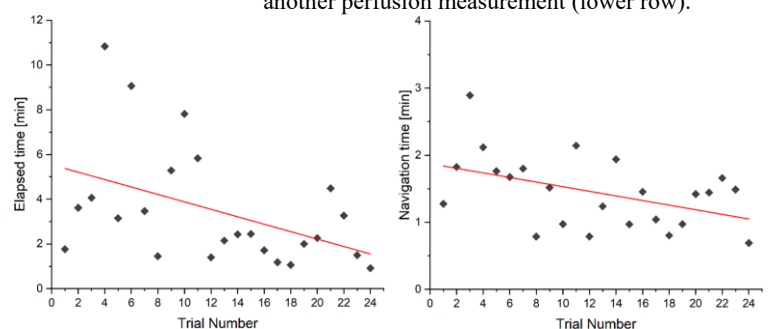


Figure 3: Measured durations of the real-time imaging part of the interventional procedures to intubate the LCA. Left shows the overall elapsed time whereas right shows the time for catheter navigation only.

**Acknowledgements:** Research support by Siemens Healthcare GmbH (Daniel Strohmeier, Axel Krafft) and grant support by the SFB1425, funded by the Deutsche Forschungsgemeinschaft (DFG, German Research Foundation #422681845) is gratefully acknowledged.

**References:** 1. Heidt T, et al. Sci Rep 2019, 2. Heidt T, et al. Eur Heart J. Suppl, 3. Özen AC, et al. IEEE Access 2022, 4. Stephan S, et al. Z Med Phys 2021

## MR-guided treatment of vascular malformations

*Clifford R. Weiss, MD FSIR FCIRSE*

Professor of Radiology, Surgery and Biomedical Engineering

The Johns Hopkins University School of Medicine and Whiting School of Engineering

[cweiss@jhmi.edu](mailto:cweiss@jhmi.edu)

@DrCliffWeiss

Vascular malformations are congenital, non-neoplastic lesions that arise secondary to defects in vasculogenesis. At the most basic level, vascular malformations are divided into high-flow (arteriovenous malformation) and low-flow (venous malformations and lymphatic malformations). Treatment is provided to ameliorate pain, cosmetic disfigurement, and functional impairment. Sclerotherapy, which is typically the first-line therapy for treating low-flow vascular malformations, is an image-guided therapy that involves the injection of a sclerosant directly into the malformation. This induces endothelial damage and necrosis/fibrosis with eventual involution of the malformation. Image-guided thermal therapies, including cryoablation and laser ablation involve freezing or heating of target tissue to induce cell death and necrosis. The choice of imaging modality is especially important both for lesion characterization and for the evaluation of treatment response. Conventionally, magnetic resonance imaging (MRI) is the modality of choice for pre- and post-intervention assessments, while ultrasound, X-ray fluoroscopy and computed tomography (CT) are used for guidance and for intra-procedural monitoring. While ultrasound offers adequate soft tissue resolution and easy real-time imaging with no exposure to ionizing radiation, many lesions cannot be completely visualized due either to “depth” or to overlying anatomy, and ultrasound is only minimally helpful in monitoring therapy due to limited field of view. Fluoroscopy has both poor soft tissue resolution and exposes the patient and operator to significant doses of ionizing radiation. CT offers both excellent soft tissue resolution / contrast and a wide anatomic field of view, however, it often allows lesion targeting by landmarks alone, does not provide real-time imaging and involves a significant amount of radiation exposure to the patient and the operator. To overcome the limitations of US, CT and fluoroscopy, MRI has emerged as an alternative for guiding and monitoring treatment of vascular malformations. MR can provide dynamic, multiplanar imaging that delineates surrounding critical structures such as nerves and vasculature. MR has the potential to replace ultrasound and X-ray fluoroscopy for needle guidance and sclerosant monitoring while reducing ionizing radiation exposure and improving intra-procedural tissue resolution. Multiple studies have demonstrated that MR-guided treatment of vascular malformations is safe and effective. This invited talk will review: 1) the use of MR for the classification and diagnosis of vascular malformations, 2) the current literature surrounding MR-guided treatment of vascular malformations, 3) a series of cases of MR-guided sclerotherapy and thermal ablation for the treatment of vascular malformations.

## **Combined 3D printed and silicone moulded vascular phantoms to develop and train catheter-based MRI-guided interventions**

1 Innovation Center Computer Assisted Surgery, Semmelweisstraße 14, Leipzig, Germany

### **Purpose**

Development of novel catheter-based medical devices for MRI-guided interventions requires testing and training of procedures. This work aims to show the development process of anatomically correct patient data based vascular phantoms for performance of developed MRI-guided interventions utilizing novel MR Compatible devices and a dedicated workflow.

### **Materials and Methods**

Anonymous computed tomography patient data has been segmented using region growing method to create 3D computer models of human aorta and vena cava systems. A corrodible core of the 3D vessel model is manufactured using additive manufacturing. Afterwards the silicone-based vessel phantom is produced in a hybrid negative casting/moulding process. The manufactured vascular structure is embedded in a Perspex housing equipped with connectors, which allow various access points. The performed hybrid moulding process is compared to state of art vessel phantom production processes like silicone moulding (Elastrat Sàrl, Switzerland) or plain stereolithographic 3D printing (Form 3, Formlabs GmbH, Germany) of flexible materials. Additionally a pulsatile flow pump (membrane pump) is connected to the vessel-system to simulate physiological blood flow. Further diverse concepts for simulation of MRI-guided interventions like Endomyocardial Biopsy (EMB), Thrombectomy, Vena Cava Filter and Stent delivery are developed.

### **Results**

It was possible to manufacture a silicone-based phantom simulating aorta and vena cava vasculature. The phantoms are mounted inside tank like housings, allowing the addition of body tissue mimicking water-binding gels like gelatine. On-site tests show promising handling and MRI-visualisation properties. To mimic thrombosis and embolisms, blood clots were used produced by using a Chandler-Loop setup and citrated swine blood.

### **Conclusion**

Patient data based vascular models can be 3D printed and moulded to allow development and training of MR guided interventions under both X-ray and MRI-guidance. The MR imaging shows realistic imaging pathology and the used material is suitable for mimicking haptic feedback comparable to a biological model. Further integration of pathologies like stenosis and thrombosis are developed. Compared to regular state of art vessel phantom production processes the performed hybrid moulding process allows to combine the advantages of flexible materials (material freedom), with patient specific 3D printing approaches. Further, the developed procedure enables to produce models with almost unlimited building space.

# Artifact exploration of metallic and non-metallic guidewires at 0.55T, 1.5T, and 3T MR systems

W. B. Buchenberg<sup>1</sup>, K. Düring<sup>1</sup>, M. Rube<sup>2</sup>, and A. J. Krafft<sup>2</sup>

<sup>1</sup>MaRVis Interventional GmbH, Krün, Germany, <sup>2</sup>Siemens Healthcare GmbH, Erlangen, Germany

**Purpose:** The ability to perform minimally invasive endovascular procedures under MRI-guidance is still limited by the portfolio of available devices. Common X-ray guidewires are made from metallic wires (e.g. nitinol) and thus, are prone to safety issues so that non-metallic products might be required for MR-guided procedures [1,2]. Here, metallic and non-metallic guidewires (doped with iron particles [3,4]) were investigated at magnetic field strengths  $B_0$  of 0.55 T, 1.5 T, and 3T.

**Material and methods:** Three MR safe glass fiber/epoxy guidewires (0.014" micro, 0.035" standard, 0.035" stiff, MaRVis Interventional GmbH, Krün, Germany) and two nitinol guidewires (0.018", 0.035"; Radifocus Glidewire, Terumo, Japan), were positioned into a water box oriented parallel and perpendicular to  $B_0$ , respectively (Fig. 1).

Imaging was performed at 0.55/1.5/3T MR systems (MAGNETOM Free.Max/Sola/Vida, Siemens Healthcare GmbH, Erlangen, Germany) using the following protocols: 2D bSSFP: voxel size =  $2 \times 2 \times 5 \text{ mm}^3$ , FA =  $70^\circ$ , TR/TE/scan time per slice: 4.4ms/2.2ms/390ms (0.55T), 2.9ms/1.5ms/260ms (1.5T), 3.5ms/1.8ms/310ms (3T); 3D bSSFP: voxel size =  $0.8 \times 0.8 \times 1.5 \text{ mm}^3$ , FA =  $70^\circ$ , TR/TE/scan time: 5.9ms/3.0ms/50s (0.55T), 4.1ms/2.0ms/34s (1.5T, 3T); 3D TSE: voxel size =  $0.4 \times 0.4 \times 1.8 \text{ mm}^3$ , FA =  $140^\circ$  (0.55T, 1.5T) /  $100^\circ$  (3T), TR/TE/scan time: 1200ms/196ms/6min.

**Results:** Figures 2a and 2b show 2D and 3D bSSFP-images of the guidewires parallel and perpendicular to  $B_0$  at three different field strengths. The tip of the glass fiber/epoxy guidewires is seen as a more pronounced dipole artifact because of a locally increased iron microparticle concentration (yellow arrows). The continuous iron microparticle doping of the glass fiber/epoxy guidewires causes well-defined signal voids at all field strengths and orientations. As expected, the artifact width depends on the orientation with respect to  $B_0$  [4]. High resolution 3D TSE images even depict separate dipole artifacts along the shaft of the non-metallic wires (Fig. 2c). In contrast, the nitinol guidewires are barely visible at 0.55T even in high resolution images so that additional markers [2] might be required to improve visualization. However, these wires cause increasing image distortion at 1.5T and 3T most likely because of local amplification of the  $B_1$  transmit field.

**Conclusion:** The MR safe glass fiber/epoxy guidewires are well visible across all field strengths and for different contrasts. The metallic guidewires might require modifications to overcome their limited visibility at 0.55T. In further studies, the visibility of the guidewires should be explored in more realistic settings (e.g. guidewire movements).

**Competing interests:** WBB is employee at MaRVis Interventional GmbH. KD is shareholder and CEO of MaRVis Interventional GmbH. MR, and AJK are employees at Siemens Healthcare GmbH.

**References:** [1] Campbell-Washburn, A. E., et al. *Radiology* (2019): 384-393. [2] Basar, B., et al. *Mag. Res. Imaging* 77 (2021): 14-20. [3] Massmann, A., et al. *Radiology* (2017): 541-551. [4] Schleicher, K. E., et al. *Mag. Res. Materials in Physics, Biology and Medicine* (2018): 235-242

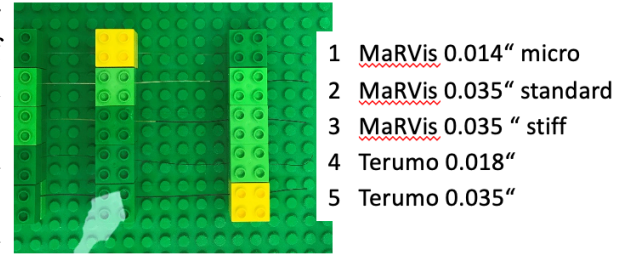
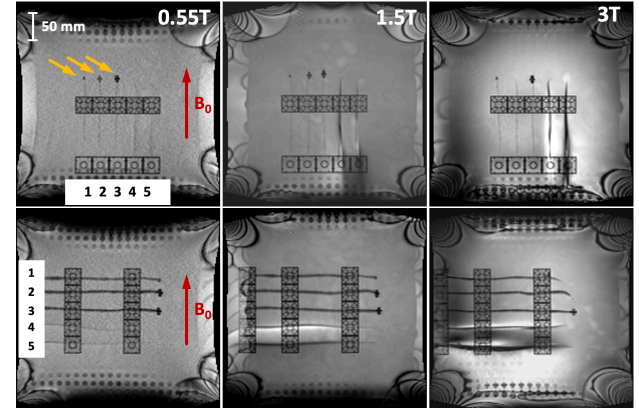
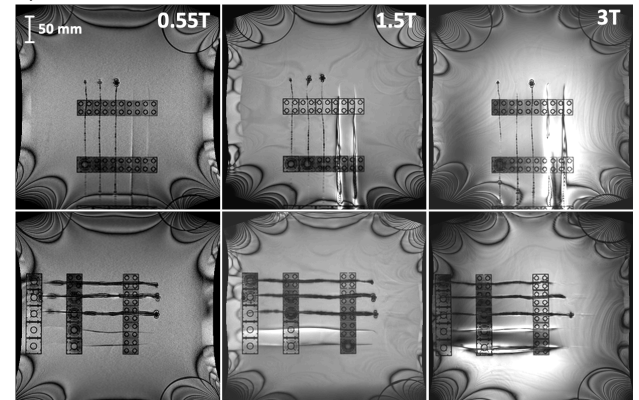


Fig. 1: Experimental setup with view from top.

## a) 2D bSSFP



## b) 3D bSSFP



## c) 3D TSE

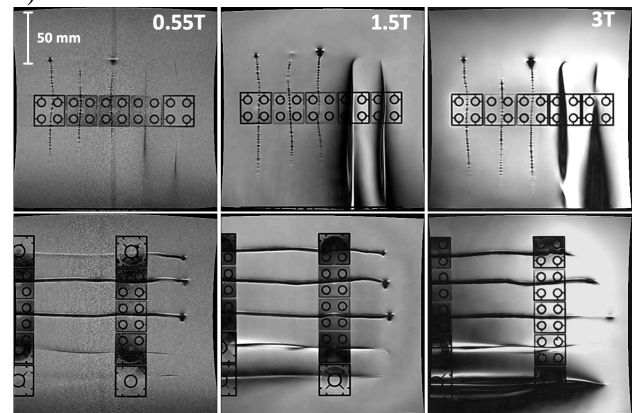


Fig. 2: a) 2D bSSFP images with guidewires oriented parallel (top row) and perpendicular (bottom row) to  $B_0$ . b) 3D bSSFP images. c) 3D TSE images.

## Techniques and devices for interventional MRI guidance

Presenter: Harald Busse

Diagnostic and Interventional Radiology Department, University Hospital Leipzig, Leipzig, Germany

### Objective

This presentation will provide an overview of MRI guidance techniques for different clinical applications, with a focus on needle interventions, and a short update on current research activities and remaining challenges.

### Background

The majority of image-guided interventions rely on ultrasound (US) or X-ray techniques, each with well-known advantages. MRI guidance becomes an option when X-ray exposure is discouraged or whenever intended targets and adjacent structures are poorly or not seen with the above imaging methods. This choice, however, comes with a number of drawbacks, such as safety hazards, need for MR-conditional tools, longer imaging times and limited space inside the bore.

### Methods and Evaluation

Major research efforts have therefore been put into the design of enabling devices and guidance techniques [1,2]. MR-conditional equipment like needles, sampling devices and interstitial applicators as well as MRI coils with space for needle insertion are commercially available, although the choice is limited. Navigation solutions, in particular for the brain, breast and prostate, were among the first systems in clinical use and have since found widespread application.

A critical step for system design is the proper integration into the MRI architecture. In this context, several MRI companies are providing a software platform for real-time scan control and image data access. Device manufacturers will have to meet stricter requirements following a recent update of the EU medical device regulations. In addition to dedicated, typically organ-specific methods, MRI interventions may still be guided iteratively ("in and out"). This approach introduces uncertainty and a delay between tool operation and image confirmation but is applicable in many body regions without the need to set up or configure extra components.

Interventional imaging will continue to benefit from the progress in diagnostic imaging. There will also be an increasing role for machine learning methods in major areas like coil technology, image contrast, acceleration techniques and image reconstruction. MRI companies have already automated parts of the diagnostic workflow (such as tablet-like in-room control panels or patient sensors), which may translate to interventional applications as well. The already wide deployment of robotic technology is also expected to make in-bore procedures more accessible (automation, precision, safety and remote manipulation) [3].

### Conclusion

Advanced guidance techniques are not essential for MRI procedures but often provide the means for refined targeting, better control or extra safety, especially for demanding access paths or less experienced interventionalists. The main challenges of interventional MRI techniques are seen in the seamless integration into a diagnostic MRI environment and proper clinical translation.

### References

- [1] Sedaghat F, Tuncali K. Top Magn Reson Imaging. 2018;27:5-8.
- [2] Busse H, Kahn T, Moche M. Top Magn Reson Imaging. 2018;27:9-18.
- [3] Hata N, Moreira P, Fischer G. Top Magn Reson Imaging. 2018;27:19-23.



# Intensity-Based Tracking Technique to Register Devices in MRI-Guided Procedures

Ivan Fomin<sup>1</sup>, Robert Kowal<sup>1</sup>, Marcel Gutberlet<sup>2</sup>, Bennet Hensen<sup>2</sup>, Frank Wacker<sup>2</sup>, Oliver Speck<sup>1</sup>, Georg Rose<sup>1</sup>  
<sup>1</sup>Otto-von-Guericke-University Magdeburg, Germany, <sup>2</sup>Hannover Medical School, Germany

**Purpose:** Tracking of manipulators, robotic assistance systems, as well as instruments such as biopsy or ablation needles is crucial for precise positioning during magnetic resonance imaging (MRI)-guided procedures, e.g. interventions. Conventionally, the position and orientation of passive markers attached to a tool can be determined through calculation of distances and angles of the respective markers to each other. [1] In this study, a new technique is evaluated to passively track tools through an intensity-based technique using the known sensitivity profile of a surface coil.

**Material and Methods:** To demonstrate the concept,  $\mu$ RIGS [2] is used which is a robotic assistance system to position instruments during minimally-invasive procedures. This device has a spatially fixed position relative to the surface coil that is used for visualization of MR-guided interventions [3]. To realize the tracking capability, a gadolinium (Gd) filled needle marker (NM, 0.5 mM concentration) and an oil reference marker (RM) were attached to the  $\mu$ RIGS instrument feed incl. a single loop coil, always in defined distance to each other as one unit (see Fig. 1a). The setup was placed at two locations on a phantom (Fraunhofer IPA) within a 3 T scanner (MAGNETOM Skyra, Siemens Healthcare GmbH), to evaluate the spatial robustness. Images were acquired by  $T_1$ w-TSE-sequences. For the analysis, the ratio of the NM- and the RM-intensity ( $I_{NM}/I_{RM}$ ) was calculated to extract the position of NM in one degree of freedom as distance  $d$  to the reference (see Fig. 1b).

**Results:** The dependency of intensity-ratios to the relative marker distance at two different locations are depicted in Fig. 1c. The closer NM is fed to the coil, the brighter NM becomes. Thereby, the curves directly follow the typical sensitivity profile of a single loop coil. Relatively,  $e_r$  increases between the two setup locations with the distance  $d$ . Up to  $d = 50$  mm the error remains under 10 %, but rises to almost 670 % at the maximum distance of 107 mm.

**Conclusion:** The presented concept demonstrates that passive MR markers can be spatially tracked using only the intensity variation of the Gd-marker within the known sensitivity profile of a surface coil. The restriction in use is the fixed position of the device to surface coils in space. In future, issues in terms of sequence dependency, coil loading, spatial Tx-inhomogeneity, and tilt limits towards  $B_0$  axis will be analyzed. This novel technique enables an additional parameter to spatially decode the position of tools during MRI-guided procedures which can increase the registration reproducibility as well as the redundancy to decrease tracking errors.

**References:** [1] Kaiser et al., IMS, 1-4, 2011. [2] Fomin et al., CDBME, 81-85, 2021. [3] Fomin et al., IGIC, 27-28, 2021.

**Acknowledgment:** The work of this paper is funded by the Federal Ministry of Education and Research within the Research Campus *STIMULATE* under the number '13GW0473A', '13GW0473B'.

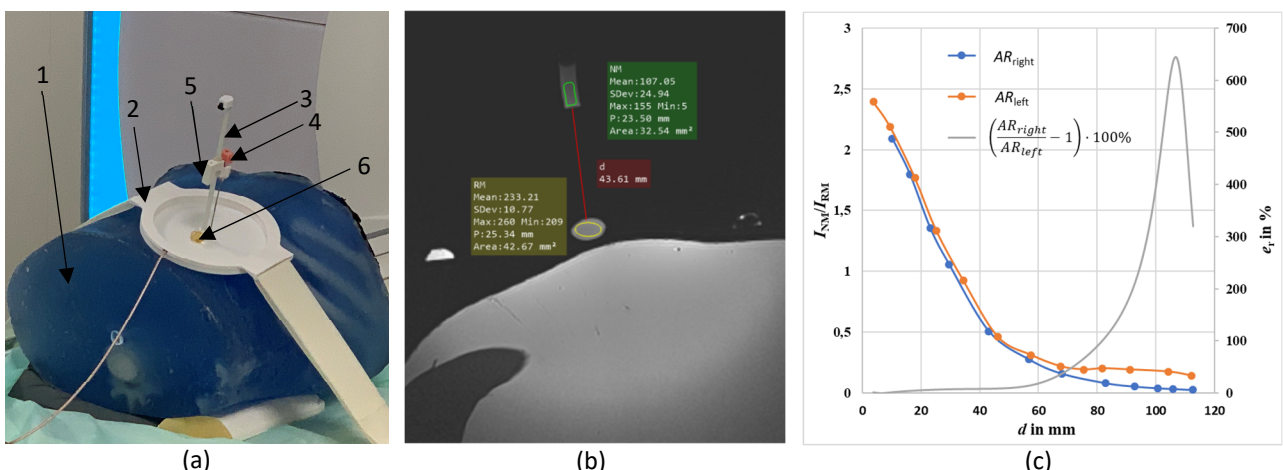


**Fig. 1:** (a) Test setup 1: Abdomen phantom, 2: Housed single loop coil, 3:  $\mu$ RIGS instrument feed, 4: 18 G Coaxial needle, 5: Gd-NM, 6: Oil-RM. (b) Marker intensities and its distance to each other from respective DICOM files. (c) Distance dependent intensity-ratio  $I_{RM}/I_{NM}$  and relative error  $e_r$  between the setup locations (right/left abdomen region (AR)).

**TITLE:** Testing of a Transperineal Guide Grid for MR guided prostate procedures using Optical and Fiducial Fusion.

**AUTHORS:** <sup>1</sup>David A. Woodrum M.D., Ph.D., <sup>1</sup>Scott M. Thompson M.D, Ph.D., <sup>1</sup>Daniel A. Adamo M.D., <sup>2</sup>Derek Lomas M.D., <sup>1</sup>Christopher P. Favazza Ph.D., <sup>1</sup>Aiming Lu Ph.D., Ph.D., <sup>3</sup>Pezhman Foroughi, <sup>3</sup>Alican Demir, <sup>3</sup>Kenny Harlan, <sup>2</sup>Lance A. Mynderse M.D.

**AFFILIATIONS:**

1 Department of Radiology, Mayo Clinic, Rochester, MN, USA

2 Department of Urology, Mayo Clinic, Rochester, MN, USA

3 Clear Guide Medical, Baltimore, MD, USA

**PURPOSE:** To describe the testing and feasibility of a transperineal guide grid based on optical fusion to aid in needle placement for biopsy and ablation.

**MATERIALS AND METHODS:** The transperineal guide grid with optical fusion was developed by Clear Guide Medical in collaboration with Mayo Clinic. The proposed tool is intended to be used in combination with the Clear Guide’s existing SCENERGY guidance software program, Clear Guide VisiMARKER, Clear Guide Optical Head, and Clear Guide CORE hardware. The hardware consists of a base plate situated under the supine semi-lithotomy patient on the MRI table (Fig 1 and 2). The base plate has holders for the guide grid holder with visible imbedded markers and leg holder plates to create workable space for needle placement. Guide grid is placed in the grid holder for needle guidance. The software will pull in a MRI T2 sequence which is used for automatic registration. Once registered the images can be scrolled with overlay of the biopsy grid. Specific needle paths can be selected and scrolled to be able to determine needle path in relation to adjacent structures.

**RESULTS:** The initial testing with volunteers demonstrates feasibility of grid positioning with the plate providing a stable platform (Fig 2). From an acquired T2 image sequence covering the grid and prostate, the software is able to automatically register the grid position and project the needle paths into the image dataset (Fig 3 and 4).

**CONCLUSION:** This system will potentially offer an optical fusion system for transperineal needle placement in the MRI environment, but it will have the flexibility to be utilized with CT or US as well. Initial testing demonstrates feasibility. Subsequent testing will be performed with patients undergoing prostate biopsy or ablation to determine the accuracy of needle guidance at the distance of the prostate (10 cm depth).

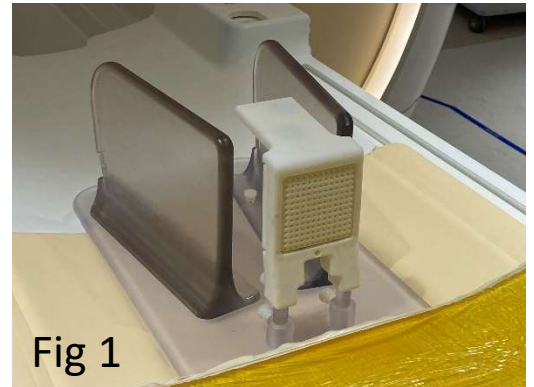


Fig 1



Fig 2

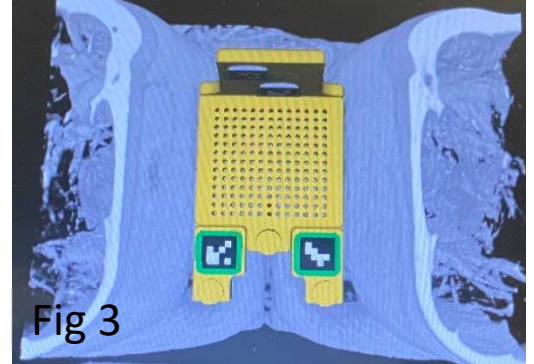


Fig 3

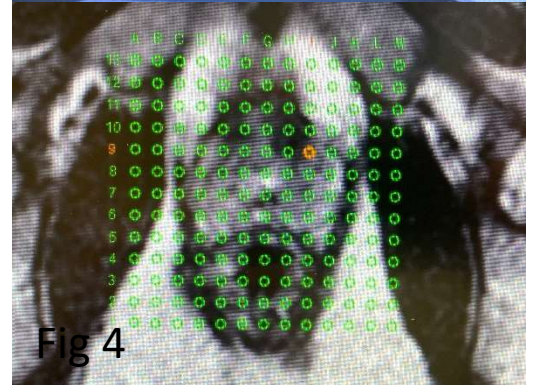


Fig 4

## TITLE

Development of a Clinical Interventional MRI Service at Mayo Clinic Rochester: 2009-2021

## AUTHORS

<sup>1</sup>Scott M. Thompson M.D, Ph.D., <sup>1</sup>Daniel A. Adamo M.D., <sup>2</sup>Erica M. Knavel Koepsel M.D., <sup>1</sup>Brian T. Welch M.D., <sup>3</sup>Derek Lomas M.D., <sup>1</sup>Devin R. Barker, R.T.(R)(MR), <sup>1</sup>David F. Ekrem, R.T.(R), R.T.(R)(MR), <sup>1</sup>Patrick L. Hanson, R.T.(R)(MR), <sup>1</sup>Wayne S. Stenzel, R.T.(R)(MR), <sup>1</sup>Katie J. Gehling, M.S.N., R.N., <sup>1</sup>Michelle Eggert, R.N., <sup>1</sup>Lori M. Cranston, R.N., <sup>1</sup>Desirae L. Howe-Clayton, <sup>1</sup>Deb Berg, <sup>1</sup>Paige Callahan, <sup>4</sup>Ernest (Matt) M. Hoffman, D.O., Ph.D., <sup>5</sup>Timothy B. Curry, M.D., <sup>1</sup>Christopher P. Favazza Ph.D., <sup>1</sup>Aiming Lu Ph.D., Ph.D., <sup>1</sup>Krzysztof R. Gorny, Ph.D., <sup>1</sup>Joel Felmlee Ph.D., <sup>3</sup>Lance A. Mynderse M.D., and <sup>1</sup>David A. Woodrum M.D., Ph.D.

## AFFILIATIONS

<sup>1</sup>Department of Radiology, Mayo Clinic, Rochester, MN, USA

<sup>2</sup>Department of Radiology, University of Wisconsin-Madison, Madison, WI, USA

<sup>3</sup>Department of Urology, Mayo Clinic, Rochester, MN, USA

<sup>4</sup>Department of Neurology, Mayo Clinic, Rochester, MN, USA

<sup>5</sup>Department of Anesthesiology and Perioperative Medicine, Mayo Clinic, Rochester, MN, USA

## PURPOSE

To describe the development and growth of a clinical Interventional MRI (iMRI) service at Mayo Clinic Rochester.

## MATERIALS AND METHODS

- iMRI Practice
  - Team members
  - Outpatient clinic
  - Inpatient service
- Clinical iMRI database was reviewed for iMRI case volumes from 1/1/2009 to 12/31/2021.
- Keys to success

## RESULTS

Clinical iMRI practice was started at Mayo Clinic Rochester in 2009 as a collaboration between diagnostic and interventional radiology (2), medical physics (2), urology (1), and anesthesiology (1). Since that time the practice has grown to include dedicated iMRI interventional radiologists (4), diagnostic radiologists (2), medical physicists (4), MR safety committee, MR technologists (4), sonography team, nurses (2), urologists (3), intraoperative neuromonitoring neurologist (2) and technologists (2), research coordinator (1) and a dedicated anesthesia team. The current iMRI practice includes a 1.5T magnet with an in-room ultrasound and cystoscopy and offers tumor ablation (cryoablation, laser, microwave, focused ultrasound), biopsies and lesion localization. The iMRI practice includes a weekly outpatient clinic for new consultations and follow-ups, a hospital-based outpatient clinic for in-person and telemedicine consultations during procedure days, an in-patient service for post-procedural care and a dedicated weekly focal prostate therapy multidisciplinary tumor board. The practice has grown substantially since 2009 with over 1400 cases performed to date (**Figure 1**), primarily consisting of prostate (754),

vascular anomaly (207), liver (138), gynecologic (11), musculoskeletal (42) and other soft tissue (225) interventions. Additionally, the iMRI practice adopted in-room US-guided inguinal nodal MR lymphangiography in 2018 with a 3-fold increase in case volumes since that time (**Figure 1**). Keys to success in building the iMRI practice thus far have been 1) multidisciplinary collaboration and team building, 2) establishing an outpatient and inpatient clinical practice, 3) institutional investment in personnel, space, equipment, and resources, 4) education of referring clinicians, 5) research and innovation, and 6) adherence to strict safety protocols overseen by the institutional MR safety committee.

## **CONCLUSION**

Development and growth of a clinical interventional MRI service offering outpatient consultations, ablation, biopsy, drainage, lesion localization and MR lymphangiography is feasible but requires 1) a dedicated iMRI team, 2) multidisciplinary collaboration and teamwork and 3) investment in personnel, space, equipment, and resources, 4) strict adherence to safety protocols in collaboration with MR Physicist team and 5) academic-industrial partnerships to foster research and innovation.

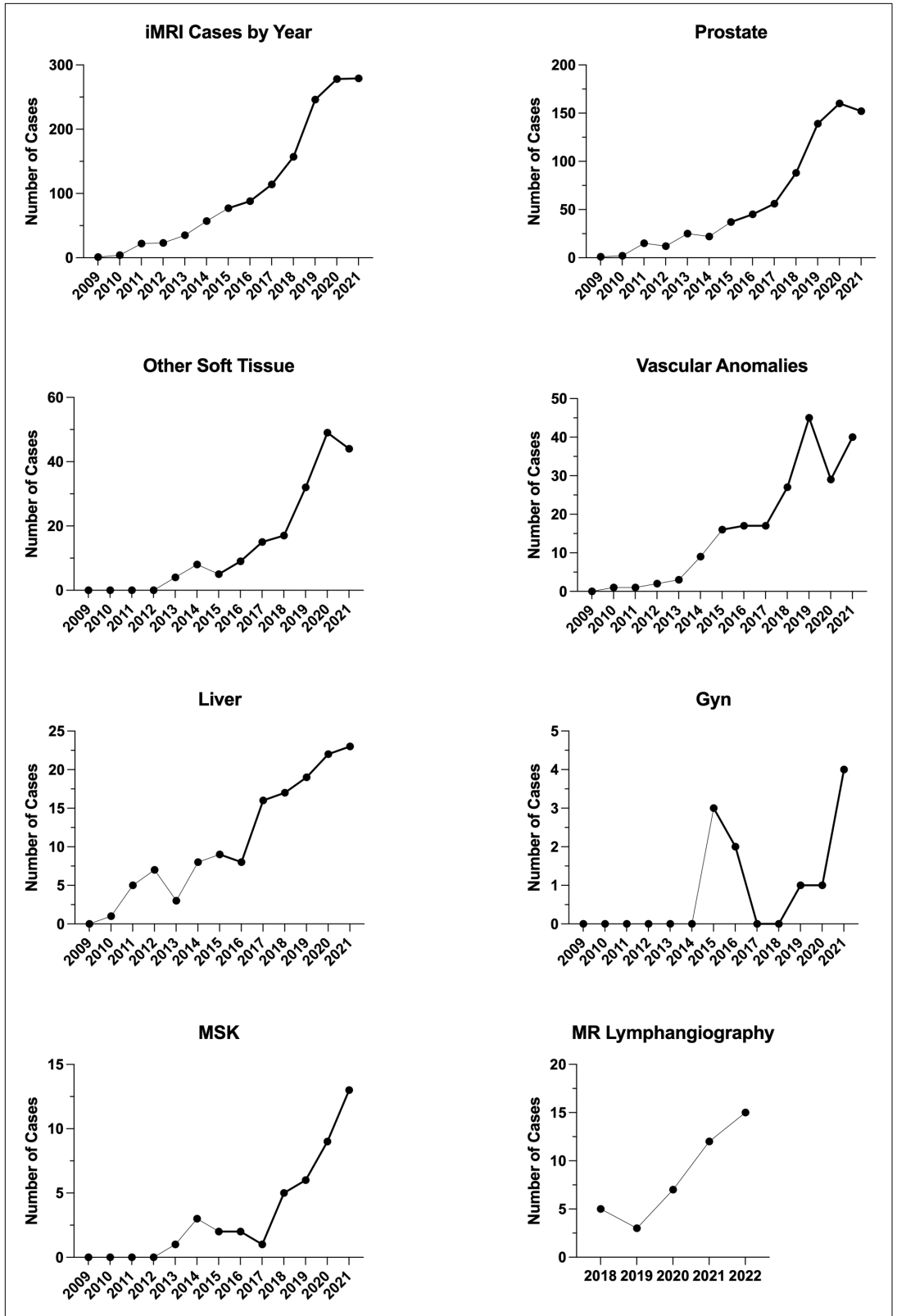


**Figure 1.** Growth of interventional MRI case volumes at Mayo Clinic Rochester from 2009 to 2021.

# **MR-guided abdominal interventions**

**F. Wacker**

**Institute of Diagnostic and Interventional Radiology**

**Hannover Medical School, Germany**

Image guided procedures in the abdomen such as fluid aspirations, abscess drainages, biopsies, targeted drug delivery and thermal ablations are routinely performed using CT and ultrasound guidance for more than 40 years. Although this is highly efficient in many patients, there is a need for more advanced and accurate guiding methods and improved therapy control that has led to the use of MRI guidance for specific procedures, at least in academic hospitals. There are many benefits that come with MRI-guidance ranging from excellent soft tissue contrast, multi-planar imaging capabilities, near real-time fluoroscopic imaging to the absence of ionizing radiation.

For MRI controlled thermal ablation, the combination of lesion visualization and MR thermometry are especially beneficial. Although direct intraprocedural temperature measurements are technically challenging, the immediate feedback helps with complete tumor destruction while, at the same time, healthy surrounding tissue can be protected. Unfortunately, the complexity of the current interventional MRI setup and workflow is a major barrier to a more widespread adoption. The goal of this presentation is, to discuss potential applications for MRI guided abdominal procedures and to highlight technical solutions, many of them developed in the research campus STIMULATE. We also present workflow improvements that helped us to make MRI guided procedures a clinical reality.

## **Ablation and Immunotherapy – a GI oncologists view**

**Arndt Vogel**

**Department of Gastroenterology, Hepatology, and Endocrinology**

**Hannover Medical School, Germany**

In 2020, almost 906,000 people globally were diagnosed with liver cancer, the most common form of which is HCC. HCC remains the third leading cause of cancer death worldwide, with a low relative 5-year survival rate of approximately 18%. The similarity between incidence and mortality (830,000 deaths/year) underlines the dismal prognosis.

Treatment options for patients with HCC are outlined in national and international guidelines. The Barcelona Clinic of Liver Cancer (BCLC) algorithm is the most widely used staging system and subdivides patients with HCC into five clinical stages, including very early stage (BCLC 0), early stage (BCLC A), intermediate stage (BCLC B), advanced stage (BCLC C), and terminal stage (BCLC D). Thermal ablation is currently recommended for early-stage HCC patients ( $\leq 2$  cm), as well as those 2-4 cm lesions not suitable for surgical resection due to anatomical reasons and/or patient conditions. Radiofrequency ablation (RFA) has been used to be the most commonly used ablation technique in the treatment of HCC. Microwave ablation (MWA) is a technology originally developed to help achieve intraoperative hemostasis. The advantages of MWA over RFA, including higher ablative temperatures, shorter interventional times and overcoming the heat sink effect (the flowing blood causes a cooling effect, thereby reducing the ablation volume) has resulted in MWA overtaking RFA as the preferred ablation technique in early HCC. Systemic therapy is the preferred treatment modality in the advanced stage and in intermediate stage patients who do not qualify for local therapies. IMbrave150 was not only the first phase III study to demonstrate a significant survival benefit compared to sorafenib, but also the first positive phase III study with an immune checkpoint inhibitor-based regimen. This trial marked the transition towards ICI-based regimens in HCC and international guidelines endorsed the combination regimen as the new standard of care in front line treatment of advanced HCC.

Percutaneous ablation of neoplastic tissue by RFA or MFA is considered a potentially curative treatment for early HCC, but recurrence rates are high. Local ablative therapies release immunogenic stimuli that can trigger an anti-tumoral immune response, which is, however, dampened by counter-regulatory mechanisms mediated through immune checkpoints, such as CTLA-4 and PD-1.

Combining local therapies with immunotherapies may shift the balance to a more robust immunostimulatory response. We therefore hypothesized that peri-interventional treatment with pembrolizumab may improve outcome of local ablative therapy and have initiated a single arm phase II trial (IMMULAB) investigating peri-interventional treatment with the checkpoint inhibitor pembrolizumab combined with RFA/MWA or brachytherapy, or - as recommended for tumor larger than 3 cm – the combination of TACE with RFA/MWA or brachytherapy in early-stage HCC with maintained liver function (Child Pugh A). The study completed enrollment 11/2021 with 30 pts (ECOG 0 or 1) for 1st line therapy in 9 German study sites, results will be presented early 2023



**TITLE:** Extreme MR Ablation Cases: The Power of MRI Guidance.

**AUTHORS:** <sup>1</sup>David A. Woodrum M.D., Ph.D., <sup>1</sup>Scott M. Thompson M.D, Ph.D., <sup>1</sup>Daniel A. Adamo M.D., <sup>2</sup>Derek Lomas M.D., <sup>1</sup>Christopher P. Favazza Ph.D., <sup>1</sup>Aiming Lu Ph.D., Ph.D., <sup>2</sup>Lance A. Mynderse M.D.

**AFFILIATIONS:**

1 Department of Radiology, Mayo Clinic, Rochester, MN, USA

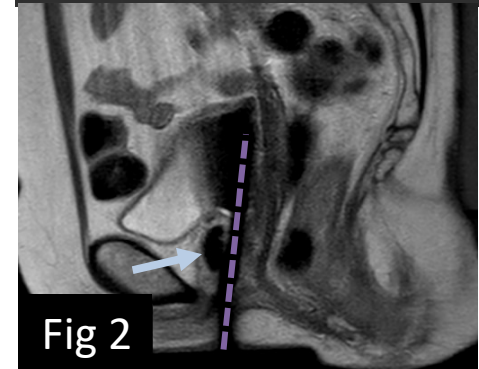
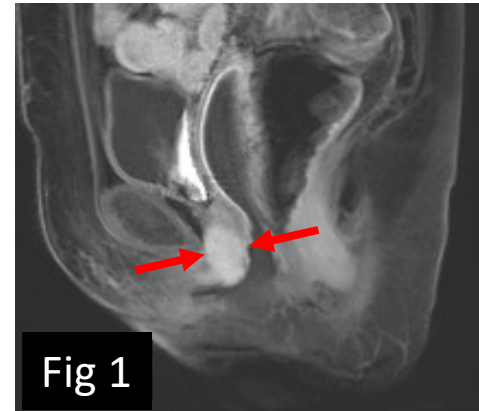
2 Department of Urology, Mayo Clinic, Rochester, MN, USA

**PURPOSE:** To demonstrate the power of MR guidance using 2 case report examples of challenging clinical cases.

**MATERIALS AND METHODS:** Retrospective review from Jan 2021 to April 2022 for challenging clinical cases demonstrating the capability of MR platform for guidance. Case 1 is a 69F with recurrent adenoid cystic carcinoma of the vulva with met to the urethra needing focal ablation (Fig 1 and 2). Case 2 is 66M with prostate cancer met to the glans of the penis (Fig 3 and 4). Both cases were performed under general anesthesia. Both utilized MR guided cryoablation for treatment with urethral warmer in place. Case 1 used a transperineal needle placement. Case 2 utilized trans-glans needle placement. Cryoablation was performed with continuous MR imaging monitoring so that the Iceball was grown to encompass the lesion with margins as permitted based on adjacent structures and skin. Patients were discharged same day. Case 1 had followup MRI at 3 months and Case 2 had followup PET choline imaging at 3 months.

**RESULTS:** Case 1 initial MRI demonstrated on MRI an enhancing mass (red arrows) within the urethra with expansion of the urethra and mass effect on the urethral canal (Fig 1). MRI cryoablation was performed with a trans perineal IceSeed cryoneedle placed within the urethral lesion parallel to the course of the urethra. Freezing (blue arrow) was performed with urethral warmer (purple dashed line) in place with careful attention to extend the edge of the iceball just beyond the edge of the mass (Fig 2). Case 2 demonstrated a PET choline avid lesion (red arrow) in the left glans of the penis (Fig 3). An IceSeed cryoneedle was placed trans-glans with US guidance through the lesion. Freezing (blue arrow) was performed continuous MR imaging with urethral warmer in place with careful attention to not freeze the urethra and to not freeze the skin (Fig 4).

**CONCLUSION:** MR guided cryoablation can be utilized for treatment of difficult lesions especially when it is necessary to maintain excellent soft tissue resolution to minimize collateral damage.



Abstract.

## MR-guided focused ultrasound in Musculoskeletal Diseases

Roberto Blanco Sequeiros, Chairman and Professor  
Department of Radiology, Turku University Hospital, Finland

High Intensity Focused Ultrasound (HIFU) is a non-invasive technique where ultrasound waves are delivered to targets within human body without injury to the skin or surrounding tissue. By focusing high-power ultrasound beams at a distance from the source, necrosis of tissues lying within the focal volume can be achieved without damage to the structures elsewhere in the path of the beam. Although other modalities can be utilized to guide HIFU therapy, MRI guidance provides several advantageous features including unparalleled depiction of anatomic detail, real time thermometry and multi-planar imaging.

As a clinical tool, MRI guided HIFU has been implemented with promising results in the treatment of both benign and malignant tumors. HIFU has been used in the management of uterine fibroids, bone metastases, prostate cancer and has been associated as a promising method in managing tumor related pain, both central and peripheral. The biological effects and possible applications related to HIFU are multitude and include immune system modulation, targeted gene/drug therapy and cellular regeneration modulation. The key in implementing HIFU system is multiparametric imaging and multidisciplinary team. As an image guided non-invasive loco-regional therapy tool, HIFU has great potential.

Concerning Musculoskeletal diseases MR guided HIFU has multitude of potential targets but it is specifically used in tumor therapy. Namely metastatic bone tumors, desmoid tumors and osteoid osteomas are treated with focused ultrasound. Other potential targets are arthrosis related pain and pigmented villonodular synovitis (PVNS).

Desmoid tumors, Aka. aggressive fibromatosis are locally infiltrative soft tissue tumors arising from musculoaponeurotic tissue without potential for metastasis. Tumor-related destruction typically leads to organ morbidity and in case of organ destruction to mortality. The lack of metastatic growth pattern makes desmoid tumors feasible targets for local therapies, of which HIFU has distinct advantages.

Osteoid Osteomas are benign osteoid tumors typical in juvenile population and with multiple treatment options, here MRI guided HIFU presents as unique non-incisional and non-ionizing method to treat and guide osteoid osteoma.

Pain from metastatic bone lesions is very common. Palliation is typically achieved with radiation therapy. MRI guided HIFU presents as “one stop” method to treat metastasis related pain from bone lesions.

This presentation discusses the utility and potential of MR guided focused ultrasound therapy in the context of musculoskeletal diseases.

## Retrospective analysis of MR-guided high intensity focused ultrasound (MRgFUS) in 65 patients with symptomatic lumbosacral facet joint arthritis

Daniel D $\ddot{u}$ x<sup>1</sup>, Markus D $\ddot{u}$ x<sup>2</sup>, Christian Stroszczyński<sup>3</sup>, Lukas Beyer<sup>4</sup>

1: Medical School of Hannover; 2: MRgFUS center Frankfurt; 3: University of Regensburg;

4: Ernst von Bergmann Hospital Potsdam

### Purpose:

Safety/efficacy of MR-guided high intensity focused ultrasound (MRgFUS) for symptomatic lumbosacral facet joint arthrosis (FJA) have been discussed in small case series [1-5]. This is a retrospective single-center study of patients with chronic lower back pain treated with MRgFUS in the largest cohort to our knowledge.

### Material and Methods:

65 patients (age: 61±12.3 years; 74% female) with symptomatic FJA were treated with MRgFUS (ExAblate 2100 (INSIGHTEC, Israel) coupled to a 1.5T MRI (GE Healthcare, USA)) in 2017 (example in **Figure 1**). FJA was diagnosed by a recent MRI, a facet joint (FJ) block was not mandatory. FJA severity (according to Fujiwara [6]), local edema/inflammation and other spine pathologies were evaluated (**Table 1**). Pain intensity and the influence of pain on daily/quality of life (QoL) were assessed per treatment by BPI, ODQ and EQ-5D-5L [7-9]. Baseline scores were compared to defined pooled follow-up time periods (**Figure 1**) and to the latest available follow-up post-MRgFUS. Complications were reported. Patients with subsequent therapy other than MRgFUS were excluded from further follow-up. Clinically significant pain improvement was defined as NRS<sub>avg.</sub> decrease ≥30% and worsening as NRS<sub>avg.</sub> increase ≥30%, respectively [10, 11]. Program R (R Core Team) used a paired t-test for statistical analyses (p≤0.05).

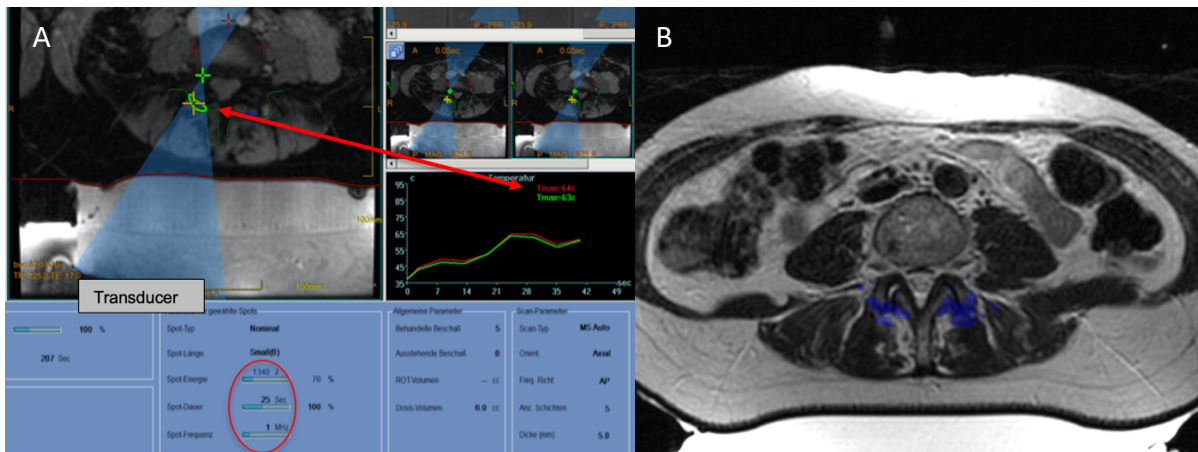
### Results:

70 MRgFUS (~2h±27min (mean)) were performed by direct FJ-targeting (409 FJs (L1-S1), of which 98% at L3-S1). FJA was predominant in L4-S1 (74-80% at least moderate, in which ≥49% were severe; 29-44% inflamed), less in L3/4 (~50% at least moderate) and rarely seen more cranially. Depending on morphology, 29 patients had an isolated FJA, 29 at least one additional spine pathology and 7 prior lumbar spine surgery. NRS<sub>avg.</sub> and NRS<sub>max.</sub> decreased from 5.4±1.7 to 3.9±1.9 and from 7.4±1.7 to 5.3±2.2 (n=70; p<0.001) at 5.8 months, respectively. Clinically significant improvement was seen in 54% (38/70) of the patients, with 59% improvement in NRS<sub>avg.</sub> (5.7±1.6→2.3±1.3), 50% in NRS<sub>max.</sub> (7.5±1.8→3.7±1.9) and improved daily life (39% in BPI; 44% in ODQ) and QoL (71% in EQ-5D-5L). Pain/QoL over time is summarized in **Figure 3**, not reaching our statistical threshold of p≤0.05 later than 10 months post-MRgFUS (reduced statistical power: 11 and 12 questionnaires at 10 and 13 months, respectively). At 13 months NRS<sub>avg.</sub> decreased from 5.2±2.1 to 2.4±1.6, of those 75% (9/12) had clinically significant improvement. Patients with isolated FJA had a 10% further decline in NRS<sub>avg.</sub> compared to the other subgroups. 3/7 patients had clinically significant improvement with prior spine surgery. 27 patients had treatment related pain (need for iv pain medication), 7 muscle cramps (self-limiting), 8 lumbar back pain (2 with NRS<sub>avg.</sub> increase ≥30%), and 5 had 1<sup>th</sup> degree skin burns. No 2<sup>nd</sup>/3<sup>rd</sup> degree skin burns or nerve palsy.

### Conclusions:

MRgFUS is safe/efficient for symptomatic FJA, potentially with lasting pain improvement. Direct FJ-targeting vs. targeting the supplying sensory nerve have different challenges/advantages, both feasible with MRgFUS. Often symptoms are a combination of symptomatic FJA and other spine disorders. In general, diagnostic FJ-blocks lead to improved success rates after therapy, but no FJ-block is superior regarding absolute number of patients with improvement and economic considerations [12]. Standardized protocols are needed for homogenous and comparable outcomes between FJ-studies.

Figure 1: Treatment Plan and Estimated Dose



**Left side:** One sonication of a right FJ. Treatment parameters (red circle), focus of sonication (green cross), thermometry (red arrow).

**Right side:** Dose map with thermal dose (blue)

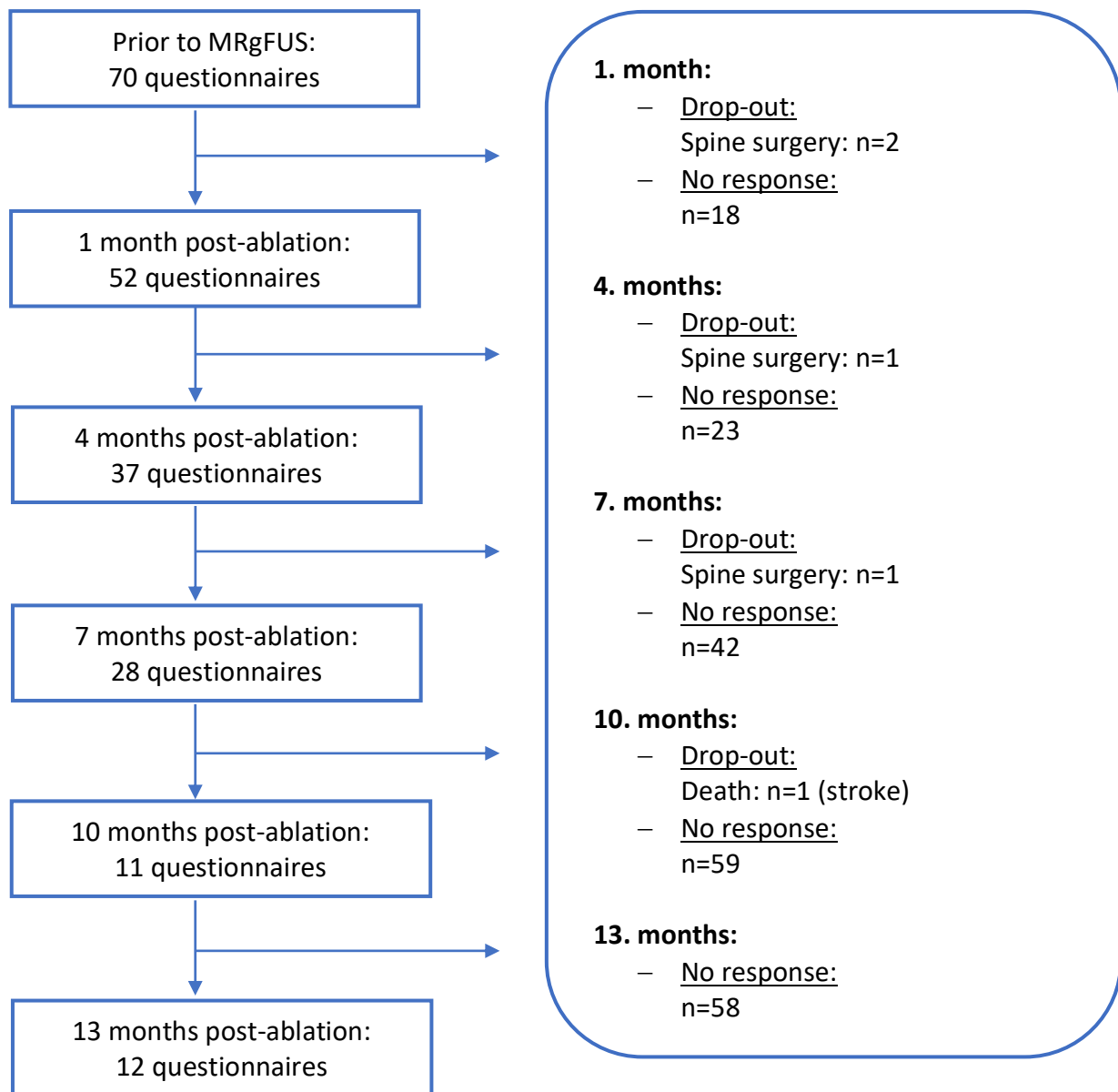
Table 1: All Patients without isolated lumbar facet joint arthrosis

Additional spine pathology	n	%	Spine Surgery	n	%
Disc Herniation	7	24%	Decompression	3	5%
Spinal Stenosis	14	48%	Fusion	2	3%
Neuroforaminal Stenosis	13	45%	Disc Surgery	2	3%
Nerve root compression	7	24%			
Spondylolisthesis (grade 1)	20	69%			
Osteochondrosis (grade 3)	1	3%			

**Left column:** all patients with additional spine pathologies possibly causing back pain.

**Right column:** all patients with spine surgery prior to MRgFUS.

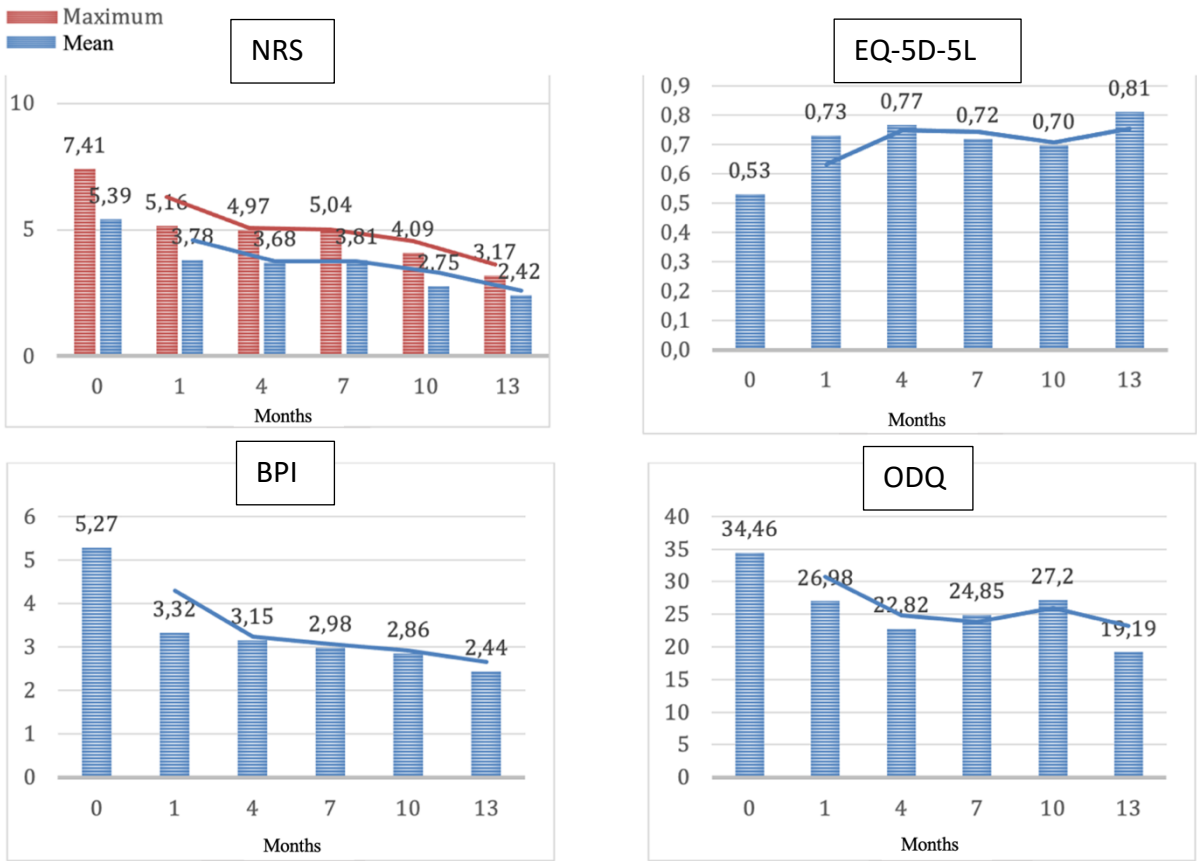
Figure 2: Time table after MRgFUS therapy (follow-up/drop-out)



**Left side:** follow-up for each time period

**Right side:** missing follow-up, drop-out and the reason for exclusion in the meanwhile

Figure 3: Change in Pain and Quality of life for all patients



**Top left image:** NRS<sub>avg.</sub> and NRS<sub>max.</sub> decrease over time for all patients.

**Top right image:** Quality of life (EQ-5D-5L) increases.

**Inferior row:** Pain is interfering less in the patient’s daily life for BPI (left side) and ODQ (right side).

## References:

1. Tiegs-Heiden CA, Lehman VT, Gorny KR, Boon AJ, Hesley GK. Improved Treatment Response Following Magnetic Resonance Imaging-Guided Focused Ultrasound for Lumbar Facet Joint Pain. *Mayo Clin Proc Innov Qual Outcomes*. 2020;4(1):109-13. Epub 2020/02/15. doi: 10.1016/j.mayocpiqo.2019.10.003. PubMed PMID: 32055777; PubMed Central PMCID: PMC7010965.
2. Namba H, Kawasaki M, Izumi M, Ushida T, Takemasa R, Ikeuchi M. Effects of MRgFUS Treatment on Musculoskeletal Pain: Comparison between Bone Metastasis and Chronic Knee/Lumbar Osteoarthritis. *Pain Res Manag*. 2019;2019:4867904. Epub 2019/10/01. doi: 10.1155/2019/4867904. PubMed PMID: 31565109; PubMed Central PMCID: PMC6745150.
3. Squarcia M G MoF, Pomes J, Moreno A, Busquets C, Barcelona ES. Effectiveness and safety of high intensity focused ultrasound guided by magnetic resonance imaging (MRgFUS) in the treatment of osteoarticular lumbar spinal pain originating from the facet joints. 2016. doi: 10.1594/ecr2016/C-1344.
4. Weeks EM, Platt MW, Gedroyc W. MRI-guided focused ultrasound (MRgFUS) to treat facet joint osteoarthritis low back pain--case series of an innovative new technique. *Eur Radiol*. 2012;22(12):2822-35. doi: 10.1007/s00330-012-2628-6. PubMed PMID: 22935902.
5. Aginsky R, LeBlang S, Hananel A, Chen J, Gofeld M, Perez J, et al. Tolerability and Feasibility of X-ray Guided Non-Invasive Ablation of the Medial Branch Nerve with Focused Ultrasound: Preliminary Proof of Concept in a Pre-clinical Model. *Ultrasound Med Biol*. 2021;47(3):640-50. Epub 2020/12/03. doi: 10.1016/j.ultrasmedbio.2020.10.019. PubMed PMID: 33261908.
6. Fujiwara A, Tamai K, Yamato M, An HS, Yoshida H, Saotome K, et al. The relationship between facet joint osteoarthritis and disc degeneration of the lumbar spine: an MRI study. *Eur Spine J*. 1999;8(5):396-401. Epub 1999/11/07. PubMed PMID: 10552323; PubMed Central PMCID: PMC3611192.
7. Cleeland CS, Ryan KM. Pain assessment: global use of the Brief Pain Inventory. *Ann Acad Med Singapore*. 1994;23(2):129-38. Epub 1994/03/01. PubMed PMID: 8080219.
8. Fairbank JC, Couper J, Davies JB, O'Brien JP. The Oswestry low back pain disability questionnaire. *Physiotherapy*. 1980;66(8):271-3. Epub 1980/08/01. PubMed PMID: 6450426.
9. Herdman M, Gudex C, Lloyd A, Janssen M, Kind P, Parkin D, et al. Development and preliminary testing of the new five-level version of EQ-5D (EQ-5D-5L). *Qual Life Res*. 2011;20(10):1727-36. Epub 2011/04/12. doi: 10.1007/s11136-011-9903-x. PubMed PMID: 21479777; PubMed Central PMCID: PMC3220807.
10. Gatchel RJ, Mayer TG, Choi Y, Chou R. Validation of a consensus-based minimal clinically important difference (MCID) threshold using an objective functional external anchor. *Spine J*. 2013;13(8):889-93. Epub 2013/03/26. doi: 10.1016/j.spinee.2013.02.015. PubMed PMID: 23523434.
11. Dworkin RH, Turk DC, Wyrwich KW, Beaton D, Cleeland CS, Farrar JT, et al. Interpreting the clinical importance of treatment outcomes in chronic pain clinical trials: IMMPACT recommendations. *J Pain*. 2008;9(2):105-21. Epub 2007/12/07. doi: 10.1016/j.jpain.2007.09.005. PubMed PMID: 18055266.
12. Cohen SP, Williams KA, Kurihara C, Nguyen C, Shields C, Kim P, et al. Multicenter, randomized, comparative cost-effectiveness study comparing 0, 1, and 2 diagnostic medial branch (facet joint nerve) block treatment paradigms before lumbar facet radiofrequency denervation. *Anesthesiology*. 2010;113(2):395-405. Epub 2010/07/09. doi: 10.1097/ALN.0b013e3181e33ae5. PubMed PMID: 20613471.

# Assessment of intercostal sonication capabilities of a dedicated transducer by MR-ARFI/thermometry

**Author List:** Fanny Dabrin<sup>1</sup>, Mathieu Guyot<sup>2</sup>, Valéry Ozenne<sup>2</sup>, Stéphane Chemouny<sup>1</sup>, Pierre Bour<sup>1</sup>, Bruno Quesson<sup>2</sup>. <sup>1</sup>Certis Therapeutics, Pessac, France; <sup>2</sup>Univ. Bordeaux, CNRS, CRMSB, UMR 5536, IHU Liryc, F-33000 Bordeaux, France,

## Purpose:

Intercostal HIFU ablation using spherical transducers remains challenging due to absorption of the ultrasound by the ribs (risks of inducing unwanted heating) and phase aberrations/reflection resulting in significant acoustic losses at the focal spot (Quesson, B. et al. Medical Physics 37,2533-2540(2010)). MR-ARFI/thermometry is used to assess sonication capabilities of a dedicated HIFU transducer for different rib spacing.

## Material and Methods:

Two ribs from a pig were positioned over a piece of muscle on a mounting enabling mechanical spacing adjustment (Figure 1). Tested values were 0.8, 1 and 1.5 cm. A 32-element transducer (13 cm focal length, with asymmetric apertures of 2 and 12 cm) was powered by a 1.6 kW generator operating at 1 MHz. A modified echo-planar imaging sequence integrated a bipolar motion encoding gradient (MEG with 20 mT/m amplitude and 3 ms duration) to image the displacement and temperature rise induced by a single ultrasound pulse [Bour, P. et al. Magn Reson Med 78, 1911-1921(2017)]. Sequence parameters: 5 slices, TE/TR/FA = 25ms/2000ms/90°, FOV= 186x192 mm<sup>2</sup>, resolution 1.5x1.5x3 mm<sup>3</sup>, 4 averages (8s update time per stack of slices). Slices were centered on the HIFU focus in a plane perpendicular or parallel to ultrasound propagation direction. A HIFU pulse of 5 ms duration (1.25% duty cycle) was synchronized with the MEG. Experiments were repeated for different acoustic powers: 68, 170 and 308 W<sub>acoustic</sub>. Displacement and temperature images were reconstructed using the method proposed in [Bour, P. et al. Magn Reson Med 78, 1911-1921(2017)] for each condition of rib spacing and acoustic power.

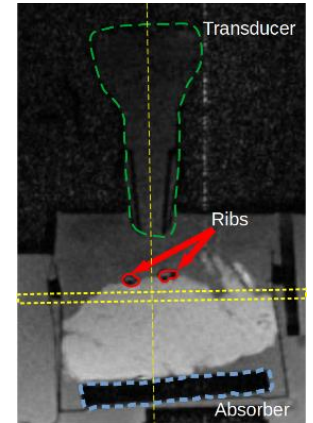


**Figure 1 :** experimental setup showing transducer position relative to the two ribs. Yellow rectangle indicates position of the central slice of the MR-ARFI/thermometry sequence.

## Results:

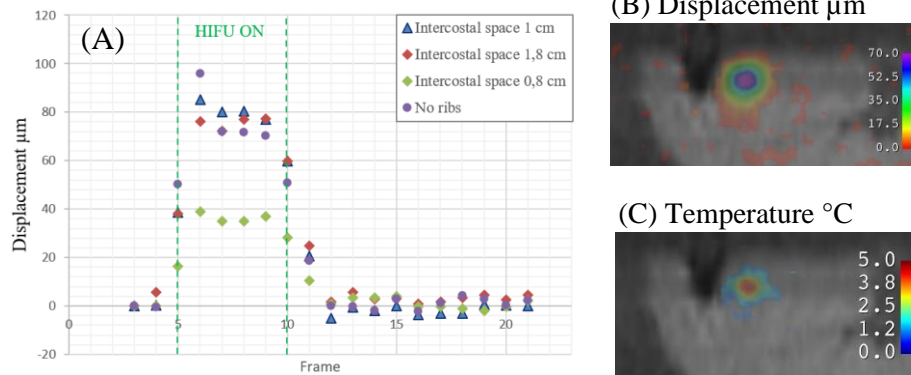


**Figure2:** (A) Evolution of maximal displacement for different intercostal spaces. Maximal displacement decreases when intercostal space is 0.8cm. (B) Representative displacement map for 1 cm rib spacing during the shot (C) Representative temperature map for 1 cm rib spacing during the shot.

**Table 1:** Summary of the displacement and the temperature values

Intercostal size in cm	Acoustic power W	Maximal displacement $\mu\text{m}$	Maximal temperature $^{\circ}\text{C}$
No ribs	68	16	1.0
	170	31	2.4
	308	96	6.4
1.80	67	14	1.4
	168	30	2.3
	307	77	4.3
1.00	70	15	1.4
	175	35	2.1
	312	85	6.4
0.80	67	11	0.6
	169	20	1.2
	307	39	3.0

Table 1 shows that maximal displacement is similar without ribs and for rib spacing down to 1 cm. Reducing spacing to 8 mm resulted in significant reduction (> 50%) of maximal displacement.

## Conclusion:

Intercostal sonication is feasible with the proposed HIFU device without significant acoustic energy loss for rib spacing above 1 cm. Further studies are required to investigate the possibility to perform non-invasive intercostal ablation using higher sonication duty cycles.



## MR-HIFU therapy of uterine fibroids – experience within an interdisciplinary fibroid center

Surup H<sup>1</sup>, Leonhardi J<sup>1</sup>, Bailis N<sup>1,2</sup>, Weisgerber C<sup>3</sup>, Handzel R<sup>3</sup>, Stark S<sup>3</sup>, Aktas B<sup>3</sup>, Martin M<sup>1</sup>, Melzer A<sup>4</sup>, Busse H<sup>1</sup>, Ebel S<sup>1</sup>, Denecke T<sup>1</sup>

<sup>1</sup> Department of Diagnostic and Interventional Radiology, University Hospital Leipzig, Germany

<sup>2</sup> Institute of Neuroradiology, University Hospital Leipzig, Germany

<sup>3</sup> Department of Gynecology, University Hospital Leipzig, Germany

<sup>4</sup> Innovation Center Computer Assisted Surgery, Leipzig University, Germany

**Background** Between 70–80% of all women will have uterine fibroids in their lifetime [1]. About a quarter of them suffer from abnormal menstrual bleeding, reproductive dysfunction or bulk-related symptoms [2] and have a lower quality of life. Unlike hysterectomy, myomectomy and uterine artery embolization, MRI-guided high-intensity-focused ultrasound (MR-HIFU) is a completely noninvasive therapy option with less complications and the advantage to preserve uterine function and fertility. On the downside, it is characterized by long procedure times and a higher risk for fibroid recurrence [3].

**Purpose** To present the workflow within an interdisciplinary treatment center for uterine fibroids and to report on our clinical experience with MR-HIFU applications.

**Methods** MR-HIFU (Sonalleve, Profound Medical, Mississauga, ON) was performed in a 3-T MRI (Ingenia 3.0T, Philips Healthcare, Best, Netherlands). Patients received analgesic and sedative medication and their vital parameters were monitored continuously. T2-weighted and T1-weighted bowel sequences were used for planning. Therapeutic and adverse tissue heating during sonication was controlled by multiplanar MR temperature mapping (6 slices in 3.5 s) in the treatment cell as well as the so-called near field (skin) and far field (sacrum). Patients are followed up by ultrasound (3 months) and MRI (6 months) with regard to fibroid volumes and remaining vascularization.

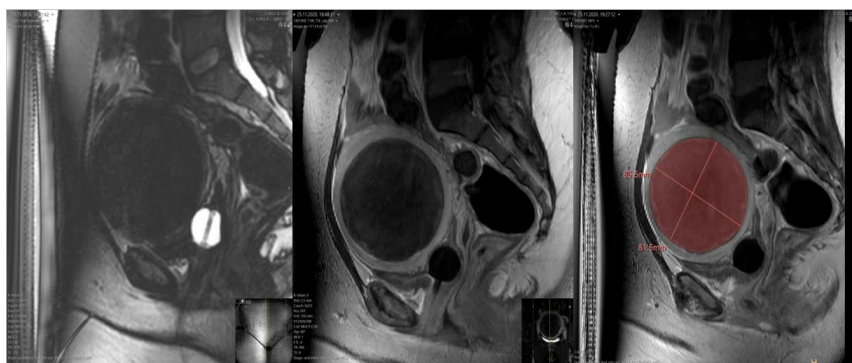


**Fig. 1.** Diagnostic T2-weighted and contrast-enhanced MR images (after MR-HIFU) in a 32-year-old patient with a massive fibroid suffering from hypermenorrhea, abdominal pressure and dyspareunia. Three months after therapy the patient reported a clear regression of clinical symptoms.

**Results** Since October 2017, a total of 62 women (28–55 years, mean: 39 years) with symptomatic uterine fibroids have been treated by MR-HIFU. The main symptoms reported were hypermenorrhea (52%)—partly related to secondary anemia (12%), dysmenorrhea (24%), bulk-related symptoms (36%), pollakisuria (16%) and conception difficulties (20%). Patients received midazolam (1–2 mg, mean: 1.2 mg) and piritramide (3–10.5 mg, mean: 4.9 mg) for analgesic sedation. Bowel loops frequently happened to lie in the beam path on the day of treatment. The bladder, rectum or both were filled to manipulate bowel and uterus positions.

Fifty-one patients were treated successfully (procedure time 3–6 h) and non-perfused volumes ranged from 3–100% (mean: 55%), an example is shown in Figure 1. Eleven therapies had to be terminated, five because of a system malfunction, five due to the presence of bowel loops within the beam path and one because of an intolerable heat pain. Thirty-four of the successfully treated patients had a solitary, rather large fibroid (mean volume: 195 ml) and 17 of them had multiple fibroids (mean total volume: 201 ml). All patients were discharged on the next day.

**Conclusions** MR-HIFU therapy presents a promising option for eligible patients with symptomatic uterine fibroids. It is widely established and was generally well tolerated by our patients, although the technical effort and time exposure is high. In an interdisciplinary fibroid center, the decision for a particular therapy can be made jointly by the patient, treating gynecologist and interventional radiologist.

**References** [1] Verpalen IM et al., *Eur Radiol.* 2020; 30(5):2473-2482.  
[2] Stewart EA et al., *N Engl J Med.* 2015; 372(17):1646-55.  
[3] Silberzweig JE et al., *Radiology.* 2016; 280(3):675-92.

## **Combination of MRI-guided focused ultrasound and radiation therapy - experimental rodent study**

Xinrui Zhang<sup>1</sup>, Sebastian Greiser<sup>2</sup>, Franziska Lange<sup>2</sup>, Robbert van Gorkum<sup>4</sup>, Marc Fournelle<sup>3</sup>, Daniel Speicher<sup>3</sup>, Steffen Tretbar<sup>3</sup>, Andreas Melzer<sup>1</sup>, Lisa Landgraf<sup>1</sup>.

<sup>1</sup>Innovation Center Computer Assisted Surgery, Leipzig, Germany.

<sup>2</sup>Fraunhofer Institute for Cell Therapy and Immunology, Leipzig, Germany.

<sup>3</sup>Fraunhofer Institut für Biomedizinische Technik, St. Ingbert, Germany.

<sup>4</sup>Institute for Biomedical Engineering, University and ETH Zurich, Zürich, Switzerland.

### **Purpose**

Focused ultrasound (FUS) can be used to physiologically change or destroy tissue in a non-invasive way. The thermal effects of FUS are known to lead to various biological effects, such as inhibition of DNA damage, reduction of tumor hypoxia and induction of apoptosis. FUS-induced moderate heating in a temperature range of 40 – 47 °C has shown to sensitize tumor cells to radiation therapy (RT) in vitro. Here, we studied radiosensitization as a combination therapy of FUS and RT in a xenograft mouse model using a newly developed magnetic resonance imaging (MRI) compatible FUS equipment.

### **Materials and methods**

The preclinical FUS phased array transducer consists of an 11x11 elements matrix array probe with an aperture size of 10x10 mm and a frequency of 960 kHz (Fraunhofer IBMT). To test its MRI-compatibility, MR images were obtained in 7 T MRI (Bruker) with a gradient echo (FLASH) sequence (Parameters: TE = 15 ms; TR = 400 ms; slice thickness = 3 mm; FOV = 4x4 cm; matrix = 256x256; flip angle = 30°; no. of averages = 1) and spin echo (RARE) sequence was run with the same geometry except TE = 20 ms, TR = 800 ms. Xenograft tumor bearing 7-15 weeks old male NMRI Foxn1nu/nu mice (Janvier Labs) were produced by subcutaneous injection of human prostate cancer cell line PC-3. Animals were treated with new FUS system in the 7T MRI at 4.8 W/cm<sup>2</sup> to reach ~45°C and hold for 30 min. Temperature was controlled via fiber optics and proton resonance frequency shift (PRF) MR thermometry in parallel. In combination group, animals were treated with FUS followed by X-ray at single dose of 10 Gy in small animal radiation research platform (XStrahl). Effects of FUS and RT were assessed via hematoxylin-eosin (H&E) staining. Tumor proliferation was detected by immunohistochemistry of Ki67 and apoptosis was measured by TUNEL assay.

### **Results**

The comparison of the MR image with and without the transducer showed reduced SNR in presence of the transducer. A field-drift of 0.0443 % was observed when the transducer was sonicating. Without the transducer, the SNR was 157.17 when using the FLASH sequence. Measurements on identical geometry with the presence of the transducer resulted in images with a SNR of 66.29. An inhibition of tumor growth by 4.6 times was observed in vivo in the FUS+RT group (85.29%) in contrast to the tumor volume of 393% in untreated control. At 40 days follow up, the impact of RT on cancer cells was significantly improved by FUS demonstrated by a reduction of cell nucleoli from 189 to 237 compared to RT alone. The tumor proliferation was reduced from 74.1% (control) to 59.4 % (RT) and 7.9 % (FUS+RT) while apoptosis was enhanced 3.7-fold in FUS+RT group compared to single RT. The result of H&E staining showed that single FUS treatment has limited effect on xenograft tumor and healthy organs.

### **Conclusion**

Our results demonstrated the feasibility of combined MRI-guided FUS and RT for the treatment of heterotopic prostate cancer in a xenograft mouse model and may provide a chance for less invasive cancer therapy through radiosensitization in the future.

# Validation of the accuracy of a new transcostal phased-array HIFU transducer dedicated to hepatic ablation

Orane Lorton<sup>1,\*</sup>, Pauline C. Guillemin<sup>1</sup>, Yacine M'Rad<sup>1</sup>, Andrea Peloso<sup>2</sup>, Sana Boudabbous<sup>1,3</sup>, Ryan Holman<sup>1</sup>, Pierre-Alexandre Poletti<sup>3</sup>, Alexis Ricoeur<sup>3</sup>, Rares Salomir<sup>1,3</sup>

<sup>1</sup>Image Guided Interventions Laboratory (GR-949), Faculty of Medicine, University of Geneva, Switzerland. <sup>2</sup>Visceral Surgery Division, University Hospitals of Geneva, Geneva, Switzerland. <sup>3</sup>Radiology Division, University Hospitals of Geneva, Geneva, Switzerland.

**Purpose** - A new high intensity focused ultrasound transducer dedicated to liver ablation has been developed and tested *in vivo* [1]. The natural strong focusing, large acoustic window and element shape and distribution allowed to perform transcostal hepatic lesions. This study aimed to assess the spatial accuracy of this transducer on MRgHIFU ablation of *in vivo* pig livers by pre-defining a target visible on MR imaging and on histological sections. **Material and methods** - A mixture of 1.5% of MR contrast agent was prepared with sterile methylene blue solution for visual assessment of the pre-defined target, as reported by Petrusca et al [2]. 0.1ml of the solution was injected in the hepatic parenchyma of female pigs (N = 3) and followed by a radiofrequency (RF) ablation to fix the marker by tissue coagulation. The RF ablation was performed under ultrasound guidance using 5W during 10s and followed by another 0.1ml mixture injection to emphasize the MR and histological contrast agent. The MRgHIFU ablation was then created in the liver tissues under MR

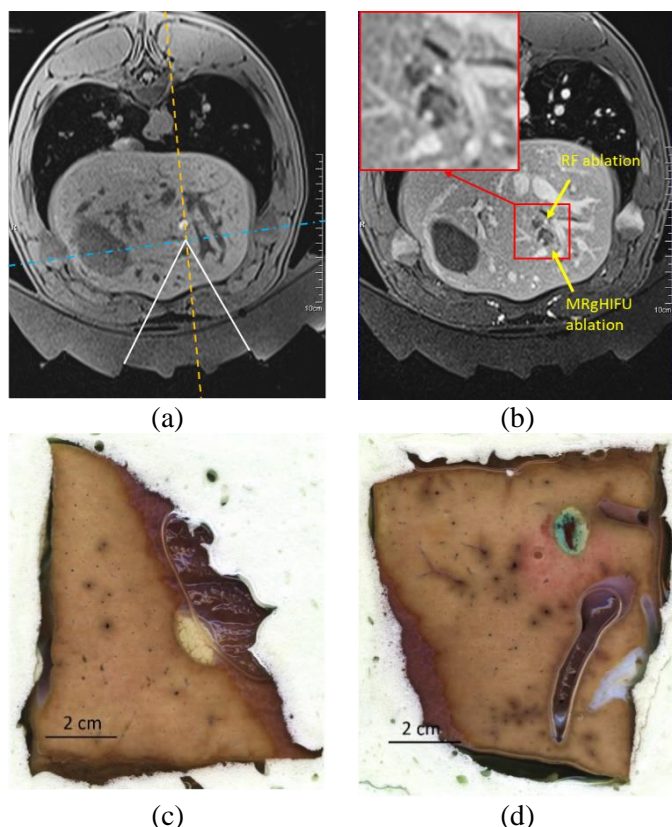


Figure 1. a) Targeting of the sonication in the transverse plane showing the RF marker in hypersignal and the expected MRgHIFU lesion at the crossing planes. b) Gd contrast-enhanced MR image of the liver after ablations. The yellow arrows indicate the RF marker ablation and the HIFU ablation at the expected location. c) Post-mortem slicing of the pig liver 01 showing c) the MRgHIFU ablation with high delineation accuracy and d) the RF ablation highlighted by methylene blue.

thermometry and distinguished from the RF ablations by choosing a target within a sphere of 10mm around the marker, depending on the close environment. The sonication were performed under apnea and did not exceed 40s. The acoustic power ranged 800-950W. MR imaging follow-up was performed at D0 and D7 and ablations were evaluated post-mortem by gross pathology after formalin fixation. **Results** - The RF coagulation was immediately visible on MR imaging and allows the MRgHIFU targeting. The peak temperature exceeded 85°C at the focal point. The HIFU ablations were also visible at D0 after Gd-contrast enhanced injections. Post-mortem examination and macroscopic pathology confirmed the presence of the RF marker and the HIFU ablation at the expected location. **Conclusion** - The RF coagulation and contrast agent injections did not induce side effects such as bleeding, oedema or infection. This study confirmed the ability to perform an ablation at a prescribed target. The MRgHIFU ablation were transcostally performed without a need for means of protection of the ribs due to the specific design of the transducer.

[1] Orane Lorton, Pauline C. Guillemin, Yacine M'Rad, et al. (2022) A Novel Concept of a Phased-Array HIFU Transducer Optimized for MR-Guided Hepatic Ablation: Embodiment and First In-Vivo Studies. *Front. Oncol.*, 30 May 2022 | <https://doi.org/10.3389/fonc.2022.899440>

[2] Petrusca L, Viallon M, Breguet R, et al. An experimental model to investigate the targeting accuracy of MR-guided focused ultrasound ablation in liver. *J Transl Med.* 2014 Jan 16;12:12.

# Towards a Specialized Software for Interventional Radiology

Julian Alpers<sup>1</sup>, Sathish Balakrishnan<sup>1</sup>, Mathews Jabaraj Soloman<sup>1</sup>, Laureen Polenz<sup>1</sup>, Juan Sebastián Sánchez López<sup>1</sup>, Mathias Becker<sup>2</sup>, Maciej Pech<sup>2</sup>, Frank Wacker<sup>3</sup> and Bennet Hensen<sup>3</sup>

<sup>1</sup>InLine-Med GmbH, Magdeburg, 39106, Germany

<sup>2</sup>University of Magdeburg, Department of Radiology and Nuclear Medicine, 39120 Magdeburg, Germany

<sup>3</sup>Hannover Medical School, Institute for Diagnostic and Interventional Radiology, Hannover, 30625, Germany

**Purpose.** The correct diagnosis and treatment of cancer patients is an urgent clinical need. Here, MRI-guidance is able to assist the performing clinicians not only during diagnosis but also during the actual intervention like biopsies or tumor ablations<sup>1</sup>. Due to soft tissue contrast, multiplanar navigation and lack of ionizing radiation it is often preferred over CT or US. Nonetheless, not all steps in the clinical workflow are unified and success of an interventional outcome highly depends on the expertise of the performing radiologist<sup>2,3</sup>. In this work, we performed a workflow analysis to identify key actions performed during minimally-invasive intervention as well as the development of a first specialized prototype to tackle common problems.

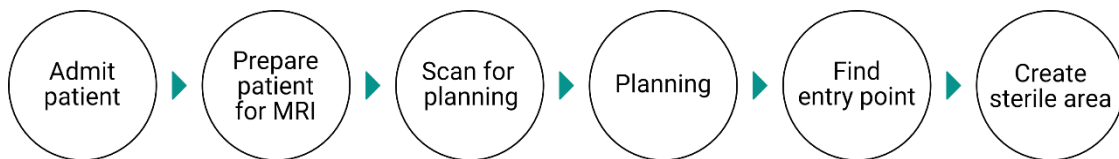


Figure 1: Non-sterile part of the unified interventional process.

**Material and Methods.** Initial analysis was conducted with two performing interventional radiologists from different hospitals. Here, a basic workflow could be derived from the interviews and protocols of the procedures. In a second step, a literature analysis was conducted resulting in 65 papers describing at least parts of the interventional workflow for minimally-invasive interventions. The basic workflow created was confirmed in most aspects and slightly adapted taking the literature results into account. In addition, a unified terminology derived from the literature was used. Based on these results, we implemented a first prototype for specialized software to aid the performing radiologist during the whole workflow procedure.

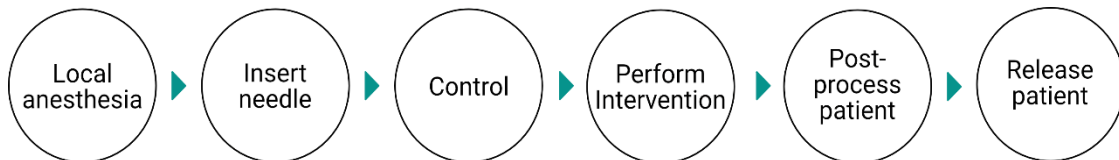


Figure 2: Sterile part of the interventional workflow.

**Results.** The workflow analysis was separated in a non-sterile (see Fig. 1) and a sterile (see Fig. 2) part of the process. In addition, we developed a first prototype (see Fig. 3) to cover the non-sterile part of the procedure covering and focusing on the core functionalities for defining entry and target points in an easy way. In addition, we provide a multi-device solution to simplify collaborative planning of interventions.

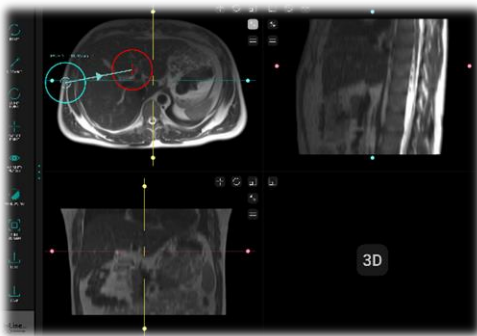


Figure 3: Software prototype showing a path planning and parts of the simplified UI.

**Conclusion.** We developed the first part of a navigational software based on a unified interventional workflow. The software does not provide unnecessary customization but focusses on the needs on an interventional radiologist while being easy to use. Future work will address the transfer of the planning data from a non-sterile environment into the sterile intervention room using scanner remote control protocols for direct scanner control.

## References

- <sup>1</sup>Reichert, A., Bock, M., Voge, M., & Krafft, A. J. (2019). GantryMate: a modular MR-compatible assistance system for MR-guided needle interventions. *Tomography*, 5(2), 266-273.
- <sup>2</sup>Moche, M., Heinig, S., Garnov, N., Fuchs, J., Petersen, T. O., Seider, D., ... & Busse, H. (2016). Navigated MRI-guided liver biopsies in a closed-bore scanner: experience in 52 patients. *European radiology*, 26(8), 2462-2470.
- <sup>3</sup>Weiss, C. R., Nour, S. G., & Lewin, J. S. (2008). MR-guided biopsy: A review of current techniques and applications. *Journal of Magnetic Resonance Imaging: An Official Journal of the International Society for Magnetic Resonance in Medicine*, 27(2), 311-325.

# Lateral Femoral Cutaneous Nerve Cryoablation for the Treatment of Meralgia Paresthetica: First Results of a Pilot Study

**Author Block** S. Walter<sup>1</sup>, D. Dalili<sup>2</sup>, J. Fritz<sup>1</sup>

<sup>1</sup>NYU Grossman School of Medicine, New York, NY, <sup>2</sup>South West London Elective Orthopaedic Centre, London, United Kingdom

**Purpose:** Symptomatic lateral femoral cutaneous neuropathy (meralgia paresthetica) may be treated successfully with perineural injections; however, a subset of patients with recalcitrant or recurring symptoms requires more effective intervention. Percutaneous cryoablation of nerves is an emerging minimally-invasive technique for the treatment of neuropathic pain. We describe the technique and outcomes of a pilot study investigating magnetic resonance neurography-(MRN)-guided cryoablation of the lateral femoral cutaneous nerve (LFCN).

## Materials and Methods

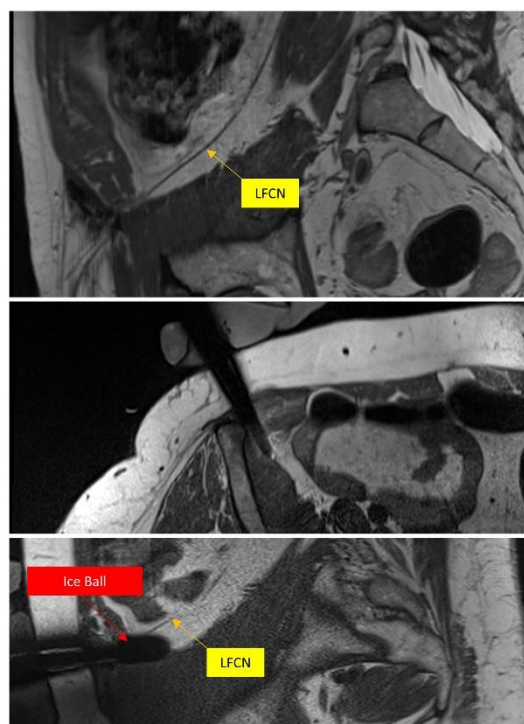
Ten patients (mean age, 52 years; range, 28 - 78 years) with selective nerve block-verified recalcitrant LFCN-mediated meralgia paresthetica were enrolled to undergo cryoablation of the LFCN. The LFCN was targeted in the retroperitoneum, proximal to the inguinal ligament. Procedures were performed under MRI guidance using clinical wide-bore MR imaging systems and commercially available cryoablation system with MR-conditional probes. Outcome variables included technical success, symptom relief measured on an 11-point visual analog scale, frequency of complications, and procedure time.

## Results

MRI-guided cryoablation of the LFCN was performed successfully in all ten patients. Real-time MRI was used to directly monitor the ice ball growth during two 6-min-freeze-3-min-active-thaw cycles, demonstrating complete ice ball incorporation of the LFCN. Mean procedure time was 98 (58-205) min. Post-interventionally, patients were treated with oral analgesia, including five days of Ketorolac and ten days of Ibuprofen. One month following cryoablation, 8/10 patients had > 50% pain relief, with mean pain scores decreasing from 8 (6-10) before to 2 (0-5) after the blocks ( $p < 0.001$ ). 6/8 patients described recurring symptoms after 10 (6-14) months. No complications occurred.

## Conclusion

MRN-guided cryoablation of the LFCN is a promising technique for treating meralgia paresthetica, permitting reliable identification of the LFCN in the retroperitoneum, selective targeting, and direct monitoring of iceball growth for intermediate-to-long-term pain relief.



### 3 Tesla Selective MR neurography-guided anterior femoral cutaneous nerve blocks for diagnosing anterior thigh neuralgia

**Author Block:** D. Dalili<sup>1</sup>, S. Ahlawat<sup>2</sup>, A. Isaac<sup>3</sup>, A. Rashidi<sup>2</sup>, J. Fritz<sup>4</sup>;

<sup>1</sup>South West London Elective Orthopaedic Centre, London, United Kingdom, <sup>2</sup>Johns Hopkins, Baltimore, MD, <sup>3</sup>Kings College London, United Kingdom, <sup>4</sup>NYU Grossman School of Medicine, New York, NY.

#### Purpose

To evaluate the clinical utility of selective magnetic resonance neurography-(MRN)-guided anterior femoral cutaneous nerve (AFCN) blocks for diagnosing anterior thigh neuralgia.

#### Materials and methods

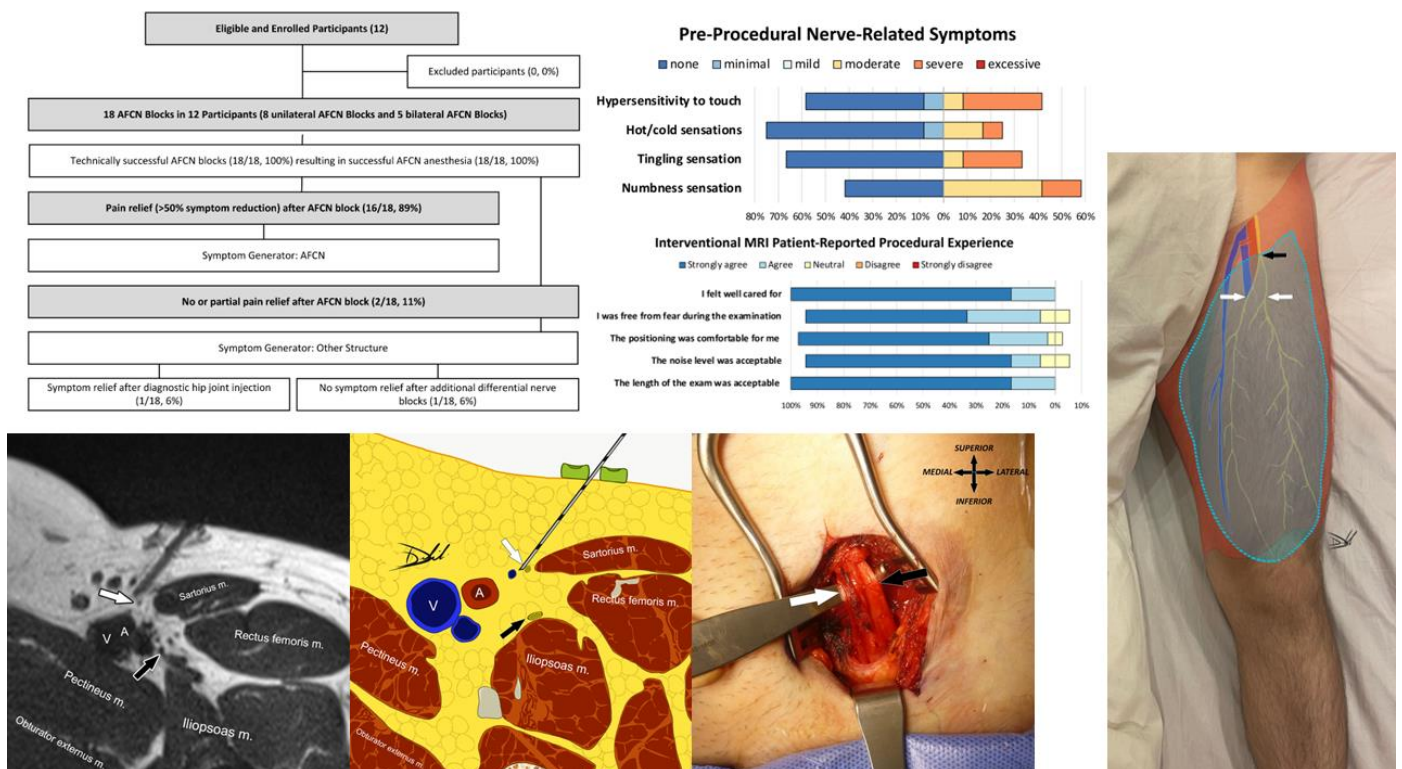
Following institutional review board approval and informed consent, participants with intractable anterior thigh pain and clinically suspected AFCN neuralgia were included. AFCN blocks were performed under MRN guidance using an anterior groin approach along the medial sartorius muscle margin. Outcome variables included AFCN identification on MRN, technical success of perineural drug delivery, rate of AFCN anaesthesia, complications, total procedure time, patient-reported procedural experiences, rate of positive diagnostic AFCN blocks, and positive subsequent treatment rate.

#### Results

Eighteen MRN-guided AFCN blocks (six unilateral and six bilateral blocks) were performed in 12 participants (6 women; age, 49 (30–65) years). Successful MRN identified the AFCN, successful perineural drug delivery, and AFCN anaesthesia was achieved in all patients. No complications occurred. The total procedure time was 19 (10–28) min. Patient satisfaction and experience were high without adverse MRI effects. AFCN blocks identified the AFCN as the symptom generator in 16/18 (89%) cases, followed by 14/16 (88%) successful treatments.

#### Conclusion

Our results suggest that selective MR neurography-guided AFCN blocks effectively diagnose anterior femoral cutaneous neuralgia and are well-tolerated



# One-Stop-Shop 3-Tesla MRI and MR-Guided MR Arthrography of The Shoulder: A Clinical Practice Evaluation with MSK Fellows

**Author Block:** D. Dalili<sup>1</sup>, A. Isaac<sup>2</sup>, J. Fritz<sup>3</sup>

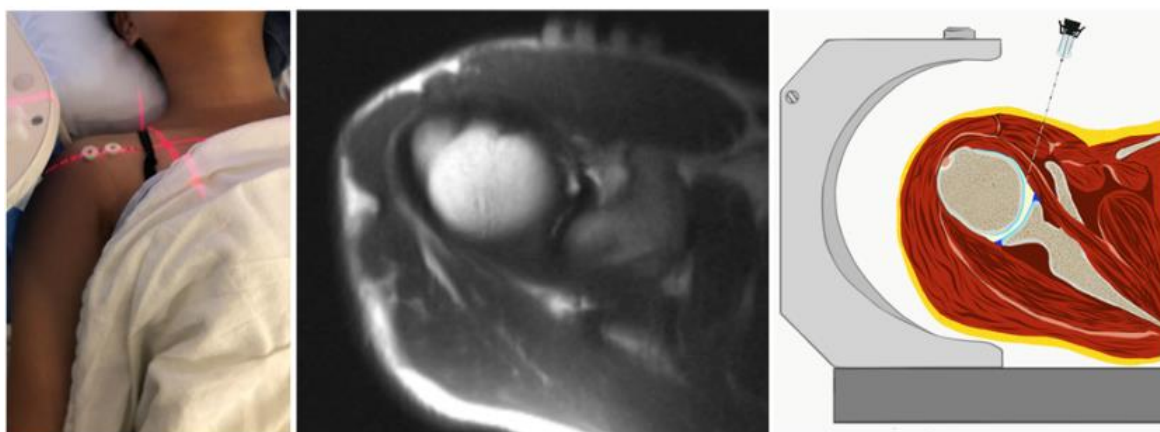
<sup>1</sup>South West London Elective Orthopaedic Centre, London, United Kingdom, <sup>2</sup>Kings College London, United Kingdom, <sup>3</sup>NYU Grossman School of Medicine, New York, NY.

**Purpose:** MRA of the shoulder can increase the diagnostic performance of MRI for internal derangement. However, MRI, glenohumeral injection, and MRA coordination may be challenging in certain practice settings, whereas MR-guided injection offers a one-stop-shop approach. We describe the technique, performance, learning curves, and patient experience of integrated 3T MRI and MRI-guided MRA.

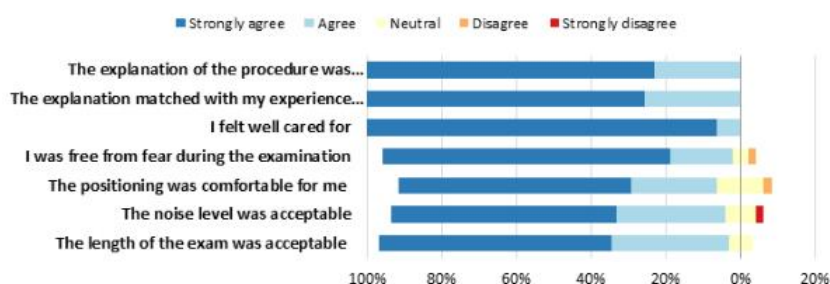
**Materials and Methods:** Following IRB approval and written consents, patients referred for combined MRI and MRA were prospectively enrolled between 2014 and 2019. Patients underwent MRI (00:23:33min acquisition time), MRI-guided glenohumeral joint injection, and MRA (00:08:016 min acquisition time) in the same setting using a commercial 3T wide-bore MRI scanner and shoulder coil. The procedures were performed by either one attending or one of 21 musculoskeletal fellows. Outcome variables including glenohumeral injection time, patient dwell time in the department, successful intra-articular injection, extravasation/capsular rupture, and major complications were compared with a matched historical cohort that underwent MRI + MRA with fluoroscopy-guided glenohumeral joint injection. Procedural patient experience and satisfaction were assessed for MR-guided MRA.

**Results:** 181 MR-guided MRAs were performed in 178 patients (114 men, 37 (11-77) years), with 100% successful intra-articular injection. MR-guided glenohumeral joint injections required 18 minutes, compared to 26 minutes under fluoroscopy ( $p < 0.001$ ). Fellows required 7-12 procedures to attain their average fastest procedure times (9-13min). The mean patient dwell time was 84 min with MRI guidance and 119 min with fluoroscopy guidance. Seven cases experienced capsular rupture with fluoroscopy (7/181, 3.87%), but none with MR guidance. Patient satisfaction was high. There were no major complications with either technique.

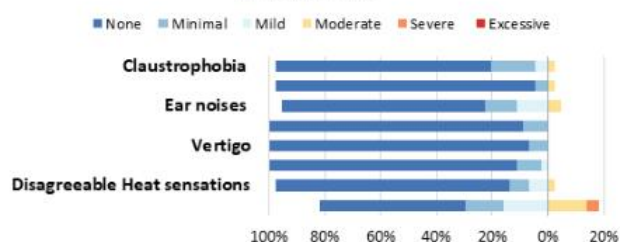
**Conclusion:** One-stop-shop 3T MR-guided MRI and MRA is effective, well-tailored, safe, and may reduce departmental patient dwell time compared to fluoroscopy-guided MRI and MRA. MSK fellows require an average of 10 procedures to attain proficiency.



**Interventional MRI Procedure Patient Satisfaction**



**Interventional MRI Procedure Related Side Effects**



# Focal MR-guided High-Dose-Rate Brachytherapy for Localized Prostate Cancer: A Prospective Clinical Trial

Enrique Gutierrez<sup>1</sup>, Matthew Ramotar<sup>1</sup>, Joelle Helou<sup>1</sup>, Srinivas Raman<sup>1</sup>, Rachel Glicksman<sup>1</sup>, Alexandra Rink<sup>1</sup>, Robert Weersink<sup>1</sup>, Peter Chung<sup>1</sup>, Alejandro Berlin<sup>1</sup>

1-Princess Margaret Cancer Centre, Radiation Medicine Program, University Health Network  
Abstract

## Purpose/Objective(s)

Focal therapy has gained traction in the management of localized prostate cancer (PCa) based on the promise of equivalent oncologic outcomes with minimal toxicity compared to whole gland therapy. However, 20-45% of patients have persistent/recurrent disease within the first 2-5 years after most commonly-used ablative methods (e.g., HIFU, cryotherapy). Based on brachytherapy's (BT) well-established and long track-record of efficacy for PCa, we sought to test the focal therapy hypothesis in a prospective clinical trial of MR-guided HDR for men with localized PCa.

## Materials and Methods

This prospective trial was approved in 2016 (UHN IRB# 16-5490; NCT02918253) for patients with clinically low- and favourable intermediate-risk prostate cancer, and a conspicuous lesion on mpMRI consistent with the area of pathological involvement. The CTV was derived from the mpMRI-defined GTV plus a 7 mm isotropic expansion, with 2 mm sup/inf added for the PTV. Implant and planning were performed with an MR-only workflow, and delivery with HDR BT. Treatment consisted of two separate implants within 14 days, to a prescription dose of 33-36 Gy in 2 sessions (BED  $\geq$  200 Gy). Biochemical recurrence (BCR) was calculated using the Kaplan Meier method. Local failure, distant metastasis (DM) and toxicity events are reported as absolute rates.

## Results

Nineteen patients have been treated, with a median age of 73 years (range 48-84), and median follow-up of 24 months (8-63). Median PSA was 6.1 ng/mL and 17/19 patients had Grade Group 2 disease. On average, the GTV and PTV corresponded to 3.56% (1.58-12.07) and 23.16% (13.71- 40.75) of the median prostatic volume (40.49 cc [ 25.57-97.6]). Median number of catheters was 7 (4-11). Median GTV D99 and PTV D95 per fraction were 23.82 Gy (18.50-31.89) and 18.71 Gy (16.01-20.64), respectively. Nine patients have undergone the 2-yr local control ascertainment; 7 with mpMRI plus biopsies, and 2 with mpMRI only. At 2-years, local control and BCR-free survival were 100%; a single BCR event has been recorded 34 months after treatment. No DM or death events have occurred. The rate of treatment-related acute and late toxicities that were graded  $\geq$  2 was 0%. Conclusion Focal MRI-guided HDR brachytherapy as monotherapy appears to have a high therapeutic ratio and is a promising technique for localized PCa. Further follow-up will determine the durability of outcomes with this approach and the need for collaborative randomized studies.

## Conclusion

Focal MRI-guided HDR brachytherapy as monotherapy appears to have a high therapeutic ratio and is a promising technique for localized PCa. Further follow-up will determine the durability of outcomes with this approach and the need for collaborative randomized studies.



Comparison of preprocedural and intraprocedural distances of the urethra to the prostatic capsule when performing prostate ablation with the TULSA-PRO device

David Sella MD, Jordan Legout MD, Ali Montazeri MD, Chandler Dora MD, Greg Frey MD, Mayo Clinic Florida

**PURPOSE:** The TULSA-PRO system combines real-time MRI, robotically driven transurethral thermal ultrasound and closed-loop temperature feedback control to perform whole gland or targeted ablation of prostate tissue. The transurethral ablation probe reaches targeted temperatures reliably at a maximum distance from the urethra of 3 cm. The distance of the urethra to the prostatic capsule often differs between the diagnostic prostate MR and the intraprocedural MR. We aim to determine a predictable change of distance from the urethra to the capsule of the posterolateral peripheral zone in the pre versus intraprocedural setting.

**MATERIAL AND METHODS:** Retrospective analysis was performed of 42 TULSA-PRO prostate ablations occurring between July 2020 and May 2022 for the primary indication of cancer. Measurements were obtained independently by 2 radiologists with subspecialty training in Body Imaging, one of whom performs the TULSA procedure. Preprocedure measurements obtained from the diagnostic prostate MR T2-weighted small FOV axial images included maximum transverse diameter of the prostate and maximum distance from the estimated position of the urethra to the prostatic capsule at the 3 to 6 and 6 to 9 o'clock positions. Intraprocedural measurements were obtained from the T2 planning images with ablation probe in place.

**RESULTS:** Mean and standard deviations were calculated for measurements obtained by each radiologist followed by a comparison of means between pre and intra measurements (average of 2 radiologists). Inter-reader reliability was calculated. A linear regression analysis was performed to predict intra measurements using pre measurements. The mean differences show a measurement difference in the position of the urethra relative to the capsule of  $4.3 \pm 2.4$  mm at the 3:00-6:00 position and  $4.1 \pm 2.1$  mm at the 6:00-9:00 position. The transverse dimension demonstrated the least difference of  $2.3 \pm 1.9$  mm.

	<b>RAD 1</b>	<b>RAD 2</b>	<b>Average measure</b>	<b>Inter-reader Reliability</b>	<b>P</b>
<b>Pre-3:00-6:00</b>	23.3 $\pm$ 4.1	24.1 $\pm$ 4.0	23.7 $\pm$ 3.8	85%	<0.001
<b>Pre-6:00-9:00</b>	23.7 $\pm$ 3.7	24.5 $\pm$ 3.9	24.1 $\pm$ 3.7	92%	<0.001
<b>Pre-Transverse</b>	48.8 $\pm$ 6.6	48.4 $\pm$ 7.0	48.6 $\pm$ 6.8	99%	<0.001
<b>Intra 3:00-6:00</b>	28.0 $\pm$ 4.0	28.0 $\pm$ 4.0	28.0 $\pm$ 3.9	93%	<0.001
<b>Intra-6:00-9:00</b>	28.1 $\pm$ 3.8	28.3 $\pm$ 3.9	28.2 $\pm$ 3.8	95%	<0.001
<b>Intra-Transverse</b>	51.0 $\pm$ 6.7	50.9 $\pm$ 6.8	51.0 $\pm$ 6.7	100%	<0.001

	<b>Pre</b>	<b>Intra</b>	<b>Mean Difference</b>	<b>P</b>
<b>3:00-6:00</b>	23.7 $\pm$ 3.8	28.0 $\pm$ 3.9	4.3 $\pm$ 2.4	<0.001
<b>6:00-9:00</b>	24.1 $\pm$ 3.7	28.2 $\pm$ 3.8	4.1 $\pm$ 2.1	<0.001
<b>Transverse</b>	48.6 $\pm$ 6.8	51.0 $\pm$ 6.7	2.3 $\pm$ 1.9	<0.001

**CONCLUSION:** Our analysis demonstrates the predicted variation in the distance of urethra to capsule on the preprocedure imaging relative to the intraprocedural imaging. This variation is based on a variety of factors including the rigidity of the ablation probe straightening the urethra, hypertrophied transitional zone, differences in imaging acquisition planes, and extrinsic deformation of the prostate secondary to the endorectal cooling device. It is possible that posterolateral peripheral zone tumors may “move” further from the ablation probe on procedure day to the extent where they reside outside the ablation zone. This possibility should be taken into consideration with regards to patient selection and demonstrates the need for a method to noninvasively predict the position of the urethra prior to obtaining the intraprocedural images.

# Estimating Uncertainty of 3D Ablation Zones using MR-Thermometry

S. Schröer, M. Gutberlet, K. Meyer zu Hartlage, J. Joaquin Löning Caballero, F. Wacker, B. Hensen  
Department of Diagnostic and Interventional Radiology, Medical School Hanover, Germany

**Objective** - MR-Thermometry allows real time monitoring of microwave ablation (MWA) procedures. In combination with the CEM<sub>43</sub> thermal dose model it can be utilized to estimate the size of ablation zones intraoperatively [1]. Unfortunately, this model is inaccurate for high temperatures as well as sensitive to magnetic field inhomogeneities and motion artifacts resulting in overestimation of the ablation zone [2][3][4][5]. Therefore, for improved decision support of the success of the procedure, in this work, we propose a probabilistic model that allows the estimation of uncertainty of the predicted ablation zone.

**Methods** - By transforming the probability density function (PDF) of the MRI measurement error according to the computations of MR thermometry and the CEM<sub>43</sub> model, the uncertainty of the predicted ablation zone is provided voxel by voxel. To evaluate the proposed algorithm, Gaussian noise with different standard deviations is introduced to an artificial dataset and its predicted uncertainty is compared to the resulting empirical uncertainty. Furthermore, uncertainty maps of the ablation zones of two microwave ablations (MWA) (ECO-100E, ECO Microwave, China, 15G) in polyacrylamide gel phantoms were calculated using Proton Resonance Frequency based MR thermometry on a 1.5 Tesla scanner (Siemens Avanto, Siemens Healthineers, Germany) based on a Multi-Echo-Stack-of-Stars sequence (echo time (TE): 10.5 ms, repetition time (TR): 14.5 ms, slice thickness: 2.5 mm, bandwidth: 1090 Hz / pixel, flip angle (FA): 15°, field of view (FOV): 320 x 320 x 60 mm<sup>3</sup>, matrix size: 128 x 128). Thermometry was performed with the microwave generator inside of the MR cabin (high electromagnetic interferences (EMI)) and with generator outside of the cabin and adding an EMI filter to the power line of the microwave applicator (low EMI).

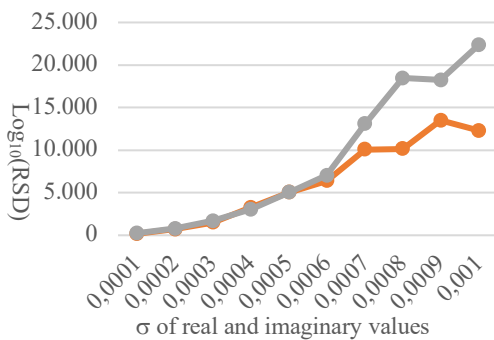


**Figure 1:** Empirical (grey) vs. Predicted (orange) Uncertainty for varying  $\sigma$

**Results** - For small standard deviations the predicted uncertainty approximately matches the empirical uncertainty and underestimates the uncertainty for standard deviations  $>0.0006$  (Fig. 1). As expected, the uncertainty map shows a reduced uncertainty in the non-heated regions compared to the ablation zone (Fig. 2) as well as the location of the microwave applicator. For the setup with increased EMI (left), the model provides higher uncertainty in areas erroneously assigned to the ablation zone. The average logarithmic relative standard deviations ( $\text{Log}_{10}(\text{RSD})$ ) in the non-heated region were 116.1 for the setup with high EMI (left) and -24.1 for the setup with low EMI (right).

**Conclusion** - The presented probabilistic model provides

uncertainties of the estimated ablation zones in real time during ablation. This may allow the interventionalist to better interpret the ablation zones assessed by MR thermometry impaired by noise and image artifacts. Future work will include further evaluation of this model in a patient study. Furthermore, the model will be extended to other sources of errors such as motion and other image artifacts.

**References** - [1] S. A. Sapareto and W. C. Dewey: Thermal dose determination in cancer therapy. *Int. J. Radiation Oncol. Biol. Physics* 1984; 10:787-800. [2] A. R. Moritz and F. C. Henriques, Jr.: Studies of Thermal Injury. ii. the relative importance of time and surface temperature in the causation of cutaneous burns. *Am J. Pathol* 1947; 23:695-720. [3] F.C. Henriques: Studies of thermal injury. v. the predictability and the significance of thermally induced rate processes leading to irreversible epidermal injury. *Arch Pathol* 1947; 43:489-502. [4] S. Suprijanto, M. Vogel, F. Vos, H. Vrooman, A. Vossepoel: Inter-frame Motion Correction for MR Thermometry. *Med Image Comput Comput Assist Interv.* 2005; 8:580-8. [5] F. F. J. Simonis, E. T. Petersen, L. W. Bartels, J. J. W. Lagendijk, C. A. T. van den Berg: Compensating for magnetic field inhomogeneity in multigradient-echo-based MR thermometry. *Mag. Reson. Med.* 2014; 73:1184-1189.

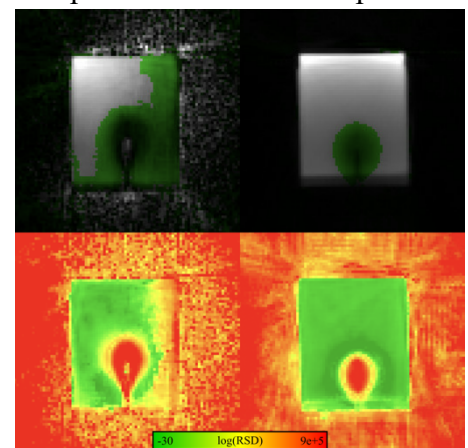


**Figure 2:** Magnitude images including the ablation zone (green area) assessed by MR thermometry (top) and the corresponding uncertainty maps (bottom) of high EMI data (left) and low EMI data (right)

## Higher resolution T1-weighted imaging of a liver lesion: a step to correlate thermal dose and lesion extent

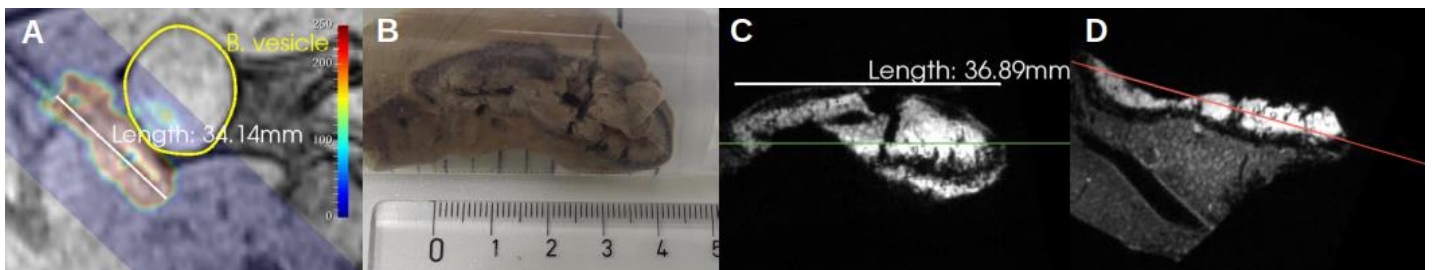
Thibaut Faller<sup>1</sup>, Dounia El Hamrani<sup>2</sup>, Pierre Bour<sup>1</sup>, Clément Marcelin<sup>3</sup>, Mathieu Guyot<sup>2</sup>,  
Valery Ozenne<sup>2</sup>, Bruno Quesson<sup>2</sup>.

<sup>1</sup>Certis Therapeutics, Pessac, France, <sup>2</sup>Univ. Bordeaux, CNRS, CRMSB, UMR 5536, IHU Liryc, F-33000  
Bordeaux, France, <sup>3</sup>CHU Bordeaux, Bordeaux, France.

**Purpose:** Microwave ablation is currently used to treat malignant liver tumors. Clinicians usually rely on the constructor's guidelines to select targeted temperature and duration of exposure. The dimensions and shape of the resulting thermal necrosis is assessed using contrast agent injection in MRI to assess the non-perfused volume, several days or weeks after the ablation. The thermal dose obtained from temperature maps with the Proton Resonance Frequency method has been shown to be a relevant parameter to assess thermal necrosis (Seror *et al.* [1], Köhler *et al.* [2]). In this study we aim to correlate T1-weighted (T1-w) high-resolution MR-images with gross pathology and thermal dose. High-resolution MRI may then be used to precisely characterize the lesion in a non-destructive manner as compared to gross pathology and histology.

**Material and methods:** This study was performed on a 1.5T Siemens scanner (Avanto fit, Siemens Healthineers, Germany). A MR-compatible microwave needle (medium size, Medwaves, USA) was inserted into the liver of a pig (33 kg, protocol approved by ethical committee) under ultrasound imaging guidance. A 5-minute ablation at 80°C target temperature measured by the device was performed under real-time MR-thermometry using a single-shot EPI sequence (Resolution: 2x2x3mm, FOV 256x256mm, 12 contiguous slices) under respiratory gating. Thermal dose maps (in Cumulative Equivalent Minutes at 43°C - CEM43) were computed using Certis Solution software (Certis Therapeutics, France) and overlaid on 3D T1-w gradient echo images acquired immediately after the ablation. The animal was sacrificed to excise the liver and the lesion was cut in the middle and fixed in formalin. After several days of fixation, samples were immersed in Fluorinert (Electronic liquid FC-770, 3M Electronics, St.Paul, USA) and imaged on a 9.4T Bruker MRI using a 3D T1-w gradient echo sequence (300  $\mu$ m isotropic, FOV:60x40x40, TE = 14ms, TR = 30ms, Flip Angle = 17°, 15 averages).

**Results:** *In vivo*, a high thermal dose (above 240 CEM43) area is measured on the last 34 mm of the probe as shown in figure (A). It covers a smaller hypersignal region in the T1-w image. On the corresponding sample (B), the lesion presents a large white zone around the probe surrounded by a red zone (B). T1-w image acquired at 9.4T clearly shows these two zones, with hyperintense and hypointense signals, which seemingly correspond to the white and red zones observed on the sample in (B).



**Analysis of liver ablation.** A: Dose map overlaid on the 3D T1-w image (scale between 0 and 250 CEM43). B: Corresponding sample immersed in Fluorinert solution. C-D: Corresponding orthogonal views of the 3D FLASH image at 9.4T (the colored line represents the slice intersection).

**Conclusion:** Coherent dimensions are observed *in vivo* (thermal dose) and *ex vivo* (T1-w and gross pathology). High resolution T1-w may be a good candidate to establish a ground truth lesion size and characterize the different lesion areas (necrotic and hemorrhagic), in 3D and in a non-destructive manner. Further gross pathology and histology will be conducted to assess cells integrity in the different areas observed on high resolution T1-w images.

**References:** [1] Seror *et al.*, Real time monitoring of radiofrequency ablation based on MR thermometry and thermal dose in the pig liver *in vivo* (2017), [2] Köhler *et al.*, Philips MR-guided High Intensity Focused Ultrasound (2011)

# Rapid 3D post-ablation assessment of thermal ablation using accelerated Wave-Encoding MRI

Author List: Quentin Lebre<sup>1</sup>, Pierre Bour<sup>1</sup>, Valéry Ozenne<sup>1</sup> and Bruno Quesson<sup>1</sup>

Univ. Bordeaux, CNRS, CRMSB, UMR 5536, IHU LIRYC, F-33000 Bordeaux, France

## Purpose

MRI-guided thermal ablation procedures are increasingly used in various organs. In addition to real-time imaging during the procedure (e.g. thermometry), rapid 2D/3D images are usually acquired immediately after thermal ablation to assess completion of the procedure or if additional ablation must be performed (Giles et al, BJR, 2019). T1-weighted imaging without or with contrast agent injection is a method of reference but requires long acquisition time, particularly in moving organs such as the heart (Guttman et al, SCMR, 2016). We present an adaptation of the Wave CAIPI sequence (Biglic et al, MRM 2015), based on a variable density subsampling mask, designed to reduce acquisition duration by a factor of 4 for rapid 3D imaging of lesions. The method is evaluated immediately after a laser ablation on a swine leg.

## Material and Methods

A wave encoded GRE sequence was implemented at 1.5T (Avanto Fit, Siemens Healthineers) with an incorporated inversion preparation module for T1-weighting (Fig 1). Wave gradients amplitude was set to 4mT/m, with 3 sinusoidal periods during the readout. Sequence parameters: TE = 5.85ms; TR = 9.9ms; Flip angle = 15°; bandwidth = 250Hz/px. The fully sampled in-vivo acquisition was reconstructed to create a reference 3D volume before retrospective subsampling (using a Variable Density Poisson undersampling mask) to simulate accelerated acquisitions. Sequence was evaluated on an anesthetized pig (33 kg body mass) after laser thermal ablation on the leg (without injection of contrast agent) and in a sheep model of cardiac infarct (including ECG triggering and navigator compensation of respiratory motion) after injection of gadolinium (to simulate a contrast, as observed in catheter-based radiofrequency ablation). Protocols were approved by ethic committee.

Sequence parameters: TE = 5.85ms; TR = 9.9ms; Flip angle = 15°; bandwidth = 250Hz/px. The fully sampled in-vivo acquisition was reconstructed to create a reference 3D volume before retrospective subsampling (using a Variable Density Poisson undersampling mask) to simulate accelerated acquisitions. Sequence was evaluated on an anesthetized pig (33 kg body mass) after laser thermal ablation on the leg (without injection of contrast agent) and in a sheep model of cardiac infarct (including ECG triggering and navigator compensation of respiratory motion) after injection of gadolinium (to simulate a contrast, as observed in catheter-based radiofrequency ablation). Protocols were approved by ethic committee.

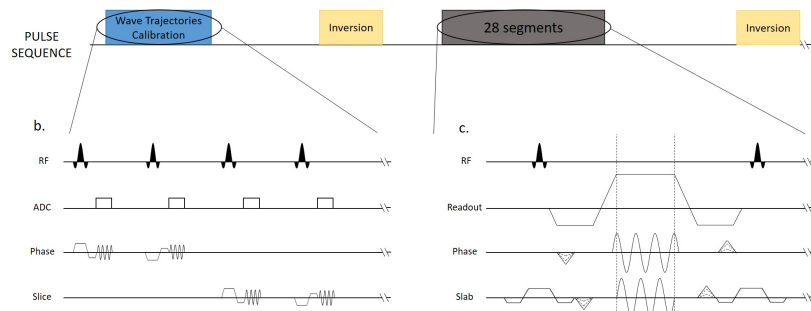


Figure 1 : Sequence Chronogram. A calibration module is needed prior to the acquisition (24 s duration) to estimate the phase added by the wave gradients.

## Results

Fully sampled (Fig. 2A, 4'30s acquisition) and subsampled (Fig. 2B, ~1'30s acquisition) transverse view of the 3D data set (1.1 mm<sup>3</sup> voxel, TI=340 ms) acquired after laser ablation on the leg show a hyperintense signal in the ablated area (red arrows). Fig. 2C (18' acquisition) and Fig. 2D (~4'30s acquisition) show a 4 chamber cardiac view with an apical cardiac infarct (1.4 mm<sup>3</sup> isotropic resolution). Despite a loss in SNR inherent to subsampling, lesions are clearly visible for both experiments.

## Conclusion

The proposed sequence provides high-resolution T1-weighted 3D images to visualize lesions. Comparison with Grappa acceleration of 4 (data not shown) shows superior image quality with the proposed technique. 3D wave encoding can be applied with and without contrast agent injection on static and mobile organs. Acceleration of 4 results in acceptable acquisition durations (4 minutes in the heart and 1'30 in the muscle) to repeat the sequence during the procedure for iterative assessment of treatment completion.

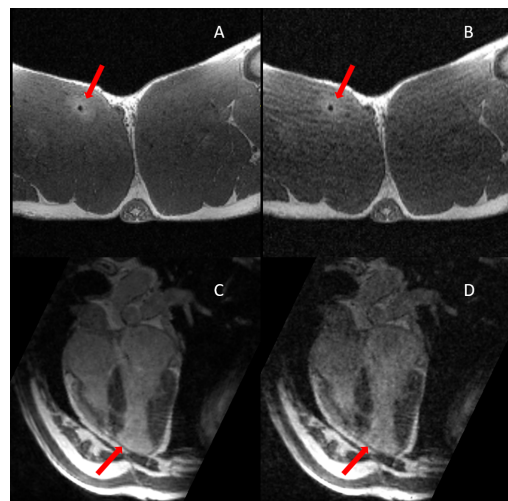


Figure 2 : Example of fully (left) and subsampled (right) images on pig leg and sheep heart.

# Real time volumetric MR-temperature monitoring during microwave ablation of a patient with hepatocellular carcinoma

Osman Öcal<sup>1</sup>, Sergio Lentini<sup>1</sup>, Pierre Bour<sup>2</sup>, Thibaut Faller<sup>2</sup>, Jens Ricke<sup>1</sup>, Olaf Dietrich<sup>1</sup>, Max Seidensticker<sup>1</sup>

<sup>1</sup>Department of Radiology, University Hospital, LMU Munich, Munich, Germany

<sup>2</sup>Certis Therapeutics, Pessac, France

## Background

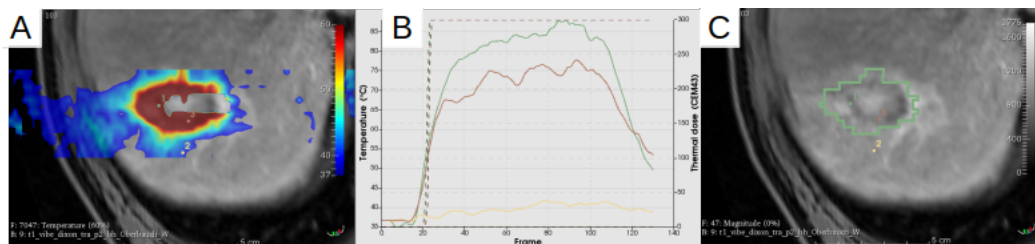
Microwave ablation of primary and secondary liver tumors is routinely used in clinical practice with curative intent. However, local recurrence due to incomplete ablation of tumor has been reported up to 6% [1, 2]. In addition to better visualization and targeting of the tumor with MRI guidance, it offers the possibility to monitor the energy delivery using temperature and thermal dose mapping [3].

## Methods

A 62-years old male patient with liver cirrhosis due to hepatitis C infection was referred for microwave ablation of hepatocellular carcinoma lesion in segment 5. Local ablation was treated under general anesthesia using a 1.5T MRI scanner (Siemens). The ablation probe (14G) was inserted under real-time MRI guidance, and ablation was performed using the AveCure microwave system (MedWave). Two rounds of ablation were monitored by MR-thermometry using respiratory triggering. Temperature and thermal dose monitoring covered the entire ablation area.

## Results

Temperature and thermal dose were successfully monitored and showed complete coverage of lesion. The targeted temperature was reached within the entire lesion. MRI images obtained 1 day and 3 months after the ablation showed no residual tumor.



## Conclusion

This report shows the feasibility of a fully MRI-guided microwave ablation procedure with real-time thermal dose monitoring.

## References

- [1] Violi, Naik Vietti, et al. "Efficacy of microwave ablation versus radiofrequency ablation for the treatment of hepatocellular carcinoma in patients with chronic liver disease: a randomised controlled phase 2 trial." *The lancet Gastroenterology & hepatology* 3.5 (2018): 317-325.
- [2] Chong, Charing CN, et al. "Prospective double-blinded randomized controlled trial of Microwave versus RadioFrequency Ablation for hepatocellular carcinoma (McRFA trial)." *HPB* 22.8 (2020): 1121-1127.
- [3] Weidensteiner, C. et al. Stability of real-time MR temperature mapping in healthy and diseased human liver. *Journal of magnetic resonance imaging: JMRI* 19, 438–446 (2004).

# Echo time selection in PRFS MR-thermometry to minimize errors in adipose tissues

Anne Josset, Jonathan Vappou, Karine Choquet, Ounay Ishak, Elodie Breton

Université de Strasbourg, CNRS, ICube, UMR7357, Strasbourg, France

**Purpose:** MRI-PRFS (Proton Resonance Frequency Shift) is the current gold standard for the monitoring of MR-guided thermal ablations. However, the resonance frequency of hydrogen nuclei present in lipids is almost independent of temperature, which causes errors in the estimated temperature in fat-containing tissues. This error depends on the water-fat fraction and varies cyclically with the echo time TE, i.e. water and fat signals interact either constructively or destructively, with local maxima being denominated in-phase and out-of-phase, respectively. Currently, the optimal TE is chosen close to the T2 of the tissue in order to optimize the phase-to-noise ratio [1]. This work discusses the importance of also considering the cyclic nature of the temperature error due to the presence of fat when choosing TE in PRFS temperature images.

**Methods:** Complex fat-water signals with in- and out-of-phase TE at 37°C were simulated at 1.5T with a single peak fat model (3.35 ppm) for various fat fractions (FF) over the temperature range 37 to 99°C. The reference phase used for PRFS is the one calculated at 37°C to imitate a realistic clinical situation. Temperature errors are calculated for each TE as the difference between PRFS-thermometry in the presence of fat and reference temperature. In addition, images at multiple in- and out-of-phase TEs were acquired with a multi-echo gradient echo sequence (acquisition time 10 s) in mayonnaise (70% fat) heated in a hot water bath. The temperature elevation was measured by PRFS for in- and out-of-phase TEs and by an optical probe (Rugged Monitoring, Québec, Canada) considered as the reference. Expected errors were also simulated considering a 70% fat model.

**Results:** Systematic temperature underestimation is found in simulation with in-phase TE while under or over-estimations depend on FF and temperature increase with out-of-phase TE (Figure 1). With 10% fat, the maximal error is -2.76 °C and 2.66°C for in- and out-of-phase TE, respectively. Mayonnaise experimental curves show good agreement with simulation (Figure 2) even though the experimental errors are larger. Temperature errors are larger for out-of-phase compared to in-phase TEs.

**Discussion:** The experiment in mayonnaise suggests that the simulated model needs to be improved, for instance with multiple fat peaks. The absolute error at 55°C is systematically smaller in-phase compared to out-of-phase. While temperature errors strongly alter thermal dose estimation, the systematic temperature underestimation found in-phase may not adversely modify the outcome of hyperthermia therapy when considering a temperature threshold to reach.

**Conclusion:** As fat-suppression is not 100% efficient [2], this work highlights the importance of careful TE selection in PRFS-thermometry in order to mitigate the effect of the presence of fat.

[1] Chung A. H et al, *Mag Reson Med* 1996, 36(5):745-52; [2] Bernstein M.A. et al, "Handbook of MRI Pulse Sequences", Elsevier Academic Press 2004

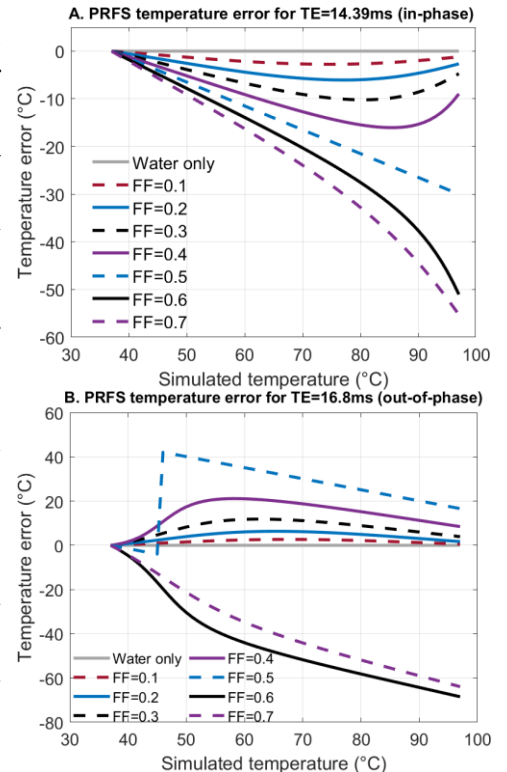


**Figure 1** – Simulated temperature errors for different fat fractions **A.** TE = 14.39 ms, in-phase; **B.** TE = 16.8 ms, out-of-phase

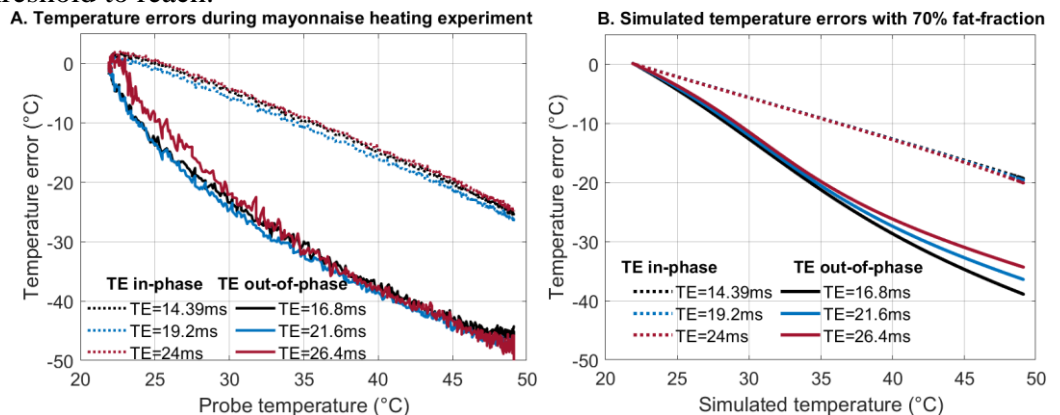


**Figure 2** – Temperature errors with 70% fat for different TEs **A.** Experimental curves between PRFS-thermometry and optical sensor in mayonnaise **B.** Simulated temperature errors

## Assessment of MR compatibility of focused ultrasound systems

Nicolas Evripidou, Marinos Giannakou, Christakis Damianou

<sup>a</sup> Department of Electrical Engineering, Computer Engineering, and Informatics, Cyprus University of Technology, Limassol, Cyprus.

### ABSTRACT

**Background:** This study presents a comprehensive assessment of the MRI compatibility issues of Magnetic Resonance guided Focused Ultrasound (MRgFUS). The effect of coil type, target size and coil placement are a few of the conditions examined. In the effort to minimize image distortion and interference with the magnet, various set-up parameters were examined.

**Methods:** The experiments were performed in a 1.5 T and 3 T MRI scanners. The main quantity measured for MRI compatibility was the signal to noise ratio (SNR). Measurements were carried out in a tissue mimicking phantom and freshly excised tissue under various activation states of the robotic system and ultrasonic transducer.

**Results:** Significant image distortion occurred when the transducer was activated due to coil and target vibrations and was getting worse as the output power was increased. It was proven that the use of a multi-channel fixed coil and a stable target was critical in increasing SNR. The motors and associated electronics should be placed outside the coil detection area so that image quality is not jeopardized. It is also crucial to have the encoders' counting pulses turned off during image acquisition since this was also shown to increase SNR remarkably. The SNR in a 3 T was much higher than the 1.5 T, and therefore it is easier to place focused ultrasound systems in higher field MRIs

**Conclusions:** The study contributes towards addressing major challenges regarding operation of an MRgFUS system in the MRI environment and raises awareness for potential sources of noise and distortion to researchers in the field. Although many years ago placing electronic systems in the MRI was challenging, it is now a common routine.

# Design of a new MR-compatible HIFU device for intercostal sonication into the heart

Author List: Mathieu Guyot<sup>1</sup>, Erik Dumont<sup>2</sup> and Bruno Quesson<sup>3</sup>

<sup>1</sup> Univ. Bordeaux, INSERM, CRCTB, U 1045, IHU Liryc, F-33000 Bordeaux, France, <sup>2</sup>Image Guided Therapy SA, Pessac, France, <sup>3</sup>Univ. Bordeaux, CNRS, CRMSB, UMR 5536, IHU Liryc, F-33000 Bordeaux, France

## Purpose

Ventricular cardiac arrhythmia is a major life threatening pathology (high risk of sudden cardiac death). Current ablative technologies rely on percutaneous insertion of a catheter to create a localized thermal lesion in the targeted myocardium using radiofrequency, cryoablation or irreversible electroporation. However, creating a transmural lesion over the ventricular wall (up to 15 mm thickness) remains highly challenging with such technologies. We present a High intensity focused ultrasound (HIFU) device designed for intercostal sonication and characterize it under MR-thermometry/MR-acoustic radiation force imaging.

## Material and Methods

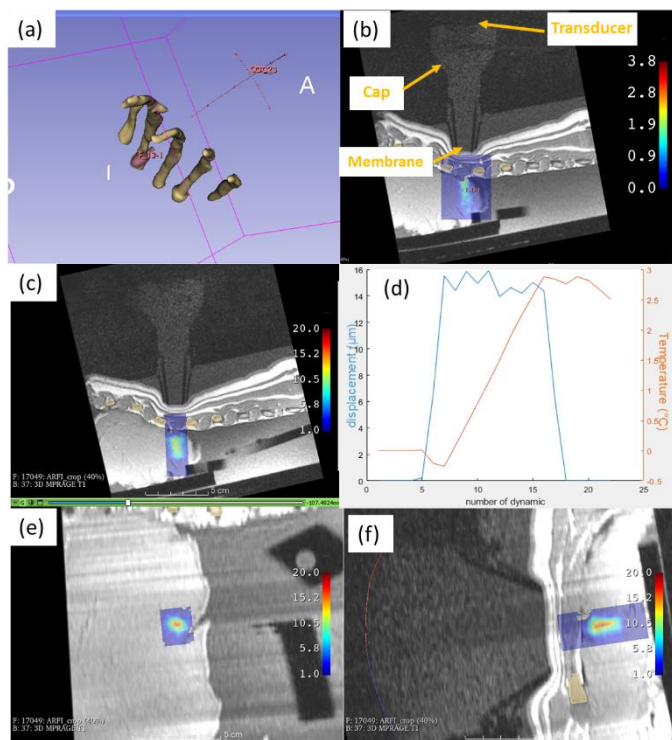
The device consists of a 32 elements HIFU transducer (Imasonic, focal 13 cm, asymmetric aperture of 12 cm and 2 cm, 1 MHz frequency) connected to a programmable generator (Image guided therapy, 32 channels, 1.6 kW peak electrical power) through an impedance matching box. A dedicated cap was 3D printed and terminated with a 50  $\mu$ m Mylar membrane, resulting in an acoustic window of 40x11 mm positioned 30 mm before the focal point. 3D Pressure field at the focus was measured in a bench test with a raster of 3D low pressure measurements (Onda, Hydrophone HGL200). A second set of measurements at high power was performed using the balance radiation force method. MR-ARFI/thermometry was performed at 1.5 T (Aera, Siemens Healthcare) using a modified single shot EPI [1] that incorporates motion encoding gradients (MEG, 20 mT/m, 2ms amplitude each) with 5 slices, TE=26 ms, FOV=188x188 mm<sup>2</sup>, resolution=1.5mm x1.5mm, 3 mm slice thickness, 4 averages, 2s repetition time. Displacement maps and temperature images were thus simultaneously measured ex vivo in a pig muscle positioned behind a pig rib cage sample (HIFU transducer positioned to sonicate between two ribs), with HIFU pulses of 5 ms synchronized with the MEG.

## Results

	Acoustic parameters
Size of Beam (-3dB)	[6 mm, 1mm, 10 mm]
Efficiency of the system (generator+ transducer)	>75%
Maximum of acoustic power	1,28 kW

**Figure 1:** characterization of the HIFU device from lab bench experiments

**Figure 2:** (a) 3D segmentation of the rib bones from a 3D MPRAGE sequence. Maximal measured intercostal space was 17 mm; (b) MR-Thermometry image showing temperature increase in the muscle beyond the ribs induced by 5 ms HIFU pulses (110 repetitions) of 460 acoustic watts (5% duty cycle). (c, e, f) MR-displacement images data showing localization and dimensions of the resulting ARFI push in 3 orthogonal directions. (d) Temperature and displacement curves measured simultaneously from the modified EPI sequence (8 second/acquisition).



## Conclusion

The device is MR-compatible and able to sonicate beyond the ribs through the intercostal space without overheating the ribs. Real-time MR-ARFI/MR-thermometry allows visualizations and characterization of local tissue displacement and temperature increase in soft tissue (muscle and intercostal space) for treatment monitoring and safety assessment. Reported experiments were intentionally performed at low acoustic energy (5% duty cycle at 40% of maximal acoustic power) for characterization purpose and resulted in moderate temperature increase (3 $^{\circ}$ C). In vivo evaluation is required to assess therapeutic capabilities of the device under higher regimes of operation in perspective of non-invasive MR guided HIFU ablation of cardiac arrhythmia.

[1] Bour et al, Magn Reson Med. 2017 Nov;78(5):1911-1921.



# Combination of MRI-guided HIFU, bioluminescence imaging and transgenic mouse model to assess efficiency of noninvasive thermal therapies for solid tumors and their microenvironments

Dounia El Hamrani<sup>1</sup>, Pauline Jeanjean<sup>2</sup>, Coralie Genevois<sup>2</sup>, Franck Couillaud<sup>2</sup>, Bruno Quesson<sup>1,3</sup>

<sup>1</sup>Univ. Bordeaux, INSERM, CRCTB, U 1045, IHU Liryc, F-33000 Bordeaux, France;

<sup>2</sup>Univ. Bordeaux, INSERM, BRIC U1312 & IMOTION EA7435, F-33000 Bordeaux, France;

<sup>3</sup>Univ. Bordeaux, CNRS, CRMSB, UMR 5536, IHU Liryc, F-33000 Bordeaux, France.

**Purpose:** To improve the efficiency of tumor treatments, one strategy is to combine therapies that alleviate tumor cells by inducing thermal coagulation necrosis while stimulating the tumor microenvironment (TME) for inducing anticancer effects (e.g. drug delivery, immunotherapy). The aim of this work is to present a dual approach using MRI-guided high intensity focused ultrasound (MRgHIFU) for non-invasive thermo-therapy and bioluminescence imaging (BLI) to visualize concomitant thermal effects targeting both thermo-ablation of tumor cells and mild hyperthermia of the TME. This technology is combined with a sophisticated transgenic mice model having different BLI reporters for tumor cells and TME.

**Material and methods:** Transgenic mice were modified to express heat-induced luciferase with a heat shock protein promoter (Hsp-Fluc) to follow the TME response by *in vivo* BLI (n=10) (X. de la Rosa et al. *Eur. J. Nucl. Med. Mol. Imaging* 2013). These mice were implanted on the hind leg with cancer cells exhibiting constitutive-luciferase expression to follow tumor cell viability (RM1-CMV-Nluc) (L. Adumeau et al. *Biochim. Biophys. Acta, Gen. Subj.* 2017). Prior and after MRgHIFU, BLI acquisition was performed using the Lumina LT imaging system (Perkin Elmer Inc.).

MRgHIFU experiments were performed on a 9.4 T MRI scanner (Bruker Biospin 9.4/30). The hind leg of the anesthetized mouse was positioned underneath a HIFU transducer (Imasonic, France) contained 8 ring elements operated at 2.4 MHz: aperture = 25 mm, focal length = 20 mm; focal point = 5 mm in length x 1 mm in width. Scout MR-images were used to position the transducer relative to the tumor and to avoid sonicating in bones and/or viscera. For MR-thermometry, a FLASH sequence was used with 3 slices positioned orthogonal to the ultrasound beam axis and centered on the focal point, TR = 25 ms, TE = 5 ms, 96 x 96 matrix size, field of view = 64 x 64 mm, in-plane resolution = 667 x 667  $\mu\text{m}^2/\text{pixel}$ , slice thickness = 1 mm, flip angle = 10°, bandwidth = 50 kHz, 2.4 s temporal resolution per stack of images.

Temperature images were processed on the fly using the water proton resonance frequency shift (PRF) technique and were displayed online in Thermoguide software (Image Guided Therapy, France) which also regulated the tumor temperature in a single pixel by automatically adjusting the output power of the HIFU generator to follow a predefined temperature-time profile. Thermometry data were re-processed offline with custom software written in MATLAB (Mathworks, ver. R2020a). In each pixel, the average temperature during the plateau of heating (i.e. 25 images for 1 min) and over 9 adjacent pixels centered on the controlled pixel was computed.

**Results:** Figure 1 shows a representative result of MRgHIFU experiment. Before heating, BLI revealed a strong signal from constitutive Nluc expression by tumor cells, but no signal from Fluc by the TME. Then, a thermo-coagulation heating protocol (temperature range from 54 to 62 °C for 1 min) was applied to tumors by MRgHIFU. After heating, an overall decrease of BLI (Nluc) signal in the tumor is observed, indicative of area of tumor thermal necrosis. In tissues surrounding the tumor (TME), BLI signal (Hsp-Fluc) displays a “ring-shaped” photon distribution resulting from moderate, non-lethal, temperature

increase surrounding the central necrotic area. This photon distribution is indicative of sufficient thermal stress to activate BLI signal (Hsp-dependent transcription of FLuc), while remaining nondestructive for the tissue.

**Conclusion:** This proof-of-concept study highlighted the advantage of modulating heat deposition by MRgHIFU in order to exploit different thermal effects in the tumor (ablative therapy by coagulation necrosis) and its microenvironment (moderate temperature increase) (P. Jeanjean and D. El Hamrani et al. *Adv. Mater. Technol.* 2022). Combination with this transgenic mouse model allows direct *in vivo* evaluation of innovative thermo-therapies strategies (ablation associated to drug delivery and/or immunotherapy) by assessing the physiological response of the tumor and TME non-invasively.

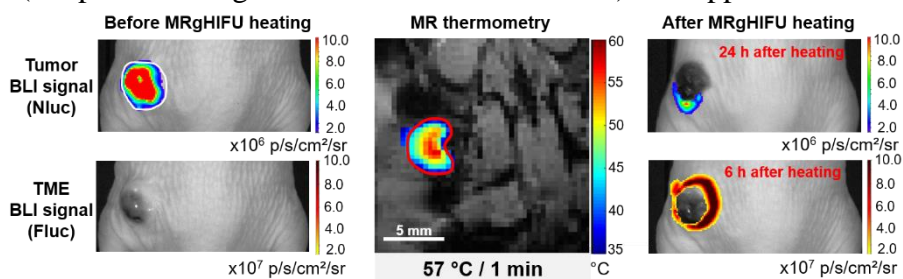


**Figure 1:** Tumor thermal ablation by MRgHIFU heating and BLI

# MR-GUIDED HIGH INTENSITY FOCUSED ULTRASOUND THERAPY MONITORING USING TRANSIENT SUPERSONIC SHEAR WAVE MR-ELASTOGRAPHY

Ounay Ishak<sup>1</sup>, Elodie Breton<sup>1</sup>, Karine Choquet<sup>1</sup>, Anne Josset<sup>1</sup>, Paolo Cabras<sup>1,2</sup> and Jonathan Vappou<sup>1</sup>

<sup>1</sup>Université de Strasbourg, CNRS, ICube, UMR7357, Strasbourg, France

<sup>2</sup>Image Guided Therapy, Pessac, France

**Purpose:** Mechanical properties are promising biomarkers of tissue structural integrity during thermal ablations [1]. While most Magnetic Resonance (MR) elastography methods rely on dedicated instrumentation, electronic steering provides a unique opportunity for generating the mechanical wave for High Intensity Focused Ultrasound (HIFU) ablation monitoring. In this work, both MR-Supersonic Shear wave Imaging (MR-SSI) and MR Thermometry (MRT) are combined to monitor HIFU ablations.

**Methods:** MR-SSI uses the same ultrasonic transducer for both mechanical wave generation and thermal ablation. Transient quasi-planar shear waves are obtained by applying several acoustic radiation force pushes successively. This mechanical excitation is synchronized with a Motion-Sensitizing Gradient (MSG) embedded in the MRI sequence to encode the displacement at different phases of the wave propagation (called “SSI steps”) [2]. The proposed process allows reconstructing shear modulus maps of the imaged medium using an edge detection approach followed by a time-of-flight-based method for the computation of shear wave velocity. Experiments were performed using a 128-element spherical HIFU transducer (1 MHz central frequency, 6 cm radius of curvature, 6 cm in aperture, Imasonic, France) driven by an MR-compatible HIFU generator (Image Guided Therapy, France). MR images were acquired on a 1.5 T MRI system (MAGNETOM Aera, Siemens Healthcare, Germany) using a single-shot gradient-echo echo-planar-imaging (EPI) sequence (TR/TE 500/29 ms, FOV 256×176 mm, slice thickness 5 mm, matrix 128×88, MSG duration 10 ms at 30 mT/m). Thermometry maps were also computed from the same MR images using the Proton Resonance Frequency Shift (PRFS) approach. The method has first been validated on a calibrated elasticity phantom containing several inclusions of different shear moduli. Then, a HIFU ablation has been performed on a gelatin phantom to assess the ability to monitor elasticity changes in real-time during the hyperthermia (120 s) and the following cooling phase (120 s). 10 SSI steps were needed for the reconstruction of one elastogram, corresponding to an acquisition time of 10 s.

**Results:** Temperature and elasticity maps (Figure 1) were obtained with refresh rates of 1 and 0.1 Hz respectively. During the HIFU ablation experiment, the PRFS temperature increased by 9 °C and the shear modulus obtained with MR-SSI decreased from 2.9 kPa ± 5% to 1.8 kPa ± 17% (Figure 2). These results indicate that the gel softens around the HIFU focus, whereas it remained steady in non-heated areas.

**Discussion:** The MR-SSI method has been shown to allow mapping both spatial and temporal variations of elasticity during a HIFU ablation. The method remains limited by its low spatial resolution and coverage. A pre-ablation acquisition may be necessary to identify the optimal number of SSI steps to cover the desired area.

**Conclusion:** Fast MR-SSI with electronic steering can be a promising technique to assess the structural changes of tissue during HIFU treatment, in parallel to temperature changes.

## References:

- [1] B. Arnal et al, IEEE TUFFC, 2011, 58(8):1603.
- [2] Y. Liu et al., PMB, 2017, 62(10):4083.

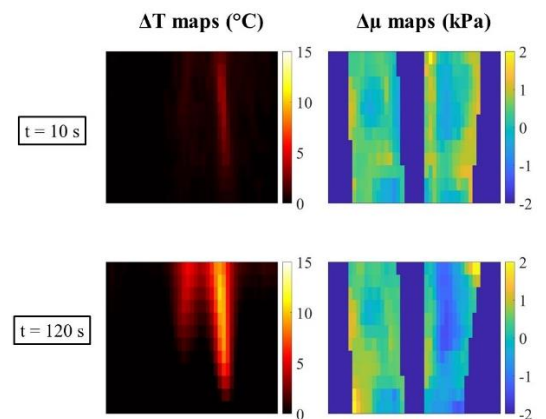


**Figure 1** – Thermometry and elastography maps before and after the HIFU ablation

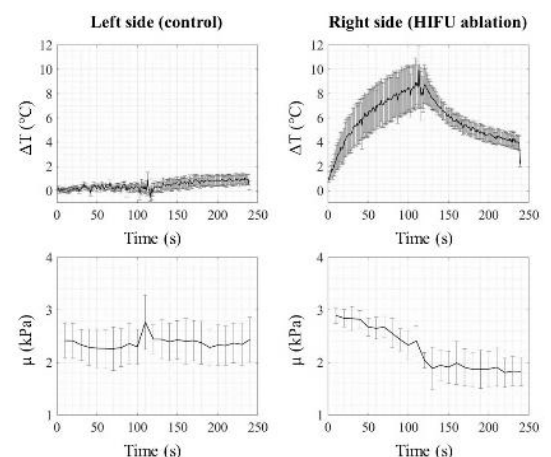


**Figure 2** – Changes in temperature and shear modulus (5×3-pixel ROI) on the left (control) and right (HIFU heating) sides of the SSI push line

## MR-HIFU as treatment option for desmoid tumors in the abdominal wall: clinical setup and first results

Leonhardi J<sup>1</sup>, Surup H<sup>1</sup>, Donig J<sup>1</sup>, Bailis N<sup>1,2</sup>, Hoffmeister A<sup>3</sup>, Schönherr T<sup>4</sup>, Niebisch S<sup>4</sup>, Gockel I<sup>4</sup>, Melzer A<sup>5</sup>, Martin M<sup>1</sup>, Ebel S<sup>1</sup>, Gößmann H<sup>1</sup>, Busse H<sup>1</sup>, Denecke T<sup>1</sup>

<sup>1</sup> Department of Diagnostic and Interventional Radiology, University Hospital Leipzig, Germany

<sup>2</sup> Institute of Neuroradiology, University Hospital Leipzig, Germany

<sup>3</sup> Department of Gastroenterology, University Hospital Leipzig, Germany

<sup>4</sup> Department of Visceral, Transplant, Thoracic and Vascular Surgery, University Hospital Leipzig

<sup>5</sup> Innovation Center Computer Assisted Surgery, Leipzig University, Germany

**Background** Desmoid tumors are rare soft tissue tumors that typically present with local invasive growth. Although they do not metastasize, the quality of life can be highly reduced [1]. While surgical resection is an option, 5-year recurrence-free survival rates may only be between 23% and 68% (depending on mutation status) [2, 3]. For larger tumors of the abdominal muscles, resection may lead to instabilities and functional impairment of daily life in the typically younger patients. MRI-guided high-intensity focused ultrasound (MR-HIFU) is a non-invasive ablation option that has been associated with tumor debulking, local tumor control and sometimes even complete remission [4].

**Purpose** To describe the clinical setup and report on our first results with MR-HIFU treatment of desmoid tumors of the abdominal wall.

**Methods** Three patients (27–32 years) with desmoid tumors of the abdominal wall underwent MR-HIFU [5, 6] (Sonalleve, Profound Medical, Mississauga, ON) with informed consent in a diagnostic 3-T MRI (Ingenia 3.0T, Philips Healthcare, Best, Netherlands). Patients typically suffered from pressure pain, movement pain, reduced physical resilience and increasing tumor size. T2-weighted, diffusion-weighted and dedicated bowel sequences were used for planning. Therapeutic and adverse tissue heating were monitored by multiplanar MR temperature mapping (6 slices in 3.5 s) in and around the treatment area (skin and thoracolumbar spine). Vital parameters were monitored. Depending on clinical presentation, patients were followed up by ultrasound and MRI (after 3 and 6 months) with regard to tumor volume and remaining vascularization. The longest available follow-up period is 12 months.

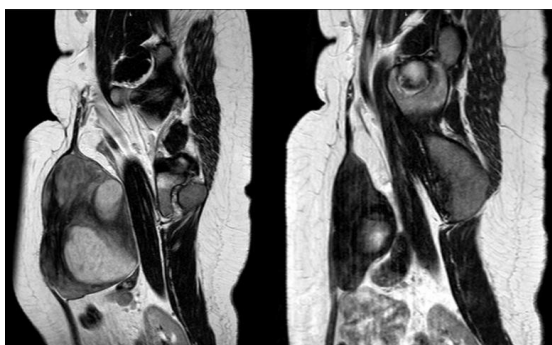


**Fig. 1.** Diagnostic T2-weighted images before and 3 months after MR-HIFU of a 31-year-old patient with desmoid tumors of the abdominal wall. MR-HIFU was preferred here because one-step surgical excision was considered likely to cause tumor spreading. Tumor volume was reduced from 863 ml to 308 ml.

**Results** Treatment was successful in all cases and took 4–6 hours. The non-perfused volume ranged between 42% and 90%. In one case with a short distance to the skin, a gel pad was used as a spacer. Despite proper analgesic medication, two patients reported very severe pain during sonications (VAS values of 7 and higher). One patient developed edematous swelling of the tumor that lasted for 14 days but did not require any further treatment. No other adverse events occurred. All patients were discharged on the next day and reported relief of their original pain symptoms within days after MR-HIFU therapy. Available follow-ups showed good local tumor control and did not show signs of tumor development.

**Conclusions** Our first cases of MR-HIFU ablation in patients with symptomatic desmoid tumors of the abdominal wall showed good local tumor control. Severe pain was reported in two cases. MR-HIFU indicates advantages over surgical treatment like rapid postinterventional mobilization, low scarring and little impairment of wall stability.

- References**
- [1] Lewis JJ, Boland PJ, et al., *Ann Surg.* 1999; 229(6):866-72.
  - [2] R Zhang, JY Chen, et al., *Int J Hyperthermia.* 2021; 38:2, 89-95.
  - [3] Master SR, Mangla A, et al., StatPearls [Internet]. 2022 Jan
  - [4] Wang Y, Wang W, et al., *Int J Hyperthermia.* 2011; 27(7):648-53.
  - [5] Voogt MJ, Trillaud H, Kim YS, et al., *Eur Radiol.* 2012; 22:411-7.
  - [6] Park MJ, Kim YS, Keserci B, Rhim H, Lim HK. *Eur Radiol.* 2013; 23:943-50.

A simple MRI-guided robotic system for breast biopsy.

A. Antoniou<sup>a</sup>, M. Giannakou<sup>b</sup>, C. Damianou<sup>a</sup>

<sup>a</sup>Electrical Engineering Department, Cyprus University of Technology, Cyprus,

<sup>b</sup>R&D, MEDSONIC LTD, Limassol, Cyprus,

## **ABSTRACT**

*Background:* A magnetic resonance image (MRI) guided robotic system dedicated for breast biopsy was developed. A rectangular grid with MRI markers was developed. The biopsy needle is hosted in a two computer-controlled motor stage which has an MRI marker.

*Materials and Methods:* The robotic device includes two computer-controlled axes (X, and Y). An agar-based phantom was developed which includes a tumour model. The tumor model is based on an agar recipe which is different from the background tissue mimicking phantom.

*Results:* The MRI compatibility and accuracy of the robotic system was assessed. The functionality of the robotic system was evaluated using MRI. The robotic system successfully guided the needle into the tumour model.

*Conclusions:* A functional MRI-guided robotic system was produced which can perform frameless breast biopsy. The prototype can be easily evaluated in humans in the future with minor modifications.

**Keywords:** breast, ablation, biopsy, ultrasound, MRI.

## **TITLE**

Prospective Observational Study of Pain Severity and Pain Interference Outcomes Following Percutaneous MRI-guided Laser Ablation or Cryoablation for Focal Painful Peripheral, Soft Tissue Vascular Malformations: 12-month Outcomes

## **AUTHORS**

<sup>1</sup>Scott M. Thompson M.D, Ph.D., <sup>2</sup>Erica M. Knavel Koepsel M.D., <sup>1</sup>Garret M. Powell M.D., <sup>1</sup>Emily C. Bendel M.D., <sup>1</sup>Haraldur Bjarnason M.D., <sup>3</sup>Stephanie F. Polites M.D., M.P.H, <sup>1</sup>Daniel A. Adamo M.D., <sup>1</sup>Desirae L. Howe-Clayton, <sup>1</sup>Christopher P. Favazza Ph.D., <sup>1</sup>Aiming Lu Ph.D., <sup>4</sup>Katelyn Anderson M.D., <sup>4</sup>Megha Tollefson M.D., and <sup>1</sup>David Woodrum M.D., Ph.D.

## **AFFILIATIONS**

<sup>1</sup>Department of Radiology, Mayo Clinic, Rochester, MN, USA

<sup>2</sup>Department of Radiology, University of Wisconsin-Madison, Madison, WI, USA

<sup>3</sup>Department of Surgery, Mayo Clinic, Rochester, MN, USA

<sup>4</sup>Department of Dermatology, Mayo Clinic, Rochester, MN, USA

## **PURPOSE**

To prospectively evaluate the 12-month pain severity and pain interference outcomes following percutaneous MRI-guided laser ablation and cryoablation of focal painful, peripheral soft tissue vascular anomalies.

## **MATERIALS AND METHODS**

Patients undergoing clinically indicated MRI-guided laser ablation and/or cryoablation for focal painful (worst pain  $\geq 6$  out of 10 on Visual Analog Scale), peripheral soft tissue vascular malformations (VM) were enrolled in an IRB-approved prospective, observational study after giving informed consent. Patients completed the Brief Pain Inventory (BPI) questionnaire prior to ablation (baseline) and 1, 3, 6 and 12-months post-ablation. Differences in pain severity and interference outcomes from baseline on a 0 to 10 scale (higher number meaning greater severity or interference) were compared using a paired t-test.

## **RESULTS**

17 patients (15 female, 2 male; mean age 28 years) underwent 24 MRI-guided and monitored ablation sessions including laser (n=21), cryoablation (n=2) or combined laser and cryoablation (n=1) for treatment of painful slow flow (venous, n=15; venolymphatic, n=1) or high flow (arteriovenous, n=1) malformations located in the lower extremity (n=11), upper extremity (n=5) or face (n=1). Twelve patients (71%) had undergone prior VA therapy including percutaneous sclerotherapy (83%), surgery (50%) or transarterial embolization (8%). Median maximal VA diameter was 5.7 cm (range 1.1 to 31.0 cm). Post-ablation patients were discharged same day (25%) or after overnight observation (75%). Mean ( $\pm$ SD) pre-ablation worst pain score was  $7.9 \pm 1.4$ . There was a significant decrease in worst pain at 1-month post-ablation ( $-3.5 \pm 2.9$ ;  $p=0.0007$ ) that was sustained at 3 ( $-3.4 \pm 3.2$ ;  $p=0.007$ ), 6 ( $-4.2 \pm 3.6$ ;  $p=0.0003$ ) and 12-months ( $-3.5 \pm 3.9$ ;  $p=0.002$ ), with similar results for average, current, and least pain scores. There was a significant improvement in most pain interference outcomes at 12-months post-ablation: general activity ( $p=0.018$ ), walking ability ( $p=0.008$ ), work ( $p=0.003$ ), sleep ( $p=0.007$ ) and enjoyment of life ( $p=0.033$ ) but not mood ( $p=0.096$ ). At baseline patients reported overall percent pain relief of

31±30%, which increased significantly 12-months post-ablation—67±35% (p=0.005). There were no major and two minor ablation related complications.

## **CONCLUSION**

These data suggest that MRI-guided and monitored thermal ablation is safe and provides early and sustained significant improvements in pain severity and pain interference outcomes during the first year of follow-up in participants with focal painful peripheral soft tissue vascular malformations.

## FIGURES

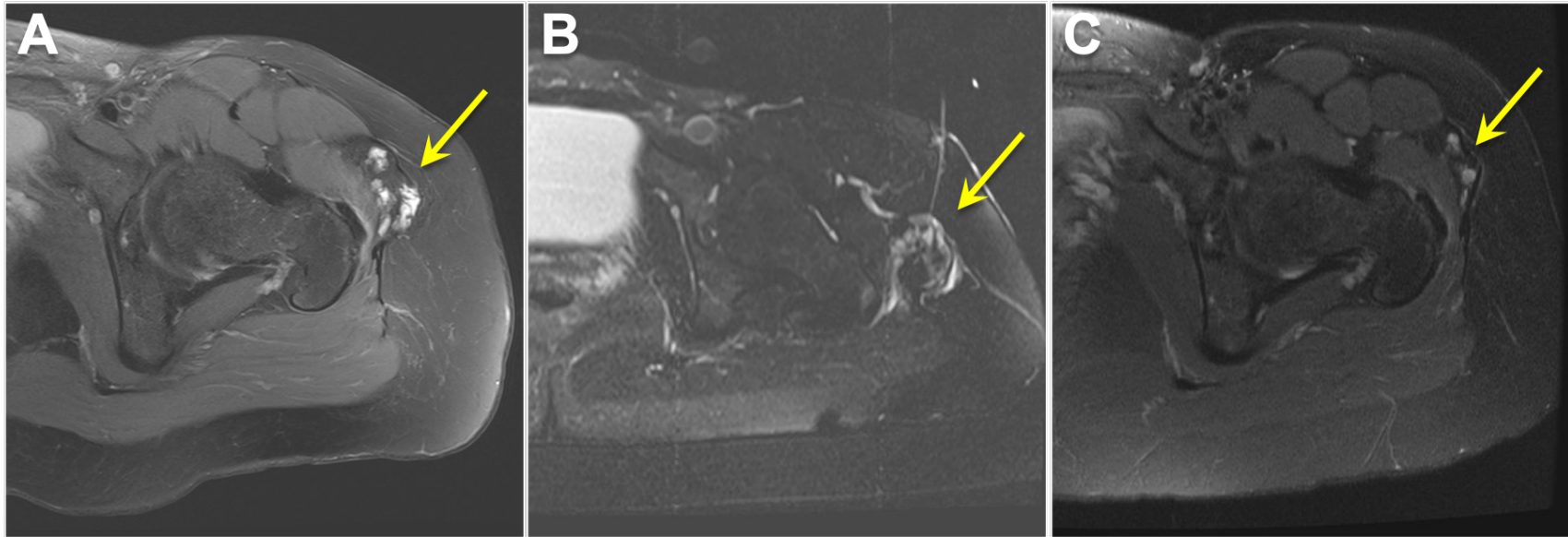


**Figure 1. Magnetic resonance (MR) imaging-guided laser ablation in a 42-year-old female patient with recurrent pain (worst pain 9/10, average pain 6/10) at location of a left lateral thigh intramuscular slow flow venous malformation after two prior percutaneous sclerotherapy treatments.** (a) The T2-weighted preablation MR image shows a hyperintense intramuscular slow flow venous malformation in the left lateral thigh (yellow arrow). The venous malformation was ablated with multiple pullback activations of the laser fiber. (b) Immediate post-ablation T2-weighted MR images shows expected post-ablation edema (yellow arrow). (c) The T2-weighted MR image at 3-year follow-up shows minimal residual hyperintense malformation (yellow arrow). Patient reported no residual or recurrent pain at 1-year post-ablation (worst pain 0/10, average pain 0/10).

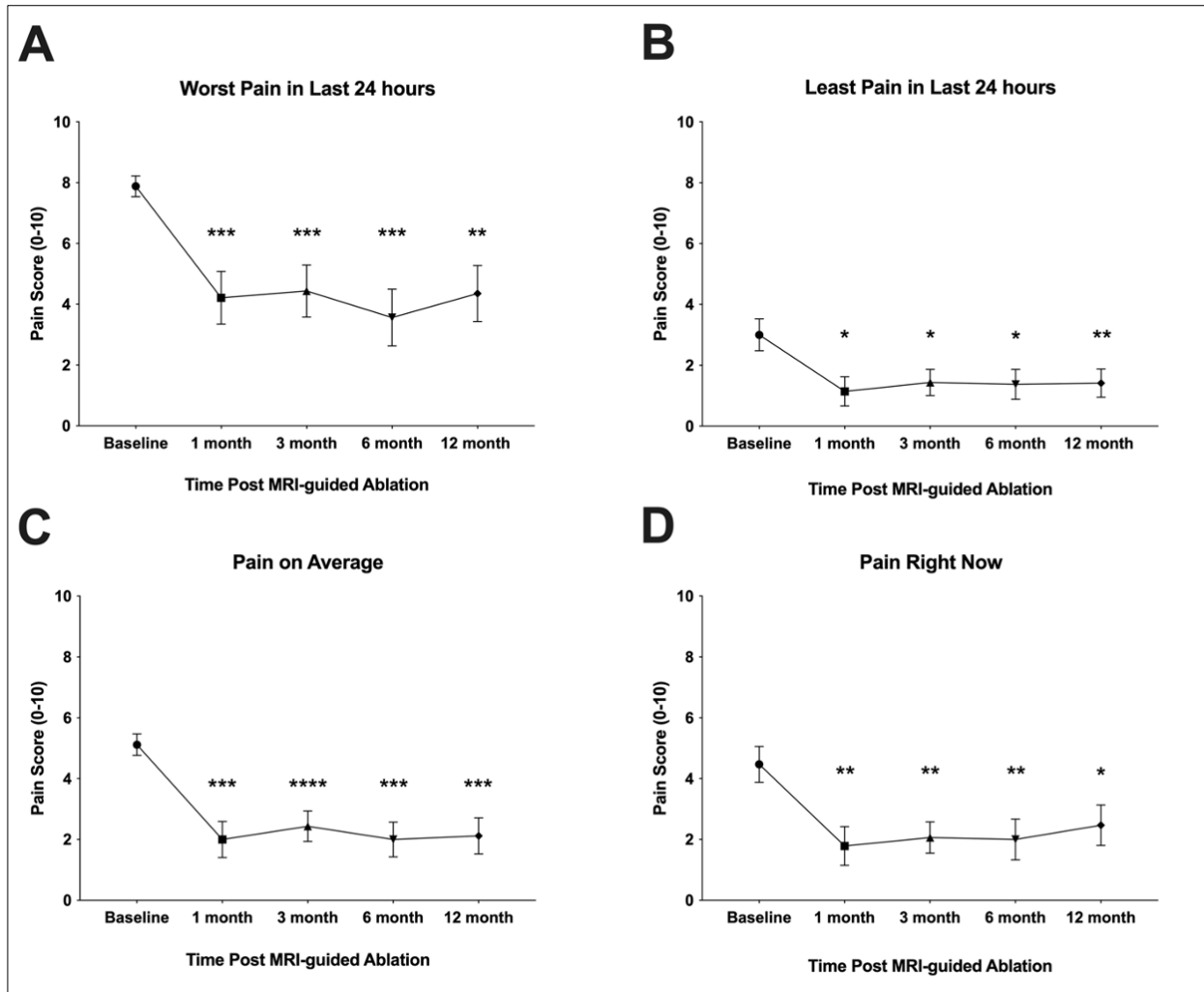


**Figure 2: Pain severity scores from the Brief Pain Inventory (BPI) at baseline and 1-, 3-, 6- and 12-months post-ablation in 17 patients undergoing MRI-guided ablation for focal painful peripheral vascular malformation.** (a) Worst pain in last 24 hours—Mean ( $\pm$ SD) pre-ablation pain score was  $7.9 \pm 1.4$ . Significant decrease in worst pain at 1-month ( $-3.5 \pm 2.9$ ;  $p=0.0007$ ), 3-months ( $-3.4 \pm 3.2$ ;  $p=0.007$ ), 6-months ( $-4.2 \pm 3.6$ ;  $p=0.0003$ ) and 12-months ( $-3.5 \pm 3.9$ ;  $p=0.002$ ) post-ablation. (b) Least pain in last 24 hours— Mean ( $\pm$ SD) pre-ablation pain score was  $3.0 \pm 2.2$ . Significant decrease in worst pain at 1-month ( $-1.6 \pm 2.3$ ;  $p=0.025$ ), 3-months ( $-1.5 \pm 2.3$ ;  $p=0.022$ ), 6-months ( $-1.4 \pm 2.1$ ;  $p=0.015$ ) and 12-months ( $-1.6 \pm 2.0$ ;  $p=0.005$ ) post-ablation. (c) Pain on average— Mean ( $\pm$ SD) pre-ablation pain score was  $5.1 \pm 1.5$ . Significant decrease in worst pain at 1-month ( $-2.9 \pm 2.3$ ;  $p=0.0004$ ), 3-months ( $-2.6 \pm 2.0$ ;  $p<0.0001$ ), 6-months ( $-3.0 \pm 2.4$ ;  $p=0.0002$ ) and 12-months ( $-3.0 \pm 2.6$ ;  $p=0.0002$ ) post-ablation. (d) Pain right now— Mean ( $\pm$ SD) pre-ablation pain score was  $4.5 \pm 2.4$ . Significant decrease in worst pain at 1-month ( $-2.3 \pm 2.9$ ;  $p=0.011$ ), 3-months ( $-2.2 \pm 2.4$ ;  $p=0.003$ ), 6-months ( $-2.4 \pm 2.7$ ;  $p=0.003$ ) and 12-months ( $-2.0 \pm 3.2$ ;  $p=0.020$ ) post-ablation. Reported p-values were calculated using a one sample (paired) t-test after calculating the intraindividual difference in pain severity score at 1, 3, 6 or 12 months from the baseline score. Data are presented as mean $\pm$ SEM. ns =  $P > 0.05$ ; \* $P < 0.05$ ; \*\* $P < 0.01$ ; \*\*\* $P < 0.001$ ; \*\*\*\* $P < 0.0001$



## MRI-guided Conventional Catheter Ablation of Isthmus-dependent Atrial Flutter Using Active Catheter Imaging

Stefan Ulbrich MD<sup>a</sup>, Yan Huo MD PhD<sup>a</sup>, Jakub Tomala MD<sup>a</sup>, Michael Wagner MD PhD<sup>a</sup>, Utz Richter MD<sup>a</sup>, Liying Pu MD<sup>a</sup>, Julia Mayer MD<sup>a</sup>, Angela Zedda MD<sup>a</sup>, Axel Joachim Krafft PhD<sup>b</sup>, Katherine Lindborg PhD<sup>c</sup>, Christopher Piorkowski MD<sup>a</sup>, Thomas Gaspar MD<sup>a</sup>

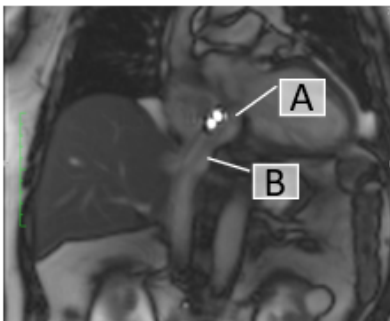
<sup>a</sup>Department of Electrophysiology, Heart Center University Dresden, Fetscherstr. 76, 01307 Dresden, Germany

<sup>b</sup>Siemens Healthcare GmbH, Erlangen, Germany

<sup>c</sup>Imricor Medical Systems, 400 Gateway Blvd, Burnsville, MN USA 55337

**Purpose:** Interventional cardiac magnetic resonance (iCMR) has been established as a radiation-free alternative comparing to standard fluoroscopy-guided catheter ablation due to cavotricuspid isthmus (CTI)-dependent atrial flutter to image anatomy, structural alterations, and further catheter guidance. The purpose of this analysis was to explore the safety, feasibility, and efficacy of CTI ablations performed completely in the iCMR suite using active catheter imaging.

**Materials and Methods:** Consecutive patients underwent iCMR-guided catheter ablation due to CTI-dependent atrial flutter. Procedures were performed in a 1.5T MRI with MR-conditional ablation catheters. Catheter guidance was achieved using active catheter imaging via integrated MR receive tip coils (**figure**). Acute success, periprocedural complications, and short-term follow-up were collected for further analysis.



A) active catheter imaging of distal and proximal receive coils in tip of the ablation catheter; B) passive image of catheter shaft

**Results:** All patients (n=15; 73% male; median age 70 years, IQR 67-82) achieved acute procedure success without any complication. The median procedure time was 43 min (IQR 33-58) with a median RF delivery time of 18 min (IQR 12-26). Post-procedure lesion visualization scanning was completed in a median of 32 min (IQR 10-42). None of the patients with a 6-month follow-up had atrial flutter recurrence.

**Conclusions:** In the iCMR suite, CTI-dependent atrial flutter ablation could be achieved safely using active catheter imaging without any complication. It further allows detailed anatomic visualization of the CTI, intra-procedural lesion visualization, and exclusion of pericardial effusion.

**Key Words:** Interventional cardiac magnetic resonance; atrial isthmus; atrial flutter; ablation

# MRI-Driven Endovascular Thrombectomy

## **Martin Francis Phelan III**

Department of Mechanical Engineering  
Carnegie Mellon University  
Pittsburgh, PA 15213, USA

## **Metin Sitti\***

Department of Mechanical Engineering  
Carnegie Mellon University  
Pittsburgh, PA 15213, USA

Institute for Biomedical Engineering  
ETH Zurich  
Zurich 8092, Switzerland

College of Engineering and School of Medicine  
Koç University  
Istanbul 34450, Turkey

## **Abstract**

MR angiography provides high resolution visualization of blood vessels for analysing stenosis, occlusions, or aneurysms. However, treatments for such severe diseases often requires the use of a guidewire/endovascular catheter to engage the obstruction. Navigating such instruments to the area of interest can be challenging due to tortuous vasculature, resulting in loss of manual torque transmission and blunt force trauma to the vessel. Catheters integrated with microcoils for electromagnetic actuation under the high, uniform magnetic field within magnetic resonance (MR) scanners (3-7 Tesla) have enabled an alternative approach for catheter operations. This work introduces an electromagnetic driller design, allowing direct tip torque control for both steering and mechanical drilling/thrombectomy. Results are demonstrated in vitro replicating a mechanical thrombectomy procedure under MR guidance. These results indicate leveraging the high field of an MR scanner can produce high torque outputs (up to 5 mN·m) for difficult-to-reach areas of the vasculature, enabling other MR-guided interventions.

## **TITLE**

Peripheral MR Lymphangiography: Integration into Clinical Workflow in a Hybrid MR-US Interventional Suite

## **AUTHORS**

<sup>1</sup>Scott M. Thompson M.D, Ph.D., <sup>2</sup>Erica M. Knavel Koepsel M.D., M.P.H, <sup>1</sup>Emily C. Bendel M.D., <sup>1</sup>Christopher P. Favazza Ph.D., <sup>1</sup>Aiming Lu Ph.D., <sup>1</sup>David Woodrum M.D., Ph.D., <sup>1</sup>Jeremy D. Collins M.D.

## **AFFILIATIONS**

<sup>1</sup>Department of Radiology, Mayo Clinic, Rochester, MN, USA

<sup>2</sup>Department of Radiology, University of Wisconsin-Madison, Madison, WI, USA

## **PURPOSE**

MR Lymphangiography (MRL) is a useful diagnostic imaging adjunct to conventional lymphangiography (CL). Abdominopelvic and thoracic MRL can be performed via ultrasound-guided nodal access or via transdermal injection via the feet. When suitable inguinal lymph nodes are not present or in patients with prior CLs via nodal access peripheral MRL is a favored diagnostic approach. Peripheral MRL also enables assessment of thigh and calf lymphatics in suspected lower extremity lymphatic disorders.

## **MATERIALS AND METHODS**

### **RESULTS**

1. MR Hybrid procedural suite configuration, ultrasound integration, and use of anesthesia for MRL.
2. Review the anatomy of the lower extremity lymphatic channels, known variations.
3. Review the method for injection of dilute gadolinium contrast into different regions of the feet to achieve opacification of unique calf lymphatic channels<sup>1</sup>:
  - a. Webspaces: Anteromedial
  - b. Medial foot to medial malleolus: Posteromedial
  - c. Lateral forefoot: Anterolateral
  - d. Posterior (heel) and posterior lateral foot: Posterolateral
4. Review imaging techniques to optimize visualization of lymphatic channels in the lower extremities
  - a. High-resolution Dixon imaging: Sagittal plane, Limited to affected Limb
  - b. Time-Resolved MR Angiography: Sagittal plane, temporal update 1 minute
  - c. T2-weighted non-contrast peripheral MRL
  - d. Dual-agent relaxation contrast MRL using Ferumoxytol (intravenous) for venous suppression<sup>2</sup>
5. Case-based review of peripheral MRL Utility
  - a. Unilateral limb lymphedema in a patient with a lymphangioma
  - b. Unilateral limb lymphedema in a patient with a lymphatic malformation of the thigh and pelvic soft tissues
  - c. Diagnosing source of post-operative lymphatic leak in patients with prior CL limiting feasibility of intranodal access

- i. Post EVAR explant with graft placement for infection, continued peritoneal leak Post CL without visualization of thoracic duct
  - ii. Post soft tissue mass resection with ongoing lymphatic leak in wound
- 6. Challenges in peripheral MRL
  - a. Distinguishing normal lymph channels from enhancing veins with “intravasation” of intradermal contrast
  - b. Diffuse venous shunting with long-standing lymphedema

**CONCLUSION**

This educational exhibit will detail the experience integrating peripheral contrast-enhanced peripheral MR lymphangiography (MRL) into a hybrid interventional suite with a 1.5T magnet at the Mayo Clinic in Rochester, MN.



Figure 1: Peripheral MRL demonstrating early (left) and late (right) progressive filling of a lymphatic malformation along the anteromedial thigh.



Figure 2: Peripheral MRL demonstrating late filling of a biopsy-proven lymphangioma (arrow) on the right without central lymphatic filling. Peripheral MRL of the left side demonstrates normal lymphatic channels with filling of inguinal lymphatics and lymph nodes, with central drainage (asterisk).

# Hybrid Deformable Registration for Motion Compensation – A Feasibility Study with Realtime 3D MRI-US.

J. Mitra<sup>1</sup>, C. Bhushan<sup>1</sup>, S. Ghose<sup>1</sup>, D. Mills<sup>1</sup>, A. Patel<sup>1</sup>, M. Tarasek<sup>1</sup>, T. Foo<sup>1</sup>, S. Wells<sup>2</sup>, S. Jupitz<sup>3</sup>, B. Bednarz<sup>3</sup>, C. Brace<sup>4</sup>, J. H. Holmes<sup>5</sup>, D. Yeo<sup>1</sup>

<sup>1</sup>GE Research, Niskayuna, NY, USA; <sup>2</sup>Depts. of Radiology and Urology, University of Wisconsin-Madison, Madison, WI, USA; <sup>3</sup>Dept. of Medical Physics, University of Wisconsin-Madison, Madison, WI, USA; <sup>4</sup>Depts. of Radiology and Biomedical Engineering, University of Wisconsin-Madison, Madison, WI, USA; <sup>5</sup>Dept. of Radiology, University of Iowa, Iowa City, IA, USA

**Purpose:** The therapeutic efficacy of microwave ablation for hepatocellular carcinoma is often limited by tumor conspicuity with conventional image-guidance techniques (US and CT), resulting in inaccurate applicator placement. Magnetic resonance imaging (MRI) offers high soft tissue contrast with large volumetric scan coverage that may improve precision of applicator placement. Current clinical practice largely depends only on US with few advanced workflows involving image fusion with rigid registration methods only. In this work, we present a hybrid deformable fusion method to align pre-interventional 3D MRI and interventional 3D US in real-time.

**Materials and Methods:** We leverage our previously developed MR-compatible, hands-free 3D US probe [1] that allows simultaneous acquisition of MRI and US images in human volunteers. It provides multimodal pre-interventional MRI (pMRI) and US (pUS) with same patient pose. In our proposed hybrid deformable registration method, pMRI and pUS images are aligned using conventional deformable registration before the intervention procedure, as it is not time-critical.

For real-time fusion of pMRI & interventional images, we leverage intra-modal deep-learning (DL) based registration that aligns pUS to interventional US (iUS) and consecutive iUS volumes by predicting deformation fields. The deformation fields are then used to deform the pMRI to match each iUS volume. Experiments were performed with respiratory data from 3 healthy volunteers, while ~1600 US volumes for DL training was obtained from one volunteer. Our method was evaluated on 3 volunteers with 20 US volumes each, collected at a temporal resolution of 4.2 volumes/sec. Expert placed landmarks were used to evaluate registration accuracy.

**Results:** Table 1 shows the landmark distance of the hybrid method i.e., between a pair of deformed pMRI-pUS (conventional registration) and 19 pMRI-iUS temporal volumes (DL registration) for all subjects, and for a fully conventional deformable registration for comparison, including computation times. Figure 1 shows the deformed MRI landmark on example reference temporal US volumes of a subject.

**Conclusions:** We demonstrated the feasibility of a multimodal hybrid deformable registration framework with registration accuracy like conventional methods but with low latency. This method for motion compensation may improve tumor targeting in interventional procedures including liver ablation. <sup>1</sup>Bednarz et al. First-in-human imaging using a MR-compatible e4D ultrasound probe for motion management of radiotherapy. Phys Med. 88, 104–110. doi:10.1016/j.ejmp.2021.06.017

Table 1 Deformed landmark distances between deformed MR and US temporal volumes for accuracy evaluation and computation times of the proposed hybrid (DL + conventional) and fully conventional deformable registration methods.

Subject	Landmark Distance (mm)		Timing (secs)	
	Hybrid	Conventional	Hybrid	Conventional
1	0.18±0.07	0.29±0.07	0.54±0.01	79.20±33.78
2	1.56±0.63	1.39±0.09	0.54±0.01	111±35.68
3	2.38±0.88	1.45±0.03	0.53±0.01	80.58±28.53

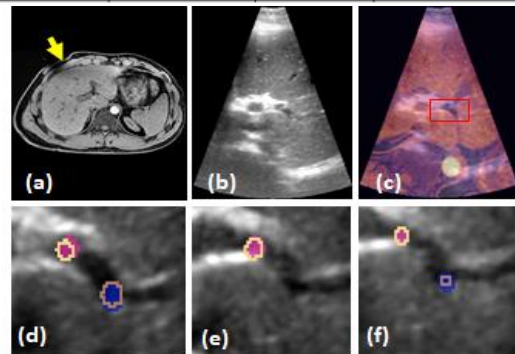


Figure 1 Hybrid deformable registration results. (a) & (b) are simultaneous MRI and US with yellow arrow showing the position of the US probe. Deformed MR on US after registration in (c). Zoomed views (within the red box of (c)) of deformed MR and US landmarks overlaid across temporal US volumes are shown in (d) – (f). Shaded regions are deformed MR landmarks, solid lines are reference US landmarks.

# Convection triggers MRI amplitude and phase signal changes during proton beam irradiation of liquid water phantoms

J. Peter<sup>1,2</sup>, S. Gantz<sup>1,2</sup>, L. Karsch<sup>1,2</sup>, J. Pawelke<sup>1,2</sup>, A. Hoffmann<sup>1,2,3</sup>

<sup>1</sup>*OncoRay – National Center for Radiation Research in Oncology, Faculty of Medicine and University Hospital Carl Gustav Carus, Technische Universität Dresden, Helmholtz-Zentrum Dresden-Rossendorf, Dresden, Germany*

<sup>2</sup>*Helmholtz-Zentrum Dresden-Rossendorf, Institute of Radiooncology – OncoRay, Dresden, Germany*

<sup>3</sup>*Department of Radiotherapy and Radiation Oncology, Faculty of Medicine and University Hospital Carl Gustav Carus, Technische Universität Dresden, Dresden, Germany*

## Purpose

In-beam MRI has recently proven capable of visualising proton beams in liquid-filled phantoms based on beam-induced local MR signal amplitude loss. This holds promise for on-line beam range verification and dosimetric as well as geometric quality assurance for hybrid MRI-proton therapy systems currently under development. The purpose of this study was firstly to determine whether, in addition to MR signal amplitude loss, the MRI phase signal is affected by the proton beam and secondly, to test whether these changes in MRI signals are triggered by beam-induced convection.

## Material and methods

A 0.22 T open MRI scanner was positioned at a horizontal proton research beamline in a clinical proton therapy facility. Both a free-floating water phantom and a soaked finely-pored floral foam-filled, convection-inhibited water phantom were irradiated with nominal proton beam energies of 200, 207 and 215 MeV at beam currents of 0, 8, 16, 32 and 64 nA. Single-slice horizontal images were acquired under simultaneous irradiation using a gradient echo-based, flow compensated time-of-flight angiography pulse sequence with flow saturation applied below the imaged slice (TE = 7 ms, TR = 19.2 ms, flip angle = 60°, total scan duration = 3 s). Phase difference images of image acquisitions with and without simultaneous irradiation were calculated from single-receiver-channel data using the complex conjugate method.

## Results

Proton beam induced signatures of MRI amplitude and phase differences could be observed in a free-floating water phantom (Fig. 1). These signatures showed a clear beam current and energy dependence. Under inhibition of beam-induced convection in the floral foam-filled phantom, no MR signal changes in both amplitude and phase could be observed during irradiation.

## Conclusion

Beam-induced convection triggers local changes in MRI signal amplitude and phase that depend on beam energy and current settings. Future work is necessary to unravel the underlying contrast mechanisms of the signal amplitude and phase changes observed during proton beam irradiation.

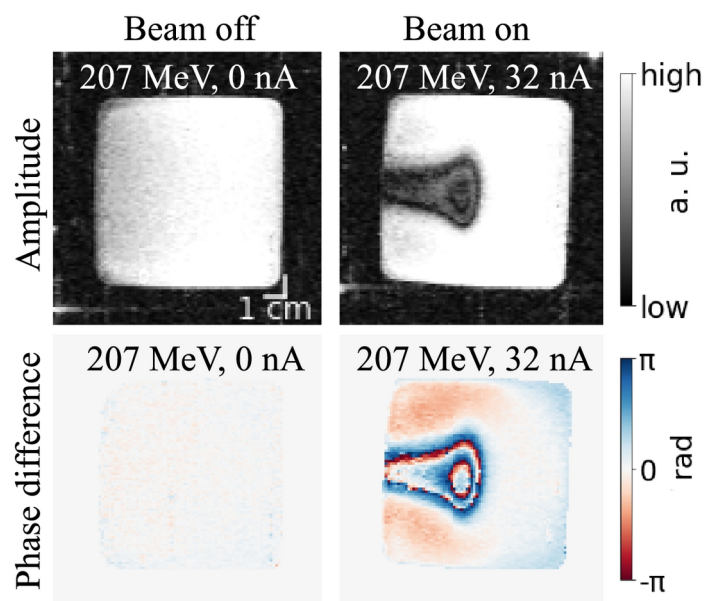


Figure 1: MRI amplitude and phase differences occur during irradiation of a free-floating water phantom.

# Improving Accuracy of White Marker Contrast-Based Rapid 3D Passive MR Biopsy Needle Localization by Utilizing a Total Variation-Regularized Image Reconstruction

Jonas F. Faust<sup>1,2</sup>, Daniel Polak<sup>1</sup>, Mark E. Ladd<sup>3,2</sup>, Florian Maier<sup>1</sup>

<sup>1</sup>Siemens Healthcare GmbH, Erlangen, Germany; <sup>2</sup>Ruprecht-Karls-Universität Heidelberg, Heidelberg, Germany; <sup>3</sup>German Cancer Research Center (DKFZ), Heidelberg, Germany

## Purpose

In MR-guided interventions, automatic biopsy needle localization allows for slice repositioning to ensure the visibility of the needle path during the procedure<sup>1</sup> to support the interventionalist. Recently, a prototype method<sup>2</sup> for rapid 3D passive needle localization was introduced that combines an undersampled 3D radial<sup>3</sup> image acquisition, employing a susceptibility-based positive *White Marker (WM)* contrast method<sup>4</sup>, with Deep Learning-based<sup>5</sup> postprocessing. The incoherent nature of undersampling artifacts

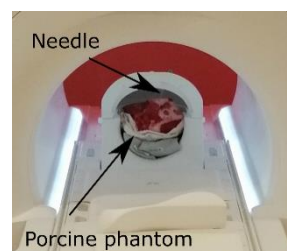


Figure 1: Ex-vivo phantom set-up for data generation.

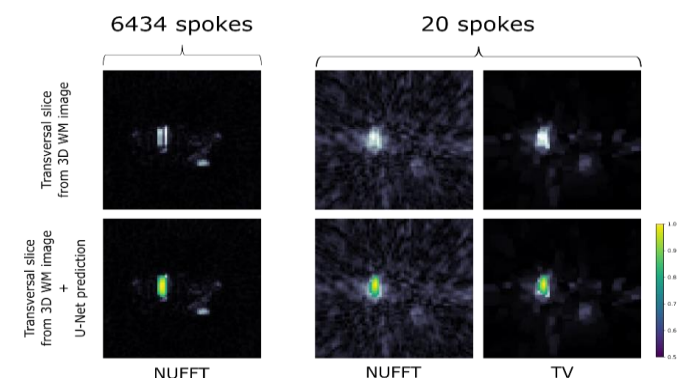


Figure 2: Example 3D image from the test set. The first row shows a transversal slice, including the WM needle artifact. The second row shows the same image, overlaid with the U-Net prediction of the needle location.

The acquired data was additionally retrospectively undersampled to 20 radial spokes and reconstructed using a NUFFT (zero-filling of k-space) and a Total-Variation (TV) regularized iterative reconstruction procedure<sup>7</sup> (coil channels were compressed into one virtual coil<sup>8</sup> for all reconstructions). A U-Net was trained separately on the differently reconstructed dataset (35 images excluded as test set) to localize the needle. For the test set, needle localization accuracy was evaluated using two measures (Fig. 3).

## Results

Fig. 2 shows an example image from the test set. The TV-regularized reconstruction presents with less visible streaking artifacts. For the test set, an improvement in median accuracy of 0.6 mm for  $\Delta x$  and  $4.2^\circ$  for  $\alpha$  was found for the TV reconstruction compared to the NUFFT for the undersampled dataset (Fig. 3).

## Conclusion

For the investigated dataset, an improvement in median needle localization accuracy using the method introduced by Faust et al. could be achieved by TV-regularizing the WM image reconstruction for high undersampling.

## References

- [1] Patil S, et al. MRM 2009;62: 935-942. [2] Faust J, et al. ISMRM 31st Annual Meeting & Exhibition 2022. [3] Chan RW, et al. MRM 2009; 61(2):354-363. [4] Seppenwoolde JH, et al. MRM 2003;50(4):784-790 [5] Çiçek Ö, et al. MICCAI 2016;424-432. [6] Block KT, et al. MRM 2007; 57:1086–1098. [7] Ong F and Lustig M. ISMRM 29th Annual Meeting & Exhibition 2019. [8] Buehrer M, et al. MRM 2007; 57:1131-1139.

for radial k-space trajectories allows for detection of the needle in the sparse WM images with a high localization accuracy even for large undersampling factors. This work explores the feasibility to further increase the needle localization accuracy by reducing undersampling artifacts through the employment of a regularized iterative image reconstruction<sup>6</sup>.

## Material and Methods

For a manually annotated dataset consisting of 319 needle poses in 7 ex-vivo porcine phantoms (Fig. 1), images were reconstructed from fully-sampled k-space (6434 spokes) using a Non-Uniform Fast Fourier Transform (NUFFT).

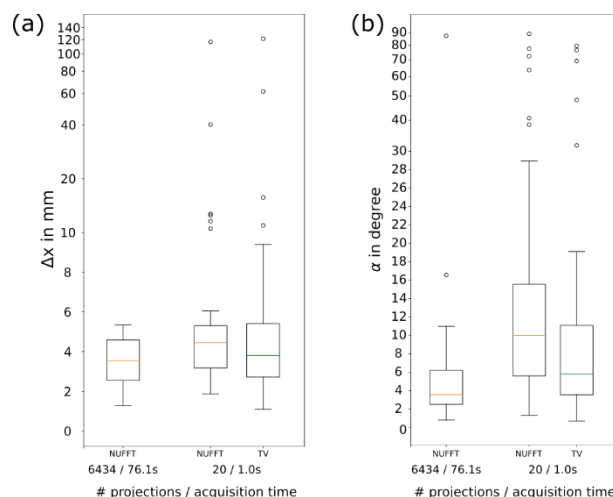


Figure 3: The accuracy of the needle localization was investigated for fully sampled (6434 spokes), as well as highly undersampled k-space (20 spokes), using two measures for comparison: the distance  $\Delta x$  between the center point of the annotation and the predicted needle path (a) as well as the angle  $\alpha$  between the ground truth needle artifact annotation and the predicted needle path (b). For the undersampled data, simple NUFFT image reconstruction was compared with a TV-regularized iterative reconstruction. Note the change from linear to logarithmic scale in the graphs.

**Authors:** Ozgur Kocaturk<sup>1</sup>, D. Korel Yildirim<sup>2</sup>, Dogangun Uzun<sup>2</sup>, Nasser Rafiee<sup>1</sup>, Robert J Lederman<sup>2</sup>

<sup>1</sup> Transmural Systems, Andover MA, USA

<sup>2</sup> Division of Intramural Research, National Heart Lung and Blood Institute, National Institutes of Health, Bethesda, MD, USA

## **TITLE: Transfer Function Measurement Setup for TRÄCRwire at 0.55T**

**INTRODUCTION:** Long metallic structures such as pacemaker leads, or interventional guidewires can cause high local temperature rises during MRI scan<sup>1</sup>. The ISO/TS 10974:2018 standard recommends using transfer function to evaluate RF induced heating on the hot spot<sup>2,3,4</sup>. In this work, we present a transfer function measurement setup for evaluating RF induced heating of an active guidewire (TRÄCRwire) during clinical use by placing it in predefined trajectories in ASTM 2182 gel phantom<sup>5</sup> and virtual human models<sup>6</sup>.

**METHODS:** The workflow of the proposed transfer function measurement method is given in Figure 1. Transfer function measurement setup is also given in Figure 2. Sim4Life electromagnetic (EM) simulation software was used for simulations after completing the in-vitro TF measurements. Same predefined trajectories were used for performing RF induced heating tests in phantom. TF was finalized by determining the calibration factors using in vitro TF measurements, tangential electric field simulations and in vitro RF induced heating test results in equation 1<sup>7</sup>.

**RESULTS:** The extracted tangential electric fields for predefined guidewire trajectory are given in Figure 3. Amplitude and phase values from in vitro TF function measurement of the active guidewire with the same insertion length is given in Figure 4.a. Figure 4.b shows In-vitro RF induced heating results with the same insertion length and trajectory. Transfer function of the active guidewire was determined for the given trajectory and the scaling coefficient was found as  $4.38611 \times 10^{-5}$ . Finally, Figure 5 shows one of the guidewire trajectories with the extracted tangential electrical fields in the virtual human model. Using the finalized TF with its calculated scaling coefficient, in-vivo RF induced maximum temperature rise at the tip of the active guidewire inside the virtual human model can be estimated as 0.344 °C.

**DISCUSSION:** RF induced heating estimation through EM simulations requires high computational power and takes very long time for each iteration. Using the TF method for implants or interventional devices decreases the computational burden significantly and it can provide precise temperature rise predictions for clinical procedures. One method for measuring the TF is by placing an electric field sensor at the tip of the device while moving an excitation probe along the whole device mimicking the applied tangential electric field. In this work we used the second method that takes advantage of the reciprocity principle. The active guidewire (TRÄCRwire) is excited from its tip and the current distribution along the wire was measured using a custom-made RF current probe.

**CONCLUSION:** RF induced heating evaluation during clinical use for 0.035” active guidewire was performed according to ISO/TS 10974:2018 standard and the method was validated using phantom data.



## REFERENCES:

1. Yeung, C. J. et.al, (2002). RF safety of wires in interventional MRI: using a safety index. *MRM*: 47(1), 187-193.
2. *ISO/TS Standard 10974:2018*, Apr. 2018.
3. Missoffe, A., & Aissani, S. (2018). Experimental setup for transfer function measurement to assess RF heating of medical leads in MRI: Validation in the case of a single wire. *Magnetic resonance in medicine*, 79(3), 1766-1772.
4. Zeng, Q. I. et. al, (2018). Investigation of RF-induced heating near interventional catheters at 1.5 T MRI: *IEEE Transactions on Electromagnetic Compatibility*, 61(5), 1423-1431.
5. ASTM Standard F2182, Apr. 2020
6. Sim4life Platform, ZMT Zurich MedTech AG.
7. Park, S. M., Kamondetdacha, R., & Nyenhuis, J. A. (2007). Calculation of MRI-induced heating of an implanted medical lead wire with an electric field transfer function. *JMRI*, 26(5), 1278-1285.

## FIGURES

1.

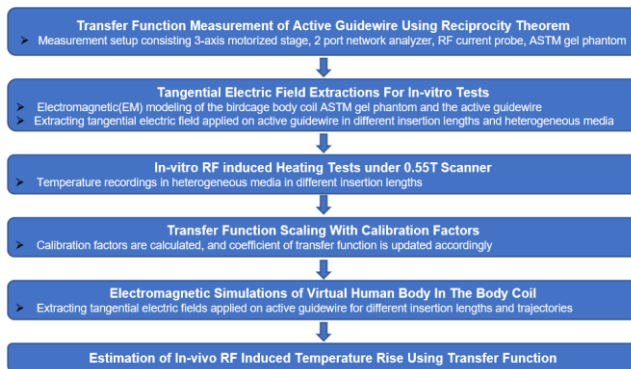


**Figure 1.** Workflow of RF induced heat estimation with transfer function method.

2.

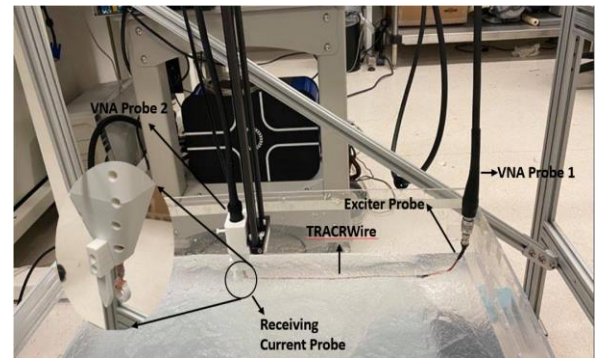


**Figure 2.** In-vitro transfer function measurement setup

3.

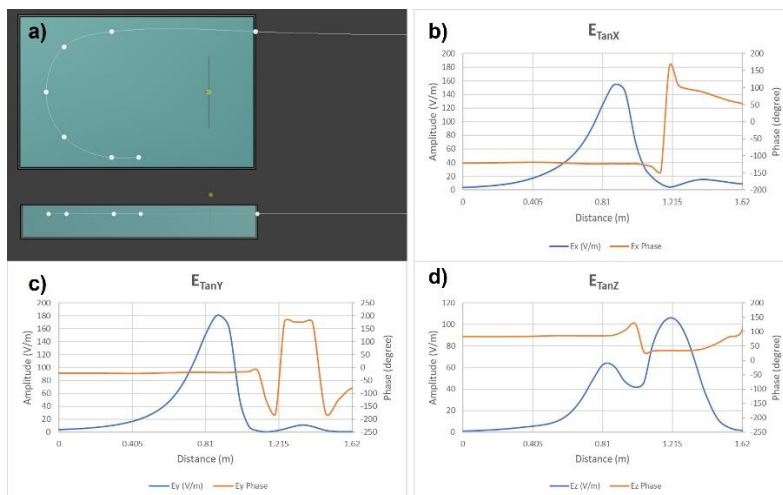


**Figure 3.** a) ASTM 2182 gel phantom model and active guidewire trajectory with 115 cm insertion length b) Electric field component along the X-axis c) Electric field component along the Y-axis d) Electric field component along the Z-axis

4.

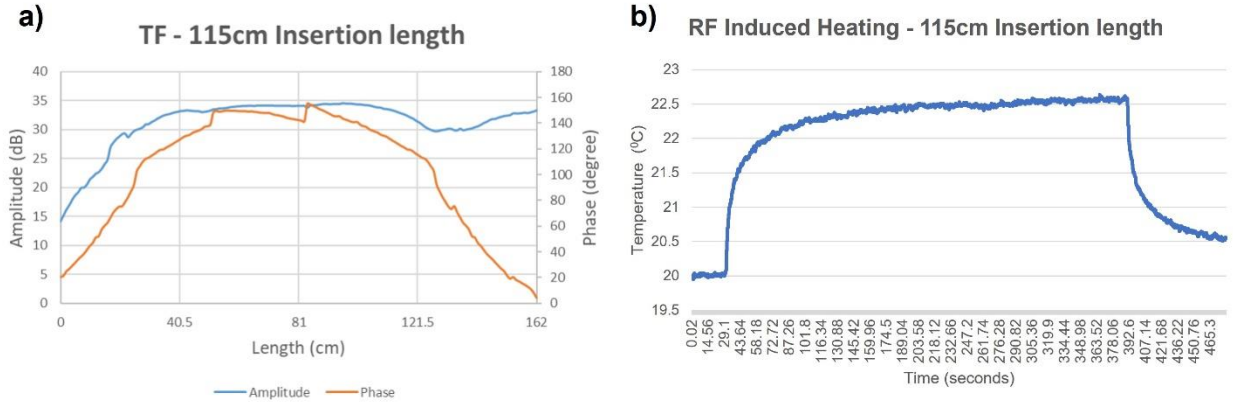


**Figure 4. a)** In-vitro transfer function measurement of active guidewire with 115 cm insertion length in the ASTM gel phantom. **b)** RF induced heating at the hot spot (distal tip) of the guidewire during a 6-minute scan.

5.

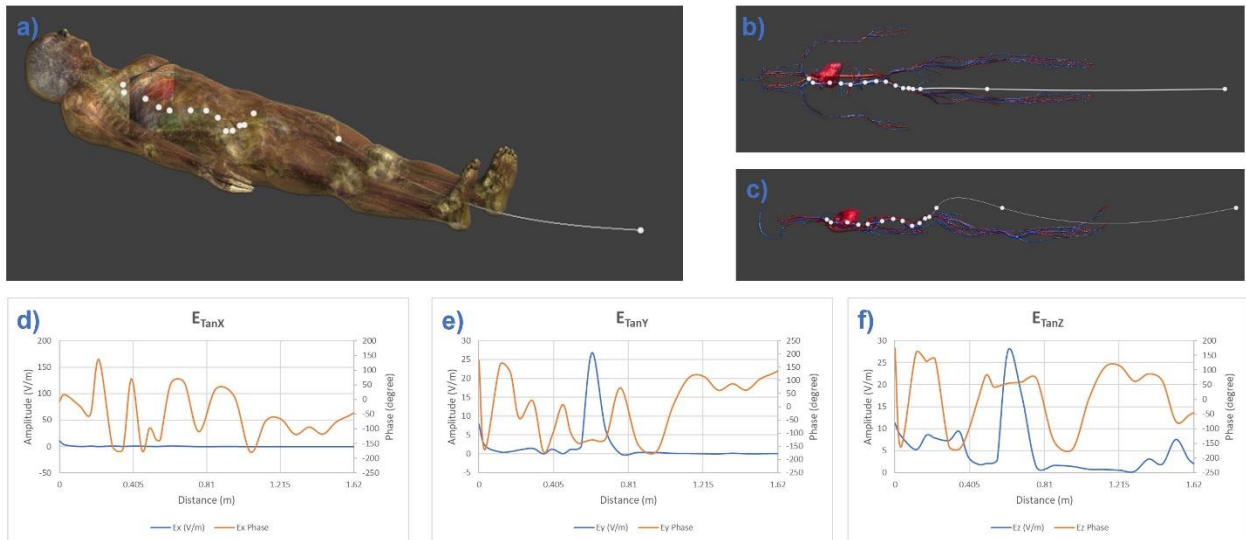


**Figure 5. a,b,c)** Sim4life Virtual human model and predefined active guidewire trajectory **d)** Electric field component along the X-axis **e)** Electric field component along the Y-axis **f)** Electric field component along the Z-axis

# MRI-Visible Pen for Marking the Entry Point of an MRI-Guided Needle Intervention

Alexander Brockmann<sup>1,2</sup>, Joachim Albrecht<sup>2</sup>, Florian Maier<sup>1</sup>

<sup>1</sup>Siemens Healthcare GmbH, Erlangen, Germany

<sup>2</sup>Research Institute for Innovative Surfaces FINO, Aalen University, Aalen, Germany

**Purpose:** During MRI-guided needle interventions such as biopsies and thermal ablation applicator placements, the marking of the entry point (EP) on the skin of the patient before disinfection is an important workflow step. Typically, the EP is marked, based on a needle trajectory defined on a 3D planning image acquired before or at the beginning of the intervention. Interventionalists often use the fingertipping (FT) method<sup>1</sup> to locate and mark the EP. Real-time imaging planes are aligned with the planned trajectory. Then, the interventionalist aligns a finger with the imaging planes during repeated acquisition. The position of the finger can be seen on two intersecting orthogonal imaging planes which are displayed on an in-room monitor. After positioning the finger, the patient table is moved out of the scanner's bore for marking the EP on the patient's skin with a felt tip. The aim of this work was to improve accuracy and marking time while keeping the flexibility of the fingertipping method. An *MR-Visible Pen (MRVP)* was designed, 3D-printed, and evaluated by comparing it to fingertipping method.

**Methods:** The MRVP was conceived to be an intuitive reusable device for interventionalists. It was designed with CAD software (*NX, Siemens Digital Industries Software, Plano, TX, USA*) and 3D-printed using a stereolithography printer (*LD-002H, Shenzhen Creality 3D Technology, Shenzhen, China*). The MRVP possesses a hollow cavity which was filled with water. A MR-compatible spring-loaded triggering mechanism was designed to allow for marking the EP with a small felt tip directly on the patient's skin within the scanner's bore by pressing a button.

For evaluation, the marking time and accuracy of the MRVP was compared to the FT method by measuring their total deviation from the located EPs to pre-marked EPs and the time needed to mark them. Instead of using a finger, the MRVP's water-filled cavity is aligned with the planned needle trajectory on the real-time images. A cylindrical phantom ( $\varnothing = 140$  mm) was used and covered with pre-marked EPs (15 pre-marked EPs / experiment varying between  $0^\circ$  to  $\pm 81^\circ$  from the phantom's centre line). Using the scanner's (*MAGENTOM Sola, Siemens Healthcare GmbH, Erlangen, Germany*) needle guidance software, the needle trajectory was planned by positioning the planned EP directly onto the pre-marked EP on the cylindrical phantom and positioning the planned target point (TP) in the centre of the phantom's cross-section. The EPs were located and marked using either FT or the MRVP during a bSSFP real-time imaging sequence (*BEAT interactive, Siemens Healthcare GmbH, Erlangen*).

**Results:** The FT workflow was compared to the MRVP workflow. The average total deviation (d) from the pre-marked EP could be nearly quartered from  $d_{FT} = 4.9$  mm to  $d_{MRVP} = 1.3$  mm. Marking duration (t) was more than halved from  $t_{FT} = 81$  s to  $t_{MRVP} = 37$  s.

**Conclusions:** The MRVP made it possible to locate and mark EPs more quickly and accurately during real-time MRI compared to FT. Since the MRVP can immediately mark the EP within the scanner's bore, it removed the necessity to keep a finger positioned on the located EP and move the patient table out of the scanner's bore and, therefore, removed a source of error. The alignment with the planned needle trajectory was more accurate due to the MRVP's straighter and more homogeneous appearance compared to a finger. In a next step, the MRVP is going to be tested by interventionalists to evaluate its usefulness in clinical workflows.

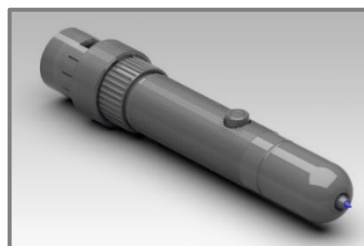
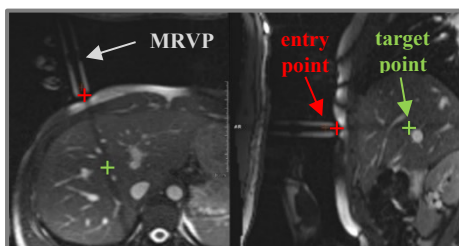


**Fig 1:** MRVP is aligned with the planned needle trajectory between the EP (red) and TP (green).

**Fig 2:** Rendered image of the MRVP's design.

## CNN-based Segmentation of Multiple Needles for Magnetic Resonance-guided Interventions

Amanda Aleong<sup>1</sup>, Peter Chung<sup>2</sup>, Alejandro Berlin<sup>2</sup>, Robert A. Weersink<sup>1,2</sup>

<sup>1</sup>Dept. of Biomedical Engineering, University of Toronto, <sup>2</sup>Dept. of Radiation Oncology, University of Toronto

**Purpose:** Magnetic resonance imaging (MRI) offers excellent visualization of soft-tissue targets for needle-based interventions such as prostate or gynecological brachytherapy. Precise needle placement is vital for the safety and efficacy of treatment and accurate treatment planning. Current techniques in the clinic employ intermittent imaging and visual inspection to assess the placement of the needle relative to a planned trajectory. However, rapid, automated identification of needles is challenging for MR images particularly with multiple needles in view, due to the presence of image noise, overlapping image intensities and the size of the needle in the image. This work employs a 3D convolutional neural network with a U-Net architecture to segment multiple needles for MR-guided prostate brachytherapy.

**Materials and Methods:** Data was obtained from 35 patients who underwent HDR prostate brachytherapy (4280 images i.e. 214 image volumes). Multislice 2D axial TSE verification scans (TE = 12 ms; TR = 2240 ms; resolution = 0.78x0.78 mm; slice thickness= 3 mm; matrix=256x256, no. of slices=20-30) were used to train and test a convolutional neural network with a U-Net architecture (depth = 4), built using Keras with a Tensorflow backend in Python. A sequential model was used with an Adam optimizer and negative Dice coefficient loss function. A SeLU activation function was applied to each convolution layer and was followed by a dropout layer with a rate of 0.1. Ground truth data was prepared as follows, using a workflow mimicking clinical practice. Needles were manually segmented using the open-source software 3D Slicer to obtain 3D binary masks to be used as the reference target data for the model. A cardinal spline model was fit along the control points and a binary mask was generated with white pixels corresponding to the needle and black pixels corresponding to background. The images were windowed, thresholded, normalized, cropped and padded to 64x64x30 voxels centered on the prostate before being passed to the neural network. The network was trained on data from 30 randomly selected patients (185 image volumes) for 100 epochs with a batch size of 4 image volumes and a validation split of 0.2. Data from remaining 5 patients (39 volumes) was used to test the performance of the model. The network returns a binary map with the pixels corresponding to the needle in white and all other pixels in black. The performance of the model is measured via the number of needles successfully identified, the maximum in-plane Hausdorff Distance between the predicted and reference masks over all the volumes and the prediction time per volume. Finally, the binary segmentation generated by the model for each image volume was used to reconstruct the individual needles. Needles were identified as 3D connected components in pixel space. The reconstructed needles were then used to assess the impact of the automated segmentation on the estimated brachytherapy dose in the 5 test cases, by comparing standard target and organ at risk dosimetric parameters for both the clinical and AI segmentations.

**Results:** The network detected 749/757 (99%) of needles in the training set and 139/146 (95%) of needles in the test set with a prediction time of 0.89 s/image volume. The maximum Hausdorff Distance observed was 2 pixels (1.9 mm) in-plane for the training and test sets with 97% of the axial HDs below two times the in-plane resolution. The axial HD gives a measure of how well the needle shaft is being delineated in the images. The max sagittal HD observed in this study for the re-sliced images was 3 pixels (9 mm). The sagittal HD provides a measure of the tip detection error. The results achieved using this model are consistent with the inter-observer errors associated with tip identification in clinical practice sourced from literature. Given that the slice thickness is 3mm in the axial direction it is within expectation that the segmentation error in this direction would be larger. Dose comparisons in the test cases showed only minor differences in expected dose delivery.

**Conclusion:** The results support the use of a U-Net model for the segmentation of multiple needles in MR image volumes. This strategy may be further adapted to MR images acquired in near real-time to facilitate the integration of real-time MR imaging in image-guided interventions. Future work will investigate the use of orthogonal slices to improve the precision with which the tip can be detected. The rapid identification of needles in MR images will assist with the assessment of needle deflection during insertion and provide feedback for needle steering using robotic strategies.

## Interactive Real-Time MRI-Guided Needle Tracking using Scanner Remote Control

Amanda Aleong<sup>1</sup>, Junichi Tokuda<sup>2</sup>, Pedro Moreira<sup>2</sup>, Ravi Seethamraju<sup>3</sup>, Gerald Moran<sup>4</sup>, Himanshu Bhat<sup>3</sup>,  
Robert A. Weersink<sup>1</sup>

<sup>1</sup>University of Toronto, Toronto, Ontario, Canada; <sup>2</sup>Department of Radiology, Brigham and Women's Hospital and Harvard Medical School; <sup>3</sup>Siemens Medical Solutions USA Inc., Boston, Massachusetts, United States; <sup>4</sup>Siemens Healthcare Ltd., Oakville, Ontario, Canada

**Purpose:** Magnetic resonance imaging provides excellent visualization of soft tissue targets for needle-based interventions such as prostate brachytherapy. The accurate placement of needles according to a treatment plan is vital for the safety and efficacy of treatment. In practice, needle deflection limits the targeting accuracy. Real-time MRI offers a means to track the needle during insertion and provide feedback for needle steering strategies. However, alignment of the real-time MR slice to the expected path may not capture the full extent of the needle as the needle tip can deviate out of the expected imaging plane. In this work, we demonstrate the feasibility of near real-time MR needle tracking, using a prototype Scanner Remote Control (SRC) add-in to interactively update the scan plane from a stand-alone PC during image acquisition.

**Materials and Methods:** Images were acquired on a 1.5T MRI scanner (Magnetom Aera, Siemens Healthcare, Erlangen, Germany). The scan parameters were updated via SRC using OpenIGTLink as a communication bridge between the scanner and a stand-alone PC. The user interface is built in 3D Slicer. Three slice configurations are available for tracking: Single slice, 3 parallel slices and 3 independent slice groups. The planned targets and entry points were defined on a multi-slice T2-weighted TSE, and the respective slice positions and orientations were computed in 3D Slicer. The needle was segmented automatically on each time step using a previously described U-Net model that was adapted for real-time imaging. The difference between the length of the needle in the real-time image and the expected needle length is used to guide the needle tracking algorithm. As a first step, automatic slice alignment was validated on the scanner. A custom 3D-printed template was positioned at the flat face of a cylindrical gelatin phantom. The guide holes in the template define 4 fixed angle needle paths ( $\pm 10^\circ$  from the vertical and  $\pm 15^\circ$  from the horizontal). For each target path, a 6F titanium alloy needle was inserted to a depth of 100 mm. Real-time MR images were acquired using a BEAT sequence (TA=0.86s/frame). During acquisition, the scan plane was updated to the expected needle trajectory via 3D slicer and validated against the known position and orientation of the inserted needles. Next, to confirm the feasibility of tracking needle deflection, the scan plane was initialized to a coronal plane capturing the expected entry point of the needle. The overall tracking time and accuracy of localization of the automated algorithm was compared to the manually tracked scan plane of the needle. The needle tracking error was measured by comparing the automatically defined needle and the manually defined needle on the real time images to the ground truth reference needle determined by manual segmentation on a final multi-slice T2-weighted TSE.

**Results:** The scan plane successfully aligns to the expected needle path as the full shaft of the needle is captured after the scan plane updates (Fig.3). The real-time imaging successfully captured the shaft of the needle with a visualization latency of 1.72s on the MR inline viewer after click-based update of the scan plane. The tracking error for automated and manual slice alignment were  $2.9 \pm 1.8$ mm, and  $2.0 \pm 1.2$ mm, respectively. The scan plane was automatically updated on each image acquisition with a refresh rate of 0.86s for the complete process of acquisition, reconstruction, image transfer, rendering, needle localization and scan plane update. The overall time for needle tracking was 6.90s for the automated case and 39.13s for the manual case.

**Conclusion:** The results demonstrate the feasibility of closed-loop feedback control of scan plane updates using remote control of an interactive real-time MR sequence. The open-source network interface enables adaptation to a variety of needle insertion strategies. The needle deviation observed in the scan plane alignment may be attributed to the printing resolution of the ground-truth template. Further tuning will be performed to optimize the search and coordinate with feedback from the MR. Currently, the success of needle tracking, and the overall tracking time is sensitive to the initialization of the scan plane for both manual and automated tracking. The algorithm requires that the needle is at least partially in view at the start of tracking. More robust needle segmentation may be achieved by training the U-Net on a larger and more diverse dataset. The real-time image-based feedback on needle deflection will support robotic control strategies for needle insertion while ensuring safe needle placement with minimum placement error.

## Acousto-optics based active MRI markers for real-time device tracking

Yusuf S. Yaras<sup>1</sup>, Lee W. Bradley<sup>1</sup>, D. Korel Yildirim<sup>2</sup>, John Oshinski<sup>3</sup>, Robert Lederman<sup>2</sup>, Ozgur Kocaturk<sup>4</sup>, F. Levent Degertekin<sup>1</sup>

<sup>1</sup> G.W. Woodruff School of Mechanical Engineering, Georgia Institute of Technology, Atlanta, USA

<sup>2</sup> Division of Intramural Research, National Heart Lung and Blood Institute, National Institutes of Health, Bethesda, MD, USA

<sup>3</sup> Department of Radiology and Imaging Sciences, Emory University, Atlanta, GA, USA

<sup>4</sup> Institute of Biomedical Engineering, Bogazici University, Istanbul, Turkey

**Purpose:** Accurate tip localization and position tracking of interventional devices are essential for clinical interventional MRI procedures. Current devices and integrated active device visualization techniques using electrical conductors are subject to RF induced heating that may impact patient safety. In this work, a novel acousto-optic (AO) MR marker with optical fiber connection is presented to eliminate RF induced heating. **Material and methods:** The AO marker consists of a small coil antenna, a piezoelectric transducer and a fiber Bragg grating (FBG) sensor at the distal end of an optical fiber (Fig. 1a). The piezoelectric transducer converts electrical signal collected by the coil into acoustic waves, which in turn modulates the light reflected from the FBG. Reflected light is converted to electrical signal by a photo detector at the proximal end of the optical fiber and fed to the transceiver coil plug of the MRI scanner. Since the received MRI signal is converted to an optical signal at the distal end and is carried out of scanner using an optical fiber, RF induced heating is intrinsically eliminated. Moreover, FBGs are inherently sensitive to ambient temperature change, which enables simultaneous temperature sensing and tracking. We previously tested the AO markers in phantom studies under 0.55T and 1.5T for functionality and visibility [1]. We also have demonstrated tracking capability of an AO marker integrated on an 8F catheter in an animal study under 0.55T (Fig. 1c) [2]. However, these studies were carried out using bulk piezoelectric transducers which limit the overall size of the marker. In this study, we implemented the AO marker using a novel PZT-based ceramic-polymer paste (PiezoPaint™, Meggitt A/S, Denmark). PiezoPaint™ is processed at temperatures below 150°C and produces flexible transducers, which enables direct deposition on optical fibers via dip-coating. PiezoPaint™ based AO marker is integrated on a 5Fr catheter with a 6-turn hand wound solenoid coil (Fig. 1b).

**Results:** Dip coating of the FBG with PiezoPaint™ resulted in an AO modulator with 0.15mm diameter (Fig. 1b), which enables easier integration with small diameter interventional devices. Sensitivity of both PiezoPaint™ and bulk piezoelectric based AO markers to an external RF field were compared at 23MHz (0.55T) and 64MHz (1.5T). Although measured signal amplitude levels are different, there is only 12 dB difference in SNR values at both frequencies. Moreover, simultaneous temperature measurement was achieved with an accuracy of  $\pm 0.11^\circ\text{C}$ . Note that sensitivity can be improved by optimizing the processing parameters and transducer geometry as these results were obtained with an initial prototype.

**Conclusion:** We demonstrated the functionality of PiezoPaint™ based AO markers for simultaneous device tracking and temperature measurement while eliminating RF induced heating risk for interventional MRI.

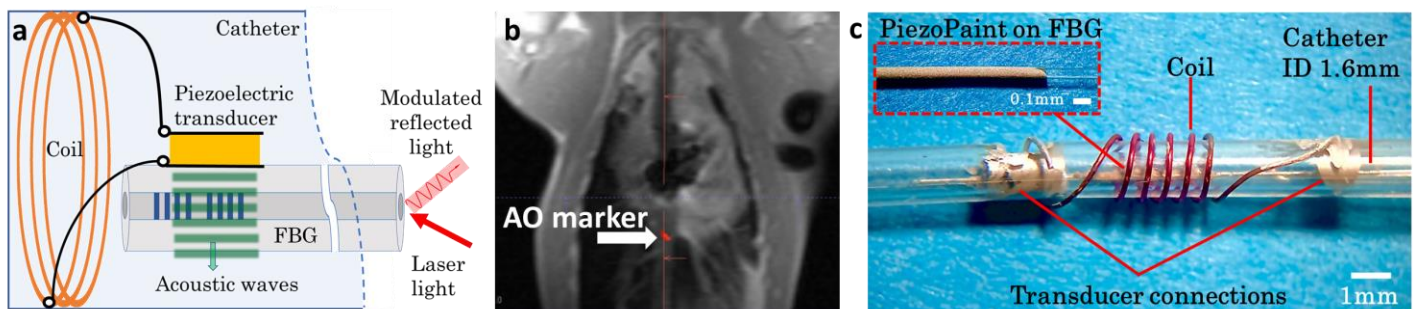


Figure 1. a) Schematic of the AO marker b) Close up photo of the PiezoPaint based AO marker integrated on a 5Fr catheter. c) Real time image of the bulk piezoelectric transducer-based AO marker in animal model [2].

1. Yaras YS, et al. Acousto-optic catheter tracking sensor for interventional MRI procedures. *IEEE Transactions on Biomedical Engineering*. 2018 Sep 5;66(4):1148-54.

2. Yaras YS, et al. Real-time device tracking under MRI using an acousto-optic active marker. *Magnetic Resonance in Medicine*. 2021 May;85(5):2904-14.

# Effects of device trajectory variations on RF-induced heating at low field MRI systems

Ali C. Özen<sup>1</sup>, Maximillian Russe<sup>2</sup>, Thomas Lottner<sup>1</sup>, Simon Reiss<sup>1</sup>,  
Isil Unal<sup>3</sup>, Sebastian Littin<sup>1</sup>, Maxim Zaitsev<sup>1</sup>, Michael Bock<sup>1</sup>

<sup>1</sup>Dept. Radiology-Medical Physics & <sup>2</sup>Dept. Radiology, Univ. Medical Center, Univ. Freiburg, Freiburg, Germany

<sup>3</sup>Dept. Radiology and Neuroradiology, UKSH, Campus Kiel, Germany

**Purpose:** Low-field high-performance MRI systems (e.g., at 0.55T) can facilitate MR-guided interventional operations as they have larger bore sizes. Advantages and potential of low-field systems were introduced in [1]. The safety margins for RF-induced heating might be higher at low fields; the purpose of this study is to test the effect of patient size and positioning, target organ (liver and heart), and body coil type at a low-field RF test bench for 4 commonly-used interventional devices (two guidewires, two catheters).

**Material and Methods:** Using our recent modified Tier-3 approach [2], high resolution E field maps of 4 devices were measured during dipole excitation at  $f_{Larmor}$  (0.55T) = 23.66 MHz. Transfer function (TF) measurements were performed by placing an electro-optic sensor (EOS)[3] at the RF heating hot spot and by applying piecewise excitation as described in [4]. TFs were calibrated using various dipole excitation patterns [2]. For temperature measurements, a gel phantom was prepared [5] with  $\epsilon_r = 82.5$ ,  $\sigma = 0.63$  S/m. To test realistic device trajectories, vascular models were constructed by 3D-printing based on the angiograms of two patients (157cm, F; 175cm M). The models ranged from the femoral artery access points via the hepatic artery (HA) to the left and right coronary arteries (CA) (Fig. 1). An RF-test bench was configured with 2 body coils, and a 4-ch temperature probe was used to monitor dynamic temperature rise during an RF pulse train (TR = 5ms, power level: 1.8W/kg). The test positions included  $\pm 10$ cm in x and y axes,  $\pm 5$ cm in z axis; right and left femoral access: RF, LF, targeting HA, RCA, or LCA. In addition, the body coils were numerically modelled and an FDTD simulation was performed (Sim4Life, ZMT, Zurich) to extract the tangential E field along the trajectories defined by the vascular models. Estimated temperature rises from field simulations and TF measurements were then compared to temperature measurements.

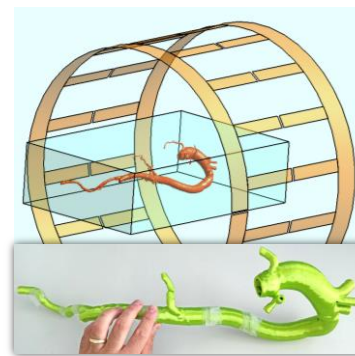


**Figure 1:** Model of a generic low-pass birdcage coil for extraction of tangential component of the simulated E fields along the realistic vascular models

**Results:** The E field mapping with the EOS showed that the hot spots are not necessarily at the tip of the device, and the TF measurements. The HA catheterization consistently resulted in less temperature rise ( $\Delta T_{max} = 0.7K$ ) than the RCA and LCA trajectories ( $\Delta T_{max} = 1.2K$ ) for all patient sizes and positioning. The difference between  $\Delta T_{max}$  for RCA and LCA was less than 0.4K. For the HA, trajectories in a 157cm/175cm patient models varied only by  $\Delta T_{max} = 0.2K / 0.3K$ . Maximum position-dependent variation below 0.5K for 90% of the cases.  $\Delta T_{max}$  from the TFs showed similar dependencies, yet up to 75% difference to the measurements. Significant differences were also observed between two body coil models.

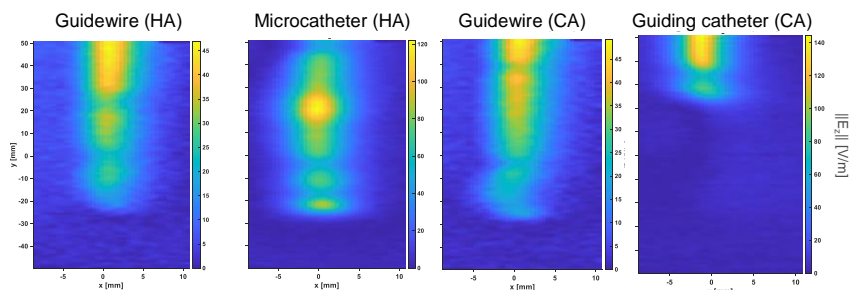


**Figure 2:** E field maps of the devices displayed on a  $20 \times 100 \text{mm}^2$  grid with 1mm resolution. Hot spots location can even be far away from the tip as the guidewires and some of the catheters have irregular wiring patterns to meet mechanical requirements during interventional operations.

**Conclusion:** Liver catheterizations with shorter insertion lengths resulted in less RF-induced heating both in temperature and TF measurements. A more accurate body coil model is required to close the gap between the TF estimation of  $\Delta T_{max}$  and the measurements. In the future, results will be compared to measurements at 1.5T to quantify the benefits of low-field interventional MRI, which could lead to an MRI system, where current commercial interventional devices can be used without modifications for interventional procedures.

**Acknowledgements:** Technical support by M. Malzacher, J. Nistler, M. Leghissa, B. Kraus of Siemens Healthineers; and Grant supports by BMBF (13GW0356B), and DFG under CRC 1425 (Project P15) are gratefully acknowledged. The mention of commercial products, their sources, or their use in connection with material reported herein is not to be construed as either an actual or implied endorsement of such products by the authors or their institutions.

**References:** [1] Campbell-Washburn AE, et al., Radiology, 293(2): 384–393 (2019), [2] Özen AC, et al. Proc ISMRM 29: 364 (2021), [3] Reiss S, et al. Phys Med Biol 60(11): 4355–70 (2015), [4] Lottner T, et al. IEEE Trans Electromagn Compat 63(3): 662–72 (2021), [5] ASTM F2182-19, W Conshohocken, PA, 2019.

# Metamaterial Inspired Surface Resonators as Wireless Coil

Robert Kowal<sup>1</sup>, Lucas Knull<sup>1</sup>, Enrico Pannicke<sup>1</sup>, Max Joris Hubmann<sup>1</sup>, Ivan Fomin<sup>1</sup>, Daniel Gareis<sup>2</sup>, Selina Scherbel<sup>2</sup>, Bennet Hensen<sup>3</sup>, Georg Rose<sup>1</sup>, Frank Wacker<sup>3</sup>, Oliver Speck<sup>1</sup>

<sup>1</sup>Research Campus *STIMULATE*, Otto-von-Guericke University, Magdeburg, Germany, <sup>2</sup>NORAS MRI products GmbH, Höchberg, Germany, <sup>3</sup>Hannover Medical School, Hannover, Germany

**Purpose:** Wireless coils can be of great advantage in the workflow of an intervention in order to reduce e.g. placement and sterilization challenges. This contribution demonstrates an inductively coupled metamaterial inspired surface resonators to enhance the receive capability of the scanner internal coils and compares the coil to a commercially available wireless coil.

**Material and Methods:** A flexible surface resonator based on metamaterial concepts [1] was developed consisting of an array of resonant unit cells (see Fig. 1a). By integration of a surrounding non-linear resonance circuit based on limiter diodes, the system is detuned during transmission. The imaging capability was examined on a 3 T scanner (MAGNETOM Skyra, Siemens Healthineers) and compared to a commercial wireless coil (see Fig. 1b, InSitu, IMRIS) [2]. Using scanner internal coils for coupling, the signal-to-noise-ratio (SNR) profile and their enhancement ratio was calculated in a homogenous phantom (cuboid, 0.5 S/m, 36x36x23 cm) respectively.

**Results:** The proposed wireless coil provided enhanced SNR in its direct proximity when coupled to the body coil (see Fig. 1c and 1d). The metamaterial inspired coil showed higher and more homogenous penetration underneath the coil center compared to the commercial coil. Additionally, its signal enhancement ratio was measured with up to 2.5-fold at a depth of almost 5 cm, central to the coil (see Fig. 1f). In contrast, the reference coil featured its significant maxima around its borders and the enhancement ratio decreases more steeply with a central signal reduction (see Fig. 1g).

**Conclusion:** The metamaterial inspired surface resonator shows a field pattern for higher penetration depth, while also maintaining high SNR in the vicinity of the resonator center compared to the commercial reference coil. Although direct access through the center is hampered, the design will be improved in this respect in the future. This type of wireless coil is a promising alternative for receiver enhancement to perform MRI-guided interventions, especially for deeper target areas.

**References:** [1] Stoja et al., *Sci. Rep.*, 16179, 2021. [2] Boop et al., *J Neurosurg. Pediatr.*, vol. 15, 539-543, 2015.

**Acknowledgement:** The work of this paper is funded by the Federal Ministry of Education and Research within the Research Campus *STIMULATE* under the number '13GW0473A', '13GW0473B' and '13GW0473K'.

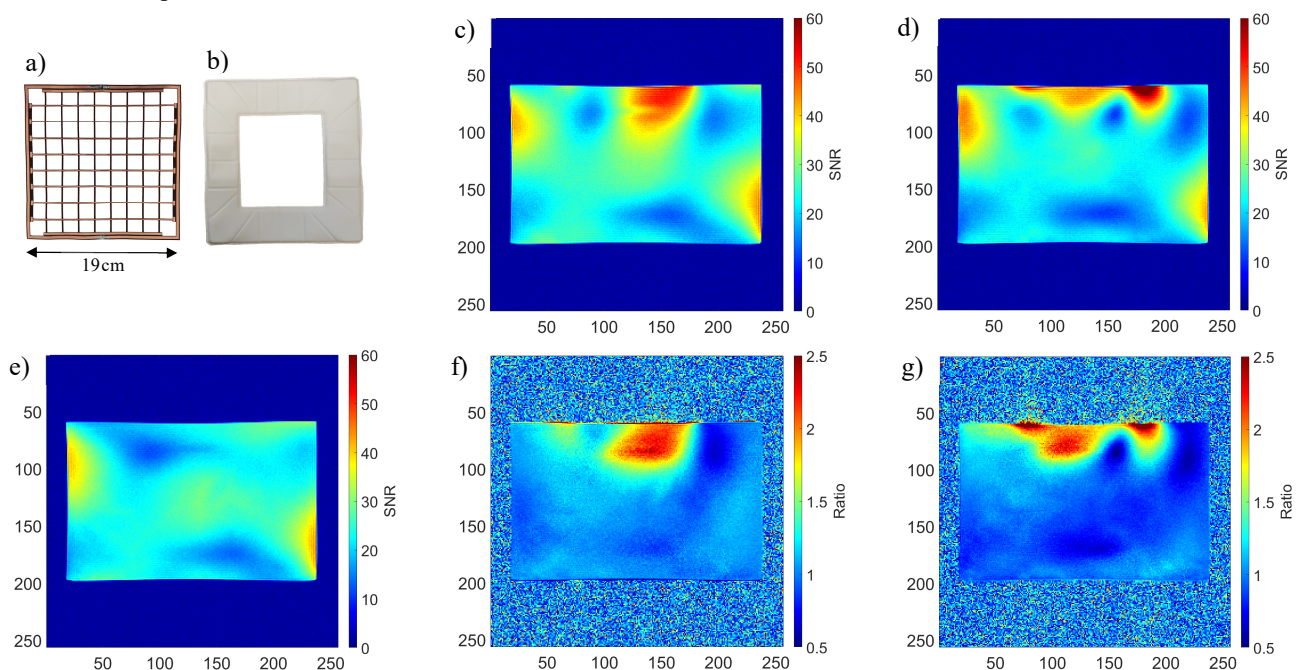


**Fig. 1:** Comparison of the wireless coils, centrally positioned on top of a homogenous phantom. Transversal SNR profiles and resonator enhancement ratios (with local resonator / body coil only). Metamaterial inspired surface resonator a), c) and f). Commercial coil (InSitu, IMRIS) b), d) and g). Reference SNR profile with body coil only for ratio calculation e).



# Multi-Channel Receive Coil for MRI-Guided Interventions

Robert Kowal<sup>1</sup>, Enrico Pannicke<sup>1</sup>, Daniel Gareis<sup>2</sup>, Selina Scherbel<sup>2</sup>, Lucas Knull<sup>1</sup>, Ivan Fomin<sup>1</sup>, Max Joris Hubmann<sup>1</sup>, Bennet Hensen<sup>3</sup>, Georg Rose<sup>1</sup>, Frank Wacker<sup>3</sup>, Oliver Speck<sup>1</sup>

<sup>1</sup>Research Campus *STIMULATE*, Otto-von-Guericke University, Magdeburg, Germany, <sup>2</sup>NORAS MRI products GmbH, H"ochberg, Germany, <sup>3</sup>Hannover Medical School, Hannover, Germany

**Purpose:** Multi-channel surface coils conventionally feature many discrete electric components implemented directly at the coil elements. In order to allow high flexibility, large access area for MRI-guided interventions and minimal costs of the coil elements, this work demonstrates the prototype of a remote decoupled multi-channel receive coil free of discrete electronic elements.

**Material and Methods:** A 2-channel receive coil based on a microstrip design [1, 2] was developed (see Fig 1a). Remote transmit-decoupling was accomplished by an impedance transformation circuit and measured by a double-probe. Non-discrete capacitive element-decoupling [3] was utilized to minimize mutual impedance of neighboring elements and maximize accessible area for the interventional team (see Fig. 1b). The coil features a total size of 25x12 cm with two square openings of 11x11 cm which can be embedded into a flexible housing. Workbench measurements as well as images of a homogenous salt water phantom (0.4 S/m, 32x32x32 cm) acquired on a 3 T scanner (MAGNETOM Skyra, Siemens Healthineers) were used to validate the proposed design.

**Results:** The 2-channel coil's tuning and element-decoupling characteristics are depicted in Fig. 1c, showing reflection and transmission coefficients of less than -30 dB. Remote transmit-decoupling was measured with a suppression of -17 dB. Acquired sensitivity profiles were typically asymmetric and presented distinctly differentiated sensitivities of the two channels (see Fig. 2) allowing parallel acquisition (see Fig. 2d).

**Conclusion:** The presented concept of a capacitively decoupled receive coil allows highly flexible multi-channel layouts. The low-profile structure can be manufactured cost-effectively as a two-layer PCB due to the absence of discrete components and provides large access areas for MRI-guided interventions.

**References:** [1] Pannicke et al., EMBC, pp. 1522-1526, 2021  
[2] Corea et al., Nat. Commun., vol. 7, 10839, 2016  
[3] Beck et al., Concepts Magn Reson Part B Magn Reson Eng, 8828047, 2020

**Acknowledgement:** The work of this paper is funded by the Federal Ministry of Education and Research within the Research Campus *STIMULATE* under the number '13GW0473A', '13GW0473B' and '13GW0473K'.

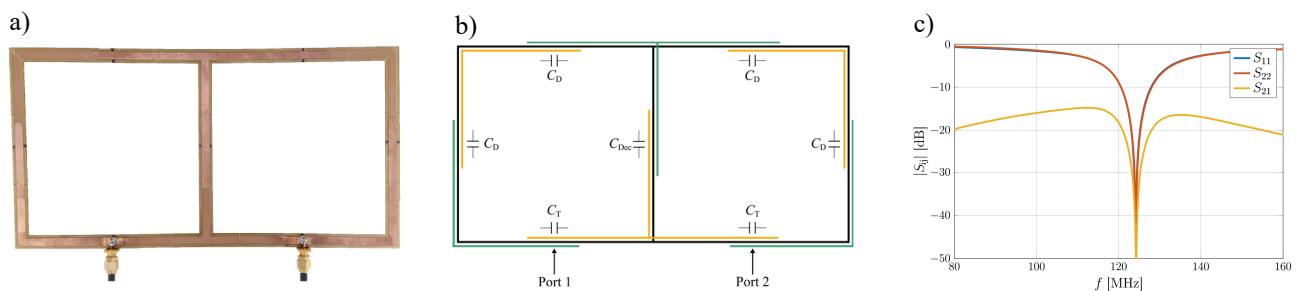


**Fig. 1:** Two-channel receive coil, a) layout, b) schematic of copper layers, c) reflection and transmission coefficients.

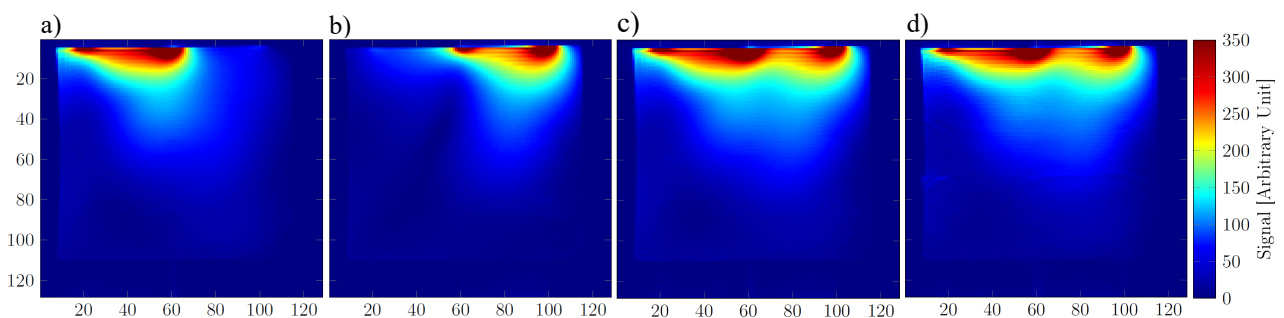


**Fig. 2:** Sensitivity profiles acquired with a 3T scanner. a) Independent Port 1, b) independent Port 2, c) combined channels, d) Parallel acquisition R=2 (GRAPPA).

## Assessing MR compatible biopsy grids for interventional procedures

E. Fischer<sup>1</sup>, K. Cleary<sup>1</sup>, K. Sharma<sup>1</sup>, N. Mouzakis<sup>1</sup>, M. Gebremeskel<sup>1</sup>, P. Yarlomenko<sup>1</sup>, R. Monfaredi<sup>1</sup>  
<sup>1</sup>Children’s National Health System, Washington, DC, USA

**Purpose.** Image-guided needle biopsy is commonly performed with CT guidance. Although CT provides good visualization of bone and soft tissue regions, it lacks the soft tissue detail provided by MRI, especially in the musculoskeletal system. During CT-guided biopsy procedures, radiopaque CT marker grids are placed on the skin over the region of interest. These markers assist the interventionalist in planning initial needle placement and trajectory. Similar devices to aid MRI-guided procedures are needed. This preliminary study assessed visualization of two custom-made MR-compatible, silicon marker grids using a gel phantom on a 1.5T scanner.

**Materials and Methods.** Two grid templates were created: one with straight parallel lines that resemble currently available commercially available CT marker grids and another designed with different shapes and numbers. The molds of the grid templates were 3D-printed in two pieces using an Objet 500 Vero white material. A layer of fiberglass mesh was then placed between the upper and lower half of the molds. The molds were clamped to each other. The cavities of the mold were then injection molded and filled with high-performance silicone rubber (Dragon Skin, Smoth-on Inc, PA) with a syringe. The silicon was left to cure for several hours. Each grid marker was then placed over the gel phantom at 0 degrees relative to B<sub>0</sub> and scanned in a head coil with T1 and T2 sequences of a Siemens Aera 1.5T scanner. The marker with the lines had axial scans obtained and the marker with the shapes had coronal scans obtained.

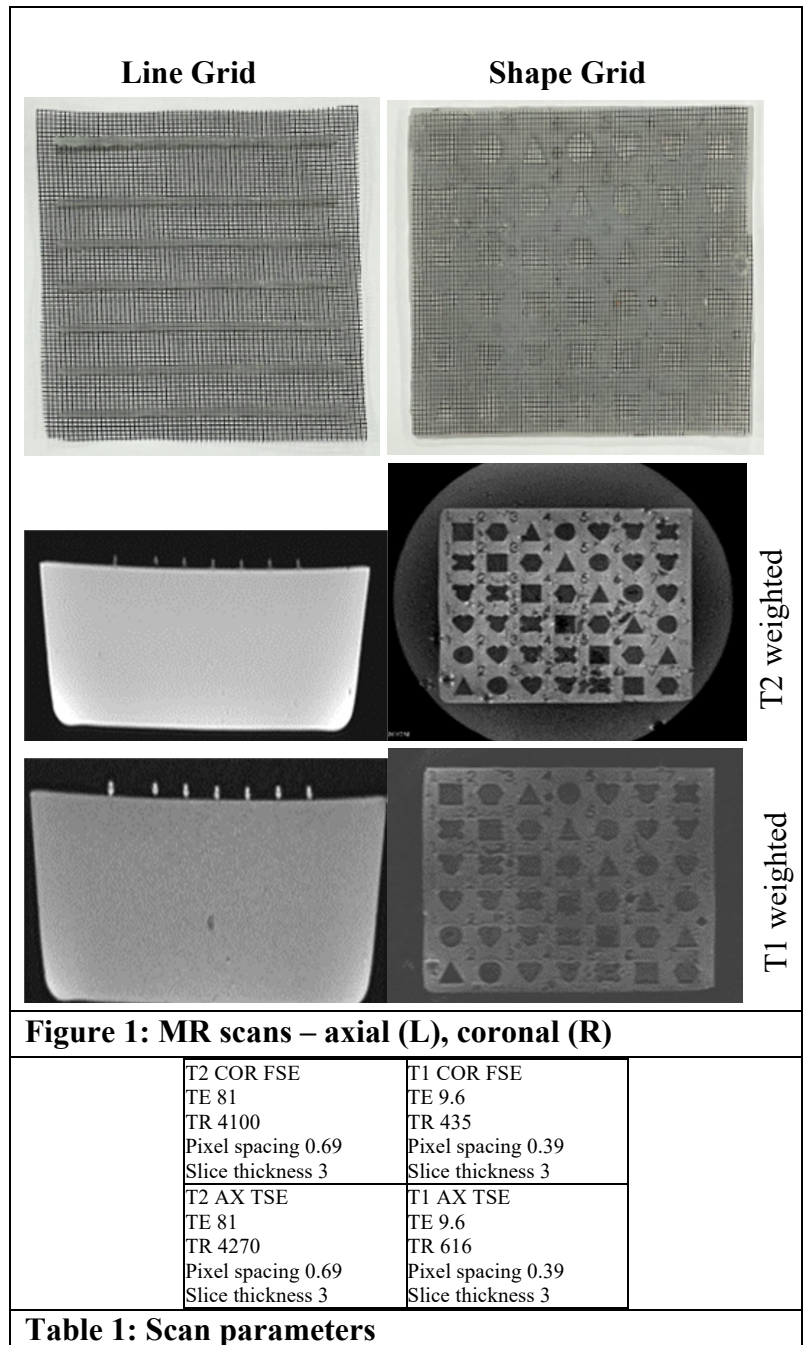


**Figure 1: MR scans – axial (L), coronal (R)**

T2 COR FSE		T1 COR FSE	
TE 81	TR 4100	TE 9.6	TR 435
Pixel spacing 0.69	Slice thickness 3	Pixel spacing 0.39	Slice thickness 3
T2 AX TSE		T1 AX TSE	
TE 81	TR 4270	TE 9.6	TR 616
Pixel spacing 0.69	Slice thickness 3	Pixel spacing 0.39	Slice thickness 3

**Table 1: Scan parameters**

**Results.** The grid markers and associated T1w and T2w images are shown in **Figure 1**. The scan parameters are shown in **Table 1**. Based on these parameters, T2w scans show improved detail of the marker over the gel phantom.

**Conclusion.** This study assessed the MR visibility of two custom-made silicon grid markers designed to aid MR-guided procedures. Further studies are being conducted to verify the usefulness of these marker grids during MR-guided biopsies and injections. In the future, they may aid MR guided, robotically assisted procedures in the bore of the magnet.

# Sensorless and Cost-Efficient Force Feedback Signal Acquisition for Bowden Cable-Driven Manipulators and Robotics during Image-Guided Procedures

Marcel Eisenmann<sup>1</sup>, Ivan Fomin<sup>1</sup>, Robert Odenbach<sup>1</sup>, Bennet Hensen<sup>2</sup>, Frank Wacker<sup>2</sup>, Georg Rose<sup>1</sup>  
<sup>1</sup>Otto-von-Guericke-University Magdeburg, Germany, <sup>2</sup>Hannover Medical School, Germany

**Purpose:** Medical manipulators and robotics are used to assist doctors during minimal-invasive surgery [1]. By introducing force feedback, physicians can be given a haptic feeling during needle positioning to increase clinical performance in interventional magnetic resonance imaging (iMRI) [2]. In the current state of scientific research, iMRI manipulators/robotics are rarely equipped with a force feedback or are using force sensors directly on actuators [3]. In this work, a sensorless and cost-efficient technique for tracking the forces during needle insertion with a cable-driven robotic assistance system without using additional sensors is presented.

**Material and Methods:** To demonstrate the force feedback technique, the  $\mu$ RIGS system [4] was used with a modified software of its control firmware. For realistic data acquisition, a puncture needle was guided into a tissue phantom [5] built up with four different material layers (see Fig. 1a). The friction forces during the penetration can be derived from the motor load that was sensed with a conventional motor driver (TMC2130, TRINAMIC Motion Control GmbH & Co. KG).

**Results:** The motor load over penetration depth showed clearly distinguishable gradients within the specific phantom layer (see Fig. 1b). Two major factors are responsible for the variation of the motor load: material-specific friction properties of each layer and the increasing penetration depth. In the zone from harder to softer material, an adaptation transition about 20 mm persisted.

**Conclusion:** The presented setup demonstrates the technical feasibility of a sensorless force feedback concept into the existing hardware structure of the cable-driven  $\mu$ RIGS-system. The data acquisition will be further analyzed in terms of a reliable correlation between force and material with its transitions which can be then used for a needle insertion controller to provide haptic feedback. This could increase the acceptance of medical robotics among surgeons and interventionists. Furthermore, a calibration of the actuator positions or the detection of any unpredictable collisions are possible.

**References:** [1] Thai et al., Adv. Intell. Syst., 1900138, 2020. [2] Hata et al., TMRI, 19-23, 2018. [3] Monfaredi et al., Ann Biomed Eng, 1479–1497, 2018. [4] Fomin et al., CDMBE, 81-85, 2021. [5] Engel et al., iMRI, 2022 (submitted).

**Acknowledgment:** The work of this paper is funded by the Federal Ministry of Education and Research within the Research Campus *STIMULATE* under the number '13GW0473A', '13GW0473B'.

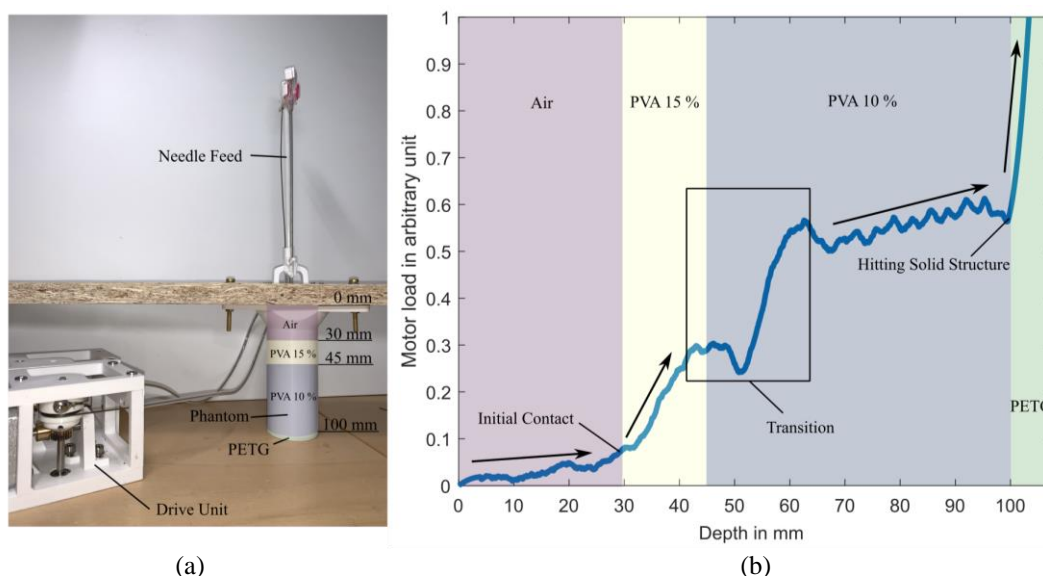


**Fig. 1:** (a) Test setup with the needle feed of  $\mu$ RIGS using a 16 G coaxial needle, drive unit and tissue phantom (Air, Polyvinyl alcohol (PVA) 15 %, PVA 10 %, Polyethylene terephthalate glycol (PETG)). (b) Motor load during needle insertion with prominent events and material specific gradients (black arrows). The graph is plotted with a moving average filter with a window size of 1000 data points.

## Multifunctional, elastic and non-metallic Bowden-cable coupling mechanism for the modularization and remote control of the $\mu$ RIGS instrument micropositioning system

Niklas Thoma<sup>1</sup>, Robert Odenbach<sup>1</sup>, Ivan Fomin<sup>1</sup>, Bennet Hensen<sup>2</sup>, Frank Wacker<sup>2</sup>, Georg Rose<sup>1</sup>  
<sup>1</sup>Otto-von-Guericke University Magdeburg, Germany, <sup>2</sup>Hannover Medical School, Germany

**Purpose:** Handling of instruments next to the patient and inside the confined space of an MRI-tunnel still is one of the most challenging aspects for interventional MRI procedures. In the past two years, the demonstrator of our  $\mu$ RIGS-system has proven great potential for universal and remotely operated iMRI [1]. It is compact in dimension, capable to support versatile instruments (e.g. biopsy- and RFA-needles) and provides a remote five degree of freedom instrument alignment above the puncture location.

Nevertheless, for future integration into the clinical iMRI-workflow specific challenges, such as enhanced patient safety, faster intervention times and the reduction of costs still need to be addressed by the system. To improve these attributes, an appropriate coupling interface mechanism is needed to split the  $\mu$ RIGS-system into a low cost, non-permanent and sterile instrument-support-portion, and on the other hand into a permanent and technically highly equipped component. As the motor unit and the instrument support unit of the  $\mu$ RIGS-system are connected via Bowden cables, a technically suitable separation of them is required. In this paper we present the results from the development and evaluation of a multifunctional, elastic and non-metallic Bowden cable coupling mechanism.

**Material and Methods:** The coupling mechanism is designed as a plug connector that links the Bowden cables from both the permanent unit and the sterile unit reliably with each other. It provides individual and remote transmission of all kinematic degrees of freedom of the  $\mu$ RIGS-system. In addition, a shiftable elastic operation mode as well as an emergency decoupling feature are integrated to minimize stress and to increase safety for the patient. The demonstrator of the coupling mechanism is fully 3D-printed and fabricated out of non-metallic material. For the evaluation of its MR-compatibility and overall functionality, the coupling mechanism was placed on an abdominal phantom (Fraunhofer IFF) inside our 3T MRI-system (Magnetom Skyra, Siemens Healthineers), see Fig. 1.

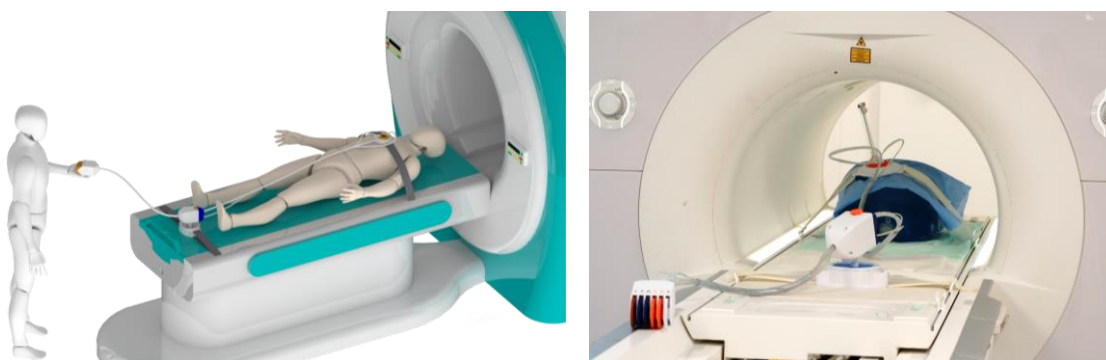


**Fig. 1:** The technical concept of the integration of the mechanical coupling unit into the  $\mu$ RIGS-system (left); and the physical demonstration setup on a phantom study inside the tunnel of the Skyra-MRI (right)

**Results:** The demonstrator-based evaluation has proven a reliable functionality of the remote motion transmission with forces of up to 128 N in combination with a friction loss of about 20-22 %. The MR-safety tests on all components didn't show any potential hazards nor any disturbances in the field of view.

**Conclusion:** This study proves a workflow-efficient design for the implementation of the  $\mu$ RIGS-system in interventional MRI procedures. The coupling mechanism provides a fast and safe connection between the low-cost instrument alignment unit and the permanent and technically complex equipped motor unit. In addition, the setup comfort of the  $\mu$ RIGS-system is highly improved. In future, the design will be tested in clinical trials.

**Funding:** The work of this paper is funded by the Federal Ministry of Education and Research within the Research Campus *STIMULATE* under the numbers '13GW0473A' and '13GW0473B'

**Reference:** [1] Fomin, I; Odenbach, R; Pannicke, E; Hensen, B.; Wacker, F.; Rose, G.:  $\mu$ RIGS - ultra-light micropositioning robotics for universal MRI; in Current directions in biomedical engineering - Berlin: De Gruyter, Vol. 7 (2021)

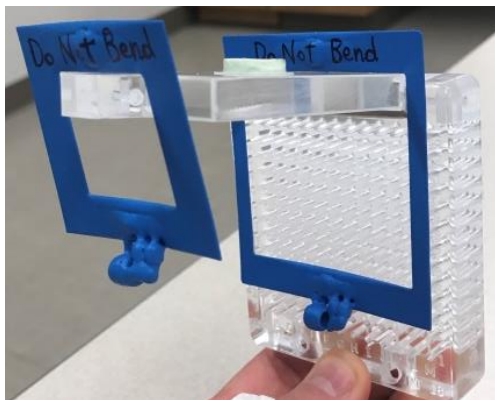
## Local MRI Wireless RF Coils to Boost Calibration Reference Signal Prior to MRI Guided Interventional Treatments

J. Felmlee PhD, A. Lu PhD, C. Favazza PhD, L. Mynderse MD\*, D. Woodrum MD PhD

Departments of Radiology and Urology\*, Mayo Clinic, Rochester Minnesota USA

**Purpose:** Our image guided therapy system’s calibration requires images that cover an extended volume including both the calibration grid as well as the tissues targeted for treatment. Three calibration reference “keys” within the calibration grid must be accurately identified within images as part of the analysis software. These keys are small “+” shaped targets that at times are difficult to visualize due to treatment geometries that require the imaging RF coils be positioned over the target tissue away from the calibration grid. If the specific calibration keys cannot be visualized well, the images used to guide patient treatment will have reduced accuracy. Wireless coils were developed to improve the image SNR from the reference keys and improve the routine calibration process prior to MRI Guided Interventional treatments.

**Methods:** The images below show the 3D nature of the calibration grid. The grid contains holes that are used to guide treatment needles in an x-y plane and contain reference keys (two keys in the corners of the grid plane and one key at the end of the projection) to calibrate the spatial dimensions of the volume. The wireless coils:



- Are passively RF blocked during body coil excitation and positioned close to the keys.
- Couple with the patient imaging coils to improve depiction of the reference keys within the acquired images.
- Are removed without affecting grid position after the calibration imaging is completed and prior to treatment.

**Results:** Analysis of calibration images acquired with and without the wireless coils show an average factor of 1.7 improvement in SNR at the locations of the calibration keys.

**Conclusions:** The wireless coils have been shown to improve the reception SNR of the calibration keys within the calibration grid and provide a simple means to improve the workflow associated with pre-treatment system calibration.

# Radiofrequency Safety of External Defibrillation Electrodes at 1.5T

W.M. Brink<sup>1</sup>, R. Oosterveld<sup>2</sup>, R.M. Verdaasdonk<sup>2</sup>

<sup>1</sup>Magnetic Detection & Imaging Group, dept. of Science and Technology, University of Twente, Enschede, Netherlands; <sup>2</sup>Biomedical Photonic Imaging group, dept. of Science and Technology, University of Twente, Enschede, Netherlands

**Purpose:** Although interventional MR imaging bears merits in addressing complex interventional procedures, providing external defibrillation in the MR environment is challenging due to the lack of commercially available MR-compatible defibrillators. This limits critical patient groups from obtaining MRI access, while these would actually benefit most from having accurate MR guidance.

Recent developments in MR-compatible defibrillation lead cables show to successfully conduct in-bore discharges of up to 360 J.<sup>1,2</sup> Furthermore, advanced shock waveform designs enable defibrillation with drastically reduced muscle contractions, minimizing patient motion during the shock delivery.<sup>3</sup> Limited insights have however yet been established in terms of MR safety. In particular, radiofrequency (RF) heating can be a confounding factor in reported skin reddening and lesions observed at the electrode borders.<sup>1</sup> Furthermore, improved RF safety of these electrodes may also warrant the use of MR-compatible defibrillation systems in other MR applications.

In this work, we evaluated the RF safety effects of external defibrillator electrodes through EM simulations and RF heating measurements in a phantom. Electrode design considerations are identified and evaluated in terms of RF heating, and a modified electrode design is proposed which aims to mitigate these risks.

**Materials and Methods: Phantom and Electrode:** A 5L rectangular phantom was made consisting of agarose gel (2% w/w) with 3 g/L NaCl for electrical conductivity adjustment. A generic AED electrode (Heartstart FR2, Philips Healthcare, Best, the Netherlands) of size 10 × 18 cm was positioned on top of the phantom, and subsequently replaced by a modified electrode, first with slits in the feet-head direction and secondly with slits in the left-right direction.

**EM simulations:** The RF field in a quadrature body coil model was simulated at 64 MHz using FDTD (XF7.4, Remcom inc., State College, PA) in a 2-mm grid to evaluate the 10g-averaged specific absorption rate (SAR<sub>10g</sub>). The resolution around the phantom ( $\epsilon_r = 50$ ,  $\sigma = 0.5$  S/m) was increased to 0.5 mm in order to accurately represent the electrode adhesive ( $\epsilon_r = 2.5$ ,  $\sigma = 0.05$  S/m). All simulated data were normalized to a nominal  $B_1^+$  of 2  $\mu$ T in the transverse cross-section of the phantom.

**RF Heating:** A high-SAR protocol was performed in a Siemens Aera 1.5T MRI system. The protocol consisted of a T<sub>1</sub>-weighted FSE sequence with minimized TR and 180° refocusing pulses to maximize RF exposure, with a duration of 20 min. Before and after each heating period, thermographic images of the phantom surface were obtained using an infrared camera (Flir One Pro-Series, Teledyne FLIR, Wilsonville, OR) after removal of the electrode.

**Results:** EM simulations of the phantom setup are shown in Figure 1, showing considerable SAR<sub>10g</sub> changes in the different defibrillation electrode configurations. When vertical slits were introduced, local SAR<sub>10g</sub> was almost doubled in comparison to having no electrode, while SAR<sub>10g</sub> decreased when introducing horizontal slits in the electrode. Thermographic images are shown in Figure 2, showing very similar heating patterns as observed in the EM simulations.

**Conclusion:** In this study we have evaluated the RF safety effects of defibrillation electrodes that can be used in-bore defibrillation setups. These data indicate that in high-SAR sequences such as FSE or bSSFP, which are very popular in interventional settings, RF heating underneath the electrode can reach levels considerably higher than previously reported.<sup>1,2</sup> The RF heating patterns showed a strong dependence on electrode design parameters, which provide avenues for further development of MR compatible external defibrillators.

## References:

1. Shusterman V, Hodgson-Zingman D, Thedens D, et al. High-energy external defibrillation and transcutaneous pacing during MRI: Feasibility and safety. *Journal of Cardiovascular Magnetic Resonance*. 2019;21(1):1-14. doi:10.1186/S12968-019-0558-Z/FIGURES/10
2. Schmidt EJ, Watkins RD, Zviman MM, Guttman MA, Wang W, Halperin HA. A Magnetic Resonance Imaging-Conditional External Cardiac Defibrillator for Resuscitation Within the Magnetic Resonance Imaging Scanner Bore. *Circ Cardiovasc Imaging*. 2016;9(10). doi:10.1161/CIRCIMAGING.116.005091
3. Schmidt EJ, Elahi H, Meyer ES, et al. Reduced motion external defibrillation: Reduced subject motion with equivalent defibrillation efficiency validated in swine. *Heart Rhythm*. 2022;19(7):1165-1173. doi:10.1016/J.HRTM.2022.02.021

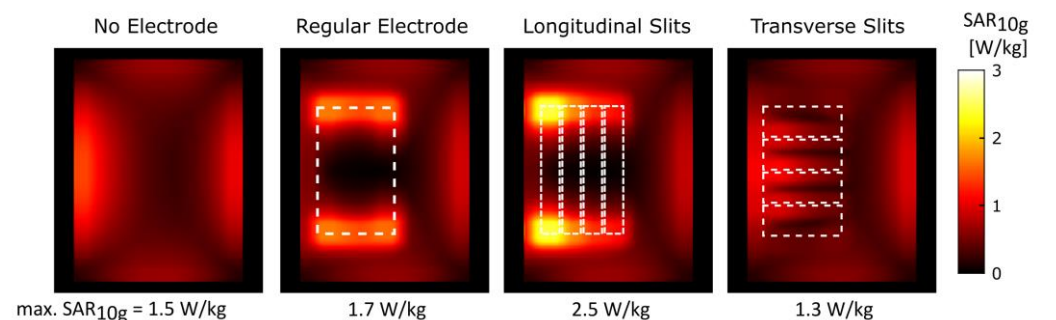


Fig.1 RF field simulation results showing SAR<sub>10g</sub> effects in different electrode configurations.

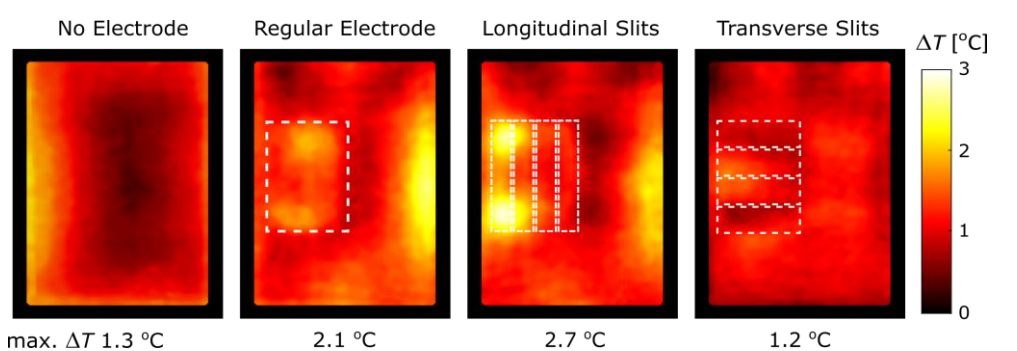


Fig.2 Thermographic measurements showing temperature increases in different electrode configurations. RF heating was increased with vertical slits and decreased with horizontal slits.

# DISPOSABLE & INTUITIVE NEEDLE GUIDE FOR NEEDLE-BASED INTERVENTIONS

Juan Sebastián Sánchez López<sup>1</sup>, Julian Alpers<sup>1</sup>, Sathish Balakrishnan<sup>1</sup>, Frank Wacker<sup>2</sup>, Bennet Hensen<sup>2</sup>, Maciej Pech<sup>3</sup> and Mathias Becker<sup>3</sup>

<sup>1</sup>InLine-Med GmbH, Magdeburg, 39106, Germany

<sup>2</sup>Hannover Medical School, Institute for Diagnostic and Interventional Radiology, Hannover, 30625, Germany

<sup>3</sup>University of Magdeburg, Department of Radiology and Nuclear Medicine, 39120 Magdeburg, Germany

**Purpose.** MRI interventions are currently established as a clinical routine for several applications<sup>1</sup>. Advantages from MRI compared to CT and US in interventions include multiplanar navigation, higher anatomic detail, better soft tissue contrast and lack of ionization radiation<sup>2</sup>. The most common approach for performing iMRI is the freehand technique in open MRI<sup>3</sup>. Yet, this approach introduces additional complications in MRI configurations with restricted space. In cooperation with OVGU Hospital and Hannover Medical School, two problems for these kind of interventions were identified. First, positioning the needle in the narrow setup and second keeping alignment during intervention.



Figure 1: Disposable needle guide

**Material and Methods.** A disposable needle guide was developed, patented and tested (see Fig. 1). The needle guide enables angulations in two directions (2 DOF) in a range of  $-45^\circ$  to  $45^\circ$ . The locking mechanism for angulation release-fixation is achieved by  $\frac{1}{4}$  rotation of the driving nut. The device was prototyped under SLA 3D printing using FLGPWH03 and FLTOTL04 resins. The base biocompatible adhesive facilitates an easy positioning on the patient's body. For multipurpose applications, the needle guide permits guidance from 12 to 18-gauge size. Additionally, a visible marker was prototyped to facilitate visualization during alignment and was evaluated in an MRI scanner (3T, Skyra, Siemens). The holding force of the device was evaluated by using a press force machine with a precision of 0.01 N force. Afterwards, the maximum lateral forces applied to needles and RF-ablation electrodes were measured.

respectively. The needle guide did not create any artifact nor presented any undesired motion due to the strong magnetic field. The needle guide probe was easily seen under T1 sequence and orthogonal MPR views (see Fig.2). Needles of different gauges and RF-electrodes were placed under specific alignments, and the devices kept the planned alignment.

**Conclusion.** The needle guide can potentially support free-hand technique in multiple applications as biopsies, periarticular therapy or thermal therapy MRI-guide. The needle-guide improves the process of holding electrodes during RF-ablation procedures avoiding external personnel for holding electrodes.

**Results.** The maximum load supported by the device was approximately 2,3N and 1,8N for vertical and horizontal position

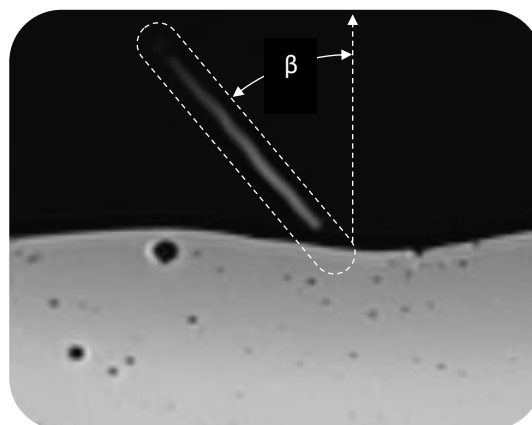


Figure 2: Visible fiducial marker inside the needle guide. Beta = angulation angle from default position.

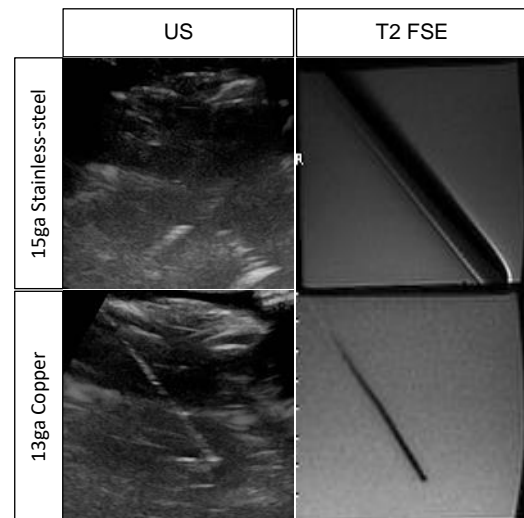
## References

- <sup>1</sup>Blanco Sequeiros, R., Ojala, R., Kariniemi, J., Perälä, J., Niinimäki, J., Reinikainen, H., & Tervonen, O. (2005). MR-guided interventional procedures: a review. *Acta Radiologica*, 46(6), 576-586.
- <sup>2</sup>Weiss, C. R., Nour, S. G., & Lewin, J. S. (2008). MR-guided biopsy: A review of current techniques and applications. *Journal of Magnetic Resonance Imaging: An Official Journal of the International Society for Magnetic Resonance in Medicine*, 27(2), 311-325.
- <sup>3</sup>Rothgang, E., Gilson, W. D., Wacker, F., Hornegger, J., Lorenz, C. H., & Weiss, C. R. (2013). Rapid freehand MR-guided percutaneous needle interventions: An image-based approach to improve workflow and feasibility. *Journal of Magnetic Resonance Imaging*, 37(5), 1202-1212.

**A Faacks, J Holmes, J Mitra, C Bhushan, D Mills, M Tarasek, D Yeo, C Brace, S Wells**  
 University of Wisconsin-Madison, Madison, WI, USA, School of Medicine and Public Health,  
 Departments of Radiology, Urology, Medical Physics, and Biomedical Engineering; University  
 of Iowa, Iowa City, IA, USA, Departments of Radiology and Biomedical Engineering; GE  
 Research, Niskayuna, NY, USA

**Purpose:** Poor tumor conspicuity with conventional image-guidance modalities limits targeting, contributes to non-diagnostic biopsy and poor oncologic outcomes after percutaneous thermal ablation. Magnetic resonance imaging (MRI) offers superior soft tissue contrast and volumetric anatomic coverage. Unfortunately, needle/applicator placement with MRI is challenging and time-consuming due to bore geometry. Hybrid deformable fusion of MRI with hands-free, electronically steerable ultrasound (US) in real-time *on the MRI gantry, outside of the bore* may optimize tumor conspicuity and targeting while providing fast and safe needle/applicator placement. There are limited needle/applicators for MRI-guided intervention, and none are optimized for the hybrid MRI-US environment. In this work, we evaluate the visual conspicuity, operator confidence and imaging artifact levels of five coaxial applicators for this hybrid imaging environment.

**Materials and Methods:** Five coaxial needle-like device were secured at a 60° angle in five of six 10 cm cubic molds and 1L of degassed 1.4% agar/0.025% gadobenate dimeglumine solution was poured and allowed to solidify around the coaxial device. Device gauge (ga) and materials were: 15-ga stainless-steel (SS) (reference standard), 10-gauge copper (Cu10), 13-ga copper (Cu13), 14-ga alumina and 14-ga zirconia. FSE T2-weighted axial MRI (TR=134ms, TE=10,000ms, FA=125, matrix 220x220, FOV 20x20cm, BW=4.17kHz, slice thickness=2mm, overlap=0.4mm) and 2D US of the six phantoms including a control (no device) was performed (Figure). Radiology faculty (n=10) and trainees (n=15) experienced in MRI and US-guided interventions reviewed the images and assessed device conspicuity and artifact on a 4-point Likert-like scale. Categorical variables were summarized with frequency counts and percentages. Continuous data was summarized with median (IQR). Responses were analyzed with the Chi-squared test and p<0.05 denoted statistical significance.



**Results:** Faculty and trainee responses were similar (p>0.4), thus collated. The reference SS device had significantly poorer conspicuity than other devices (p<0.0001) and was similar to control (no device) (p=0.47). MRI conspicuity of the SS device was rated high by 25/25 respondents, but with artifacts that were significantly more severe than other needles (moderate/severe=18/25; p<0.0001). Applicator identification (25/25, 25/25, 24/25, 25/25), perceived conspicuity (88%, 100%, 92%, 80% as ‘good’ or ‘excellent’) and confidence (88%, 96%, 88%, 88% as ‘confident’ or ‘very confident’) were high at US for Cu10, Cu13, alumina and zirconia devices. Confidence improved (88%, 92%, 100%, 100%) and artifact was rated as negligible by most respondents (88%, 80%, 80, 88%) for Cu10, Cu13, alumina and zirconia.

**Conclusions:** Copper, alumina and zirconia coaxial needle-like devices produce minimal artifact on MRI, are highly visible on US and improve operator confidence.



# Simultaneous T2-weighted MRI of 2 Orthogonal Slices for Real-time Lesion Tracking

Samantha Hickey<sup>1</sup>, Andreas Reichert<sup>1</sup>, Wolfgang Ptacek<sup>2</sup>, Thomas Bortfeld<sup>3</sup>, and Michael Bock<sup>1</sup>

<sup>1</sup>Dept. of Radiology, Medical Physics, Medical Center University of Freiburg, Faculty of Medicine, Univ. of Freiburg, Germany

<sup>2</sup>ACMIT GmbH, Wiener Neustadt, Austria, <sup>3</sup>Division of Radiation Biophysics, Dept. of Radiation Oncology, Massachusetts General Hospital and Harvard Medical School, Boston, MA, USA

**Introduction** MRI in radiotherapy (RT) provides unparalleled soft-tissue contrast for real-time tumor visualization<sup>1</sup>. Current MR-guided RT procedures use T1-weighted spoiled GRE, or T1/T2-weighted balanced steady state free precession sequences to monitor the procedure in real-time<sup>2,3</sup>. T2-weighted MR images, however, inherently provide better visualization of pathology allowing for accurate target delineation. Conventional T2-weighted MR sequences, unfortunately, have a low temporal resolution. In this work, we introduce a real-time sequence (PSIF-CROSS<sup>4</sup>), which simultaneously acquires two T2-w orthogonal slices. The sequence was used to monitor breathing motion in a volunteer and in an abdominal breathing phantom to track the motion of an embedded target.

**Methods** The PSIF-CROSS sequence measures the spin echo ( $S'$ ) component of a steady state signal<sup>5</sup> in two orthogonal slices (Fig.1). Therefore, the phase encoding and slice selection directions of both slices are interchanged and the readout direction is shared<sup>3,6</sup>. The sequence was implemented on a 3T whole body MR system (MAGNETOM Prisma, Siemens Healthineers). Multiple images were acquired in a volunteer ( $\alpha = 30^\circ$ , TR/TE = 7.92/3.95ms, BW = 870Hz/px, SL = 6mm, FOV = 350mm<sup>2</sup>, matrix = 192, PF = 6/8, phas res = 80%, TA = 0.91s.) and in an abdominal breathing phantom with artificial target lesions ( $\alpha = 30^\circ$ , TR/TE = 8.20/4.09ms, BW = 870Hz/px, SL = 6mm, FOV = 325mm<sup>2</sup>, matrix = 192, PF=6/8, phas res = 80%, TA= 0.94s.) using the spine and body array coils for signal reception. In a postprocessing step, the target was contoured in MATLAB (v. 2021b, MathWorks, Inc., MI, USA) using the *Image Segmenter App* (flood fill) and then the centroid of the target was calculated automatically in both slices.

**Results & Discussion** The PSIF-CROSS sequence resolved kidney motion in a volunteer and the motion of an embedded target in a phantom, in both slices simultaneously (Fig.2+3). The automatically determined centroid of the embedded target resembles periodic breathing motion (Fig.4). In the slice overlap region, residual signal artifacts from the interference between the two slices were observed, but these artifacts could be shifted to the margin of the FOV by phase cycling<sup>7</sup>. Minor dephasing also occurred due to motion, however, could be reduced by increasing the temporal resolution, e.g. by implementing parallel imaging. In summary, the sequence can acquire T2-w orthogonal real-time images at a high temporal resolution, resolve motion in an abdominal phantom, and track a target in both slices, which can be used in MR-guided interventions or RT.

**Acknowledgements** This work was supported in part by a grant from the German Federal Ministry for Economic Affairs and Energy (BMWi) under the grant program “Zentrales Innovationsprogramm Mittelstand (ZIM),” grant number ZF4535603BA9, as part of the IraSME funding “E-GantryMate.”

**References** [1] Kurz C, et al. *Radiat Oncol.* 2020;15(93). [2] Tryggstad E, et al. *Med Phys.* 2013;40(9):091712. [3] Mickevicius NJ, et al. *Magn Reson Med.* 2017;78(5):1700-1710. [4] Hickey S, et al. In: *Proc. Int. Soc. Mag. Reson. Med.* Vol. 30. London, United Kingdom, May 2022, p. 1714. [5] Gyngell ML. *Magn. Reson. Imaging.* 1988; 6:415-9. [6] Krafft AJ, et al. *J. Magn. Reson. Imaging.* 2013;38(6): 1510-1520. [7] Tseytlin M. *Z Phys Chem (N F).* 2017;231(3):689-703.

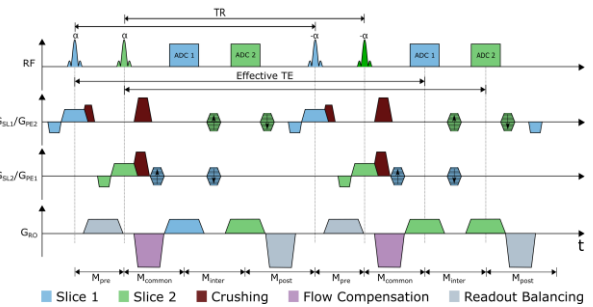


Fig.1 PSIF-CROSS sequence diagram.

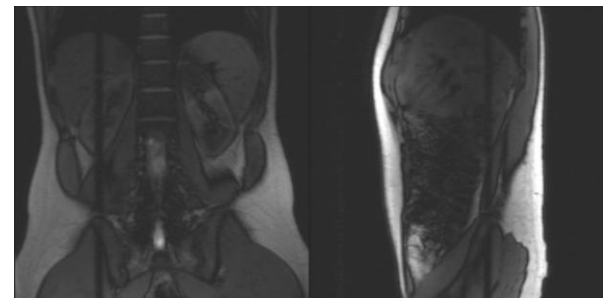


Fig.2 PSIF-CROSS abdominal images of a volunteer.

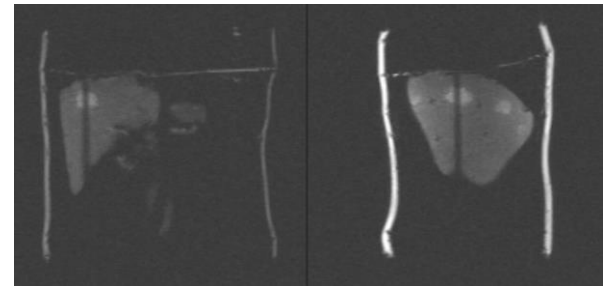


Fig.3 Abdominal motion phantom (L: slice 1 coronal, R: slice 2 sagittal).

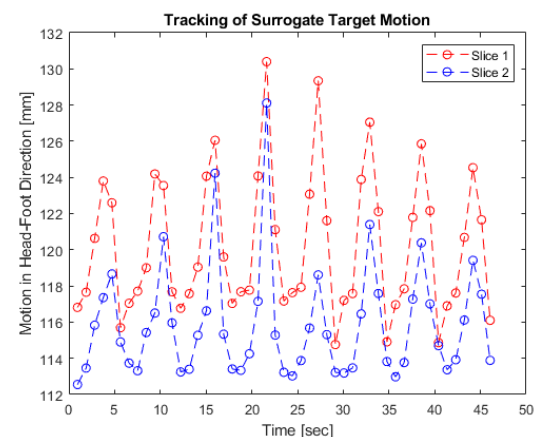


Fig.4 Breathing cycle determined by target tracking.

# InGrid – Finding Incision Points the Easy Way

Sathish Balakrishnan<sup>1</sup>, Julian Alpers<sup>1</sup>, Juan Sebastián Sánchez López<sup>1</sup>, Mathias Becker<sup>2</sup>, Maciej Pech<sup>2</sup>, Frank Wacker<sup>3</sup> and Bennet Hensen<sup>3</sup>

<sup>1</sup>InLine-Med GmbH, Magdeburg, 39106, Germany

<sup>2</sup>University of Magdeburg, Department of Radiology and Nuclear Medicine, 39120 Magdeburg, Germany

<sup>3</sup>Hannover Medical School, Institute for Diagnostic and Interventional Radiology, Hannover, 30625, Germany

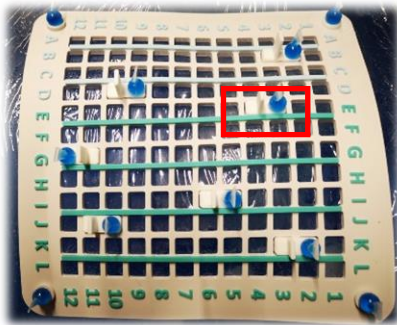


Figure 1: InGrid including four corner markers and seven test markers. Highlighted marker could not be detected

**Purpose.** The incidences and deaths of cancer increase every year<sup>1</sup> and require greatest medical attention. Beside open surgery, minimally-invasive procedures like thermoablations have become widely used in the clinical context<sup>2</sup> but finding the correct incision point and orientation angle for the applicator on the patient can be a challenging and time consuming task<sup>3</sup>. In this work, we present the first accuracy results of InGrid, an optimized navigational grid for MRI-guided minimally-invasive intervention.

**Material and Methods.** Our navigational grid (InGrid) is focused on finding the incision point on the patient during minimally-invasive interventions. Because the tool itself is not visible in the MR data set four small markers are placed in the corners of the grid.

These markers appear hyperintense in the images and can be easily detected using basic image processing algorithms. We performed accuracy tests by automatically detecting the four corner markers inside the MR planning data set (Siemens Magnetom Skyra 3T) automatically. In addition, seven additional markers were placed on InGrid as seen in Fig. 1. These markers are the ground truth position of the grid cells. Afterwards, the patient's skin mask was extracted from the data set, displayed as a virtual model and the grid-like structure of InGrid was recomputed (see Fig. 2). Here, the recomputed center points of each cell was compared to the position of the seven accuracy test markers to compute the average Euclidean distance.

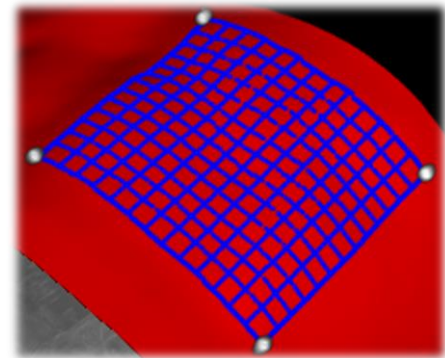


Figure 2: Virtual reconstruction of the grid on the patient's surface. White spheres show the detected markers.

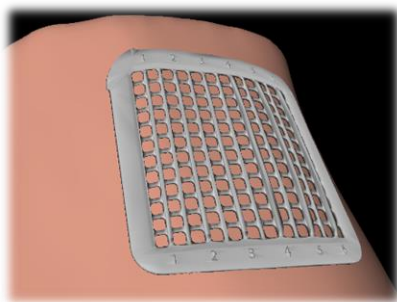


Figure 3: Virtual representation of the real grid on the patient's surface extraction.

**Results.** Accuracy results show that six out of seven test entry points could be detected successfully. Marker E7 (see Fig. 1) could not be recomputed on the virtual grid. The mean Euclidean distance for the other markers was  $0.89 \pm 0.42\text{mm}$  with a maximum error of 1.8mm.

**Conclusion.** We developed an MR compatible navigational grid called InGrid to support radiologists with the task of finding the correct incision point during minimally-invasive interventions. Results show that the accuracy of our virtual grid is less than 1mm in average compared to the reality. Future tasks will be the in depth testing in the clinical environment to also test the benefits regarding

time. We highly believe that our tool is capable of reducing the amount of time needed and simplify the daily life of a radiologist.

## References

- <sup>1</sup>Sung, H. et al. Global cancer statistics 2020: Globocan estimates of incidence and mortality worldwide for 36 cancers in 185 countries. *CA: a cancer journal for clinicians* 71, 209–249, DOI: 10.3322/caac.21660 (2021).
- <sup>2</sup>Ruiter, S. J., Heerink, W. J. & de Jong, K. P. Liver microwave ablation: a systematic review of various fda-approved systems. *Eur. radiology* 29, 4026–4035, DOI: 10.1007/s00330-018-5842-z (2019).
- <sup>3</sup>Arnolli, M. M., Hanumara, N. C., Franken, M., Brouwer, D. M., & Broeders, I. A. (2015). An overview of systems for CT-and MRI-guided percutaneous needle placement in the thorax and abdomen. *The International Journal of Medical Robotics and Computer Assisted Surgery*, 11(4), 458-475.

# Modularizable, MRI-Compatible and Elastic Abdominal Phantom to Perform Dynamic Interventional Experiments under Simulated Respiratory Cycles

Katja Engel<sup>1</sup>, Ivan Fomin<sup>1</sup>, Thomas Gerlach<sup>1</sup>, Bennet Hensen<sup>2</sup>, Marcel Gutberlet<sup>2</sup>, Frank Wacker<sup>2</sup>, Georg Rose<sup>1</sup>  
<sup>1</sup>Otto-von-Guericke-University Magdeburg, Germany, <sup>2</sup>Hannover Medical School, Germany

**Purpose:** To prove the functionality and safety of medical devices (e. g. robotics and ablation systems to perform magnetic resonance imaging (MRI), computer tomography (CT) or sonography (US) guided interventions) usually phantom and animal studies are required. Available phantoms are limited in global functionalities and animal studies are not only costly but also ethically scrutinized [1]. In this work, a customizable abdominal phantom with multiple properties is presented to perform different experiments in image-guided and minimal-invasive procedures.

**Material and Methods:** For the partial abdominal phantom polyvinyl alcohol cryogel (PVA-C) (KurarayPoval™ 15-99, Kuraray Europe GmbH) was used to simulate the liver, liver lesions and muscle tissue. Two-component-silicone (Silixon10, Silikonfabrik.de) represents the skin. Ribs and the spine were 3D-printed with polyethylene terephthalate glycol (PETG) and embedded in the muscle segment. To evaluate the imaging properties scans were performed using a 3T MRI scanner (Skyra, Siemens Healthcare GmbH) with a  $T_2w$ -TSE- and a  $T_1w$ -VIBE-sequence (see Fig. 1b, c). The relaxation times of each phantom part were determined from the MR images with a  $T_1w$ -MPRAGE- and a  $T_2w$ -SE-sequence. The Young's modulus was assessed by compression test on the universal testing machine (zwickiLine Z0.5, ZwickRoell GmbH), see Fig. 1d. For assessment of temperature resistance, the state of PVAC was documented after local heating for 5 min. using a microwave ablation system (Medwaves AveCure™, ascafamed GmbH).

**Results:** The  $T_1$ -deviation for the phantom liver ( $T_1$ : 993±83 ms) was +19% to the real liver tissue, for muscle ( $T_1$ : 799±49ms) it was -33%, for the created liver lesion  $T_1$  was 840±46 ms [2,3]. The  $T_2$ -deviation for muscle was -3% ( $T_2$ : 36±1 ms) and +27% for skin layer ( $T_2$ : 38±8ms) [2,3].  $T_2$ -times for the liver and the liver lesion was 65±7ms, respectively 63±2ms. Young's modulus of PVA-C was increased by 11% compared to human liver tissue (0,1239N/mm<sup>2</sup>) [4]. A peak temperature of 60°C and a melted area of 6 to 11 mm diameter around the tip of the microwave applicator were found.

**Conclusion:** In this work, an elastic puncturable, semi-temperature-stable and MRI-compatible phantom was presented, which nearly simulates the abdominal human anatomy as well as the physiology. The modularization concept allows an individual configuration of phantom parts and its properties. The future work will focus on further improvement of the mechanical, thermal, and imaging properties as well as on the fabrication and repair of the entire abdominal region and its anatomical structures. Furthermore, a drive unit will be used to compress the elastic phantom to simulate organ movement imitating respiratory motion. This phantom may help in the development and safety testing of medical devices in addition to or as an alternative to animal and human studies as well as cadaver testing.

**References:** [1] de Jong et al., IJCARS, pp. 2177-2186, 2019, [2] de Bazelaire et al., Radiology, pp. 652-659, 2004, [3] Mesrar et al., Skin Res. Technol., pp. 289-294, 2017, [4] Karimi et al., Dig Dis, pp. 150-155, 2018.

**Acknowledgements:** The work of this paper is funded by the Federal Ministry of Education and Research within the Research Campus STIMULATE under the number '13GW0473A', '13GW0473B'.

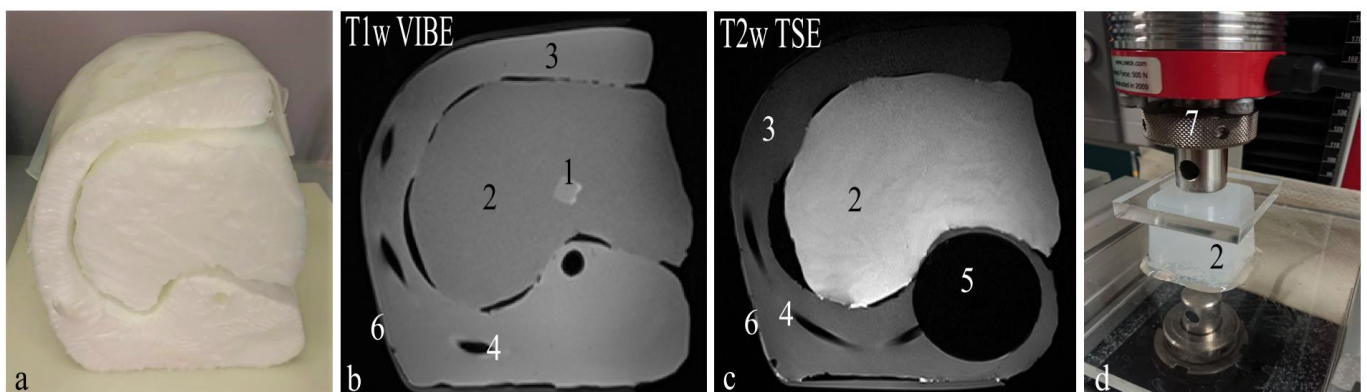


**Fig. 1** (a) Caudal view of the manufactured phantom. (b,c)  $T_1w$ -w VIBE and  $T_2w$ -w TSE transversal slice images. (Phantom parts: 1: lesion (15% PVA-C), 2: liver (10% PVA), 3: muscle (15% PVA-C), 4: ribs (PETG), 5: spine (PETG), 6: skin (10ShA silicone). (d) Young modulus assessment (7: universal testing machine stamp).

# A new multi-source MR-LITT device for creating conformal ablations

**Author list:** Manon Desclides<sup>1,3</sup>, Guillaume Machinet<sup>2</sup>, Christophe Pierre<sup>2</sup>, Valéry Ozenne<sup>1</sup>, Stéphane Chemouny<sup>3</sup>, and Bruno Quesson<sup>1</sup>.

<sup>1</sup>Univ. Bordeaux, CNRS, CRMSB, UMR 5536, IHU Liryc, F-33000 Bordeaux, France, <sup>2</sup>ALPhANOV, Talence, France, <sup>3</sup>Certis Therapeutics, Pessac, France.

## Purpose

Percutaneous clinical ablation devices usually create a heating pattern with an ellipsoid shape. Output power and duration of application are the only degrees of freedom, which does not allow adjustment of the heating shape. To overcome this limitation, we designed a Laser Interstitial Thermal Therapy (LITT) device allowing creating various heating patterns. We present here in vivo results in pig muscle monitored by real-time 2D multi-slice MR-thermometry.

## Materials and methods

A 6-multimode-fiber bundle (200  $\mu\text{m}$  core diameter per fiber, each connected to a 976 nm laser diode) was shaped to create a radial propagation of each laser beam over  $60^\circ$  and distributed over  $360^\circ$  (Alphanov, France). Several illumination patterns were tested: 1 fiber only (2W during 180 s), 2 fibers in opposite directions (2W during 180 s on each) and 4 contiguous fibers (1.5W during 180 s on each). The laser probe was inserted into the leg muscle of and anesthetized swine (N=2, 33 kg body mass, protocol approved by ethic committee). 6 slices of a single shot EPI sequence positioned perpendicular to the laser tip were acquired every second on a 1.5 T clinical scanner (Avanto, Siemens Healthineers): TE=21 ms, FOV=180x180 mm<sup>2</sup>, 3 mm slice thickness, FA=60°, GRAPPA acceleration=2, bandwidth/pixel = 1445 Hz. Images were processed online to visualize 3D temperature and thermal dose images (Certis Therapeutics, France).

## Results

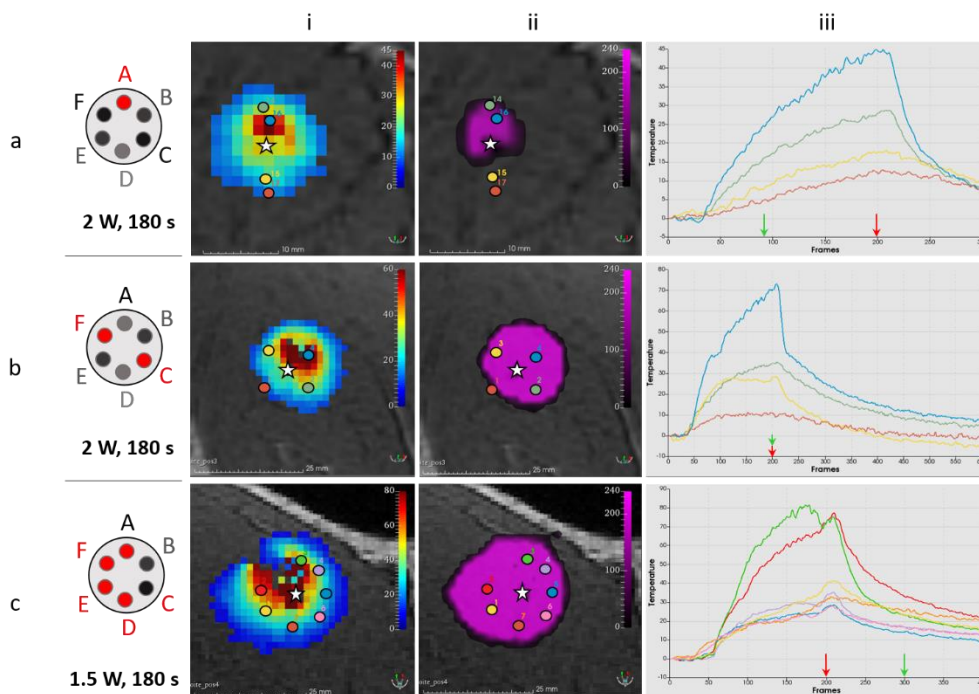


**Figure 1:** Results of the different heating patterns: single fiber (a), 2 fibers (b) and 4 fibers (c). Schematics on the left show activated fibers (red circles). White star in (i) and (ii) represent the center of the laser fiber bundle. Temperature images (i), thermal doses maps (ii) and temperature evolution of pixels selected in images (iii). Red and green arrows in (iii) indicate the dynamic number of the corresponding temperature (i) and thermal dose maps (ii), respectively.

Three heating patterns could be successfully created with the same device and visualized on temperature/thermal dose maps during the procedure.

## Conclusion

The proposed LITT device is MR-compatible and allows creating various heating shapes that can be visualized in real-time by rapid volumetric MR-thermometry, opening interesting perspectives for conformational tumor treatment.

## Investigation of Microwave ablation using dual applicators with real-time MR thermometry

Aiming Lu<sup>1</sup>, Liqiang Ren<sup>1</sup>, Krzysztof R Gorny<sup>1</sup>, Joel P Felmlee<sup>1</sup>, Christopher P Favazza<sup>1</sup>, Daniel A Adamo<sup>1</sup>, Scott M Thompson<sup>1</sup>, David A Woodrum<sup>1</sup>

<sup>1</sup>Department of Radiology<sup>1</sup>, Mayo Clinic, Rochester, MN, US

**Purpose:** The purpose of this work is to investigate the effectiveness of MRI-guided microwave ablation (MRgMWA) using two microwave applicators simultaneously, including heating risk, the impact of elevated noise level and intermittent electromagnetic interference (EMI) on MR image quality, especially real-time MR thermometry.

**Material and Methods:** Experiments were conducted on a 1.5T MRI scanner and with two MRI-configured MWA systems. Experiments using a small phantom were first performed to evaluate the impact of MW system on MR image quality. Ex-vivo porcine tissue phantom MWA experiments were then conducted with either one or two applicators inserted ~10 cm into the fresh tissue samples. Three MWA experiments were performed with two applicators spaced 2.6, 3.6, and 4.6 cm apart and in parallel to each other. A fourth MWA experiment was performed with one applicator. During each ablation of 10-minute duration, MR thermometry data were continuously collected. Fiberoptic temperature sensors were attached to the applicators to measure the temperature change at the tissue surface continuously during location verification MRI sequences with both a high specific absorption rates (SAR) sequence and the MR thermometry sequence. K-space EMI correction was performed to suppress the intermittent EMI for improved temperature and tissue damage maps.

**Results:** No significant RF-heating was measured at the tissue surface with either one or two applicators during MR imaging when the MW generator was turned off or in standby mode. Although temperature rises of  $18.2 \pm 3.3^\circ\text{C}$  and  $19.7 \pm 2.6^\circ\text{C}$  were measured during MW ablations using a single or two applicators, respectively. The difference is insignificant ( $p > 0.5$ ). The introduction of an additional microwave system resulted in a drop of relative SNR from  $88.1 \pm 2.9\%$  with one applicator activated to  $54.6 \pm 6.4\%$  with both activated. Temperature and tissue damage maps with acceptable image quality were obtained, especially after EMI corrections.

As expected, smaller spacing between two applicators (e.g., 2.6 cm) resulted in consolidated coverage of the treatment zone sooner while large spacing (e.g, 4.6 cm) would create a larger overall treatment zone. In all experiments the length of the treatment zone along the applicator shaft was unaffected relative to ablation using single applicator. The ablation zone in the single applicator case had consistently smaller maximal width and area throughout the entire ablation procedure (Figure 1). Quantifications of the treatment zone dimensions at the end of the treatments were summarized in Table 1.

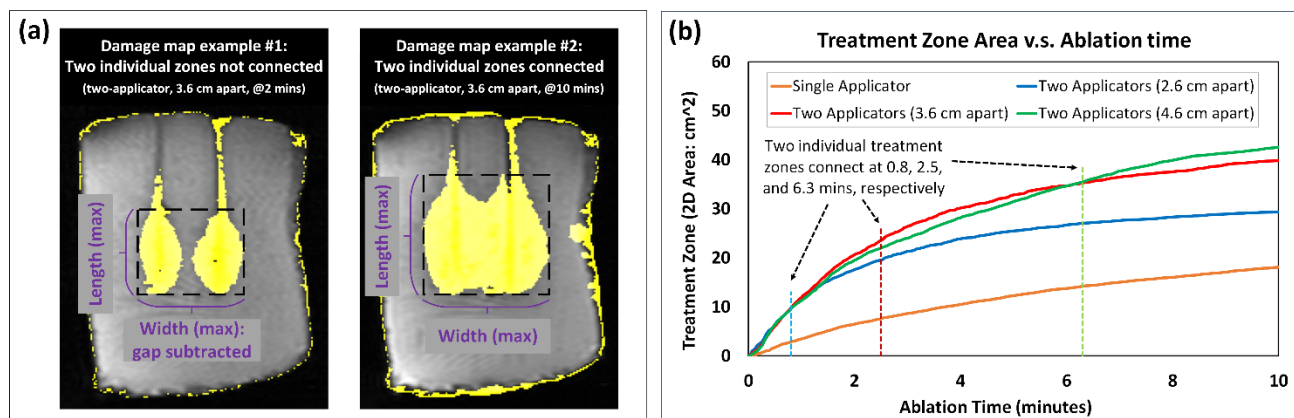


Fig. 1. Treatment zone size change as a function of ablation time.

Table. 1. Summary of the measured dimensions for all four scenarios after 10-minute ablations

	Single Applicator	Two Applicators (2.6 cm apart)	Two Applicators (3.6 cm apart)	Two Applicators (4.6 cm apart)
Length (cm)	6.1 ± 0.1	6.2 ± 0.1	6.4 ± 0.1	6.7 ± 0.1
Width (cm)	4.2 ± 0.5	5.9 ± 0.1	7.2 ± 0.1	8.1 ± 0.4
Area (cm <sup>2</sup> )	18.6 ± 0.9	29.4 ± 0.4	39.9 ± 0.6	42.6 ± 0.9

**Conclusion:** This work demonstrated that despite the decrease in image SNR when two microwave applicators are simultaneously applied, acceptable real-time MRT can still be obtained for MRgMWA. Simultaneous use of two MW applicators could significantly increase the treatment efficiency with a larger ablation zone especially when distances between two applicators and treatment duration are properly selected based on specific size, shape, and location of the target tumor.

# Feasibility of Quantitative MR-Based Hypoxia Measurements during MR-guided Gynecological Brachytherapy

Junichi Tokuda<sup>1</sup>, Gregory J. Ekchian<sup>2</sup>, Robert A. Cormack<sup>3</sup>,  
Michael Dyer<sup>3</sup>, Evangelia Kaza<sup>3</sup>, Michael J. Cima<sup>4, 5</sup>

<sup>1</sup> Department of Radiology, Brigham and Women's Hospital, Boston, MA, <sup>2</sup> Stratagen Bio Inc, Boston, MA, <sup>3</sup> Department of Radiation Oncology, Brigham and Women's Hospital, Boston, MA, <sup>4</sup> Koch Institute for Integrative Cancer Research, and <sup>5</sup> Department of Materials Science and Engineering, Massachusetts Institute of Technology, Cambridge, MA

**Purpose.** High-dose-rate (HDR) brachytherapy plays a crucial role in the management of gynecologic cancers (1). Brachytherapy places small radioactive sources near or in direct contact with the tumor volume through thin catheters enabling high radiation doses to a target with rapid fall-off to protect adjacent structures. Tumor hypoxia is known to increase resistance to radiation therapy leading to increased local failure rates and reduced disease-free survival (2). However, there is no established method to detect tumor hypoxia in a clinical routine. To address this unmet need, we developed a novel oxygen-sensing catheter with embedded oxygen-sensitive silicone for *in vivo* quantitative MR-based oxygen measurement. Since silicone materials have oxygen-dependent T1 relaxation times (3), the oxygen concentration in the tissue surrounding the catheter can be obtained by measuring the T1 relaxation of the silicone in the catheter during MRI-guided catheter placement. We assess the feasibility of oxygen measurement during MRI-guided brachytherapy of the cervix.

**Materials and Methods.** This IRB-approved pilot study was performed as part of a standard MR-guided interstitial brachytherapy implant procedure under a 3T MRI scanner (Verio DOT, Siemens). Brachytherapy catheters were modified to incorporate custom silicone near their tips which are exposed to the tumor environment. One to two oxygen sensing catheters were implanted at the beginning of the procedure. These catheters were measured with MRI at the end of the procedure and replaced with standard brachytherapy catheters. An inversion recovery turbo spin echo (IR-TSE) sequence with multiple inversion times (TIs) was used with the following parameters to obtain the T1 of the silicone: TR/TE=3000/15ms, matrix=256×256, FOV=120mm<sup>2</sup>, slice thickness= 2mm, 10 TIs ranging between 80-2200ms. The study has a 2-stage design with a four-patient safety lead-in followed by three additional patients for a total accrual of seven patients. Feasibility was defined as the acquisition of data from at least one oxygen sensor per patient.

**Results.** All seven participants had at least one oxygen-sensing catheter placed safely. MR images of the catheters were acquired at all TIs, successfully depicting the signals from the silicone. Feasibility was successfully achieved in all seven patients.

**Conclusion.** Quantitative MR measurements of a custom oxygen-sensitive silicone are feasible in a clinical 3T scanner. Experience from this study will be used to inform chemical composition and mechanical design for the next generation of oxygen-sensing catheters that could be implanted for the duration of the HDR treatments. Such catheters could enable longitudinal measurements throughout the tumor and at multiple time points during treatment. These measurements could be combined with adaptive HDR planning (4) to drive the high dose regions inherent to brachytherapy onto the hypoxic regions to counteract the radio-resistance of hypoxic cells and improve treatment outcomes.

**References.** (1) Chino J, et al. *Pract Radiat Oncol.* 2020 Jul;10(4):220–234. (2) Fyles A, et al. *J Clin Oncol.* 2002 Feb 1;20(3):680–687. (3) Liu, VH et al. *Proc Natl Acad Sci USA* 2014 111(18):6588-93. (4) Guthier, C.V. et al. *Med Phys.* 2017 4(12):6117-27.

**Acknowledgments.** This work is supported by NIH R43CA261401, a Bridge Project Grant, and the Image-Guided Therapy Center (NIH P41 EB028741). GE was previously supported by the Koch Institute Quinquennial Cancer Research Fellowship and the Kavanaugh Translational Innovation Fellowship.

## **Investigation of thermal injury risks from high-pressure gas supply line (HPGSL) during MR guided cryoablation**

Aiming Lu<sup>1</sup>, Liqiang Ren<sup>1</sup>, Christopher P Favazza<sup>1</sup>, Joel P Felmlee<sup>1</sup>, Daniel A Adamo<sup>1</sup>, Scott M Thompson<sup>1</sup>, Lance A Mynderse<sup>2</sup>, David A Woodrum<sup>1</sup>

<sup>1</sup>Department of Radiology, Mayo Clinic, Rochester, MN, USA

<sup>2</sup>Department of Urology, Mayo Clinic, Rochester, MN, USA

**Purpose:** To investigate the potential MRI-induced RF heating risk and frostbite risk during freezing when the high-pressure gas supply line (HPGSL) is placed close to the patient during MRI-guided cryoablation.

**Material and methods:** *Ex-vivo* experiments were performed on a 1.5T MRI scanner using an MRI-conditional VISUAL ICE cryoablation system. To investigate the potential RF heating risks, three experiments were performed with a cryoneedle inserted into a chunk of porcine tissue. The tissue sample was placed ~10 cm off the patient table center and covered by a layer of operating room (OR) towel serving as a thermal insulation layer between the tissue and HPGSL. The HPGSL was arranged to have a small segment (~3cm) in contact with the towel. Temperatures were recorded during executions of a T2-weighted sequence (2'30'', SAR: 2.3W/kg) via four thermal sensors: one was placed on the tissue surface below the middle of HPGSL segment contacting the towel and three attached to HPGSL (one in the middle and one close to the end of that segment and the 3<sup>rd</sup> one ~15 cm away from the segment). Two experiments were performed with the HPGSL either unplugged or plugged into the mobile connection panel (MCP) of the system. With HPGSL plugged in, a third one was performed with a 2.5 cm thick insulation pad inserted between the HPGSL and the towel. For frostbite risk investigation, cryoablation experiments were performed with the cryoneedle inserted into a container filled with saline. Temperature changes during a 5-minute and 7-minute freezing procedures were again measured with three thermal sensors attached to the HPGSL and one insulated from HPGSL by either a single layer OR towel or both the towel and the pad at ~15cm away from the cryoneedle shaft, respectively.

**Results:** Temperature rises on the HPGSL due to MRI-induced RF heating were localized to the segment close to the tissue. With a single layered OR towel for insulation and the HPGSL unplugged, the maximum tissue surface temperature rises were about 5-6°C after three consecutive executions of the T2W sequence. With the HPGSL plugged into the MCP, temperature rise of more than 40°C was observed on the tissue surface after a single T2W scan. With a layer of OR towel and an insulation pad and the HPGSL plugged in, no significant temperature rise was observed at all four locations.

For frostbite risk investigations, the temperature drops along the HPGSL reduced with increased distances from the cryoneedle shaft. With only a single layer of OR towel for insulation, the maximum temperature drop was about 20°C at 15cm from the shaft end. No temperature rises or drops were observed when the thick insulation pad was inserted between thermal sensor and HPGSL.



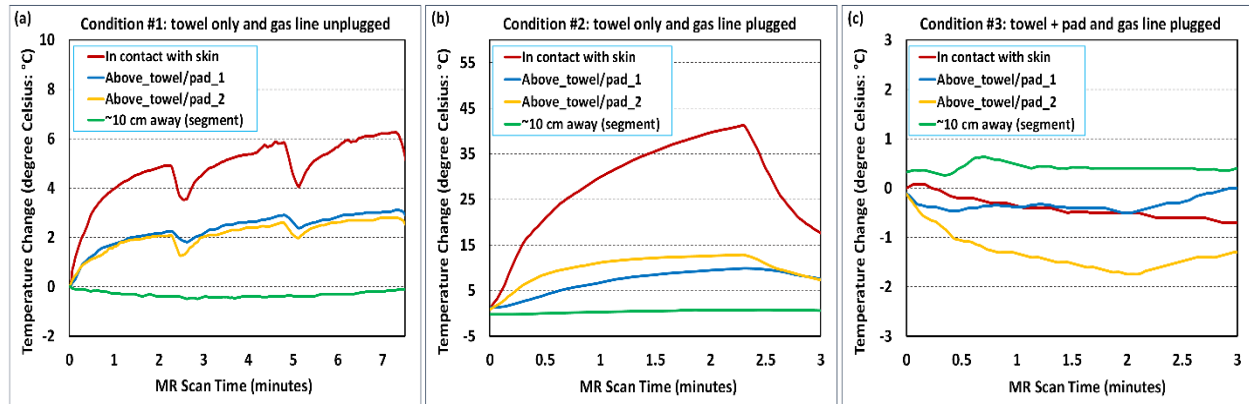


**Figure 1:** Temperature changes at tissue surface and at three different locations (one in the middle of the segment in contact with the tower, one close to the end of the segment, and one ~15cm away from the segment) along HPGSL during MRI.

**Conclusions:** Skin injury could occur during MR guided cryoablation due to MRI-induced RF heating in the HPGSL and/or frostbite when the HPGSL is placed close to the patient. To mitigate these risks, sufficient insulation between HPGSL and patient skin should be applied.

# Free-breathing T1-weighted 3D sequence in MR-guided liver interventions: Evaluation of workflow and diagnostic quality

## Corresponding author

Julian Glandorf, M.D., Institute for Diagnostic and Interventional Radiology (OE 8220), Hannover Medical School, Carl-Neuberg-Str. 1, 30625 Hannover, Germany.

E-Mail: [glandorf.julian@mh-hannover.de](mailto:glandorf.julian@mh-hannover.de)

**Authors:** Julian Glandorf<sup>1</sup> M.D., Dominik Horstmann<sup>1</sup> M.Sc., Marcel Gutberlet<sup>1</sup> PhD., Daniel Markus Dux<sup>1</sup> M.D., Frank Wacker<sup>1</sup> M.D, Bennet Hensen<sup>1</sup> M.D.

1. Institute for Diagnostic and Interventional Radiology, Hannover Medical School, Hannover, Germany.

**Key words:** MRI intervention, workflow, position control, MR-guidance, ablation

**Purpose:** To evaluate workflow efficiency and diagnostic quality of a free-breathing T1-weighted 3D radial vibe sequence (SIEMENS FREEZEit StarVIBE) compared to a T1-weighted Volumetric Interpolated Breath-hold Examination (SIEMENS VIBE) sequence for needle position control in MR-guided liver interventions.

**Methods:** MRI procedures were performed on a 1.5T SIEMENS Aera MRI. Datasets of 12 patients with liver metastases and hepatocellular carcinomas undergoing MR-guided liver interventions were analyzed retrospectively. The patients were either under general anesthesia or local anesthesia. A near real-time steady-state free precession sequence (BEAT\_IRTTT) for needle tracking and a T1-weighted 3D sequence for needle position control were used repetitively until the final needle position was reached. In total, 15 series of the free-breathing StarVIBE were compared to 18 series of the standard VIBE sequence in terms of their workflow efficiency, which was evaluated by calculating the time interval between two consecutive live scans for needle tracking (BEAT2BEAT-Time). The diagnostic quality of both sequences was compared by the SNR within 8 comparable slices, which was estimated from the ratio of the mean signal in defined ROIs and the mean signal in background ROIs. The CNR was calculated by subtraction of the SNR values of healthy liver and liver lesion ROIs. Values are given as mean±SD.

**Results:** Although not significantly, the BEAT2BEAT-Time showed a clear tendency to be shorter for the StarVIBE compared to the VIBE sequence, 216±101s vs. 241±136s, ( $p = 0.57$ ). While the mean SNR of the healthy liver was not significantly higher in the StarVIBE, 240±92 vs. 136±67, ( $p = 0.06$ ), the mean SNR of the lesion was significantly higher in the StarVIBE, 169±74 vs. 86±43, ( $p = 0.03$ ). However, the mean CNR was not significantly higher in the StarVIBE sequence, 71±48 vs. 50±32, ( $p = 0.37$ ).

**Conclusion:** An optimized Siemens StarVIBE sequence can simplify the workflow of MR-guided liver interventions by avoiding the respiratory arrest needed for control imaging, while providing superior visualization of the tumor. A tendency towards an improvement of the measured parameters is indicated, which was not significant due to the small number of patient cases and the corresponding high standard deviation.

# Reduction of Electromagnetic Interferences of a commercially available MR approved microwave generator

Löning C., J. Joaquin<sup>1,2</sup>; Meyer zu Hartlage, Karen<sup>1,2</sup>; Gerlach, Thomas<sup>2</sup>; Oliver Speck<sup>2</sup>; Wacker, Frank<sup>1,2</sup>; Hensen, Bennet<sup>1,2</sup>; Gutberlet, Marcel<sup>1,2</sup>.

<sup>1</sup>Hannover Medical School, <sup>2</sup>Magdeburg Research Campus STIMULATE.

**Purpose:** Magnetic resonance (MR-) guided microwave ablation (MWA) is an advanced minimally invasive treatment of hepatic malignancies. In addition, MR thermometry allows treatment monitoring during ablation and therefore potentially allows thermal treatment even near high-risk areas like bowel, lung, and heart. While commercially available microwave generators are approved for its safe use in an MR environment, MR imaging during ablation (like MR thermometry) may be affected by increased noise due to electromagnetic interferences (EMI) as illustrated in figure 1.

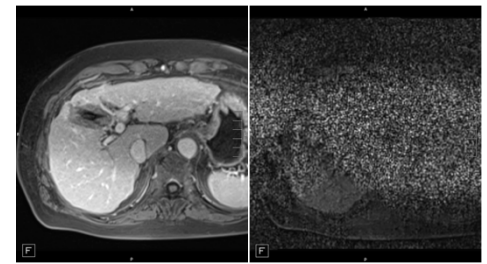


Figure 1: Example of MR-image without (left) & with active MWA-system (right) in MR-environment

Purpose of this work was to modify a commercially available MR approved microwave generator to reduce its EMI and therefore create the conditions for clinically applicable MR thermometry during MWA. The effect of placing a modified MWA-System outside (setup 1) and inside (setup 2) the MR-cabin is demonstrated In this approach.

**Material and methods:** To reduce EMI, a commercially available MR approved MWA system (ECO-100E, ECO Microwave, China) was modified by installation of a low-noise power supply unit and by shielding of the line cable with a copper braid sleeve and radiofrequency (RF) chokes [1]. The modified system was tested for EMI on a 1.5 T scanner (Avanto, Siemens Healthineers) by placing it outside the

MR-cabin and introducing the line cable through the waveguide (setup 1) and by placing it entirely inside the MR cabin (setup 2). RF noise (centre frequency: 63.6022 MHz, span: 500 kHz, vector size: 16384, 3000 repetitions) and signal-to noise ratio (SNR) of MR imaging using a spoiled gradient echoes sequence (GRE) as typically used in MR thermometry (FOV: 15 x 15 cm, TE: 7 ms, TR: 20 ms, flip angle: 18 °, slice thickness: 5 mm, base size: 128, bandwidth: 390 Hz/px, rep.: 50) were measured in a water phantom near the microwave applicator. The SNR was calculated by dividing the mean values from the signals within the phantom by the standard deviation of the signal in an object-free region. GRE-images and noise spectra were measured with a multi-channel surface coil. As reference measurements were performed before installation of the microwave generator at the MR system. EMI were tested with the microwave applicator in active mode with a power of 80 W.

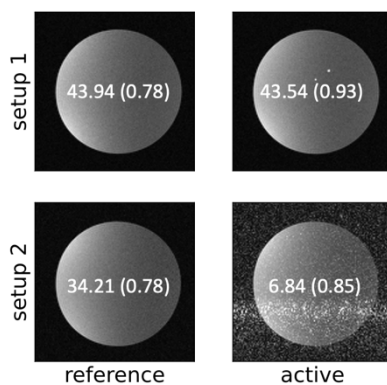


Figure 2: GRE images in reference and active for setup 1 and 2. Mean SNR-value (and standard deviation) over 50 repeated GRE images.

**Results:** In figure 2, mean and standard deviation (in parentheses) of the SNR-values are shown. In comparison to setup 1, the SNR-values in setup 2 are decreased. The corresponding noise spectrum in figure 3 shows an overall increase of the noise level with additional spikes for setup 2 whereas for setup 1 no significant difference to the reference spectrum is observed. The frequency range of the measured GRE images is highlighted by a green area in the noise spectra. A spike in the spectrum of setup 2 in active mode can be related to the RF artefact in the GRE image in figure 2.

**Conclusion:** The proposed modification used with setup 1 drastically reduced EMI compared to setup 2 and therefore allows MR imaging at high SNR while the microwave generator is active. This is an important step towards clinical application of MR thermometry for monitoring of MWA.

**Reference:** [1] Gorny K. Practical implementation of robust MR-thermometry during clinical MR-guided microwave ablations in the liver at 1.5 T. Phys Med. 2019 Nov;67.

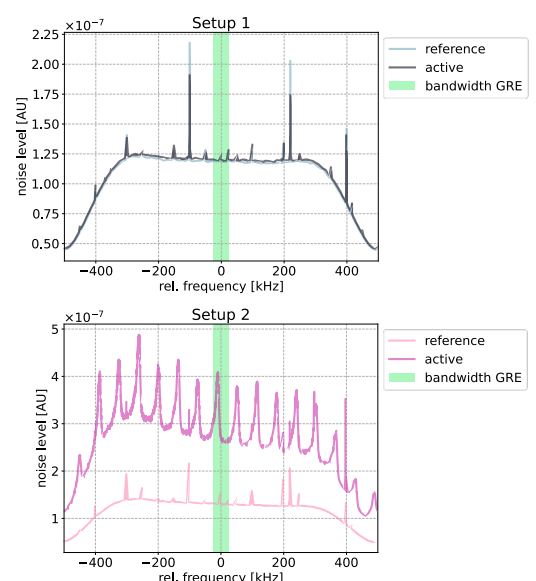


Figure 3: Spectrum for setup 1 & 2.

**TITLE:** Technical evaluation of motor evoked potential monitoring during MR-guided cryoablation of the shoulder

**AUTHORS** <sup>1</sup>Christopher P Favazza, <sup>1</sup>Scott M Thompson, <sup>2</sup>Ernest M Hoffman, <sup>1</sup>Joel P Felmlee, <sup>1</sup>Brian T Welch, <sup>1</sup>Daniel A Adamo, <sup>1</sup>David A Woodrum, <sup>1</sup>Aiming Lu

**AFFILIATIONS**

<sup>1</sup>Department of Radiology, Mayo Clinic, Rochester, MN, USA

<sup>2</sup>Department of Neurology, Mayo Clinic, Rochester, MN, USA

**Purpose:** Pre-procedural testing to evaluate potential RF heating risks and image quality penalties associated with motor evoked potential (MEP) monitoring during MR-guided cryoablation of the shoulder.

**Methods and Materials:** Using a porcine tissue phantom, a series of ex vivo experiments were conducted mimicking the clinical configuration for MEP monitoring during MR-guided cryoablation near the brachial plexus. Two needle electrodes were placed on the sides of the phantom “head” to simulate transcranial stimulation. Two needle electrode pairs and a ground electrode were placed in the “arm” to mimic muscle recording. Fluoroptic temperature sensors were inserted near the tips of all 7 electrodes. The phantom was placed “head” first into the scanner. To minimize heating risks, stimulation and recording/ground wires were routed along the center of the bore and exited the back and front of the scanner, respectively. Stimulation and recording wires were routed through a waveguide and connected to the nerve monitoring system outside the scan room. Along with a single high specific absorption rate (SAR) T2-weighted sequence (2.5 W/kg), a series of proton-density (PD)-weighted sequences used to monitor cryoablations were executed with different combinations of experimental variables that influence heating—wire path, position relative to bore wall, and SAR. Heating was measured with thermal sensors and recorded. Image quality was assessed qualitatively by calculating the average contrast-to-noise ratio (CNR) on the PD images. Clinical workflow of interleaving MEP and image acquisitions was evaluated.

**Results:** Maximum temperatures rises of 0.6, 0.8 2.8 and 0.4°C were respectively measured for high SAR T2, PD monitoring sequence at 14 minutes (SAR= 1.9 W/kg), PD with phantom shifted to touch the bore wall, and low SAR PD (0.7 W/kg) with phantom touching bore wall. Image quality was adequate with an average CNR=117. Stimulation was successfully interleaved between successive PD monitoring acquisitions with low noise signal reception in absence of active MRI.

**Conclusions:** RF heating risks can be sufficiently minimized to allow for intraprocedural nerve monitoring during MR-guided cryoablation, especially when a low SAR sequence is used. Image quality is not significantly degraded. MEP monitoring is feasible and can be operated in between MR image acquisitions.

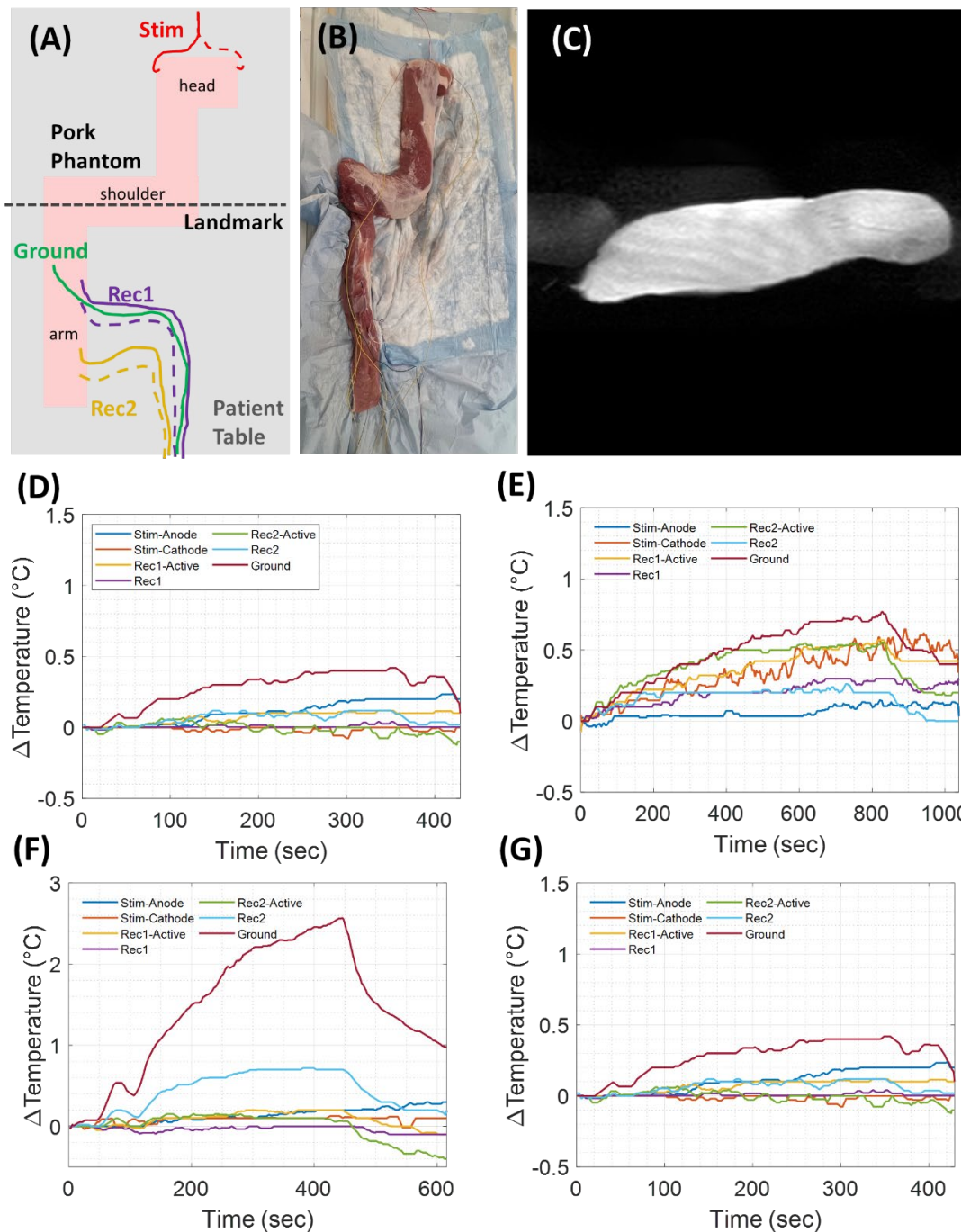


**Figure:** (A) Schematic and (B) photo of phantom set-up with stimulation and recording/ground electrodes. (C) Sample PD-weighted monitoring image acquired with MEP monitoring connected. (D-G) Thermal profiles for each electrode during (D) high SAR T2-weighted sequence (2.5 W/kg), (E) 14-minute PD-weighted monitoring sequence, (F) PD-weighted monitoring sequence after phantom shifted laterally to be in contact with bore wall, (G) low SAR PD-weighted monitoring sequence with laterally shifted phantom.

**TITLE:** MR Guided Cryoablation of Renal Masses

**AUTHORS:** <sup>1</sup> Daniel A. Adamo M.D., <sup>1</sup> Scott M. Thompson M.D, Ph.D., <sup>1</sup> Aiming Lu Ph.D., Ph.D., Christopher P. Favazza Ph.D., <sup>2</sup> Erica Knavel Koepsel M.D., <sup>3</sup> Lance A. Mynderse M.D., <sup>1</sup>David A. Woodrum M.D., Ph.D., <sup>2</sup>

**AFFILIATIONS:**

1 Department of Radiology, Mayo Clinic, Rochester, MN, USA

2 Department of Radiology, University of Wisconsin-Madison, Madison, WI, USA

2 Department of Urology, Mayo Clinic, Rochester, MN, USA

**PURPOSE:** To demonstrate feasibility and short-term followup of using MR guided cryoablation for treatment of native renal masses

**MATERIALS AND METHODS:** Retrospective review from September 2018 to April 2022 for patient's treated with MR guided cryoablation renal masses for biopsy proven or suspected renal neoplasms. Patient's underwent MR guided cryoablation using a percutaneous needle placement under general anesthesia. Cryoablation was performed with continuous MR imaging monitoring so that the iceball was grown to encompass the lesion with margins as permitted based on adjacent structures (ie ureter, colon, etc.). Patients were discharged same day. Follow up imaging was obtained 6 months after the ablation, and then subsequently at 6–12-month intervals.

**RESULTS:** Review demonstrated 7 patients with 7 procedures during this time frame. All patients in the review were men with average age of 69.2 years (65-75). The average size of the ablated mass was 1.28 cm (0.9 – 2.8 cm). Pathology was available in 5 patients: 4 demonstrating renal cell carcinoma and 1 demonstrating a metastasis from prostate adenocarcinoma. Following ablation, local recurrence was seen in 1/7 (14%) patient, while 6/7 (86%) patients demonstrated no findings for recurrence at most recent follow-up imaging. Average length of follow up was 1.82 years (664.5 days). The one patient with recurrent neoplasm occurred in a patient with autosomal dominant polycystic kidney disease with oncocytic subtype cystic RCC.

**CONCLUSION:** MR guided cryoablation can be utilized for treatment of renal neoplasms. Although the retrospective review was small and follow-up relatively short, local recurrence rates were low.

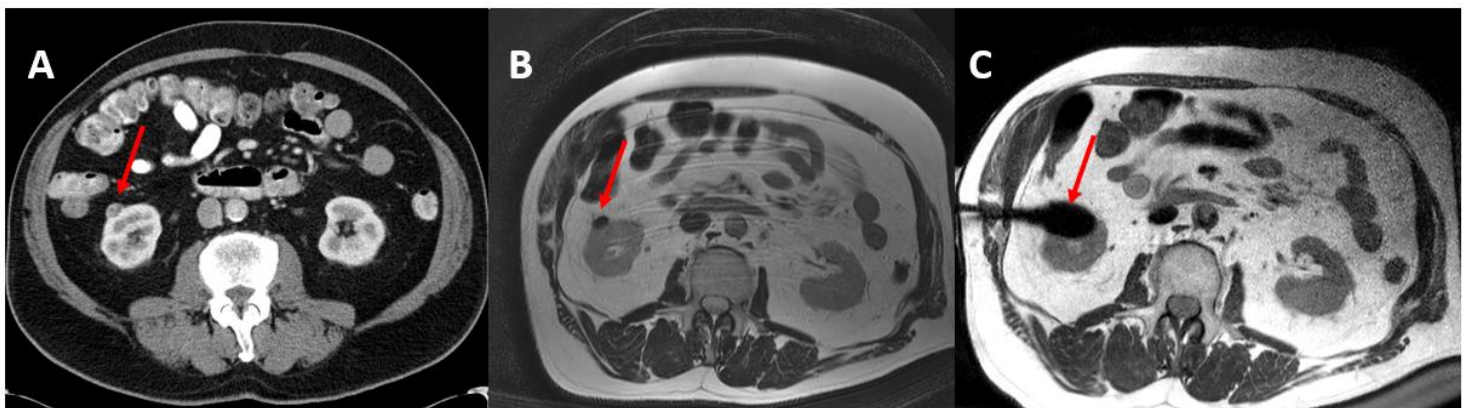


Figure 1. (A) Axial contrast enhanced CT demonstrating an enhancing right renal mass (arrow), which was T2 hyperintense on MRI (B). MRI guided cryoablation (C) demonstrated excellent iceball coverage

## Shaft heating risk mitigation during MRI-guided microwave ablation using non-actively-cooled applicators

Aiming Lu<sup>1</sup>, Liqiang Ren<sup>1</sup>, Joel P Felmlee<sup>1</sup>, Christopher P Favazza<sup>1</sup>, Daniel A Adamo<sup>1</sup>, Scott M Thompson<sup>1</sup>, David A Woodrum<sup>1</sup>

<sup>1</sup>Department of Radiology, Mayo Clinic, Rochester, MN, US

**Purpose:** The purpose of this work is to investigate whether potential thermal damage to the tissue near the metallic applicator shaft could occur due to execution of MR sequences (RF-heating) or the microwave field and evaluate the potential using ultrasound gel applied at insertion site to mitigate the skin burn risk.

**Material and methods:** Ex-vivo porcine tissue experiments of MRgMWA were conducted on a 1.5T scanner (Ingenia, Philips, Best, Netherlands). Two identical MRI-configured MWA systems each consisting of microwave generator and MRI-conditional non-cooled applicators were used (Avecure, MedWaves Inc., San Diego, CA) [4-6]. Unless otherwise mentioned, the microwave applicators were inserted into the tissue phantom at a depth of 10 cm (Figure 1a). Neoptix fiberoptic temperature sensors (Qualitrol, Fairport, USA) were attached to the applicators to measure the temperature change at the tissue surface continuously.

To evaluate the RF-heating in the applicators, MR imaging was performed using a sequence with relatively high specific absorption ratio (SAR) sequence (2.1W/kg). The experiments were repeated with the porcine tissue phantom and the two applicators positioned at several different geometric orientations inside the scanner bore. Different combinations of applicator status such as whether they were connected to the microwave generators and whether the generators were powered off and in standby mode were tested.

To investigate impact of applicator insertion depth and spacing of the applicators on shaft heating, two sets of experiments were performed: one with a single applicator and one with two applicators. In the single applicator experiments, six ablations were performed with different applicator insertion depth into the tissue with/without a cylindrical (~3cm in diameter) layer of ultrasound gel surrounding the applicator at the insertion site: 4cm insertion depth with/without 8cm thickness gel, 8cm insertion depth with/without 4cm thickness gel, 10cm insertion depth with/without 2cm thickness gel. The effective insertion depth of the applicators inside both tissue and ultrasound gel was therefore maintained at ~12cm. In the set of experiments with two applicators, three experiments were performed with the applicators inserted in parallel at 2.6, 3.6 and 4.6cm apart respectively. The ablation duration was 10 minutes for all these experiments unless otherwise indicated and each individual MWA procedure was performed on a piece of fresh tissue to achieve similar initial tissue condition.

**Results:** No significant RF-heating at tissue-air interfaces was found in any applicator orientation investigated. Figure 1 shows measured temperature increases resulting from the activation of the MWA system in case of a single applicator (Figure 1a) and two simultaneous applicators (Figure 1b), where were  $18.2 \pm 3.3^\circ\text{C}$   $19.7 \pm 2.6^\circ\text{C}$  similar in both scenarios. Therefore, introducing an additional applicator did not increase the shaft heating risk. The temperature increases at the tissue surface were measured as 73, 31, and  $14^\circ\text{C}$  (without gel) and 40, 16, and  $6^\circ\text{C}$  (with gel) for MWA with the applicator insertion depth of 4, 8, and 10cm in the tissue phantom (Figure 1c). The tissue surface temperature rises were significantly reduced at deeper applicator insertion depth. Application of ultrasound gel at the applicator insertion site reduced the tissue surface temperature rises significantly in all cases.

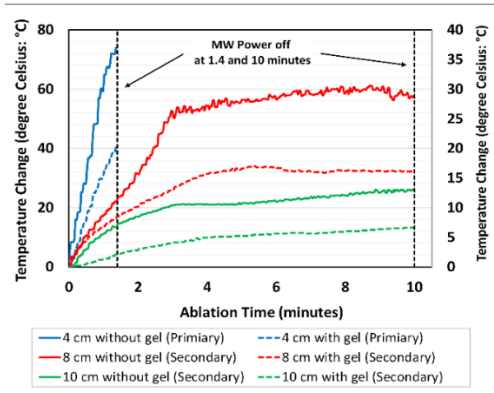


Figure 1. Surface temperature changes during MWA. With ultrasound gel applied, the temperature rise measured at the tissue surface were dropped from 73°C to 40°C, 31°C to 16°C, and 14°C to 6°C for MWA with the applicator insertion depth of 4, 8, and 10 cm.

**Conclusion:** Negligible temperature changes due to RF-heating were observed using the MWA system. Significant temperature increases were measured during MWA due to action of MWA system, which can be mitigated by increasing the applicator insertion depth. Further reduction in temperature change could potentially be achieved by using ultrasound gel.



# Evaluation of Cryoablation Probe Artifacts at 0.55 T

Florian Maier<sup>1</sup> and Jurgen J. Fütterer<sup>2</sup>

<sup>1</sup>Siemens Healthcare GmbH, Erlangen, Germany

<sup>2</sup>Department of Medical Imaging, RadboudUMC, Nijmegen, The Netherlands

## Purpose

Recently, 0.55 T MR scanners with 80 cm bore diameter were introduced. Large bore diameters can facilitate MR-guided percutaneous needle interventions such as cryoablation procedures. The additional space can provide more freedom in the selection of cryoablation probe trajectories.

However, reduced  $B_0$  field strength affects the susceptibility artifacts of devices [1,2] such as cryoablation probes and, hence, their visibility in MR images. In this work, the artifact size was evaluated using prototype interactive pulse sequences at 0.55 T.

## Material and Methods

The experiments were performed on a 0.55 T MR scanner (*MAGNETOM Free.Max*, Siemens Shenzhen Magnetic Resonance Ltd., Shenzhen, China) using the prototype pulse sequences *BEAT interactive* and *HASTE interactive (iMRI for MAGNETOM Free.Max WIP)*, Siemens Healthcare GmbH, Erlangen, Germany). The following pulse sequence parameters were used:

bSSFP: flip angle =  $90^\circ$ , TE = 2.78 ms, TR = 5.56 ms, TA = 549 ms, matrix =  $192^2$ , resolution =  $1.5 \times 1.5 \text{ mm}^2$ , slice thickness = 4.0 mm, bandwidth = 668 Hz/pixel, GRAPPA acceleration = 2, partial Fourier = 7/8.

GRE: flip angle =  $50^\circ$ , TE = 5.52 ms, TR = 11.83 ms, TA = 1088 ms, matrix =  $160^2$ , resolution =  $1.5 \times 1.5 \text{ mm}^2$ , slice thickness = 4.0 mm, bandwidth = 147 Hz/pixel, GRAPPA acceleration = 2.

HASTE: flip angle =  $180^\circ$ , TE = 114 ms, TR = 2400 ms, matrix =  $192^2$ , resolution =  $1.5 \times 1.5 \text{ mm}^2$ , slice thickness = 4.0 mm, bandwidth = 200 Hz/pixel, GRAPPA acceleration = 2.

Imaging was performed using an *ex vivo* phantom (porcine liver tissue). For each phantom, an MRI compatible 17G cryoablation probe (*MRI IceRod*, Boston Scientific, Marlborough, MA, USA) was positioned to enclose angles of  $0^\circ$ ,  $45^\circ$ , and  $90^\circ$  between the cryoablation probe and  $B_0$  direction. Images were acquired with three sequences for each probe position.

For evaluation, the diameter of each artifact (full width) was measured for all pulse sequence protocols and probe orientations.

## Results

Fig. 1 shows the probe artifacts for each cryoablation probe orientation and Tab. 1. summarizes the artifact diameters measured.

	$90^\circ$	$45^\circ$	$0^\circ$
bSSFP	$9.7 \pm 0.5 \text{ mm}$	$8.0 \pm 0.3 \text{ mm}$	$1.1 \pm 0.2 \text{ mm}$
GRE	$10.3 \pm 1.0 \text{ mm}$	$9.0 \pm 0.4 \text{ mm}$	$1.9 \pm 0.3 \text{ mm}$
HASTE	$4.9 \pm 0.4 \text{ mm}$	$3.1 \pm 0.7 \text{ mm}$	not visible

**Tab. 1:** Mean and standard deviation of artifact diameter.

## Conclusion

The artifacts of the used cryoablation probe were clearly visible on bSSFP and GRE images and allow for in-bore probe placement under MR guidance. On HASTE images the probe artifact was visible for  $45^\circ$  and  $90^\circ$  if phase encoding direction was set orthogonal to the probe direction.

## References

[1] Basar B *et al.*, Magn. Reason. Imaging 77 (2021). [2] Buchenberg WB *et al.*, ISMRM Workshop on Low Field MRI (2022).

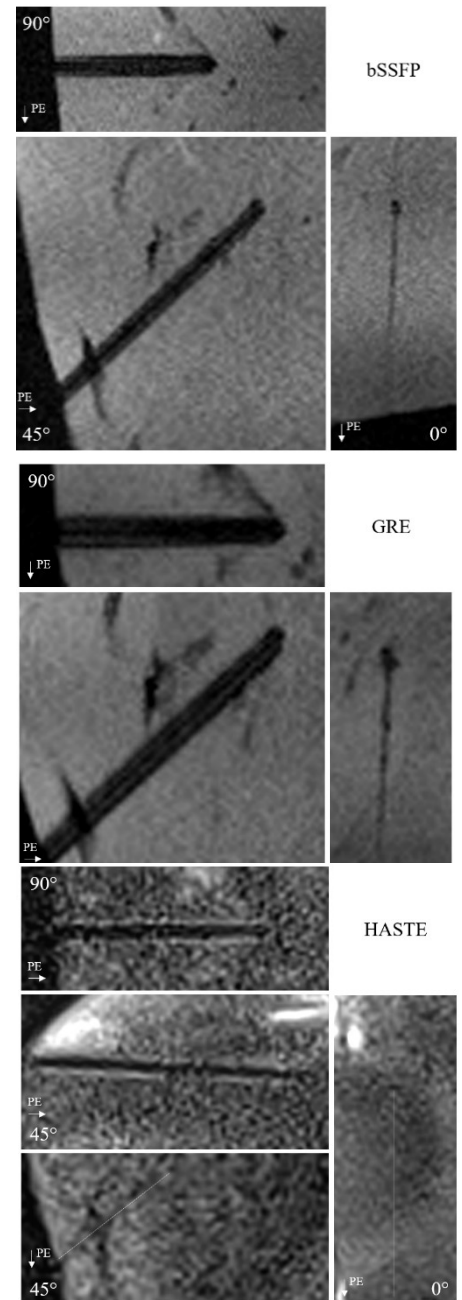


**Fig. 1:** Cryoablation probe artifact appearance in bSSFP, GRE, and HASTE images. Angles between  $B_0$  and probe  $90^\circ$ ,  $45^\circ$ , and  $0^\circ$ . White arrow shows phase encoding (PE) direction. Dashed line shows position of non-visible probe.

## Investigation of cryoneedle induced RF heating risk during MRI-guided cryoablation at 1.5T

Aiming Lu<sup>1</sup>, Christopher P Favazza<sup>1</sup>, Joel P Felmlee<sup>1</sup>, Scott M Thompson<sup>1</sup>, Lance A Mynderse<sup>2</sup>, David A Woodrum<sup>1</sup>, Krzysztof R Gorny<sup>1</sup>

<sup>1</sup>Department of Radiology, Mayo Clinic, Rochester, MN, USA

<sup>2</sup>Department of Urology, Mayo Clinic, Rochester, MN, USA

**Purpose:** To investigate the RF heating risk induced by the cryoneedle during MRI-guided cryoablation and potential strategies to mitigate the risk in a set of phantom experiments.

**Materials and methods:** Experiments were performed on a 1.5T scanner using the Visual-ICE MRI system on porcine tissue phantoms. RF heating during MRI was investigated using sequences with different SAR level ( SAR 2.1W/kg, 1.9 W/kg, 1.2W/kg and 0.7W/kg). The sequence with the highest SAR was used by default. The cryoneedles and gas lines were configured as typically used in prostate (the cryoneedles are often inserted near iso-center and the gas lines run along the longitudinal direction) and liver/non-prostate (the cryoneedles are inserted at an angle to the horizontal plane and the gas lines are run either on top of the patient near the bore center or close to the edge of the bore) treatments. The gas line was connected to the Visual-ICE system via a mobile connection panel (MCP). Fiber-optic temperature sensors were placed adjacent to the cryoneedle at the surface of the phantom and/or the tip of the cryoneedle to record temperature changes during imaging in all tests.

In the “prostate” configuration, an acrylic grid was used for guiding cryoneedle-insertion and the IceRod cryoneedle was advanced ~8cm into the phantom using an Angiocath through the center and 4 corner grid holes. The center hole was roughly aligned to the scan bore center. At the grid location with the highest heating, the measurement was repeated with the cryoneedle insert depth varied from 2-10 cm in steps of 2cm. In the “liver/non-prostate” configuration, the cryoneedle was inserted ~10cm into the phantom. Four experiments were conducted with and without the use of a catheter needle using both the straight and bent Ice-Rod needles. The gas line run along roughly the center of the bore and along the side of the bore. The experiments were repeated with the gas line connected and disconnected from MCP.

**Results:** RF heating was consistently observed in the experiments. In the “prostate” configuration, the measured temperature change during the T2W sequence at the tissue surface varied with cryoneedle insertion locations and depth. The highest temperature increase was 6.3°C when the cryoneedle was furthest from bore center (~5cm). Virtually no heating was observed when the gas line was disconnected from the MCP. In the “liver” configuration, significant (>85°C) and rapid (1.9°C/sec) temperature increases were observed. the angiocath used was charred near the tip, and signs of RF burns were observed along its length. A much lower temperature rise of ~20°C was observed without the Angiocath.

Similar heating phenomenon was for straight and bent cryoprobe. Heating was strongly dependent on configuration of cryoneedle and the gas line. Positioning the cryoneedle gas lines along the bore center resulted in significant heating reduction. The RF heating decreased nearly linearly with decreased SAR. Disconnecting the gas line from the MCP during MRI resulted in negligible RF heating. Moving the MCP away from the bore also appeared to reduce the heating.

**Conclusion:** Significant RF heating/burn could result MRI during cryoablation depends on the configuration of the cryoneedles and gas lines. We have demonstrated several strategies which could be used to mitigate these risks, including careful configuration of the cryoneedles and gas lines, using low SAR sequences, disconnecting the gas lines when possible and optimally positioning the MCP unit.

## TITLE

Intraoperative Neurophysiological Monitoring with Motor Evoked Potentials during MRI-guided Cryoablation: Initial Feasibility, Safety and Clinical Experience

## AUTHORS

<sup>1</sup>Scott M. Thompson M.D, Ph.D., <sup>2</sup>E. Matthew Hoffman D.O., Ph.D., <sup>1</sup>Garret M. Powell M.D., <sup>2</sup>Tatsuya Oishi, M.D., <sup>2</sup>Laura R. Schmidt, R. EEG T., <sup>2</sup>Teresa P. Velez, <sup>1</sup>Daniel A. Adamo M.D., <sup>1</sup>Christopher P. Favazza Ph.D., <sup>1</sup>Aiming Lu Ph.D., <sup>1</sup>Joel Felmlee Ph.D., and <sup>1</sup>David Woodrum M.D., Ph.D.

## AFFILIATIONS

<sup>1</sup>Department of Radiology, Mayo Clinic, Rochester, MN, USA

<sup>2</sup>Department of Neurology, Mayo Clinic, Rochester, MN, USA

## PURPOSE

To determine the feasibility, safety, and effectiveness of intraoperative neuromonitoring with real-time motor evoked potential (MEP) monitoring during MRI-guided soft tissue cryoablation.

## MATERIALS AND METHODS

Patients undergoing MRI-guided soft tissue cryoablation in proximity to major motor and sensory nerves with real time intraoperative motor evoked potential (MEP) monitoring were retrospectively reviewed after obtaining informed consent. Pre-ablation and immediate post-ablation neurologic exams were performed. Following diagnostic imaging and cryoprobe placement, stimulation and recording electrodes for MEP were placed by the intraoperative neurophysiological monitoring (IONM) team with care to maintain a strict linear course of the electrode wires without touching the patient or the bore. Baseline MEPs were obtained and cryoablation was initiated with real-time MR monitoring in low-SAR mode. MEPs were obtained when MR imaging paused between series during freezing and compared to baseline. Following completion of cryoablation, final MEPs were obtained, MEP electrodes were then removed, and completion diagnostic MR imaging performed at normal SAR mode. All needle electrode sites were examined for evidence of skin burns. Neurologic exam was repeated in the post-anesthesia recovery unit.

## RESULTS

Between April 21-June 10, 2022, three patients underwent MRI-guided soft tissue cryoablation with MEP monitoring for 1) a painful vascular malformation in the right subscapularis muscle in close proximity to the lower trunks of the brachial plexus (**Figures 1 and 2**), 2) neuralgia of the posterior femoral cutaneous nerve in proximity to the right sciatic nerve, and 3) right posterior obturator lymph node prostate cancer metastasis in proximity to the sciatic and obturator nerves. MEP were obtained at baseline, intra-procedurally and post-ablation in all patients. The magnetic field did not significantly interfere with MEP recording. Diagnostic intraprocedural MR images were obtained during iceball monitoring without artifact or image quality degradation from the intermittent MEP monitoring. The iceball came within 8 mm of the brachial plexus in patient 1 (**Figure 3**) and abutted the sciatic nerve in patients 2 and 3. There were no changes in the MEP signals during the freeze-thaw cycles or at completion of the cryoablation compared to baseline. There were no changes in motor or sensory exam following the cryoablation compared to

baseline, and no patient reported weakness or paresthesia. There were no skin burns at any of the MEP electrode sites.

## CONCLUSION

These initial data suggest that intraoperative neurophysiological monitoring of motor evoked potentials during MRI-guided cryoablation is feasible, safe, and effective. Development of a strict safety protocol in collaboration with neurologists and MRI physicists is essential to ensure diagnostic electrophysiologic data and MR images while preventing thermal skin injury.

## FIGURES

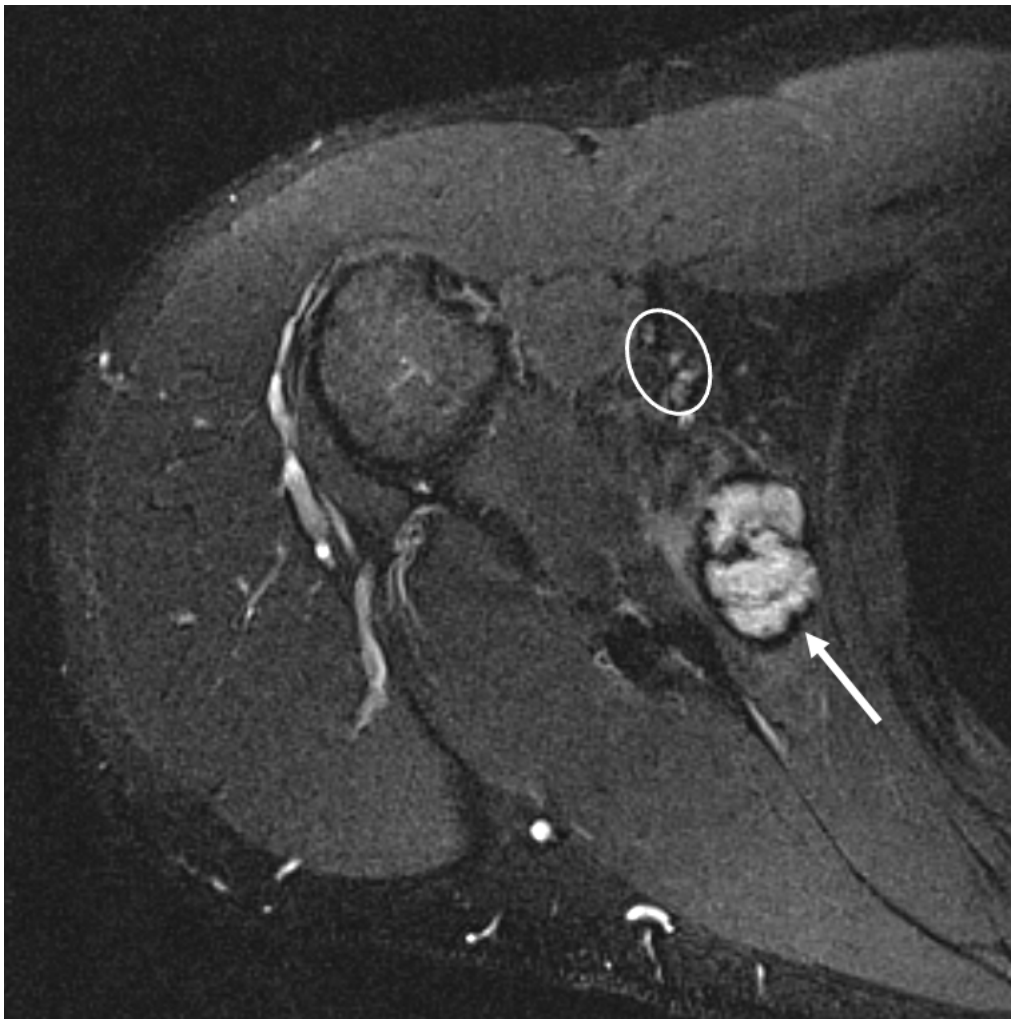


**Figure 1.** Preprocedural axial short tau inversion recovery sequence demonstrates a lobulated hyperintense intramuscular lesion in the subscapularis with a dark hemosiderin rim and perilesional edema (arrow) consistent with a vascular malformation. The lesion is 1.4 cm posteromedial to the brachial plexus at the level of the transition from the cords to the branches (oval).

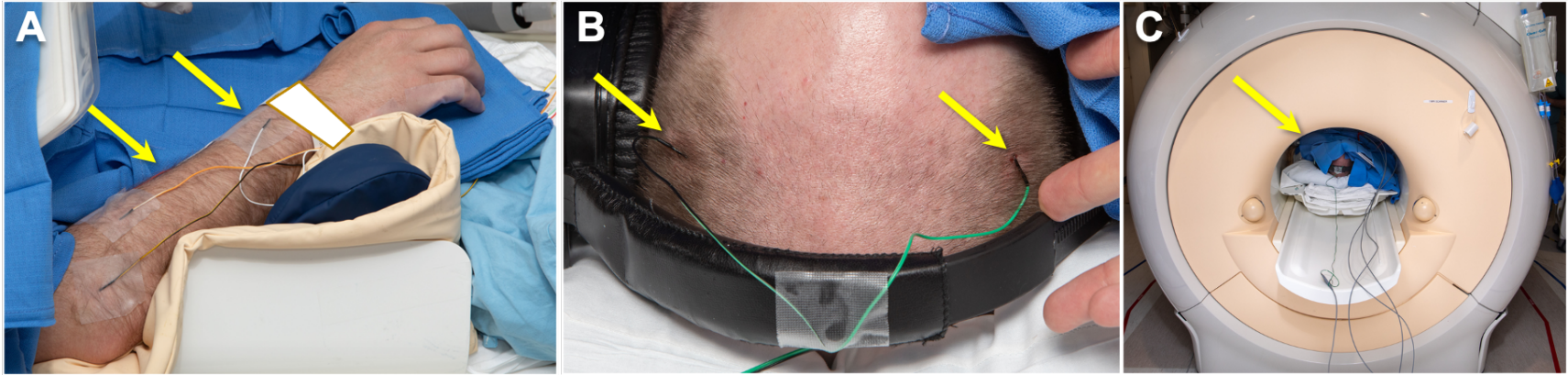


**Figure 2.** Motor evoked potential electrode setup with placement of electrodes in A) the right upper extremity and B) the scalp. C) Patient positioned within the MR bore with exiting MEP electrodes.

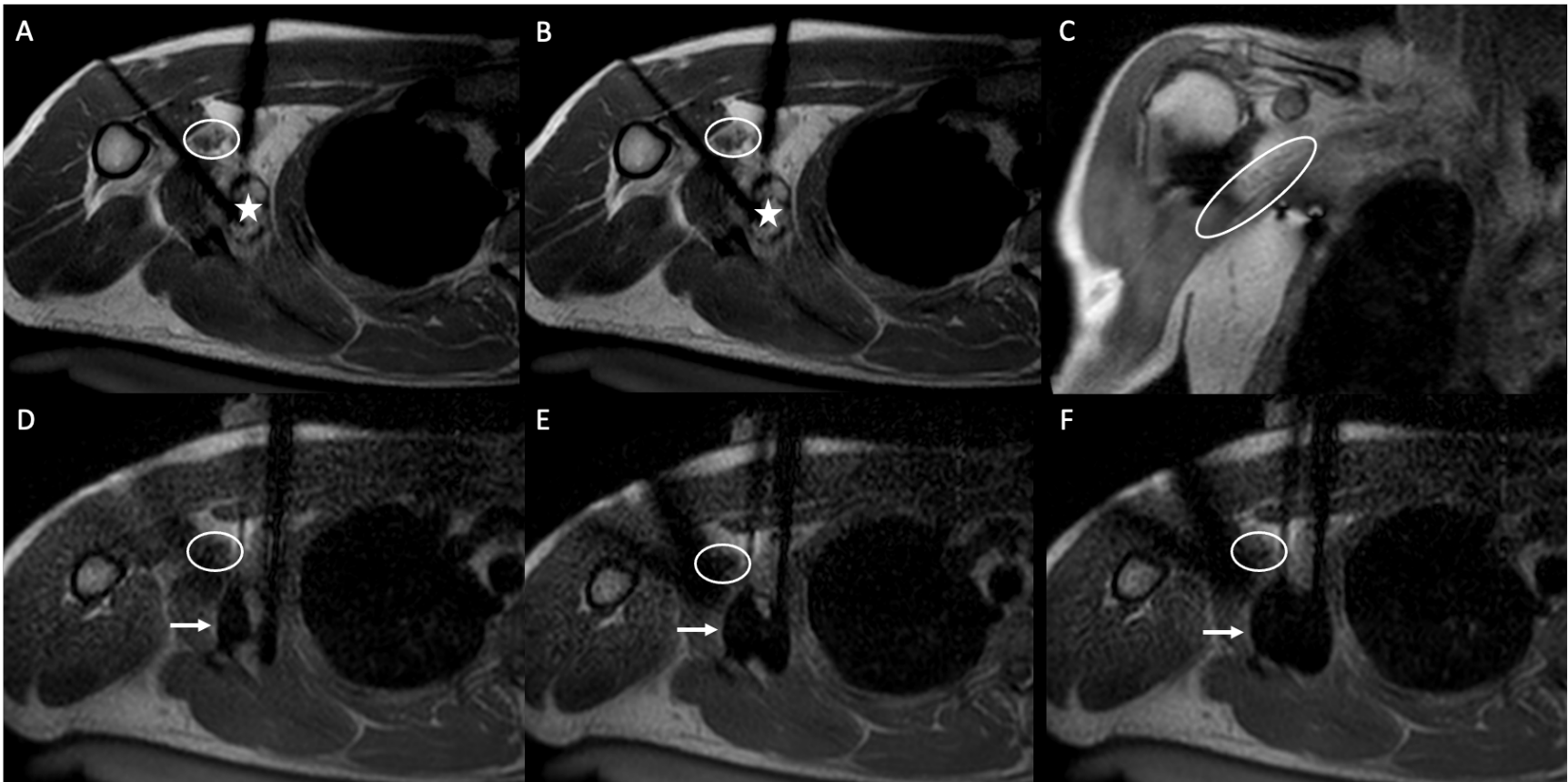


**Figure 3.** MR guided cryoablation with the probes within the vascular malformation (star in A-B) which have been placed superolateral and inferomedial to the brachial plexus and axillary vessels (oval in A-F). Progressive enlargement of the ice ball (arrows D-F) during a freezing cycle which comes within 8 mm of the traversing brachial plexus and axillary vessels.

## **MRI-guided high-dose-rate interstitial brachytherapy of small hepatic malignancies (d ≤ 12 mm) – use of the gadoxetic-acid plateau phase**

Ebel S<sup>1</sup>, Meyer HJ<sup>1</sup>, Prasse G<sup>1</sup>, Seehofer D<sup>2</sup>, Berg T<sup>3</sup>, Hering K<sup>4</sup>, Kuhnt T<sup>4</sup>, Busse H<sup>1</sup>, Hofmann A<sup>1</sup>, Gößmann H<sup>1</sup>, Denecke T<sup>1</sup>

<sup>1</sup> Department of Diagnostic and Interventional Radiology, University Hospital Leipzig, Germany

<sup>2</sup> Department of Hepatobiliary Surgery and Visceral Transplantation, University Hospital Leipzig, Germany

<sup>3</sup> Department of Gastroenterology, Hepatology, Infectiology and Pneumology, University Hospital Leipzig, Germany

<sup>4</sup> Department of Radiation Therapy, University Hospital Leipzig, Germany

**Background** MRI provides a wealth of structural and functional tissue information and is also commonly used for sheath positioning for high-dose-rate interstitial brachytherapy in afterloading technique. Reliable visualization and exact localization of small hepatic malignancies (d ≤ 12 mm) to be treated by brachytherapy, however, can be challenging without the use of an adequate contrast medium (gadoxetic acid).

**Purpose** To investigate the feasibility, technical success and safety of using the gadoxetic acid plateau for tumor visualization during percutaneous MRI-guided afterloading of small hepatic malignancies (d ≤ 12 mm).

**Methods** This is a retrospective case study of 12 patients (3 female), 59.7 ± 12.1 years old (mean ± SD), with small hepatic malignancies (d ≤ 12 mm) nodules that were not visible in non-contrast MR images. The decision for an afterloading treatment of the patients had been made in an interdisciplinary tumor board. Procedures were carried out in a 1.5-T MRI (Magnetom Aera, Siemens Healthcare, Erlangen, Germany).

Feasibility was assessed by analyzing proper identification of the target tumor, tumor delineation during MRI-guided needle positioning and number of needle adjustments required for accurate sheath placement. Technical success was defined as subsequent high-dose-rate interstitial brachytherapy with a tumor coverage of ≥ 99%. Safety was assessed from reports of procedure-related complications.

**Results** In all 12 cases, the target tumors were not visible in non-contrast MR images but in the late post-contrast phase (gadoxetic acid). Mean (± SD) tumor diameter was 10.1 (± 1.1) mm. The number of needle adjustments was 7 (± 4). The technical success rate was 100% and no major complications were reported. Follow-up imaging (after 6.1 ± 4.3 months) showed no local tumor progression or recurrence. One patient (8.3%) showed a new extrahepatic tumor manifestation.

**Conclusions** Use of the gadoxetic-acid plateau phase for MRI-guided brachytherapy of otherwise MR-occult lesions is a feasible approach for an effective and safe treatment of small hepatic malignancies.

# MR-based Volumetric Assessment of Thyroid Nodule Radiofrequency Ablation in Anthropomorphic Phantoms

T. Boers<sup>1</sup>, G. Wennemars<sup>2</sup>, S.J. Braak<sup>3</sup>, M. Versluis<sup>1</sup>, S. Manohar<sup>1</sup>, W.M. Brink<sup>2</sup>

<sup>1</sup>Multi-Modality Medical Imaging Group, University of Twente, Enschede, the Netherlands; <sup>2</sup>Magnetic Detection & Imaging Group, University of Twente, Enschede, the Netherlands; <sup>3</sup>Department of Radiology, Ziekenhuisgroep Twente, Hengelo, the Netherlands

**Purpose:** Despite the advantages of minimally invasive treatment for thyroid nodular disease, it is only applied in approximately 3-28% of the cases, with surgical removal being performed most often.<sup>1</sup> Thermal ablation treatments such as radiofrequency ablation (RFA) can however provide a safe and effective alternative to thyroidectomy with a reduced risk for hypothyroidism and other complications.<sup>2</sup>

To improve efficacy of thyroid nodule ablation, improved planning and monitoring technologies and training programmes are needed to help guide and train clinical staff in improving needle placement and thereby reducing ablation margins while preserving nearby critical structures.<sup>3,4</sup> Previous research has evaluated the use of thermochromic inks for the assessment of ablation zones, which involves time-consuming mechanical dissection of the phantom and provides only cross-sectional information on the extent of the ablation zone.

In this work, we evaluate an MR-based volumetric approach for ablation zone assessment in anthropomorphic thyroid-mimicking phantoms. By leveraging the temperature-sensitive MR-properties of proteins, which change during coagulation, the attained ablation temperature is imprinted in the phantom material and can be quantified by means of  $T_2$  mapping.<sup>5</sup> By incorporating both the thyroid nodule compartments as well as surrounding structures, a realistic simulation of the ablation procedure can be realised.

## Materials and Methods: Phantom construction and characterization:

Tissue-mimicking phantoms were constructed using polyacrylamide (PAA) gel as described in Boers et al.,<sup>4</sup> here omitting thermochromic ink and incorporating 5% (v/v) of egg-white proteins. The phantom material was first characterized by constructing 24 cylindrical phantoms which were heated to target temperatures of 48-78 °C in a temperature-controlled water bath. Each phantom was heated for 15 minutes and monitored to ensure that a homogeneous temperature distribution was reached.

An anthropomorphic phantom was then created by preparing 3D moulds of the anatomical structures of the thyroid, thyroid nodule, as well as the trachea, nerves and blood vessels, and subsequently filling the parts of the phantom in consecutive stages inside a rectangular container. The thyroid nodules were then ablated using an internally cooled 7-mm, 18G, monopolar ablation needle (STARmed Co., Goyang, South Korea).

**MR system and protocol:** MR data were acquired in a 1.5T MRI system (Aera, Siemens Healthineers, Erlangen, Germany). Reference  $T_2$  maps were obtained in the cylindrical phantoms using a 3D fast spin echo sequence (FSE) with the following settings: FOV = 192×192×64 mm, 1 mm<sup>3</sup> isotropic voxel size, TR/TE<sub>eq</sub>/ΔTE = 1000/40-280/40 ms, number of refocusing pulses = 64, echo spacing = 10 ms. The same sequence was acquired in the anthropomorphic phantom with two ablated nodules.  $T_2$  maps were generated by fitting the data to a 2-parameter single exponential model using a custom post-processing procedure implemented in MATLAB. The  $T_2$  characteristics were then fit to a linear model for temperatures higher than 55 °C to enable direct data conversion.

**Results:** Figure 1 shows the  $T_2$  characterization results, which were used to fit the conversion curve to map  $T_2$  into temperature. Figure 2 shows the resulting ablation temperature maps obtained in the anthropomorphic phantom, overlaid over an FSE image. Figure 3 shows a 3D rendering of the ablation zone ( $T > 65$  °C). Volumetric analysis indicated that both ablation zones covered approximately 72% of the corresponding nodule.

**Conclusion:** MRI offers a quantitative strategy to non-invasive volumetric assessment of thyroid nodule ablation procedures in anthropomorphic phantoms.

This approach offers a test-bed for the development of planning and monitoring technologies, as well as provide a realistic tool for training programmes aimed at improving the efficacy of thyroid nodule ablation. Future studies will aim to evaluate ablation procedures during flow, and the evaluation of treatment planning strategies.

## References:

1. Hegedüs L, Frasoldati A, Negro R, Papini E. *European Thyroid Journal*. 2020;9(4):194-204. doi:10.1159/000506513
2. Trimboli P, Castellana M, Sconfienza LM, et al. *Endocrine* 2019 67:1. 2019;67(1):35-43. doi:10.1007/S12020-019-02019-3
3. Papini E, Monpeyssen H, Frasoldati A, Hegedüs L. *European Thyroid Journal*. 2020;9(4):172-185. doi:10.1159/000508484
4. Boers T, Braak SJ, Versluis M, Manohar S. *European Radiology Experimental*. 2021;5(1):1-10. doi:10.1186/S41747-021-00230-4/TABLES/3
5. McDonald M, Lochhead S, Chopra R, Bronskill MJ. *Physics in Medicine & Biology*. 2004;49(13):2767. doi:10.1088/0031-9155/49/13/001

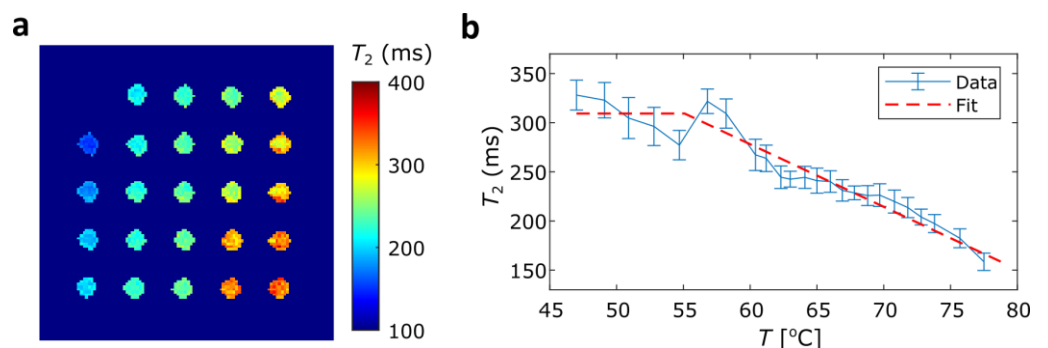


Figure 1. Phantom  $T_2$  characterization as a function of temperature. Shown are  $T_2$  maps (a) and fitted transition curve (b).

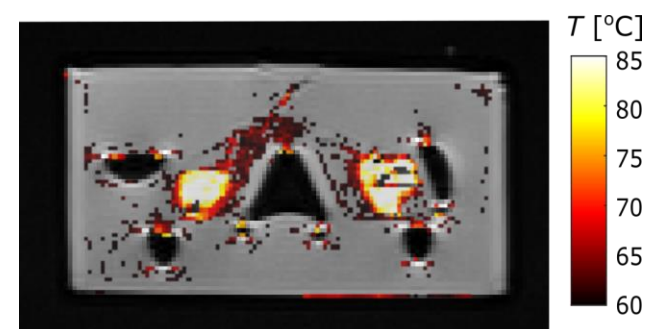


Figure 2. Overlay of the temperature map on an FSE image, indicating a sharp transition around the ablation zone.

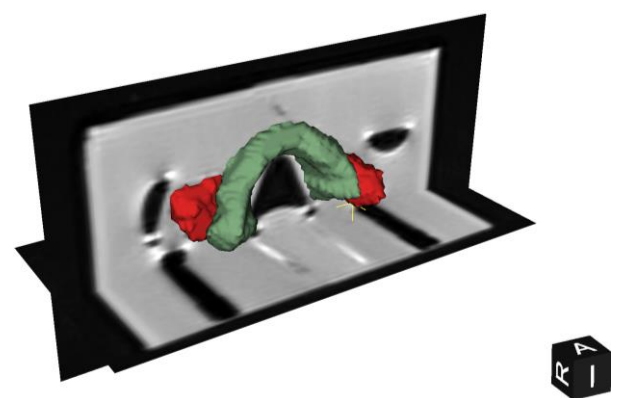


Figure 3. 3D rendering of the ablation zones (red) projected onto the thyroid (green) and surrounding phantom (grey).



## Author Index

Adamo, Daniel	12, 14, 52, 53, 59, 87, 119 122, 126, 128, 129, 133
Ahlawat, Shivani	33, 35, 72
Aktas, Bahriye	67
Albrecht, Joachim	101
Aleong, Amanda	102, 103
Alpers, Julian	70, 113, 116
Anderson, Katelyn	87
Antoniou, Anastasia	86
Artazkoz, Juanjo	8
Auloge, Pierre	31
Bailis, Nikolaos	67, 85
Balakrishnan, Sathish	70, 113, 116
Barkati, Maroie	19
Barker, Devin	53
Beauchemin, Marie-Claude	19
Becker, Mathias	70, 113, 116
Bednarz, Bryan	95
Beliveau-Nadeau, Dominic	19
Belker, Othmar	21, 30
Bendel, Emily	87, 93
Berg, Deb	53
Berg, Thomas	37, 137
Berlin, Alejandro	19, 74, 102
Bernardes, Mariana C.	26
Beyer, Lukas	61
Bhat, Himanshu	29
Bhushan, Chitresh	95, 114
Bibic, Adnan	5
Bijvoet, G.P.	43
Bjarnason, Haraldur	87
Blanco Sequeiros, Roberto	60
Bock, Michael	41, 46, 105, 115
Boers, Tim	138
Bortfeld, Thomas	115
Boudabbous, Sana	34, 69
Bour, Pierre	22, 25, 28, 66, 77, 78, 79
Braak, Sicco	138
Brace, Chris	27, 95
Brace, Christopher	114
Bradley, Lee W.	104
Breton, Elodie	31, 80, 84
Brink, Wyger	112, 138

Brockmann, Alexander	101
Bruesch, Inga	23
Buchenberg, Waltraud	49
Buelo, Collin	27
Bulte, Jeff	5
Busse, Harald	7, 37, 50, 67, 85, 137
Cabras, Paolo	31, 84
Callahan, Paige	53
Chaldoupi, S.M.	43
Chan, Rosanna	10, 16
Chemouny, Stéphane	28, 66, 118
Chen, Yue	40
Choquet, Karine	80, 84
Chung, Peter	19, 74, 102
Cima, Michael J.	121
Cleary, Kevin	40, 108
Collins, Jeremy	93
Cormack, Robert A.	121
Corr, Kateri	10, 16
Couillaud, Franck	83
Cranston, Lori	53
Curry, Timothy	53
Dabrin, Fanny	66
Dalili, Danoob	33, 35, 71, 72, 73
Damianou, Christakis	81, 86
Degertekin, F. Levent	104
Delouya, Guila	19
Demir, Alican	52
Denecke, Timm	7, 37, 50, 67, 85, 137
Desclides, Manon	28, 118
Dietrich, Olaf	22, 25, 79
Dominguez, Dennis	34
Donig, Julian	85
Dora, Chandler	75
Dorfer, Christian	3
Dumont, Erik	31, 82
Dumoulin, Charles	40
Dyer, Michael	121
Düring, Klaus	49
Düx, Daniel	124
Düx, Daniel Markus	61
Düx, Markus	61
Ebel, Sebastian	37, 50, 67, 85, 137
Eggert, Michelle	53
Ehregut, Constantin	7

Ehtiati, Tina	6
Eisenmann, Marcel	109
Ekchian, Gregory J.	121
Ekrem, David	53
El Hamrani, Dounia	77, 83
Engel, Katja	117
Evripidou, Nikolas	81
Faacks, Aaron	27, 114
Faller, Thibaut	22, 25, 77, 79
Faust, Jonas F.	97
Favazza, Christopher	12, 14, 52, 53, 59, 87, 93 111, 119, 122, 126, 128, 129, 132 133
Felmlee, Joel	53, 111, 119, 122, 126, 129, 132
Finelli, Antonio	10, 16
Fischer, Elizabeth	40, 108
Fomin, Ivan	39, 51, 106, 107, 109, 110, 117
Foo, Thomas	95
Foroughi, Pezhman	52
Fournelle, Marc	68
Franz, Toni	7
Frey, Greg	75
Fritz, Jan	32, 33, 35, 40, 71, 72, 73
Fu, Yingli	6
Fütterer, Jurgen	13, 131
Gangi, Afshin	31
Gantz, Sebastian	96
Gareis, Daniel	106, 107
Gaspar, Thomas	91
Gebremeskel, Mikias	108
Gehling, Katie	53
Genevois, Coralie	83
Geng, Ruiqi	27
Gerlach, Thomas	117, 125
Gertner, Mark	16
Ghai, Sangeet	10, 16
Gholami Bajestani, Denis	44, 48
Ghose, Soumya	95
Giannakou, Marinos	81, 86
Glandorf, Julian	124
Glicksman, Rachel	74
Gockel, Ines	85
Gorny, Krzysztof	53, 119, 132
Greiser, Sebastian	68
Gronski, Phillip Alexander	23
Guillemin, Pauline C.	34, 69

Gunderman, Anthony	40
Gutberlet, Marcel	21, 23, 24, 30, 51, 76, 117 124, 125
Gutierrez, Enrique	74
Gutt, Moritz	24
Guyot, Mathieu	66, 77, 82
Gößmann, Holger	7, 37, 50, 85, 137
Haj-Mirzaian, Arya	35
Hammersen, Vincent	44
Handzel, Romy	67
Hangel, Gilbert	3
Hanson, Patrick	53
Harlan, Kenny	52
Hata, Nobuhiko	38
Hegel, Alexander	44
Heidt, Timo	46
Hellms, Susanne	23
Helou, Joelle	19, 74
Hensen, Bennet	21, 23, 24, 30, 39, 51, 70 76, 106, 107, 109, 110, 113, 116 117, 124, 125
Hering, Kathrin	137
Hernando, Diego	27
Hickey, Samantha	115
Hoeger, Kim	44
Hoffman, E. Matthew	53, 126, 133
Hoffmann, Aswin	96
Hoffmeister, Albrecht	85
Hofmann, Andrea	37, 137
Holman, Ryan	69
Holmes, James	27, 95, 114
Holtackers, R.J.	43
Horn, Lars-Christian	7
Horstmann, Dominik	24, 30, 124
Howe-Clayton, Desirae	53, 87
Hubmann, Max Joris	106, 107
Huo, Yan	91
Iordachita, Iulian	40
Isaac, Amanda	33, 35, 72, 73
Ishak, Ounay	80, 84
Jabaraj Soloman, Mathews	70
Jaubert, Olivier	45
Jeanjean, Pauline	83
Jochimsen, Thies	44
Jonigk, Danny	23

Joseph, Lisa	19
Josset, Anne	80, 84
Jupitz, Sydney	95
Kadoury, Samuel	19
Karsch, Leonhard	96
Kasprian, Gregor	3
Kaza, Evangelia	121
Khalil, Adham	6
Kikinis, Ron	1
Knavel Koepsel, Erica	53, 87, 93, 128
Knull, Lucas	106, 107
Kocaturk, Ozgur	98, 104
Kowal, Robert	51, 106, 107
Kowalik, Grzegorz	42
Krafft, Axel Joachim	29, 49, 91
Kraitchman, Dara	6
Kuddannaya, Shreyas	5
Kuhnt, Thomas	137
Kuroda, Kagayaki	20
Kwon, Eugene	12, 14
Ladd, Mark E.	97
Landgraf, Lisa	44, 68
Lange, Franziska	68
Lauper, Nicolas	34
Lebret, Quentin	78
Lederman, Robert	98, 104
Legout, Jordan	75
Lentini, Sergio	22, 25, 79
Leonhardi, Jakob	67, 85
Levesque, Vincent M	26
Li, Gang	40
Lindborg, Katherine	91
Linder, Nicolas	7
Linz, D.	43
Littin, Sebastian	105
Liu, Zhihuiamy	19
Lomas, Derek	12, 14, 53, 59
Lorton, Orane	34, 69
Lottner, Thomas	41, 46, 105
Lu, Aiming	12, 14, 52, 53, 59, 87, 93 111, 119, 122, 126, 128, 129, 132 133
Löning Caballero, J. Joaquin	21, 24, 30, 76, 125
M'Rad, Yacine	69
Machinet, Guillaume	28, 118

Maier, Florian	97, 101, 131
Majeed, Waqas	29
Malik, Shaihan	42
Manohar, Srirang	138
Marcelin, Clément	77
Martin, Mireille	67, 85
Maturana, Enrique	34
Mayer, Julia	91
McCluskey, Stuart	10, 16
McDannold, Nathan	4
Melzer, Andreas	44, 48, 67, 68, 85
Meyer zu Hartlage, Karen	21, 30, 76, 125
Meyer, Hans Jonas	37, 50, 137
Mihl, C.	43
Mills, David	95, 114
Milosavljevic, Srdjan	41
Mitra, Jhimli	95, 114
Monfaredi, Reza	40, 108
Montalt-Tordera, Javier	45
Montazeri, Ali	75
Moran, Gerald	103
Moreira, Pedro	15, 103
Mouzakis, Nicholas	108
Mulik, Christina	44, 48
Muthurangu, Vivek	45
Mynderse, Lance	12, 14, 52, 53, 59, 111, 122 128, 132
Ménard, Cynthia	19
Nabavi, Arya	2
Navarro-Domenech, Inmaculada	19
Neofytou, Alexander	42
Nicolas, Benedicte	19
Niebisch, Stefan	85
Nies, H.M.J.M.	43
Nieves, Mari	42
Nijveldt, R.	43
Odenbach, Robert	39, 109, 110
Odéen, Henrik	29
Oishi, Tatsuya	133
Oosterveld, Ralph	112
Oshinski, John	104
Ozenne, Valéry	25, 28, 45, 66, 77, 78, 118
Öcal, Osman	22, 25, 79
Özen, Ali	41, 46, 105

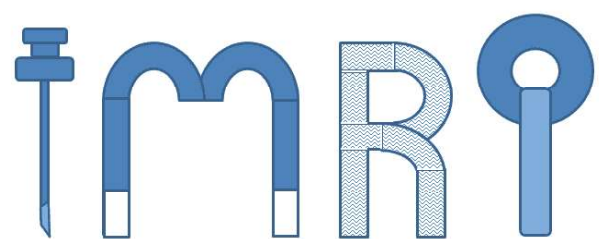
Pang, Jianing	29
Pannicke, Enrico	106, 107
Parker, Dennis	23, 29
Patel, Aqsa	95
Pawelke, Jörg	96
Pech, Maciej	70, 113, 116
Peloso, Andrea	69
Perlis, Nathan	10, 16
Peter, Juliane	96
Phelan, Martin	92
Pierre, Christophe	28, 118
Piorkowski, Christopher	91
Planas, Montse	8
Polak, Daniel	97
Polenz, Laureen	70
Poletti, Pierre-Alexandre	34, 69
Polites, Stephanie	87
Powell, Garret	87, 133
Prasse, Gordian	37, 50, 137
Pruckner, Philipp	3
Pruy, Eva	44
Ptacek, Wolfgang	115
Pu, Liying	91
Puig, Josep	8
Pushparajah, Kuberan	42
Pérez de Tudela, Anna	8
Quesson, Bruno	25, 28, 45, 66, 77, 78, 82 83, 118
Rafiee, Nasser	98
Raman, Srinivas	19, 74
Ramotar, Matthew	74
Rashidi, Ali	33, 35, 72
Razavi, Reza	42
Reich, C. Martin	44, 48
Reichert, Andreas	41, 115
Reimert, Daniel	21, 30
Reiss, Simon	41, 46, 105
Ren, Liqiang	119, 122, 129
Rice, Cheri	6
Richter, Utz	91
Ricke, Jens	22, 79
Ricoeur, Alexis	69
Rink, Alexandra	19, 74
Rose, Georg	39, 51, 106, 107, 109, 110, 117
Roujol, Sebastien	42
Rube, Martin	49
Rumpel, Regina	23
Russe, Maximillian	105

Rössler, Karl	3
Sabri, Osama	44
Sala, Sònia	8
Salomir, Rares	34, 69
Schaefers, Gregor	44
Schaudinn, Alexander	7
Schauer, Senta	44
Scheffler, Max	34
Scherbel, Selina	106, 107
Schmid, Michael	44
Schmidt, Laura	133
Schröer, Simon	76
Schönherr, Till	85
Seehofer, Daniel	37, 137
Seethamraju, Ravi	26, 103
Seidensticker, Max	22, 25, 79
Sella, David	75
Shakeri-Zadeh, Ali	5
Shakoor, Delaram	33
Sharma, Karun	40, 108
Sitti, Metin	92
Smink, J.	43
Smit-Fun, V.M.	43
Speck, Oliver	51, 106, 107, 125
Speicher, Daniel	68
Stark, Sylvia	67
Steeden, Jennifer	45
Steinmetz, Michael	44
Stenzel, Wayne	53
Stoianovici, Dan	40
Stroszczyński, Christian	61
Stöckli, Alex	34
Sundaramurthy, Aravindhan	19
Surup, Hans	67, 85
Sánchez López, Juan Sebastián	70, 113, 116
Tarasek, Matt	27
Tarasek, Matthew	95, 114
Taussky, Daniel	19
Tempany, Clare	9, 15
Thió-Henestrosa, Santi	8
Thoma, Niklas	39, 110
Thompson, Scott	12, 14, 52, 53, 59, 87, 93 119, 122, 126, 128, 129, 132, 133
Tokuda, Junichi	15, 26, 103, 121
Tollefson, Megha	87
Tomala, Jakub	91



Tomschik, Matthias	3
Tretbar, Steffen	68
Tuncali, Kemal	15, 26, 36
Ulbrich, Stefan	91
Unal, Isil	105
Uzun, Dogangun	98
van der Kwast, Theodorus	10, 16
van Gorkum, Robbert	68
Vappou, Jonathan	31, 80, 84
Velez, Teresa	133
Verdaasdonk, Ruud	112
Verloh, Niklas	41
Vernooy, K.	43
Versluis, Michel	138
Vilanova, Joan C	8
Vogel, Arndt	57
Vogele, Michael	41
von Zur Mühlen, Constantin	46
Vondran, Florian W. R.	23
Wach, Benoit	31
Wacker, Frank	21, 23, 24, 30, 39, 51, 56 70, 76, 106, 107, 109, 110, 113 116, 117, 124, 125
Wagner, Michael	91
Wais, Jonathan	3
Walczak, Piotr	5
Walter, Sven	71
Weersink, Robert	19, 74, 102, 103
Weisgerber, Christiane	67
Weiss, Clifford R.	6, 47
Welch, Brian	53, 126
Wells, Shane	27, 95, 114
Wennemars, Germen	138
Werlein, Christopher	23
Wildberger, J.E.	43
Wittauer, Eva-Maria	23
Woodrum, David	12, 14, 52, 53, 59, 87, 93 111, 119, 122, 126, 128, 129, 132 133
Yaras, Yusuf S.	104
Yarmolenko, Pavel	108
Yeo, Desmond	27, 95, 114
Yildirim, D. Korel	98, 104
Yon, Maxime	45

Zaitsev, Maxim	105
Zedda, Angela	91
Zhang, Xinrui	68
Zisman, Alex	16



imri

ISBN 978-3-00-073471-7